Microfabrication Methods to Improve the Kinetics of the Yttria Stabilized Zirconia – Platinum – Oxygen Electrode

by

Joshua L. Hertz

B.S. Ceramic Engineering
Alfred University, 2000

SUBMITTED TO THE DEPARTMENT OF MATERIALS SCIENCE AND ENGINEERING
IN PARTIAL FULFILLMENT OF THE REQUIREMENTS FOR THE DEGREE OF

DOCTOR OF PHILOSOPHY
IN MATERIALS SCIENCE AND ENGINEERING

AT THE
MASSACHUSETTS INSTITUTE OF TECHNOLOGY

SEPTEMBER 2006

Authored by ____
Joshua L. Hertz
Department of Materials Science and Engineering
August 14, 2006

Certified by____
Harry L. Tuller
Professor of Ceramics and Electronic Materials
Thesis Supervisor

Accepted by ____
Samuel M. Allen
POSCO Professor of Physical Metallurgy
Chair, Departmental Committee on Graduate Students

Microfabrication Methods to Improve the Kinetics of the Yttria Stabilized Zirconia – Platinum – Oxygen Electrode

by

Joshua L. Hertz

Submitted to the Department of Materials Science and Engineering
on August 14, 2006
in Partial Fulfillment of the Requirements for the Degree of
Doctor of Philosophy in Materials Science and Engineering

ABSTRACT

Solid oxide fuel cells are a potential electrical power source that is silent, efficient, modular, and capable of operating on a wide variety of fuels. Unfortunately, current technologies are severely limited in that they provide sufficient power output only at very high temperatures (>800°C). One reason for this is because the electrodes have very poor (and poorly understood) kinetics. The work described in this dissertation involves the microfabrication of model systems with triple phase boundary lengths that varied over an order of magnitude to systematically quantify and ultimately improve the kinetics of platinum electrodes on the surface of yttria stabilized zirconia electrolytes.

Platinum electrodes with well controlled geometry were sputtered onto the surface of bulk YSZ and onto sputtered YSZ thin films. An unexpected result was found whereby YSZ films of composition $Y_{0.09}Zr_{0.91}O_{2-x}$ had an ionic conductivity remarkably enhanced by a factor of 20-30. This is attributed to the films exhibiting nanometric grain sizes and thereby stabilizing the cubic morphology at considerably lower yttrium levels than is normally needed. This metastable cubic phase is suspected of having reduced defect ordering. Grain boundary resistance, which in YSZ is normally due to impurities that segregate and block ionic transfer, was found to also be significantly reduced in YSZ films. The films had a specific grain boundary conductivity enhanced by a factor of 30-100 compared to the bulk polycrystalline sample. This was believed to be due to the very low impurity content of the film grain boundaries.

Concerning the electrode polarization resistance, it was found that the electrodes placed on bulk standards and films deposited at high temperatures were on par with the best electrode conductance values from the literature. However, when the electrolyte surface was a film deposited at reduced temperature, the resistance decreased further by a factor of 300-500. The cause of this was revealed to be silicon contamination on the surfaces of the poorer-performing electrolytes. Triple phase boundary length-specific resistances as low as $3.7 \cdot 10^4$ Ω·cm at 378°C and $4.0 \cdot 10^7$ Ω·cm at 215°C were measured; these appear to be the lowest ever recorded. The measurements are possibly the first electrochemical characterization of nearly silicon-free YSZ surfaces. This study emphasizes the key role of chemical purity at the electrode-electrolyte interface.

Photolithography alone is unlikely to give technologically useful triple phase boundary lengths. In an attempt to achieve the triple phase boundary lengths needed for a practical device, reactive co-sputtering was used to produce composite Pt-YSZ thin films with a bi-continuous network morphology and grain sizes on the order of 30 nm. Such intimate mixing of the electronic and ionic conducting phases created an effective mixed ionic-electronic conductor with the entire surface of the film electrochemically active to the electrode reaction. The best processing conditions resulted in electrodes with an area specific polarization resistance less than 500 Ω·cm^2 at 400°C and, by extrapolation, 10 Ω·cm^2 at 511°C and 1 Ω·cm^2 at 608°C. These films may enable operation of a micro-solid oxide fuel cell at intermediate temperatures (400-500°C), and perhaps even lower temperatures with further microstructural optimization.

Thesis Supervisor: Harry L. Tuller
Title: Professor of Ceramics and Electronic Materials

To Jacy

CONTENTS

CHAPTER 1. INTRODUCTION

CHAPTER 2. EXPERIMENTATION

CHAPTER 3. RESULTS

CHAPTER 4. DISCUSSION

CHAPTER 5. CONCLUSIONS

APPENDIX A. NUMERICAL SOLUTION OF RESISTANCE

APPENDIX B. THERMAL STABILITY OF YSZ FILMS

FIGURES

TABLES

ACKNOWLEDGEMENTS

As I complete my formal education, I would like to first thank the great teachers in my life. I am forever grateful to Mrs. Jahowski, Mrs. Reynolds, Ms. Schuessler, and Prof. Amarakoon. I especially want to express my deep and sincere gratitude to Mr. Ayotte, my chemistry teacher in high school; he is a large part of how I came to be here.

The last teacher on this list, only by chronology, is my doctoral advisor, Prof. Harry Tuller. He has repeatedly proven his deep knowledge of the field, intuition for the future of research, and true concern for my professional development. It is through his support that this document, the research described herein, and my growth as a scientist over the past 6 years, was possible.

I thankfully acknowledge the other members of my thesis committee for their time and desire to assist me. It has been rewarding to work with Prof. Thompson, Prof. Jensen, and Prof. Wardle. Prof. Jensen is especially thanked for his principal role in the MURI program.

My officemates and colleagues have assisted me in completing this work and made it a pleasure to do so. I sincerely thank them for their knowledge, for their help, for their coffee breaks and—where noted—for their data. I heartily thank Ytshak Avrahami, Chelsea Baertsch, Anja Bieberle, Kurt Broderick, Pete Capazzoli, Jianyi Cui, Jussi Hiltunen, Takeo Hyodo, Woochul Jung, Il-Doo Kim, Woosik Kim, Roel van de Krol, GJ La O', Jyrki Lappalainen, Scott Litzelman, Christoph Lutz, Tim McClure, Yongki Min, David Quinn, Avner Rothschild, Huankiat Seh, Dilan Seneviratne, Libby Shaw, Martin Søgaard, Todd Stefanik, Steve Weiss, Ben Wilhite, and Namiko Yamamoto.

My time on MIT's campus was never better than Wednesday evenings after 5:30. My memories from the Muddy Charles Pub with Joe, Nate, Ryan, Dave, and Dan will outlast, I'm sure, anything I learned in the classroom or lab. Thanks to all of you.

I have been blessed with a caring family that grew substantially during my time at MIT. Thank you Matt, Sarah and Shoshanna; Rod, Patti, Slade, and the rest of the Lellocks.

The support and love from my parents have been ceaseless, tireless, and too often thankless. I hope they accept my efforts at being a good scientist, person, and (someday…) parent as thanks.

Above all, I would like to thank my wife. She has been a traveling companion and a running buddy, my financial patron and comic relief, a gentle critic and an enthusiastic supporter, a best friend. This thesis is a testament to her patience and dedication.

Finally, I gratefully acknowledge the funding source of my research, the DoD Multidisciplinary University Research Initiative (MURI) program administered by the Army Research Office under Grant No. DAAD19-01-1-0566. This work made use of the Shared Experimental Facilities supported by the MRSEC Program of the National Science Foundation under award number DMR 02-13282.

Figure 0. The author crunches data, somewhere in the White Mountains.

Quia ursus pusilli ingenii…

CHAPTER 1. INTRODUCTION

1.1 Motivation

Since the dawn of the industrial revolution, humanity has become evermore reliant on chemical energy sources with high energetic density. Whereas early civilizations used wood and other biomass-based energy sources, advanced machinery required greater energy density and the switch to coal and eventually petroleum was made. Having inexpensive access to these energy resources has enabled the many advances and conveniences of modern industrialized society; however, for two reasons the utility of these resources appears to be reaching a decline. First, the supply of accessible petroleum in the Earth is fixed, and civilization appears to be at or near Hubbert's Peak, the long-predicted moment in time where humanity's rate of global oil recovery reaches a maximum[1]. Though the worldwide demand for oil will continue to grow, the supply will decline, and thus the cost of this energy source will rise. Second, there now appears to be statistically significant global climate change due to anthropogenic gases such as carbon dioxide[2]. The release of these gases into the atmosphere, mainly from combustion of coal and petroleum, may soon have substantial negative effects on the global economy, not to mention the health and welfare of people and other life forms.

For these reasons, methods of deriving more usable energy per unit of input chemical energy are needed. Energy conversion via combustion processes has been optimized to achieve net efficiencies of 20-30% (for gasoline internal combustion engines[3]); however, because they use a thermal conversion route, they are inherently limited by Carnot cycle-type thermodynamic inefficiencies. As a result, methods for producing electrical energy from chemical energy sources that are not hindered by such efficiency limits are in high demand.

In the long term, as petroleum and even coal reserves are depleted, the chemical energy must be derived from renewable sources. One such source may be hydrogen, but many technical hurdles remain before transitioning to the "hydrogen economy." These include finding ways to renewably produce and densely store the gas. Cellulosic ethanol and other biologically derived chemical energies are promising alternatives that avoid these concerns. Unfortunately, such complex and often impure hydrocarbon fuels can be more difficult to convert to electrical energy. A premium is placed on a power technology that can directly utilize hydrocarbon fuels with flexibility in the fuel choice.

In addition to these global energy concerns, there are energy issues at the small, portable scale. Portable devices such as laptops and cell phones currently rely upon batteries to supply electrical power. As the functionality of these devices has grown, the amount of power they need has substantially increased. The energy content of the battery thus depletes more rapidly, allowing for less usage before recharging. This issue is critical for the military[4], since one of the key limiting parameters on the length of time that a soldier can be on a mission is the weight of the batteries he must transport with him. To address such matters, an advanced portable power technology with increased energy density is needed.

All of the concerns described above may have a common solution, and that is the solid oxide fuel cell. There is much promise in this technology, and prototypes have been successfully demonstrated. On the other hand, despite increased efficiency in fuel usage, solid oxide fuel cells are not currently economically competitive with combustion generators. In addition, portable solid oxide fuel cells have not been demonstrated outside of a few laboratory settings[5-7]. One of the main hindrances is the lack of understanding about the kinetics of the electrode processes and the resultant inability to produce electrodes that can operate at reduced temperatures[8]. This increases the cost of stationary solid oxide fuel cells, since expensive materials that are stable at high operating temperatures must be used in the construction. It also reduces the viability of portable solid oxide fuel cells, since high temperatures reduce the thermomechanical robustness of these thin film devices[9-11]. The work described in this dissertation involves the use of microfabrication techniques to quantify and improve the electrode kinetics of solid oxide fuel cells. This information can be used to design optimal electrodes that can be used at reduced temperature and thereby allow solid oxide fuel cells to be an economically competitive energy solution at both stationary and portable size scales.

1.2 Fuel Cells

Grove first discovered fuel cells over 160 years ago[12], though at the time the basic working principles were not well understood. The field of electrochemistry has since advanced and the operation of fuel cells can now be explained from basic thermodynamic and kinetic theory. Applying this increased knowledge has allowed commercialization for niche applications since at least the 1960's, when alkaline fuel cells supplied electrical power during early space flight. This type of fuel cell still supplies electrical power on board the space shuttle, but other types of fuel cell technologies are now nearing broader commercialization. No system has yet been more widely adopted, primarily due to high capital cost[13]. The low temperature fuel cell technologies require, as did Grove's original device, expensive platinum catalysts. On the other hand, high temperature fuel cells do not need such high catalytic activity and so can use cheaper catalyst materials. Unfortunately, they suffer from high processing costs and expensive balance-of-plant materials in order to make the systems stable at the extreme operating temperatures. Some observers believe that fuel cells will enter the market when capital costs reach below \$1000/kW[14].

1.2.1 Principles of Operation

At heart, the fuel cell is not very different from a battery in that both directly transform chemical energy into electrical energy via a galvanic cell. As in any electrochemical cell, the presence of an electrically insulating, ion conducting electrolyte creates a coupling between the chemical potential and the electrical potential. The main difference between fuel cells and batteries is that fuel cells use continually supplied reactants instead of two permanent, ion-bearing solids at the electrodes. The benefit of this arrangement is that the energy storage function of the device is decoupled from the electrode function, providing more liberty to choose the reductant and oxidant, optimizing perhaps for increased energy density or reduced cost. Though presumably the reactants could be in liquid or even solid form, they are nearly always gaseous and will be considered so for the remainder of this thesis.

The operation of a fuel cell can be understood by considering the motion of the mobile ions. The important thermodynamic gradient that causes ionic species *i* to move is the electrochemical potential, $\tilde{\mu}_i$, given by

$$\tilde{\mu}_i = \mu_i + n_i \cdot F \cdot \phi \tag{1}$$

where μ_i is the chemical potential, ϕ is the electrical potential, F is Faraday's constant = $9.6484 \cdot 10^4$ $\mathrm{C \cdot mol^{-1}}$, and n_i is the charge number of the species. The operation of a fuel cell is initiated by flowing a reductant stream (i.e., fuel) and an oxidant stream across opposite sides of an ionically conducting electrolyte. This creates a chemical potential gradient for the mobile ion, which must in whole or in part be a constituent of either the reductant or oxidant. Equilibrium is reached when the electrochemical potential is uniform across the electrolyte, so the chemical potential gradient is matched by an electrical potential gradient that is equivalent in magnitude but opposite in sign. The electrical potential difference created can be used to drive an electronic current through an external load, powering the device.

The electrical potential difference, or voltage, across an electrochemical cell can be derived by equating the Gibbs free energy due to the chemical potential gradient

$$\Delta G = \Delta G^0 + RT \ln\left(\frac{a_{red}}{a_{ox}}\right) \tag{2}$$

with the Gibbs free energy due to an electrical potential gradient

$$\Delta G = -n \cdot F \cdot \Delta\phi \tag{3}$$

to derive the Nernst equation:

$$\Delta\phi = \Delta\phi^0 - \frac{RT}{n \cdot F} \ln\left(\frac{a_{red}}{a_{ox}}\right) \tag{4}$$

where ΔG is the Gibbs free energy; ΔG^0 is the standard molar reaction free energy—for a typical fuel cell this is similar to the thermodynamic heating value of the fuel; R is the universal gas constant = 8.3144 $J{\cdot}mol^{-1}{\cdot}K^{-1}$; T is the absolute temperature; a_{red} and a_{ox} are the chemical activities of the species at the reductant/electrolyte (anode) and oxidant/electrolyte (cathode) interfaces, respectively; and $\Delta\phi$ is the electrical potential difference across the cell. $\Delta\phi^0$, related to ΔG^0 by equation 3, is the potential difference when the chemical species on either side of the electrolyte are in their standard states, for then the chemical activities are defined as 1 and $\Delta\phi=\Delta\phi^0$. It therefore represents the cell potential at equilibrium—the zero-current or open circuit voltage—at standard temperature and pressure.

To derive usable power, some of the electromotive force must be used to drive a current through an external load. Whenever current flows, the system is taken out of equilibrium and the actual output voltage is reduced. There are a number of causes of the reduced voltage, called overpotentials or polarizations and given the symbol η, and they are placed into three categories: ohmic polarization, concentration polarization, and activation polarization. An illustration of how the different polarization mechanisms reduce the useable voltage is given in Figure 1.

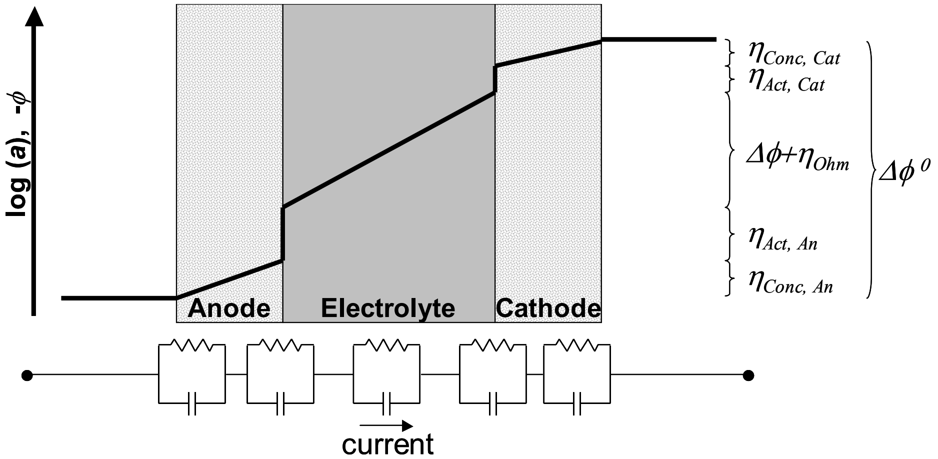

Figure 1. Upon a schematic cross-section of a fuel cell is plotted a line that represents, on a logarithmic scale, the chemical activity of the mobile ion and equivalently, on a linear scale, the negative electrical potential. At the endpoints, the activities are set by the composition of the fuel and air, but they are reduced before reaching the electrolyte by concentration and activation polarizations. The voltage output is equal to the difference in voltage across the electrolyte minus the ohmic polarization. An equivalent circuit, with a resistor and parallel capacitor for each loss mechanism, and an arrow indicating the direction of internal current flow during operation is also shown.

More details on each of the polarization mechanisms are given below. Each of the mechanisms is presented with regard to an applied electrical potential and an associated loss due to the impeded flow of electrochemical species. It is important to note that in an operational fuel cell device, the applied potential gradient is chemical, not electrical. However, under the assumption that all electrochemical reaction occurs at the triple phase boundary (explained in section 1.2.3) such that the electron and ionic defect concentrations are invariant, examinations of the loss mechanisms by electrical tests are analogous to those that are seen during device operation[15].

1.2.2 *Ohmic Polarization*

The ohmic polarization is the voltage drop that occurs due to the resistance of the electrolyte to the flow of ions. It is termed ohmic because the resistance is independent of current, and so the ohmic polarization is the simple product of the current, i, and the resistance, R:

$$\eta_{ohm} = i \cdot R \tag{5}$$

The resistance is analogous to electronic resistance in a metal with an equivalently defined conductivity, σ_{ion}, and equivalent dependence on geometric parameters: path length, l, and cross-sectional area, A:

$$R = \frac{l}{\sigma_{ion} \cdot A} \tag{6}$$

The relative need to increase the electrolyte conductivity is dependent upon the fuel cell technology and will be discussed in relation to solid oxide fuel cells in section 1.2.6. Reducing the path length of the ionic current also reduces the resistance. Thin film electrolytes, with thickness less than 1 μm, are being tested for a few different fuel cell technologies and will be discussed further in section 1.2.7.

1.2.3 *Activation Polarization*

The activation polarization arises from thermodynamic irreversibilities in the electrochemical reactions. The electrochemical half reactions at the electrodes can be written generically as

$$\mathrm{Ox} + n \cdot \mathrm{e}^{-} \Leftrightarrow \mathrm{Re} \tag{7}$$

where Ox is the oxidized species, Re is the reduced species, n is the number of electrons transferred, and the direction of the reaction is forward at the cathode and reverse at the anode. One of the species, Ox or Re, must be in the gas phase while the other is the mobile ion in the electrolyte. Because the mobile ion comes from a substance external to the electrode, the overall half-reaction necessarily includes a number of sub-reactions. These include the gas phase diffusion of the reactant to the electrode or electrolyte surface; adsorption; dissociation; ionization; surface diffusion to the electrochemically active site; incorporation of the ion into the electrolyte; and, on either the anode or cathode, reaction of the ion to create the waste product. This complex series of steps, illustrated for an oxygen reactant at a platinum cathode/zirconia electrolyte interface in Figure 2, is made more complex by the fact that some of the steps occur in parallel or may be placed in a different order. Poor diffusion in the gas phase is generally treated as concentration polarization, and so will be discussed in greater detail below. A rate limiting reaction step in any of the other subreactions is termed activation polarization.

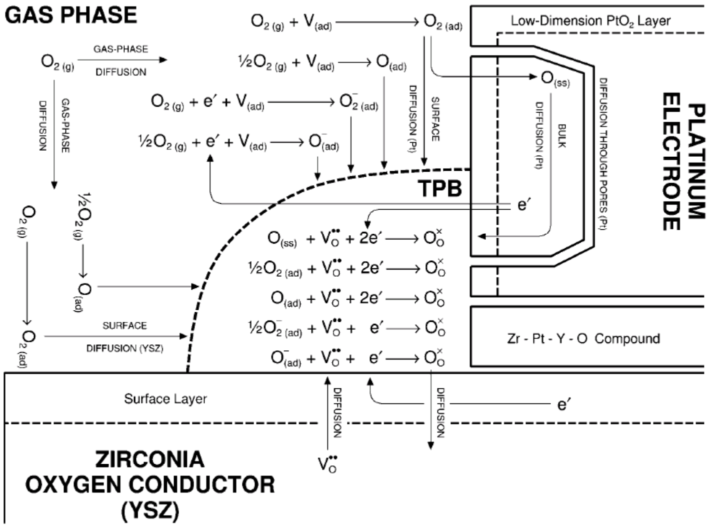

Figure 2. The many reaction mechanisms, occurring in series and in parallel, that bring an oxygen reactant into the surface of a zirconia solid electrolyte in the presence of a platinum electrode. Reprinted from reference 16.

The complexity of this series of reactions has unfortunately limited the scientific rigor of its study. Study of the electrode reaction has tended to remain empirical. It has also meant that the electrode kinetics are highly dependent upon the operating conditions, the composition of the materials, and the materials' surface structure and chemistry, among other variables; as a result, the identity and speed of the rate limiting step often vary between laboratories and even experiment to experiment. Empirically, the activation polarization is found to follow Tafel kinetics

$$\phi = a + b\log i \tag{8}$$

with voltage, ϕ, depending logarithmically on current, i, and experimentally derived fitting parameters a and b. This can be explained using the Butler-Volmer model of interfacial kinetics.

To derive this model[17], just one of the subreactions—generally the one with the largest activation barrier—is considered to be rate limiting. According to standard kinetic theory, reaction rates of the forward and reverse reactions will depend on the difference in energy levels between the activated and non-activated states. A reaction rate constant, k, can be found by

$$k = \kappa \frac{RT}{h} \exp\left(-\frac{\Delta G}{RT} \right) \tag{9}$$

where κ is a unit-less transmission coefficient that represents the probability of an activated complex to be transmitted to the state opposite its source (i.e., reactant becomes product and vice-versa), h is Planck's constant, and ΔG represents the difference in energy between the source state and the activated state (see Figure 3). The rate of reaction, v, in units of mol·cm^{-2}·s^{-1}, is found by multiplying k by the concentration of the source, C, and can be equated to a current, i, by multiplying by the area, *A*, and charge per mole, *n·F*

$$v = k \cdot C = \frac{i}{n \cdot F \cdot A} \tag{10}$$

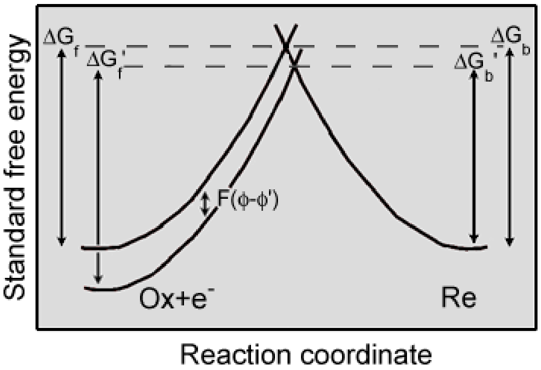

Figure 3. The free energy of electrochemical species in a reduction reaction as a function of a reaction coordinate. Energy minima are found at the reactant and product states, and a maximum is at the activated state. At equilibrium, the product and reactant energies are equal, $\Delta G_f = \Delta G_b$. Application of an electrical potential decreases the energy of the electron by $F \cdot \Delta\phi$, causing $\Delta G_f' \neq \Delta G_b'$ such that the system leaves equilibrium and a net reaction occurs. Adapted from reference 17.

As *ΔG* and the surface concentrations can be different for the two source states, forward and reverse reaction rates may be unequal and a net reaction rate $v_{net} = k_f \cdot C_R - k_b \cdot C_P$ then exists, where the subscripts *f*, *b*, *R*, and *P* refer to forward, backward, reactant, and product, respectively. This yields a net current

$$i = n \cdot F \cdot A\left(k_f \cdot C_R - k_b \cdot C_P\right) \tag{11}$$

If an electrical potential $\Delta\phi$ is applied, the energy states of the electrons in the electrodes are changed by $-F \cdot \Delta\phi$. The reaction rate constants thus become

$$k_f = A_f \exp\left(-\frac{\Delta G_f}{RT}\right)\exp\left(-\frac{\alpha F \Delta\phi}{RT}\right) \tag{12}$$

and

$$k_b = A_b \exp\left(-\frac{\Delta G_b}{RT}\right)\exp\left[\frac{(1-\alpha)F\Delta\phi}{RT}\right] \tag{13}$$

where the pre-exponential terms have been grouped into constants A_f and A_b and α is the transfer coefficient, a unit-less parameter that corrects for asymmetry in the energy barrier.

At some potential, ϕ^0, the reaction will be at equilibrium ($k_f \cdot C_R = k_b \cdot C_P$) with the reactant and product concentrations equal ($C_R = C_P$), so that $k_f = k_b = k^0$. Referenced to this potential, the rate constants become

$$k_f = k^0 \exp\left[-\frac{\alpha F\left(\phi - \phi^0\right)}{RT}\right] \tag{14}$$

and

$$k_b = k^0 \exp\left[\frac{(1-\alpha)F\left(\phi - \phi^0\right)}{RT}\right] \tag{15}$$

Substituting these into equation 11 yields the current/potential relationship under activation polarization

$$i = n \cdot F \cdot A \cdot k^0\left[C_R \exp\left(-\frac{\alpha F\left(\phi - \phi^0\right)}{RT}\right) - C_P \exp\left(\frac{(1-\alpha)F\left(\phi - \phi^0\right)}{RT}\right)\right] \tag{16}$$

By letting $\phi = \eta_{Act} - \phi_{eq}$, the reference potential is shifted to the equilibrium potential, ϕ_{eq}, defined by experimentally chosen C_R and C_P, and equation 4, the Nernst equation. The voltage is now the overpotential required to cause the electrochemical reaction to proceed away from equilibrium, so the symbol used is η_{Act}, the activation polarization. Grouping all of the pre-exponential terms into an exchange current, i_0, the Butler-Volmer equation is derived:

$$i = i^0\left[\exp\left(-\frac{\alpha F \eta_{Act}}{RT}\right) - \exp\left(\frac{(1-\alpha)F \eta_{Act}}{RT}\right)\right] \tag{17}$$

From this equation, it can be seen that i_0 represents the current that flows, equally in both directions, at equilibrium. The first exponential describes the forward current and the second exponential describes the backward current (see Figure 4). At large overpotentials, one of the two terms in equation 17 will become insignificant and the resultant current-potential relationship will follow that described by the empirically derived Tafel equation (equation 8), thus validating the model.

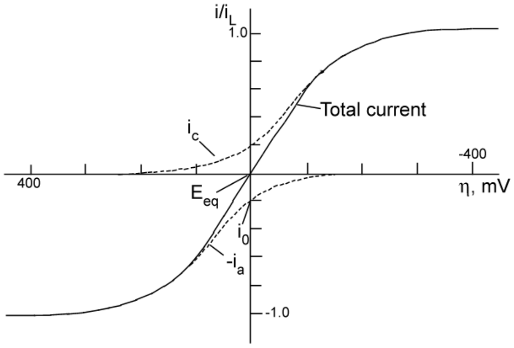

Figure 4. The forward current, i_c, and backward current, i_a, in an electrochemical half-cell sum to the total current. Cathodic current is defined as positive. At high potentials a limiting current, i_L, is set by mass transfer kinetics. α=0.5 and i_0/i_L=0.2. Adapted from reference 17.

One special case of equation 17 that will be important in the context of this dissertation occurs at low overpotentials. Since $\exp(x) \approx 1 + x$ for small values of *x*, the equation can be approximated for small η_{act} as

$$\eta_{Act} = -\frac{i}{i^0} \cdot \frac{RT}{F} \tag{18}$$

The negative sign results from the traditional convention in electrochemistry, used throughout this derivation, that cathodic currents are positive even though they require negative voltages. From this quasi-linear relationship, a charge transfer resistance can be derived,

$$R_{CT} = \frac{\eta_{Act}}{i} = \frac{RT}{i^0 F} \tag{19}$$

This resistance is the slope of the linear region around E_{eq} in Figure 4. Measurements performed at low voltages can thus be used to measure the charge transfer resistance, which predicts the kinetic reaction rate of an electrode. This resistance alone, however, is not fully sufficient to calculate the resistance of an electrode at large voltages, since the transfer coefficient is still unknown. This also assumes that the rate limiting reaction step remains the same at all voltages.

Reducing activation polarization is accomplished in two ways. First, the materials chosen for the electrode and/or electrolyte can be more catalytically active. This reduces the energy of the activated state of the rate limiting step, increasing k^0 and thereby the kinetic rate. Second, the concentration of sites that are active to the electrochemical reaction can be increased. Since the half-reactions in a fuel cell involve a gaseous species, an electron, and an ionic species, the reactive sites must be in some local vicinity to the gas phase, the electrode phase, and the electrolyte phase[18]. This fact was discovered as early as Grove's original paper[12] and has since been validated by a number other studies[18]. This region of contact is known as the triple phase boundary (TPB), shown as the dash-enclosed region of Figure 2. Increasing the amount of TPB length per unit area is accomplished by using composite electrodes, with interpenetrating networks of electrolyte, electrode, and pore phases (see Figure 5). These microstructures can be further optimized for composition and grain/pore size.

As the common intersection of three volumes, the TPB is ostensibly a one-dimensional region. It nevertheless has some volume, due to the non-zero electron conductivity of the electrolyte, ionic conductivity of the electrode, and/or gas permeability of either solid phase. Any of these will broaden, to some extent, the region over which reactions can occur, giving some width and depth to the TPB. This idea can be carried further by intentionally using a material that is highly conductive to both ions and electrons as the electrode. Such mixed ionic electronic conductors (MIECs) relieve the need for a TPB and enable the half-reactions to occur everywhere along the gas-MIEC surface.

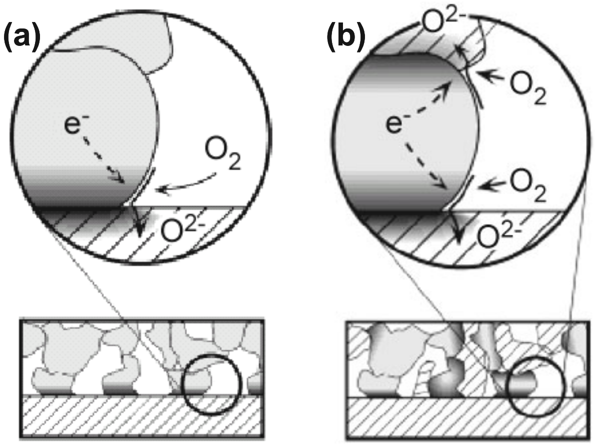

Figure 5. Electrochemically active sites are only found where the white gas phase, gray electrode phase, and hashed electrolyte phase meet. (a) The single phase electrode has active sites only at the planar interface. (b) The composite electrode has active sites throughout the thickness. The composite is expected to have reduced activation polarization. Reprinted from reference 18.

1.2.4 Concentration Polarization

Concentration polarization, as mentioned above, is due to insufficient gas phase diffusion of reactants. When the electrochemical reactions proceed at a sufficiently high rate, reactants become depleted near the electrode/electrolyte interfaces. By Raoult's law, chemical activity is proportional to the concentration. The Nernst equation (equation 4) therefore demands that reduced concentration leads to reduced voltage. Using equation 4, the overall voltage across the electrolyte when concentration overpotential exists is given by

$$\Delta\phi = \Delta\phi^0 - \frac{RT}{nF}\ln\left(\frac{a_{red}^{int}}{a_{ox}^{int}}\right) \tag{20}$$

where the superscript *int* indicates that the chemical activities at the anode/electrolyte and cathode/electrolyte interfaces are different than away from the interface. The rest of this discussion will be simplified by considering polarization only at the anode, such that a_{ox} terms can be ignored, and the subscript *red* will be dropped. Analogous arguments and equations can be written for the alternative case. Writing η_{conc} for the electrical potential drop due to the concentration gradient,

$$\eta_{conc} = \frac{RT}{nF}\ln\left(\frac{a^{int}}{a^{react}}\right) \tag{21}$$

where a^{react} is the chemical activity at a far distance from the interface, equal to that in the original reactant stream. The dependence of this polarization on current can be estimated by modeling the flux of the chemical species as Fickian diffusion through a boundary layer of thickness δ. The flux J of species i per unit of cross-sectional area is

$$J_i = -D\nabla\mu_i \approx -D\frac{a^{react} - a^{int}}{\delta} \tag{22}$$

where D is the diffusivity. The current density flowing through the cell, j, is this flux multiplied by the charge per mole of the species

$$j = -nFD\frac{a^{react} - a^{int}}{\delta} \tag{23}$$

The maximum flux through the boundary layer will occur when the reactant is completely depleted at the electrolyte interface, for then the largest gradient in activity is found. Defining a limiting current density, j_L, for this situation gives

$$j_L = -nFD\frac{a^{react}}{\delta} \tag{24}$$

Rearranging equations 23 and 24 and inserting them into equation 21 yields an expression for the concentration polarization as a function of the current flowing through the cell:

$$\eta_{conc} = \frac{RT}{nF}\ln\left(1-\frac{j}{j_L}\right) = \frac{RT}{nF}\ln\left(1-\frac{i}{i_L}\right) \tag{25}$$

where the second equality uses the current instead of current density since the ratios are equivalent.

In order to reduce the concentration polarization, there must be rapid diffusion of the gas reactants to the electrode/electrolyte interfaces. This implies a need for electrodes that have high open porosity so that gases can quickly reach the triple phase boundaries. For any well-designed fuel cell, there is sufficient porosity so that the concentration polarization becomes a significant loss mechanism only at very high currents.

Special attention must be paid to the concentration polarization at the electrode to which the mobile ion travels because the fuel cell reaction products are created there. Diffusion of the reactants to the electrolyte interface necessarily implies diffusion of the products away from the interface. This is particularly important when the waste stream is not gaseous. Low temperature fuel cells can produce liquid water wastes that must be quickly distributed away from the electrodes to prevent ‘flooding.’ This can be done by treating the electrode surfaces to make them hydrophobic.

1.2.5 Device Performance

Real devices can suffer two additional loss mechanisms, and they concern two different leakage mechanisms through the electrolyte. The first is crossover of the reactants from one side of the electrolyte to the other, either through pores or by some other permeation mechanism. This reduces the chemical potential gradient across the electrolyte, lowering the voltage output from the cell. It also wastes reactant so that the overall efficiency of the system is decreased. The second leakage is electron (or hole) conduction through the electrolyte. Because no material is perfectly insulating to electron conduction, there will always be some amount of electron current that travels through the electrolyte rather than the external circuit. The current available to the load is thereby reduced. A generalization of the Nernst equation can be used to account for electron conduction through the electrolyte[19]:

$$\Delta\phi = \Delta\phi^0 - \frac{RT}{n \cdot F} \int_{a_{ox}}^{a_{red}} \frac{\sigma_{ion}}{\sigma_{ion} + \sigma_{electron}} d\ln a \tag{26}$$

where σ_{ion} and $\sigma_{electron}$ are the ionic and electronic conductivities, respectively. These two loss mechanisms are active even when no current flows through the external load, and so can be perceived by a reduced voltage when the system is held at open circuit.

Additional losses found within complete fuel cell systems come from inefficiencies in the balance of plant components that supply the reactants, collect the current, condition the electrical output to line voltage alternating current, perform thermal management, and perhaps preprocess the fuel into usable form. These will not be considered further as they are not directly related to the fuel cell and are highly dependent on the individual system being engineered.

A common way of displaying the performance of a fuel cell is by plotting the voltage against the current, as in Figure 6. When no current flows through the external circuit, then the potential is the open circuit voltage, V_{OC}. Theoretically, this is the same as the Nernst voltage for any given oxidant/fuel combination. In practice, the V_{OC} is reduced by the leakage mechanisms described above. If some current is allowed to flow, the various polarization mechanisms will lead to a voltage that decreases monotonically with increasing current. At the extreme, when there is zero resistance in the external circuit, there can be no voltage drop and the current is the short circuit current, I_{SC}.

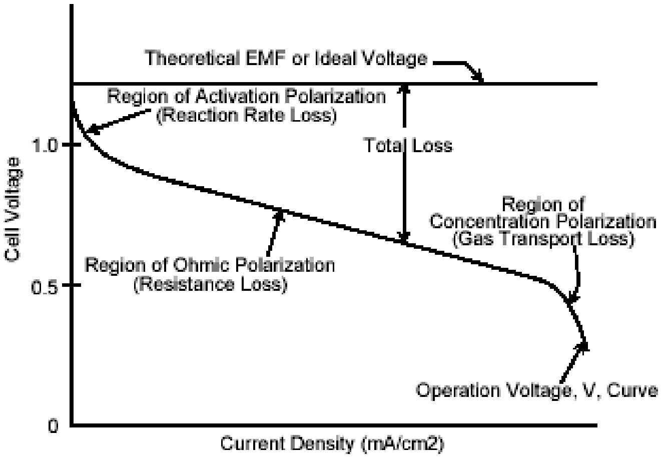

Figure 6. The voltage vs. current output of a theoretical fuel cell is plotted. The open circuit voltage, V_{OC}, is the intercept on the voltage axis. The short circuit current, I_{SC}, is the intercept (not shown) on the current density axis. Reprinted from reference 20.

At any point on the performance curve, the voltage output is equal to the ideal, Nernst potential minus the total loss, equal to the sum of all of the overpotentials.

$$\phi_{operating} = \phi_{Nernst} - \eta_{tot} = \phi_{Nernst} - \left(\eta_{Ohm} + \eta_{Act} + \eta_{Conc}\right) \tag{27}$$

In general, only one of the polarization mechanisms is dominant at any specified operation point, with activation polarization likely to be dominant at low currents and concentration polarization dominant at high currents. In a plot like Figure 6, the dominant loss mechanism regions can often be identified by concave up, linear, and concave down curvature of the activation, ohmic, and concentration polarization regions, respectively.

It is trivial to improve the performance of a fuel cell device by increasing the cross sectional area. For this reason, many materials and device parameters are normalized to this area. The charge transfer resistance and the resistance of the electrolyte are often given as area specific resistance (ASR) with units of $\Omega\cdot\text{cm}^2$. Similarly, currents and powers are often given as current and power (area) densities, as in the *x*-axis of Figure 6.

The power of any electric device is the product of the voltage and current, $P = V \cdot I$. While the voltage monotonically decreases as current increases, the power output goes through a roughly parabolic curve, with some operation point that gives maximal power output, P_{max}. Device performance curves are typically presented as overlaid plots of voltage and power density versus the current density. A set of such plots for a high performance solid oxide fuel cell is given in Figure 7.

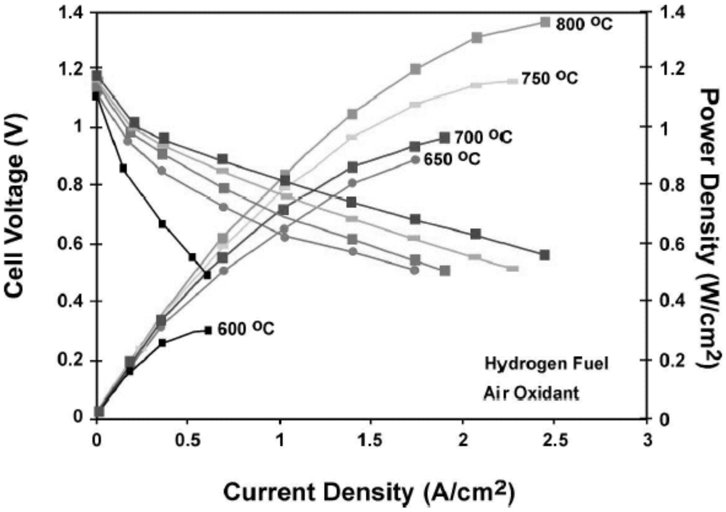

Figure 7. A set of overlaid voltage-current and power-current plots demonstrates the output of a high performance solid oxide fuel cell at a few temperatures. The open circuit voltage, V_{OC}, is the intercept on the voltage axis. The short circuit current, I_{SC}, is the intercept (not shown) on the current density axis. The maximum power output, P_{max}, is the peak of the power density curves. While I_{SC} and P_{max} depend on the kinetics, and thus are highly temperature sensitive, V_{OC} is set by thermodynamics, and so is relatively insensitive to temperature. Reprinted from reference 21.

The operation point of maximum power output is not necessarily the most desirable, because it is generally not the operating point of maximum efficiency. One may choose, depending on the application, to operate a fuel cell at the point of maximum power output, the point of maximum efficiency, or between the two at a point of optimized operation cost[14]. The maximum possible efficiency of a fuel cell comes from the ratio of the maximum possible useful energy output to the stored chemical energy input

$$efficiency = \frac{\Delta G}{\Delta H} \tag{28}$$

Strictly speaking, this efficiency can only be met when a fuel cell operates reversibly. The overall irreversibility of the device can be found in the ratio of the operating voltage to the ideal voltage so that the efficiency of the fuel cell can be expressed as[20]

$$efficiency = \frac{\phi_{operating} \cdot \Delta G}{\phi_{Nernst} \cdot \Delta H} \cdot \delta \tag{29}$$

where the additional factor δ is the proportion of the fuel that is electrochemically oxidized as opposed to that which is chemically oxidized by gas leakage or is sent unused to the exhaust. Real systems may, of course, use combined cycle generators or heat and power cogeneration to more efficiently use the fuel energy.

By equation 29, operating the fuel cell at lower current density, where the operating voltage is closer to the Nernst potential, increases the efficiency. On the other hand, low current density implies low power density and so a fuel cell with larger cross sectional area is required to create the same total power. The key to creating fuel cells with both high efficiency and large power density is therefore to reduce the polarizations so that at a sufficient power output level, the actual voltage is as close as possible to the ideal voltage.

For nearly all technologically important fuel cells, air is the oxidant because it can be used without added cost or system weight. Hydrogen is often used as the reductant (i.e., fuel) for a number of reasons. First, it is highly reactive and so places fewer burdens on the catalytic properties of the anode material. Second, there are electrolytes with high conductivity for hydrogen ions. Thus, for fuel cells employing these electrolytes, pure hydrogen is the simplest fuel and does not require further fuel processing. Third, it reacts only to form water, without the possible complications of solid decomposition products such as carbon. On the other hand, hydrogen is expensive, difficult to store in a dense manner, and prone to leakage. For these reasons, it is beneficial to feed hydrocarbon fuels directly to the fuel cell. This is possible if the fuel cell operates at sufficiently high temperatures that the carbon-carbon and carbon-hydrogen bonds can be broken and the fuel can be fully oxidized to carbon dioxide and water.

With hydrogen as the fuel and oxygen or air as the oxidant, the overall chemical reaction that powers the fuel cell is

$$2H_2 + O_2 \Rightarrow 2H_2O \tag{30}$$

The electrolyte splits this reaction into two half-reactions, the details of which depend on which mobile ion is being transferred through the electrolyte (see Figure 8). Nevertheless, reduction always occurs at the cathode and oxidation at the anode and one of the ionic species then migrates through the electronically insulating electrolyte. If the electrolyte transports hydrogen ions, such as in polymer electrolyte membrane fuel cells and phosphoric acid fuel cells, then the half reactions at the anode and cathode are, respectively,

$$\text{and} \qquad \begin{array}{l} H_2^{(g)} \Rightarrow 2H^+ + 2e^- \\ O_2^{(g)} + 4H^+ + 4e^- \Rightarrow 2H_2 \end{array} \tag{31}$$

These can be compared with the generic half-reaction of equation 7. To connect the half reactions, the hydrogen ion passes through the electrolyte and the electron through the external load. If the electrolyte transports oxygen ions (perhaps as part of a complex ion), as in solid oxide, molten carbonate, and alkaline fuel cells, then the half reactions are

$$\text{and} \qquad \begin{array}{l} O_2^{(g)} + 4e^- \Rightarrow 2O^{2-} \\ O^{2-} + H_2^{(g)} \Rightarrow H_2O + 2e^- \end{array} \tag{32}$$

and the oxygen ion passes through the electrolyte to connect the half-reactions. After the fuel and oxygen react, the waste products are emitted as exhaust. These processes are illustrated for the various fuel cell technologies in Figure 8.

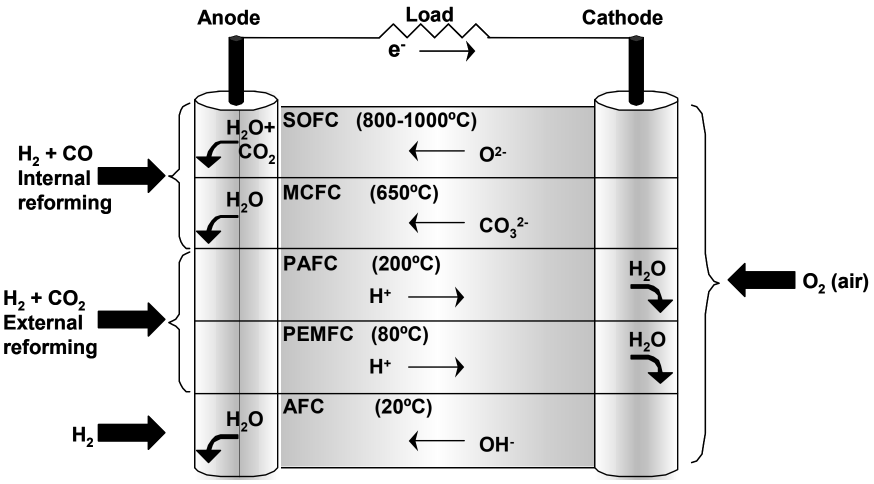

Figure 8. The common fuel cell types, showing the motions of the mobile ions through the electrolyte and the associated fuel types. AFC = alkaline fuel cell, PEMFC = polymer electrolyte membrane fuel cell, PAFC = phosphoric acid fuel cell, MCFC = molten carbonate fuel cell, and SOFC = solid oxide fuel cell. Adapted from reference 22.

1.2.6 Solid Oxide Fuel Cells

A fuel cell using a ceramic electrolyte was first reported by Baur and Preis in 1937[23]. This was the first of a class of fuel cells, now termed solid oxide fuel cells (SOFC), characterized by a solid metal oxide electrolyte that is conductive to oxygen ions. The use of a ceramic for the electrolyte is advantageous in that these materials are generally highly chemically and thermally stable. SOFCs are, in some sense, the only fuel cell technology with all of the components made of solid materials. MCFCs, PAFCs, and AFCs have liquid electrolytes and the PEMFCs have a hydrated polymer electrolyte so that water management is still a key concern. The use of solid components gives the SOFC structural stability and eliminates the corrosion and containment issues associated with liquid electrolytes.

The drawback to a solid electrolyte is that there are relatively few solid materials that have ionic conductivities on par with liquid electrolytes. The ceramic oxygen conductors all have highly thermally activated conductivities, with values only approaching that of liquid electrolytes at very high temperatures (>600°C). The necessity of operating at such elevated temperatures drives the engineering of the other SOFC components. In particular, the device housing and the sealant between the fuel and oxidant chambers must be stable for extended times at operating temperature and during power up/down thermal cycling. The additional expenses associated with high temperature platforms have been one of the main contributors to high SOFC capital costs. Research into ways to reduce the operating temperature is active[24].

There are a few benefits to operating at elevated temperatures, however. First, the electrochemical reaction kinetics are accelerated, thus reducing the catalytic activity requirements of the electrode materials. Whereas lower temperature fuel cells need highly catalytic platinum, SOFCs can use cheaper substitutes[25]. Second, at high temperatures it is easier to break C-C bonds and thus hydrocarbons can be directly utilized at the anode[26]. Third, the high temperatures of the exhaust gases can be used to increase efficiency, using a combined cycle or cogeneration. One of the goals of current SOFC research is to engineer a device that operates at a sufficiently high temperature to use cheap catalysts and hydrocarbon fuels, yet at a low enough temperature to use cheaper sealant and housing components.

The primary requirement of the electrolyte is to be highly conductive to oxygen ions and highly resistive to electrons. Electrolytes in an SOFC are exposed to both the oxidizing cathode and reducing anode environment. They must therefore also be stable at high temperatures in both environments. The traditional electrolyte, used ever since the first ceramic fuel cell, is stabilized zirconia (zirconium oxide). This material has satisfactory properties, the main concern being somewhat low ionic conductivity at low temperatures. Research into electrolytes with improved conductivity has been active for many years and, while some have been identified, they have tended to be materials with insufficient chemical or electrochemical stability[27]. The properties of stabilized zirconia are discussed at length in section 1.3.

The anode must satisfy the requirements of high electron conductivity and stability in a reducing environment. Ideally, it is also catalytic towards fuel oxidation, has a similar thermal expansion coefficient to the electrolyte, and is inexpensive. Base metals satisfy these requirements, and nickel is the traditional choice[25]. Typically, a porous composite is made of nickel and the electrolyte for three reasons: to increase the TPB length, to reduce high temperature agglomeration of the nickel particles, and to reduce thermal expansion mismatch.

The cathode has all of the same requirements as the anode material, except that it works in an oxidizing environment and is ideally catalytic towards the reduction reaction. Base metals will quickly oxidize in this environment, so either a noble metal or an oxide conductor must be used. The latter are typically used for cost reasons, traditionally lanthanum-strontium manganite (LSM)[25]. Similarly to the anode material, it is often made into a composite with the electrolyte. Variations in the composition, particularly with respect to replacement of the B-site cation with other transition metals or alkaline earths, are being investigated to improve the kinetic reaction rates[24].

The electrolyte in an SOFC conducts species from the oxidant instead of the fuel, so potentially any fuel that combines with oxygen can be used. The disadvantage of this arrangement is that the exhaust gases are released into the fuel stream instead of the air. This inherently limits the fuel utilization, since increased fuel utilization implies increased concentration polarization[28]. This is less of an issue for fuel cells with pure hydrogen at the anode and exhaust produced on the air/cathode side. Airflow can then be increased to purge the exhaust since air is cheap, both literally and in the sense of zero added system volume and weight.

1.2.7 Micro Solid Oxide Fuel Cells

Unlike turbine technologies, fuel cells have no inherent size-dependence of the efficiency, and therefore may be useful in size scales from megawatts to microwatts. Small fuel cells have the potential to be portable power sources similar to batteries, but with a few compelling advantages. First, when the energy content of a device is depleted, they can be nearly instantly refueled, perhaps by switching out a refillable or recyclable canister. There are certainly pragmatic issues with this idea, such as the ease of carrying around multiple canisters and the implications of consumers bringing fuel onboard commercial aircraft. However at least for some applications, the speed of refuel and the ability to refuel in a remote location may hold significant advantages. Second, because fuel cells have no chare/recharge cycle, these devices are expected to have longer useable lifetimes then batteries. Third, and perhaps most important, as seen in Table 1, the energy density of hydrocarbon fuels is much higher than that contained within available battery technologies. The actual energy density of a fuel cell device will be reduced from that of the fuel because of the inefficiencies in operation and the volume and mass of the device. However, even after accounting for this, there is potential for portable power with an order of magnitude or even greater increase in energy density compared to batteries. Capital cost has been a factor in delaying the implementation of larger fuel cells, since competing combustion-based technologies are so pervasive and have been so well optimized. On the other hand, portable fuel cells would compete against a somewhat expensive alternative—long-life batteries—in a market willing to bear premium costs[29].

Table 1. The energy densities of prominent battery technologies and fuels (upper heating value used). Battery values reprinted from reference 29 and fuel values calculated from reference 30.

	Battery technologies				Fuels			
	Lead-acid	Nickel-cadmium	Nickel-metal hydride	Lithium ion	Hydrogen	Methane	Ethanol	Gasoline (Octane)
Mass Energy Density [W·hr·kg^{-1}]	30	40	60	130	39000	15000	6300	13000
Volumetric Energy Density [W·hr·l^{-1}]	80	130	200	300	350[a]	1065[a]	5000	9100

[a] Gas pressurized to 100 atm.

With such promise, a large number of groups in academia and industry have been researching ways to produce portable micro fuel cells. Cowey et al. estimate[31] that over 1700 programs worldwide are demonstrating sub-1 kW fuel cells. Polymer electrolyte membrane fuel cells have been the focus of the vast majority of these efforts because they operate at relatively low temperatures. Some of these even appear to be nearing commercialization[32]. Subsequent discussions will be focused on the comparatively little research reported to date on micro-solid oxide fuel cells (µSOFC). There have been efforts, for reasons explained below, to use thin film electrolytes in traditional, large scale SOFCs[33-35]. These are sometimes referred to as thin film SOFCs; however, they are not of a suitable size or design for a battery replacement.

As mentioned in section 1.2.6, one of the main reasons that solid oxide fuel cells are operated at high temperatures is because only then is the ionic conductivity of the ceramic materials sufficiently high. Figure 9 shows an Arrhenius plot of the ionic conductivity for a few well-known oxygen ion conductors. Also shown is a typical goal value for the area specific resistance of the ohmic polarization, $R_0 = 0.15\ \Omega\cdot\text{cm}^2$. With a specified ASR, the conductivity is directly correlated with a required thickness. Therefore, on the right axis is given the maximum electrolyte thickness that provides an ASR at or below the goal. Electrolytes produced by traditional ceramic means of powder processing typically result in thicknesses of at least 100's of μm. From the figure, it can be seen that this requires operation temperatures of over 800°C for $(ZrO_2)_{0.9}(Y_2O_3)_{0.1}$ and upwards of 600-700°C for the other materials. Using thin film processing methods to produce the electrolyte, on the other hand, can result in dense ceramics with thicknesses of only 100's of nm or possibly less. This potentially allows the fuel cell to operate at 300°C or less for the higher conductivity materials and even for the zirconia material (discussed in more detail in section 1.3), operation at 400°C or less may be possible.

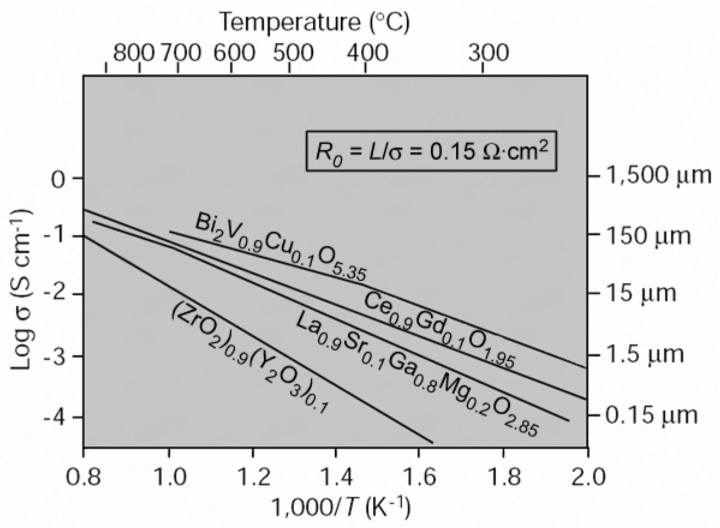

Figure 9. The ionic conductivity of various oxide ion conductors is plotted versus inverse temperature. With a goal area specific resistance of 0.15 $\Omega\cdot\text{cm}^2$, a one-to-one correlation between conductivity and thickness can be made. Adapted from reference 22.

The previous discussion has assumed uniform current density within the electrolyte. Since charge transfer can occur only near the triple phase boundaries, the current in the near surface region of the electrolyte is constricted into these regions. The triple phase boundaries are found at the edges of electrode particles, so whenever the electrolyte thickness approaches the electrode particle size, the added resistance of the constriction becomes significant. The resistance then ceases to decrease linearly as electrolyte thickness is reduced[36], however the ohmic losses are still likely to be insignificant when compared to the activation polarization losses[37]. As a case in point, Xu, et al., reported a SOFC using a 10 μm thick YSZ electrolyte[38]. At temperatures between 600°C and 750°C, the cell resistance was about 20% due to the electrolyte resistance and 80% due to electrode polarization.

For activation polarization, there is a significant geometric disadvantage to using thin film electrodes. The relevant geometric parameter for activation polarization is the triple phase boundary length per unit of projected surface area. Traditionally processed electrodes are thick, porous composites and thereby have a large TPB length accessible through the thickness. Figure 10 shows that the resistance of such anodes and cathodes decreases as the thickness is increased, not reaching optimal values until the electrodes are greater than 10 µm thick. Thin films are typically not porous, thick, or composites. Therefore, it can be difficult to produce a thin film electrode with low activation polarization. The cathode and anode reactions are temperature activated so, all else being equal, thin film electrodes would need to be operated at *increased* temperature compared to the traditional counterparts. Since micro fuel cells must operate at reduced temperatures, this becomes the biggest hindrance for a µSOFC to achieve reasonable power output. Finding methods to decrease the activation polarization of thin film electrodes therefore forms one of the chief purposes of this dissertation.

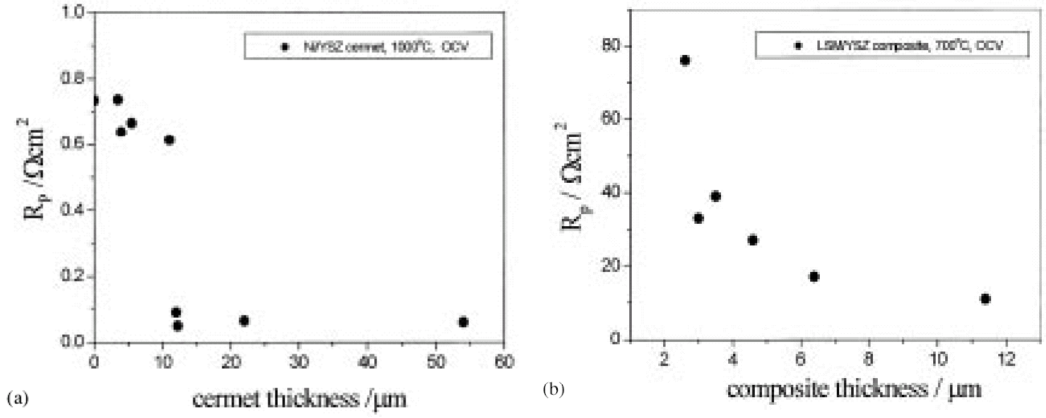

Figure 10. The area specific polarization resistance of (a) a composite anode and (b) a composite cathode as a function of the layer thickness. The polarization increases significantly at thickness less than 10 µm. Reprinted from reference 39.

The third polarization mechanism, concentration polarization, is not likely to be an issue for µSOFCs[37]. Thin film electrodes decrease the diffusion distance for the reactants in the gas phase, and so micro-fuel cells are likely to have low concentration polarization.

One of the main difficulties in fabricating a fuel cell from thin films concerns the need for process gases to access the triple phase boundaries of the anode and cathode. Using the planar architecture typical to thin film devices requires the use of a substrate that is either innately porous or made so by etching. On the other hand, the electrolyte must be dense in order to prevent leakage of the gases from one chamber to the other. Therefore, the fuel cell stack must form a freestanding membrane that is mechanically robust. This may be particularly troublesome during thermal cycling, since the coefficient of thermal expansion of traditional substrates like silicon ($\alpha = 3 \cdot 10^{-6}\ K^{-1}$) are substantially different from that of traditional SOFC materials, like YSZ ($\alpha = 10 \cdot 10^{-6}\ K^{-1}$)[9]. Nevertheless, design diagrams to identify reliable geometries have been made[9,10], using assumptions of the mechanical properties of the films and the fracture mechanics of the structures. The electrodes, similar to the substrate, can be either porous single phase materials or alternatively made into composites with the electrolyte material such that triple phase boundaries are present on the film surface.

The last main obstacle for μSOFCs lies in maintaining an efficient energy balance despite heat losses to the substrate and packaging. While there is no inherent size dependence of efficiency for a fuel cell, there are such dependences on the amount of heat lost to the surroundings. A portable device implies that the user-contactable packaging must be at or near room temperature. The high temperature, active portion of a μSOFC is in close proximity to the packaging, so significant heat losses may occur. Heat loss by conduction to the substrate is expected to dominate for simple geometries, with the loss perhaps exceeding the electrical power produced[9,10]. Efficient thermal insulation schemes, including advanced vacuum packaging, may be required to improve the efficiency of the devices[40].

Lawrence Livermore National Laboratory has had a concerted research effort into micro fuel cells integrated onto silicon substrates, with a similar design used to produce polymer electrolyte and solid oxide fuel cells[5,41-43]. A start-up company, UltraCell Corporation (Livermore, CA), appears to be licensing the technology to produce prototype stage, 10-25 watt polymer electrolyte micro-fuel cells using dilute methanol fuel[44]. The general design is shown in Figure 11(a).

The design employs deep reactive ion etching to create ‘pores’ in the silicon substrate. A low stress silicon nitride membrane covers this frame and provides a dense substrate on which to deposit the thin films. After the fuel cell films are deposited, pores are etched into the silicon nitride membrane, as seen in Figure 11(b). The membrane size is given as 2 × 2 mm, though it is unclear whether this is the area of the etched silicon substrate or the total area exposed through the silicon nitride pores.

The design includes an integrated electrical resistance heater. This is used to turn on the fuel cell by heating the device to operating temperatures and is powered by a rechargeable micro-battery packaged with the device. The authors state that once the fuel cell is operating, the resistive heater will be powered by the fuel cell itself[43], though presumably improved thermal insulation would allow steady state operation without wasting energy through a resistive heater.

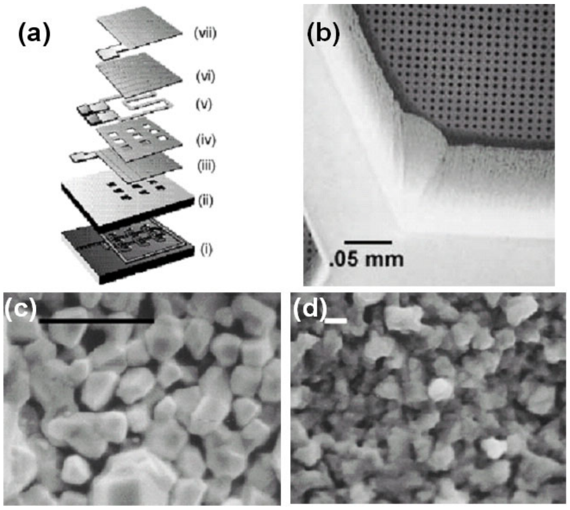

Figure 11. Different views of the LLNL μSOFC. (a) A schematic view with (i) micromachined substrate manifold, (ii) thermal and electrical insulation, (iii) thin film anode, (iv) electrical insulating layer, (v) electrical resistance heater, (vi) thin film electrolyte, and (vii) thin film cathode. (b) Viewing from the bottom, the silicon manifold (light gray) is formed into a hexagonal support structure, supporting the silicon nitride (dark gray) insulation layer with smaller pore structure. (c) Top view of a porous, sputtered nickel anode (bar = 1 μm). (d) Top view of a porous, sputtered silver cathode (bar = 1 μm). Reprinted from reference 41.

The μSOFC uses a porous nickel film for the anode [Figure 11(c)] and a porous silver film [Figure 11(d)] for the cathode. The films were made porous by sputtering them at high pressures and at elevated substrate temperature[45]. The electrolyte used is a dense thin film of YSZ, formed by sputtering from a $(ZrO_2)_{0.94}(Y_2O_3)_{0.06}$ target. The nickel and silver layers are 0.5 μm thick, while the YSZ is 2 μm thick.

The devices were measured using dilute hydrogen as a fuel (humidified Ar – 4% H_2) and air as the oxidant. Power output curves are given in Figure 12. The maximum power outputs reported by the group are 6 $mW \cdot cm^{-2}$ at 390°C, the lowest temperature reported, and 145 $mW \cdot cm^{-2}$ at 600°C, the highest temperature. The stability of the power output and the device itself are not known, since the device was measured once, dwelling only 10 minutes at each temperature.

The electrodes used in the LLNL μSOFC are both single-phase, reducing the TPB length to just the perimeter of the electrode particles at the electrolyte interface. From Figure 11 (c) and (d), the electrode particle sizes appear to be roughly 300 nm – 1 μm. Reducing these particle dimensions, or creating a porous composite of the materials with the electrolyte, would likely decrease the activation polarization. Since this is expected to be the dominant loss mechanism, improved electrodes should lead to enhanced device performance. Replacing the YSZ electrolyte with a doped ceria may improve device performance, though probably because ceria is more catalytically active at the electrode interfaces and not, as suggested[42], due to decreased electrolytic resistance.

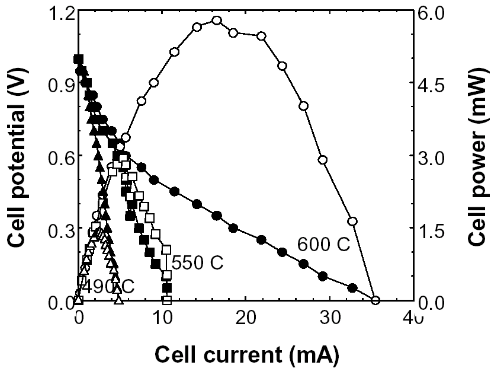

Figure 12. Power output from the LLNL µSOFC. Reprinted from reference 41.

Chen, et al. from U. Houston reported a µSOFC built on a 6 µm thick nickel foil substrate[6]. Pulsed laser deposition was used to deposit onto the foil a YSZ film of about 2 µm thickness. Photolithography was then used to define an etch pattern in the nickel foil, creating 70 µm diameter holes, separated by roughly 30 µm. To increase the TPB length, a 6 µm thick, porous nickel oxide-YSZ composite film was then deposited onto the etched nickel side of the structure, contacting the YSZ through the holes. No details could be found for the deposition conditions or properties of this composite film. A 6 µm thick, porous $La_{0.5}Sr_{0.5}CoO_3$ (LSC) film was deposited by pulsed laser deposition onto the other side of the YSZ electrolyte. The maximum power output from this cell was 30 mW·cm^{-2} at 480°C and 110 mW·cm^{-2} at 570°C, very similar to the LLNL device. This device gave stable power output for 6 hours.

Shao, et al., reported a µSOFC operating in the so-called single chamber mode[7]. In this mode, the anode and cathode are placed in the same atmosphere, a mixture of the fuel and oxidant gases[46]. The chemical potential gradient that drives the fuel cell is created by the anode material being selectively catalytically active to the oxidation reaction and the cathode to the reduction reaction. This mode has the advantage of not requiring a seal between two gas environments. However, it has a number of disadvantages, including: reduced V_{OC}, since the catalytic selectivities of the different electrodes are not perfect; reduced fuel utilization, since very high flow rates are found necessary for reasonable power output[47]; and increased safety concerns, since fuel and oxidant are mixed (though typically in ratios outside the explosive range).

The Shao µSOFC was fabricated largely through powder processing methods. A 0.7 mm thick, porous composite of nickel and Sm-doped ceria (SDC) was dry pressed and served as the anode and substrate. A 20 µm thick SDC electrolyte was dry pressed on top and then a 5-10 µm thick $Ba_{0.5}Sr_{0.5}Co_{0.8}Fe_{0.2}O_3$ (BSCF) cathode was sprayed from a powder suspension on top of that[48]. Finally, a 10 µm thick Ru and pure ceria anode catalyst layer was added to the bottom of the substrate.

The power output of the fuel cell was measured in a mixed propane/oxygen/He atmosphere. The most compelling feature of the fuel cell was that after initiating the cell operation in a furnace, the device could be removed from the external heat source and placed in thermal insulation. The device would then continue to operate as long as gas flow was maintained. In this thermally self-sustained mode, power outputs reached roughly 250 $mW \cdot cm^{-2}$. Electrolyte resistance was found to be responsible for more than half of the total polarization, so the power output may be improved significantly using a thinner electrolyte.

Whether the device is truly a micro-fuel cell or could be portably carried is debatable. The processing methods are not typically considered microfabrication. Also, since the thick substrate served as the anode, there is a large thermal mass that must be heated during initialization and then maintained at operating temperature. A supplementary battery to provide the start up energy and the insulation used to contain the heat would add significantly to the size and weight of a packaged device. Finally, fuel utilization was estimated to be only 1%. This must be improved significantly before the device is competitive with the energy densities of existing battery solutions.

1.3 Yttria Stabilized Zirconia

Yttria stabilized zirconia (YSZ) has been studied since at least 1850. Commercial use came first in Nernst glowers, light bulbs that predated tungsten filaments, in which YSZ was used as the resistive component[49]. The main benefit was that they could operate in open air, since YSZ is stable in oxidizing environments. It was recognized as a conductor of electrical charge before it was known that the charge was carried by ions. Due in part to its extraordinary chemical and thermal stability, YSZ is now used or being researched for a number of applications, including thermal barrier coatings, high-K dielectrics, optical coatings, oxygen sensors, and solid oxide fuel cells. YSZ satisfies all of the basic requirements for a solid oxide fuel cell electrolyte, namely, chemical stability in both reducing and oxidizing environments, high ionic conductivity, low electron conductivity, low cost, and ease of fabrication.

YSZ products can be formed by standard ceramic powder processing, but are commonly also made in thick film, thin film, or single crystal form (the latter of use as the synthetic gem cubic zirconia). Except for some of the thin film processing techniques, YSZ must be processed at very high temperatures. The melting point of YSZ is, like most ceramics, exceedingly high (2680 °C) and temperatures in excess of 1200°C, and often 1500°C, are required to achieve sufficient atomic mobility for sintering to occur. As will be illustrated, such high temperatures have significant impacts on the properties of the final product.

Impurities also impact the properties of YSZ products. The impurities likely come from the source material, which is primarily the mineral zircon ($ZrO_2 \cdot SiO_2$). In addition to silica, zircon typically has significant concentrations of HfO_2, Al_2O_3, Fe_2O_3, and TiO_2[50]. Vaßen, et al., found using ICP-OES that YSZ powders from three commercial suppliers typically had over 100 ppm each of CaO, Fe_2O_3, SiO_2, Al_2O_3, CeO_2, MgO, and TiO_2 impurities[51].

1.3.1 Bulk Properties

Pure zirconium oxide, ZrO_2, adopts the monoclinic crystal structure at room temperature, transforming to a tetragonal phase at 1170°C, the cubic fluorite structure at 2370°C, and then finally a liquid at 2680°C[27]. The cubic phase is the one usually desired for electrochemical applications. As seen in Figure 13, the fluorite crystal structure has a face-centered cubic array of cations with a simple cubic-like array of anions in the 4-fold coordinated interstices. The monoclinic and tetragonal structures are slight distortions of this structure. The mechanical integrity of objects made from pure zirconia is degraded during thermal cycling because of a volume expansion of around 4.5% and shape change of around 7% during the monoclinic to tetragonal phase transition[52].

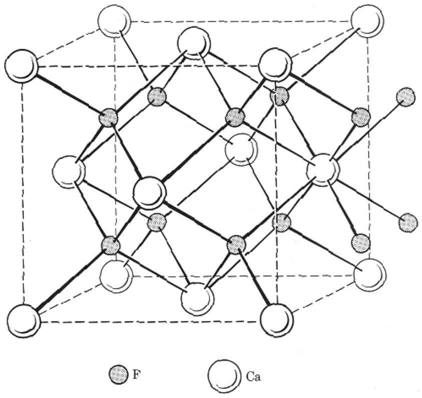

Figure 13. The fluorite crystal structure. In stabilized zirconia, the gray anions are oxygen and the white cations are zirconium and any other metals added as dopants. Reprinted from reference 53.

Zirconia will readily form solid solutions with many lower valence metals, including alkali metals and rare earths. These dopants substitute on the zirconium cation site and improve the thermomechanical integrity by stabilizing the high temperature phases of zirconia down to room temperature. With modest doping, the tetragonal phase is stabilized at room temperature, and with increased doping, the cubic phase is made stable from room temperature up to the melting temperature. The concentration required to stabilize the cubic phase depends on the dopant added.

Yttria is the most common dopant for reasons explained below. A phase diagram of the ZrO_2-Y_2O_3 system is shown in Figure 14. There remains some controversy about the phase diagram, since phase equilibria can take extraordinarily long times to achieve at low temperatures, but generally in bulk YSZ, a minimum of about 2% Y_2O_3 is needed to obtain a mixed tetragonal-cubic phase and a minimum of 8% Y_2O_3 is needed for a fully cubic phase.

The second function of the dopants is to increase the ionic conductivity by creating oxygen vacancies. A dopant ion like Y^{3+} acts as an acceptor, since it has a lower valence than the Zr^{4+} it replaces. In zirconia, the formation energy for ionic defects is less than the electronic band gap, so the charge imbalance is compensated by ionic defects, namely oxygen vacancies. In Kröger-Vink notation, the incorporation reaction for an yttria dopant is

$$Y_2O_3 \xrightarrow{ZrO_2} 2Y_{Zr}^{'} + V_O^{\bullet\bullet} + 3O_O^{\times} \tag{33}$$

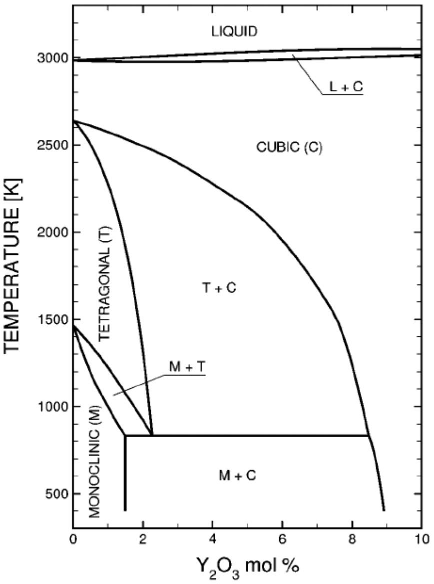

Figure 14. The ZrO_2-Y_2O_3 phase diagram. Reprinted from reference 54.

An ionized dopant and a vacancy are attracted to each other by both coulombic forces and local elastic strains in the lattice. The vacancy is made mobile when it overcomes the energy barrier of these attractive forces. To reduce the coulombic attraction, a singly charged dopant like $Y_{Zr}^{'}$ (Y^{3+}) is preferable to a doubly charged dopant like $Ca_{Zr}^{''}$ (Ca^{2+}). To reduce the lattice strain interaction, dopants with ionic radii similar to zirconium are desired. Scandium ions, which form a singly charged dopant and have radii very similar to zirconium, give the highest conductivity, but lower materials cost and moderately high ionic conductivity make yttria the most common dopant.

Oxygen ion conduction is via a vacancy mechanism, so increasing the dopant concentration increases the concentration of vacancies and, at first glance, the conductivity. In reality, at high vacancy concentrations, clusters of ordered vacancies form, reducing their mobility. This effect manifests itself as a reduction in conductivity with increased dopant concentration as well as an increase in the activation energy for conduction at low temperatures. Below about 800°C in YSZ, vacancy ordering occurs, and there is an additional energy barrier required to transport the vacancy. The causes and effects of vacancy ordering can be neatly summarized by Figure 15, which shows the ionic conductivity of YSZ as a function of the Y concentration for a few different temperatures. There is an optimal concentration, found at about the tetragonal-cubic phase transition point. As temperature is reduced, the more highly doped materials experience a more rapid decrease in conductivity as the vacancies order. Standard YSZ compositions are near the optimum conductivity. Composition is often indicated by the percentage of oxide dopant: 8YSZ = $(ZrO_2)_{0.92}(Y_2O_3)_{0.08}$ = $Zr_{0.852}Y_{0.148}O_{1.926}$. Such a composition may also be referred to as "8 mol% YSZ" or "8% by oxide."

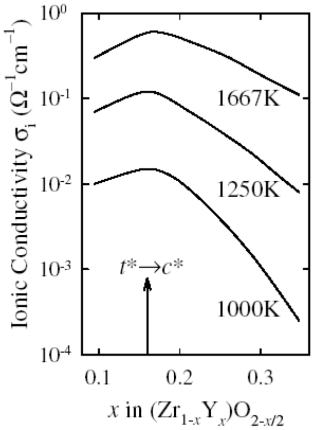

Figure 15. The ionic conductivity of YSZ as a function of the Y dopant concentration, at three different temperatures. The vertical arrow represents the boundary between the lower doped tetragonal phase and higher doped cubic phase. Reprinted from reference 55.

An expression for the temperature dependence of the ionic conductivity of YSZ can be derived as follows[56]. The conductivity of ionic charge carriers, σ, in an electric field is expressed as

$$\sigma = \frac{\gamma J_d^2 q^2 N_c f_h}{kT} \tag{34}$$

where γ is a geometric factor determined by the crystal structure; J_d is the jump distance, a submultiple of the lattice parameter; q is the charge of the carrier (for the oxygen vacancies in YSZ this is equal to twice the electron charge); N_c is the concentration of mobile carriers; and f_h is the frequency of successful ion site-hopping. The last two variables are exponentially dependent upon temperature:

$$N_c = N_0 \exp\left(-\frac{\Delta G_A}{kT}\right) \tag{35}$$

where N_0 is the total vacancy concentration and ΔG_A is the energy of vacancy cluster association; and

$$f_h = f_{h0} \exp\left(-\frac{\Delta G_m}{kT}\right) \tag{36}$$

where f_{h0} is the ion hopping attempt frequency ($10^{12} - 10^{13}$ Hz for oxide ions[27]) and ΔG_m is the energy of vacancy migration. The temperature dependence of conductivity is thus

$$\sigma = \frac{\sigma_0}{kT} \exp\left(-\frac{\Delta G_A + \Delta G_m}{kT}\right) = \frac{\sigma_0}{kT} \exp\left(-\frac{\Delta G_\sigma}{kT}\right) \tag{37}$$

Migration energies in YSZ are larger than the association energies. The association energies increase with dopant concentration, leading to the behavior described by Figure 15, above.

An Arrhenius plot of the conductivity of standard composition YSZ, as measured in a number of different studies, is shown in Figure 16. The logarithm of the σT product is plotted against the inverse temperature. According to equation 37, a linear relationship results with the slope proportional to the activation energy of ionic conduction, ΔG_σ.

The data values in Figure 16 are in very good agreement with each other, despite the very different processing methods and, likely, impurity levels. The total range in values at any temperature is just over 1 order of magnitude. The increase in activation energy below about 600°C can be seen, with the higher-dopant concentration materials experiencing a larger increase (cf. the two sets of data from reference 56 and the two from reference 62).

Electrons and holes are present within YSZ from thermal carrier generation. The band gap of YSZ is quite large, however, so their concentration is usually much lower than that of the oxygen vacancies and essentially all current is carried by the ionic defects. Nevertheless, minority carriers play a role in some electrical and electrochemical properties. This may include the activation polarization, since it relies upon electrons at the triple phase boundary.

The total concentration of electronic carriers is determined by the band gap according to

$$n \cdot p = N_C \cdot N_V \cdot \exp\left(-\frac{E_G}{kT}\right) \tag{38}$$

where n and p are the concentrations of electrons and holes, respectively; N_C is the density of states in the conduction band; N_V is the density of states in the valence band; and E_G is the band gap energy. The relative concentration of electrons and holes is determined by the reduction reaction at low oxygen partial pressures

$$2\mathrm{O}_\mathrm{O}^\times \rightarrow 4\mathrm{e}' + 2\mathrm{V}_\mathrm{O}^{\bullet\bullet} + \mathrm{O}_2^{(\mathrm{g})} \tag{39}$$

and the oxidation reaction at high oxygen partial pressures

$$2V_O^{\bullet\bullet} + O_2^{(g)} \rightarrow 2O_O^{\times} + 4h^{\bullet} \qquad (40)$$

These yield mass action constants for reduction, K_R

$$K_R = n^4 \cdot \left[V_O^{\bullet\bullet}\right]^2 \cdot p_{O_2} \qquad (41)$$

and for oxidation, K_O

$$K_O = \frac{p^4}{\left[V_O^{\bullet\bullet}\right]^2 \cdot p_{O_2}} \qquad (42)$$

where p_{O_2} is the oxygen partial pressure.

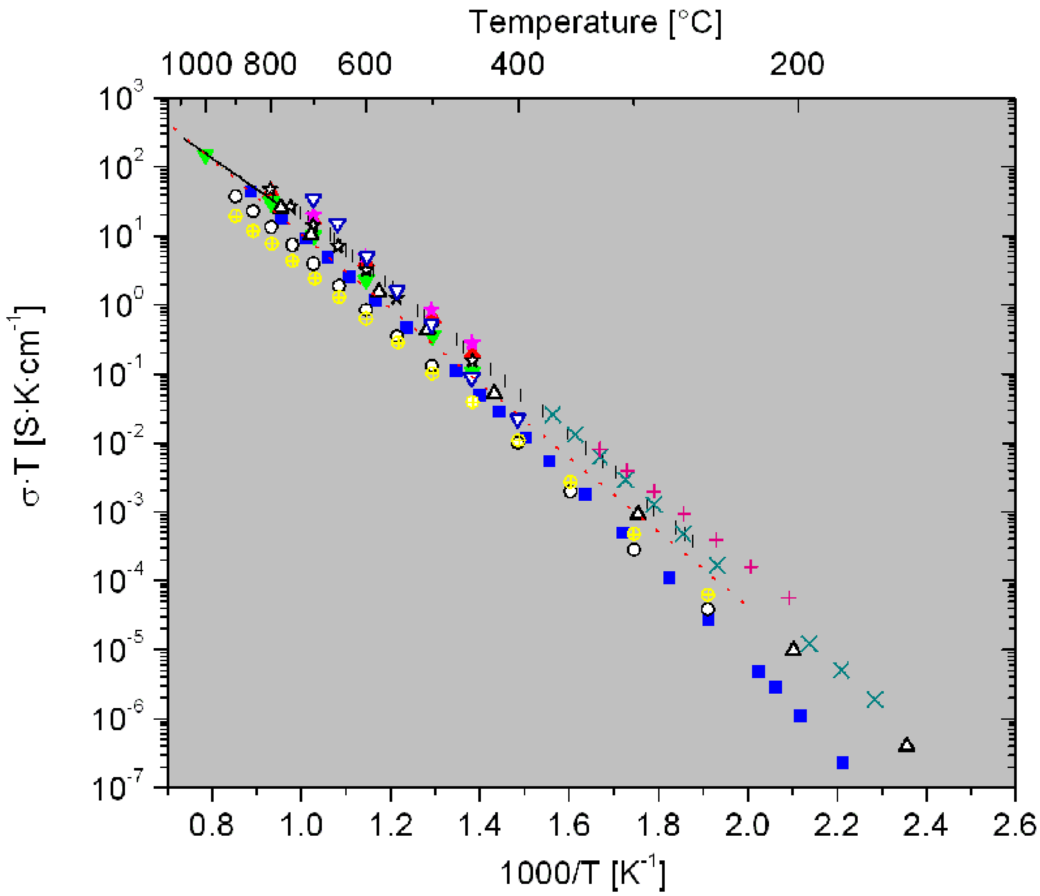

Figure 16. An Arrhenius plot of the ionic conductivity of YSZ taken from a number of literature sources. Bulk samples. Reference 57: ▲ = 8.7YSZ single crystal, ▼ = 10YSZ bulk polycrystal; ■ = reference 58, 12YSZ single crystal; I = reference 59, 9.5YSZ single crystal; reference 56: × = 8.4YSZ polycrystal, + = 4.8YSZ polycrystal; solid line = reference 60, 8YSZ polycrystal; ★ = reference 61, polycrystal composition unspecified; dotted line = reference 62, polycrystal composition unspecified. Thin film samples. ☆ = reference 61, PLD-grown 7.5 YSZ; reference 62: O = polymer precursor 8.7YSZ, ⊕ = polymer precursor 4.8YSZ; △ = reference 63, sputtered 10YSZ; ▽ = reference 64, solution deposited 8.7YSZ.

In YSZ, the concentration of oxygen vacancies is independent of p_{O_2} because it is set constant by the dopant level: $2\left[V_O^{\bullet\bullet}\right]=\left[Y_{Zr}'\right]$. Therefore, from equations 41 and 42, at low oxygen partial pressures $n \propto \left[p_{O_2}\right]^{-1/4}$, and at high oxygen partial pressures $p \propto \left[p_{O_2}\right]^{1/4}$. Assuming that electron and hole mobilities are not functions of their concentrations, then the conductivities are directly proportional to the concentrations. The electron, hole, and ion conductivities in 8YSZ were measured between 800 and 1000°C and over a range of oxygen partial pressures by Park and Blumenthal[60] and are presented in Figure 17.

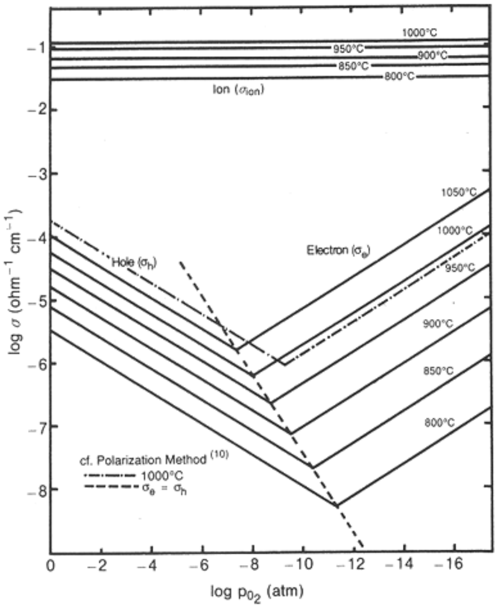

Figure 17. Ion, electron, and hole conductivity of 8YSZ between 800-1000°C. Reprinted from reference 60.

1.3.2 Grain Boundary Properties

The properties of polycrystalline YSZ are keenly affected by the grain boundaries. This is believed to be due predominantly to the presence of impurities found there. Vaßen observed that impurities, particularly SiO_2 and Al_2O_3, improved the sintering behavior of YSZ. This hints that they play an especially important role at the grain boundaries[51]. Ingo and Padeletti found that dissolved impurities preferentially segregated to the grain boundaries during high temperature sintering and formed mechanically weak zones[65]. Using x-ray photoelectron spectroscopy (XPS), Auger electron spectroscopy (AES), and secondary ion mass spectrometry (SIMS) on the fracture surfaces of YSZ thermal barrier coatings, this strength-limiting grain boundary phase was identified as a sodium silicate containing significant aluminum and yttrium. The segregated layer thickness was estimated at only 20-30 nm, so these highly surface sensitive techniques were required. Sintering at as low as

900°C created a grain boundary phase with nearly as much Si and Na as Y.

Hughes used XPS on fracture surfaces of YSZ pellets made from high purity raw materials and sintered between 1200°C and 1700°C[66]. The fracture surfaces created by thermal shock formed along grain boundaries and so exposed the grain boundary phase. Though the bulk impurity level of Si was only 60 ppm, the Si/Zr ratio at the fracture surfaces was between 6% and 20% and the Y/Zr ratio was between 28% and 35%, thus indicating a silicate composition far removed from the bulk phase. Hughes identifies the phase as a sodium-yttrium silicate and notes that adding high purity alumina to the batch before sintering successfully scavenged the silica.

Silicates are typically poor conductors of oxygen ions[53],so the presence of the siliceous phase can be expected to hinder the motion of oxygen through the electrolyte. Two models are typically used to understand the grain boundary resistance in ceramics: the brick layer model, shown in Figure 18(a), and the constriction model, shown in Figure 18(b). The difference between the two models is that the brick layer model supposes complete coverage of each electrolyte grain (brick) by a higher resistance grain boundary phase (mortar), while the constriction model assumes that a grain boundary phase of insignificant conductivity partially covers the grains, leaving small areas of direct grain-to-grain contact through which all current must flow.

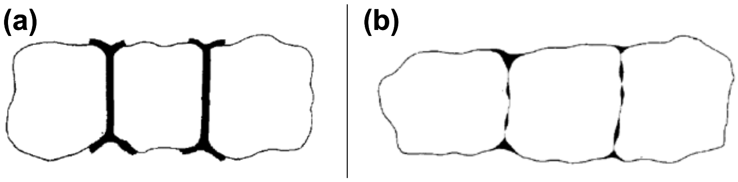

Figure 18. A schematic view of the (a) brick layer model and (b) constriction model for grain boundary resistance in electronic ceramics. In each, grains are white with grain boundary phase in black. Reprinted from reference 67.

On the basis of these assumptions, the grain boundary capacitance is that of the glassy phase in both models, but the resistance is that of the glassy phase for the brick layer model and that of a reduced electrolyte contact area for the constriction model. Therefore, if the activation energy of grain boundary conduction is similar to that of the electrolyte bulk, then the constriction model is normally assumed. This model was first advanced by Bauerle, who used this argument to reason that the constriction model more closely resembles the grain boundary resistance in YSZ containing typical impurity levels[68]. Concurring with this, most reports derive an activation energy of grain boundary conduction between 1.08 eV and 1.16 eV[69], only slightly larger than for the bulk. In contrast, silicon impurities in CeO_2-based electrolytes have been shown to create a much higher activation energy for grain boundary conductivity, and the brick layer model is assumed[70].

Impedance spectroscopy, which is more fully discussed in section 1.4, is often used to separate the grain and grain boundary contributions to the total electrical resistance of YSZ. A companion study to reference 66 combined impedance spectroscopy with XPS to determine that the grain boundary resistance YSZ correlated with the amount of silicate phase between neighboring grains[71]. At higher sintering temperatures, the silicates dewetted from the grain boundaries and moved into triple points and to the sample surface, thereby reducing the grain boundary resistance without affecting the bulk resistance.

A study by Badwal compared the grain boundary resistance of pressed YSZ pellets made from different raw materials[67]. The activation energy of the grain boundary resistance was nearly the same in all, despite different impurity contents. This is consistent with the constriction model, since different grain boundary impurity phase compositions are expected from each. Especially interesting was the comparison between a very high purity 3YSZ powder with <20 ppm SiO_2 content and the same powder after intentionally adding more typical impurity levels of 870 ppm SiO_2, as well as Na_2O, TiO_2, and CaO. The bulk resistivity was nearly identical, but the grain boundary resistivity increased by nearly 1.5 orders of magnitude, thus indicating greater coverage of the grains by the impurities.

A study at MIT found that the grain boundary resistance of calcia stabilized zirconia (CSZ) could be affected by the grain size[72]. This occurs because as the grain size decreases, the total grain boundary volume increases. Since the overall impurity concentration is fixed, decreased grain size translates to decreased impurity phase coverage per grain. Pellets of CSZ containing <80 ppm SiO_2 were sintered under various conditions to achieve grain sizes ranging from 0.14 μm to 11.4 μm. Total impurity coverage at grain boundaries was measured by STEM microanalysis and was around 1 monolayer for the more coarse-grained samples but less than 0.1 monolayer for the finest-grained sample. A grain boundary thickness was calculated using the measured capacitance and an assumed dielectric constant, and this was used to determine a specific grain boundary conductivity. At 1 monolayer of impurity coverage, the specific grain boundary conductivity was about 10^3 less than the bulk conductivity. At 0.1 monolayer of coverage, it was less than the bulk conductivity by a factor of about 10^2. The last result may indicate an intrinsic, limiting case for the grain boundary conductivity.

Along those lines, Guo has published a couple of articles that describe evidence of space charge at the grain boundary of zirconia leading to an intrinsic grain boundary resistance[69,73]. In YSZ, Guo contends that the space charge attracts the negatively charged dopant ions and repels the positively charged vacancies. This reduction in the mobile charge carrier concentration locally depresses the conductivity. Similar to the work by Aoki, et al., high resolution TEM confirmed that high purity YSZ samples in these studies had no siliceous phases at the grain boundaries, yet a specific grain boundary resistance larger than the bulk by a factor of 10^2-10^3 was found. Additions of alumina and titania were effective in adjusting the space charge width and thereby increasing and reducing, respectively, the grain boundary resistivity.

1.3.3 Surface Properties

Similar to the grain boundaries, impurity species segregate to the external surfaces of YSZ. Even after treatment at rather moderate temperatures, Hughes and Badwal, using XPS, found that the external surfaces of YSZ had Si and Y concentrations far greater than in the bulk[74]. Pellets of YSZ from both low and high purity powders were pressed, sintered at 1500°C, polished, and then given another heat treatment at various temperatures to cause segregation to occur. The Y/Zr ratios were the same as the bulk, about 0.07, in the as-polished specimen, but increased to about 0.1 after an 800°C heat treatment and about 0.17 after 1500°C. The Si/Zr ratios were immeasurably low for the polished specimen, but were between 0.1 and 0.2 at all temperatures for the pellets made from high purity starting powder and as high as 0.33 for the lower purity material. Further details were given in a later study by the authors[75]. In this study, the Y spectra from XPS were resolved into two distinct bonding states: an oxide and a silicate, indicating that Y was present in both phases near the surface. Furthermore, depth profiles showed that the segregated phase grew to thicknesses greater than a monolayer as the annealing time increased.

Whereas the previous work was on polycrystalline YSZ, Hughes continued this work by examining the segregation of impurities to the surfaces of single crystal YSZ[76]. Most notable from this work was that segregation was found to occur very quickly. For example, at 900°C, the Si/Zr ratio on the surface stabilized to around 0.07 after only about 12 minutes of treatment (plus the considerably longer heat up and cool down times). Hughes also reported on the location of the oxygen XPS peaks. This is of particular interest to SOFC applications since the bonding state of the oxygen is the aspect of the surface most likely to change the activation polarization. Hughes reported one main oxygen peak at 529.8 eV, assigned to Zr-O bonded oxygen, and minor peaks at 531 eV and 532.3 eV, to which no definite meaning was assigned. However, for two reasons the higher energy peaks should be assigned to Si-O bonded oxygen. First, the magnitudes of these peaks scaled with impurity concentration. Second, the higher binding energy peaks have been associated with Si-O oxygen by other studies. A paper by Damyanova, et al., examined different compositions of zirconium silicates as well as mechanically mixed zirconium and silicon oxides using XPS[77]. From this, an oxygen peak at 529.9 eV is definitively assigned to the Zr-O bond and is easily distinguished from a peak at 532.5 eV, indicating a Si-O bond. Similarly, Matsuoka, et al., found a dominant peak at 530.12 eV for pure ZrO2 films, with a shoulder at 531.86 eV that may be due to the Si substrate[78].

Bernasik, et al., reported similar results to Hughes and Badwal, noting Si and Y enhancement at the surface starting at around 1000°C[79]. After treatment for 5 hrs at 1400°C, contamination was so severe as to deplete the Zr concentration in the outer few nanometers to around 50% of the cations, with Si contributing most of the rest.

Whalen, et al., used a surface sensitive x-ray fluorescence technique and found a correlation between Si and Y segregation[80]. Specifically, increased Si content in the YSZ increased the concentration of both Si and Y segregated species on the surface after annealing. This study confirmed the findings of others that the segregation occurs quickly—Y surface concentrations were stabilized within the first 3 hrs of treatment.

Segregation of other dopants in stabilized zirconia was studied by Theunissesn, et al.[81] by AES and XPS. They confirmed that Y segregates to the surface of zirconia in YSZ and also found that it was the main segregant in ternary doped systems, including Y,Ce-ZrO_2 and Y,Ti-ZrO_2. Significantly enhanced surface compositions of Ce and Ti were also found in those systems. The segregation layers were measured to be 2-4 nm thick. Similar to the work of Aoki described above[72], this study found that the surface concentration of Y decreased as the grain size decreased, due to depletion of the bulk.

While the ability of Y and impurities to segregate to the surface is well established, the effect of this on the properties is not. Zhu, et al., found that heterogeneous catalysis of methane partial oxidation on YSZ surfaces is highly dependent on the outermost surface composition[82]. While pure ZrO_2 displayed poor catalytic activity, high purity YSZ had high activity. Sintering of low purity YSZ led to surface coverage by impurities, mainly CaO, as well as a collapse of catalytic activity.

Of particular concern to SOFCs are the effects that surface impurities have on the electrode polarization. Adler stated in a comprehensive review article of SOFC cathodes that “while the impact of certain impurities (particularly silica) on the properties of ion conductors is well known, there have only been a few studies to date that really investigate the impact of these impurities on electrode performance.”[18] Knowing from the studies mentioned above that even high purity ceramic ion conductors are undoubtedly coated with a thin impurity layer after being processed at high temperatures, this must be considered a key outstanding question to understanding SOFC electrode polarization behavior.

One of the few studies to which Adler was surely referring was a series of papers by de Ridder, et al.[83-86]. In the first articles[83,84], low energy ion scattering (LEIS) was used to study the surface composition of YSZ. LEIS is even more surface sensitive than XPS. Only the outermost monolayer is measured by this technique; unfortunately, it has poor ability to discern atomic species of similar mass, such as Y (mass = 89 amu) and Zr (naturally abundant isotope masses = 90 to 96 amu). To circumvent this issue, isotopically enriched ^{94}Zr was used to create nominally pure YSZ samples. After calcining the samples at temperatures equaling or exceeding 1000°C, the surface was found to be completely covered by Na, Si, and Ca, with no Y or Zr present. Underneath the impurity layer was found a high Y content segregation layer, of about one monolayer thickness. An intriguing estimate was made by the authors, i.e., bulk impurity levels would have to be reduced to below 10 ppm before the surfaces could be impurity free.

In later papers by the group[85,86], surface analysis was combined with ^{18}O/^{16}O isotope exchange experiments to measure exchange kinetics. In one experiment, the fraction of oxygen ions exchanged at the surface was compared to the coverage of the surface with CaO. As seen in the open symbols of Figure 19(a), a linear relationship was found. Two key conclusions can be drawn. First, because exchange decreased as coverage increased, the surface impurities do indeed strongly inhibit the oxygen surface exchange of YSZ. Second, because the relationship is linear, the surface impurities have little effect on the surface exchange reaction except to block available exchange sites. The closed symbols plotted in Figure 19(a) are the fractions of oxygen exchanged at the surface when corrected for the actual amount of exposed YSZ surface area (multiplied by 1-CaO coverage). These values are relatively constant, lending further credence to the conclusions.

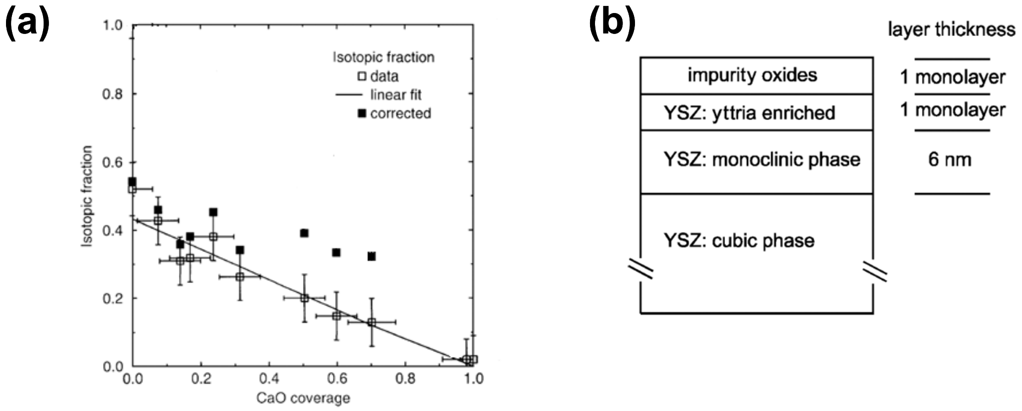

Figure 19. (a) The fraction of oxygen exchanged after 2hr at 500°C for YSZ samples with various degrees of surface coverage by CaO impurities before (□) and after (■) correcting for the amount of YSZ surface exposed. (b) The structure of YSZ surfaces after high temperature processing, as determined by de Ridder, et al. Adapted from references (a) 85 and (b) 86.

In another experiment, samples were first sputter cleaned with Ar ions to remove the impurity layer, then annealed at 500°C to restore the oxygen stoichiometry, and finally placed in furnaces with an enriched ^{18}O atmosphere for 10 or 120 minutes at temperatures between 0°C and 500°C. Interestingly, the activation energy of the surface exchange was similar to that measured for monoclinic ZrO_2. In addition, the ^{18}O diffusion profile indicated two zones with different diffusivity values: a ~6 nm thick surface zone with diffusivity similar to monoclinic zirconia and a bulk zone with diffusivity similar to YSZ. Based on this, the authors conclude that Y segregation to the surface creates a subsurface Y depleted region. This region adapts a monoclinic-like phase structure, as expected from the phase diagram (Figure 14). From this experiment, the authors proposed that YSZ surfaces after high temperature processing have the structure pictured in Figure 19(b).

Another group that has tried to correlate impurities with SOFC electrode performance is at Risø National Laboratory, Denmark. The irreproducibility of electrode behavior both within one experiment as well as between different laboratories is mentioned by the authors as probable evidence of impurity-controlled behavior[87]. In one set of experiments, bent Ni wire was used as a small anode on the surface of YSZ[88,89]. Ni wires of 99.8% and 99.995% purity were used, and the higher purity wire had as little as one tenth of the polarization resistance. After measurement at 1000°C, the wires were removed and impurities were found at the contact region using time-of-flight secondary ion mass spectrometry (TOF-SIMS). Impurities were found to cover the YSZ surface, as expected, but were also found in the contact regions of the Ni wires. Reduced amounts of impurities, particularly Mn, were found in the higher purity Ni contact area. This may be the cause of the reduced resistance, though because Ni is known to play a catalytic role in the fuel oxidation at the anode, impurities on the Ni surface are also likely to play a role.

Finally, a paper by Zhang, et al., should be mentioned[90]. In this work, the surfaces of a YSZ electrolyte were etched with an HF or HF + HCl solution. Composite anodes (NiO + YSZ) and cathodes (LSM + YSZ) were then applied and the fuel cell measured using a H_2 fuel. The power output of the fuel cell at 1000°C increased from 0.48 $W \cdot cm^{-2}$ for the unetched electrolyte to 0.52 $W \cdot cm^{-2}$ for an electrolyte etched for 2 hr and 0.61 $W \cdot cm^{-2}$ for the an electrolyte etched for 20 hr. Most of this benefit is likely to have come not from cleaning of impurities, however, but from thinning of the electrolyte. Since measurements were performed at 1000°C, any impurities removed by the etching will have re-segregated to the surface. Contrary to the authors' claims, it is doubtful that the etching improved the electrode performance, since most of the triple phase boundary should be found within the composite electrodes. These were applied after etching.

1.3.4 Sputtered and Other Thin Films

Thin films of YSZ have been studied for a number of applications, especially high-*k* dielectrics and miniaturized electrochemical devices. A number of research groups have reported the production of YSZ films by techniques including hot and cold wall chemical vapor deposition; sol-gel methods using dip coating or spin coating; powder methods such as tape casting, electrophoresis, or spraying;

and physical vapor deposition methods, including evaporation, sputtering, and pulsed laser deposition. These production methods for YSZ were reviewed recently[91]. A YSZ film may be expected to exhibit very different properties from the bulk, since it may have different microstructure, phase, stress state, stoichiometry, lattice parameter, purity, etc.

Fuel cell electrolytes, especially when they are thin, must be dense to avoid fuel leakage. This requirement can complicate the use fabrication techniques with metalorganic or oxide powder precursors, since high sintering temperatures are often required to eliminate porosity. Physical vapor deposition routes, especially sputtering, can produce thin yet highly dense films, even with low processing temperatures. The low temperatures can make the processing easier, but may also lead to the material adopting an amorphous or metastable phase. Sputtering has the benefit of being already in use in industry for coating substrates up to very large areas. (Coincidentally, sputtering was first observed by Grove, the scientist who created the first fuel cell[92].) One drawback to physical vapor routes is that they require vacuum, making processing more cost and time intensive.

Producing oxide films with a vacuum-based technique can be somewhat tricky in that the film stoichiometry is liable to be oxygen deficient. The target or source material used can be either the oxide itself or a combination of the required cations as metals. In either case, oxygen may be introduced into the vacuum to maintain or create the needed stoichiometry. It may be easier in some cases to preserve the stoichiometry from oxide sources, but metal sources have several benefits. The higher vapor pressure, thermal conductivity, and ductility of metallic phases can help achieve high deposition rates. The latter two aspects are especially important in sputtering, where highly localized heating can fragment a ceramic target. In addition, the electrical conductivity of metals allows DC sputtering power to be used instead of more difficult RF sputtering power. Finally, metals are usually available in higher purity than the corresponding oxides.

The issues of achieving the proper stoichiometry and phase is demonstrated by Kao, who compared the properties of films produced on room temperature substrates by ion-beam sputtering from a pure Zr (metal) target and a YSZ (oxide) target[93]. Films from both targets were reported as slightly oxygen deficient, with films from the metal target slightly more so. The biggest difference between the films was the phases present. Films produced from the oxide target consisted of a dense distribution of ~24 nm monoclinic crystallites (despite the Y stabilizer in the target and, presumably, the film) in an amorphous matrix. By annealing, the films changed into a mixture of monoclinic and cubic phase. Films from the metal target were largely amorphous, with a sparse distribution of extremely fine cubic crystallites (despite no stabilizer present). By annealing at 450°C, these films were nearly fully transformed into the cubic phase, which is rather surprising for pure zirconia.

Bolouz, et al., reported on the phase of films sputtered using RF sputtering from YSZ targets containing different amounts of Y stabilizer[94]. Films from a target of 8YSZ, which is fully cubic as a bulk ceramic, exhibited both cubic and monoclinic x-ray diffraction peaks. Targets with increased Y concentrations, 15YSZ and 20YSZ, gave films with only cubic peaks. Grain sizes were estimated from the peak broadening to be 20 nm, 18 nm, and 16 nm for films from 8YSZ, 15YSZ, and 20YSZ, respectively.

A report from Gao, et al., found phase relationships for sputtered films that closely mirrored that found for bulk materials[95]. Films with 2.2 and 4.9 mol% Y_2O_3 had tetragonal phase, while films with over 8.6 mol% Y_2O_3 had only cubic phase, as detected by Raman spectroscopy.

YSZ films have been deposited by sputtering from a Zr_xY_{1-x} metal alloy target by a few research groups. Hobein, at al., used this technique with a $Zr_{0.2}Y_{0.8}$ target over a range of oxygen partial pressures and at substrate temperatures between 500°C and 700°C[96]. In all cases when using a NiO-YSZ substrate, but especially at lower oxygen partial pressures, cubic and tetragonal phase YSZ films were produced. Thiele, et al., also used this technique and achieved dense, cubic YSZ films with 15 nm grain size and measured them to have an ionic conductivity similar to bulk values[97]. Jankowski and Hayes described their use of the technique as part of the Livermore μSOFC effort[98,99]. They reported that films with a low sputtering rate were fully oxidized and cubic, but films with a very high sputtering rate were oxygen deficient and contained an orthorhombic phase.

The conductivity of YSZ films is generally reported as similar to bulk values, and the activation energies are almost always very close to the bulk values (values from a few thin film studies are included as noted in Figure 16). The work of Kosacki, et al., stands as an exception to this. In one study, the ionic conductivity of both YSZ and doped ceria films could be enhanced by as much as two orders magnitude[100]. Dense, crystalline films were produced by a polymeric precursor spin-on technique followed by heat treatment at 300°C – 1200°C. The grain size of the resultant film was a strong function of the treatment temperature and ranged from 1 to 220 nm. The conductivity of films with the smallest grain size was enhanced by nearly 2 orders of magnitude. At this point it remains unclear as to the reason for the increased conductivity in the nanocrystalline films. One speculation is that the organic precursors leave some remnant after being heat-treated at the lower temperatures. Tuller has speculated that substrate interactions or humidity may play a role[101]. Along these lines, another study led by Kosacki examined the measured resistance of ultra thin YSZ films deposited on MgO substrates[102]. In this study, the resistance decreased as the film thickness decreased. This was believed to occur due to an anomalous conduction mechanism at the film-substrate and/or film-gas interface. The resistance could be split with reasonably consistent results into an interfacial resistance that was not a function of the thickness in parallel with a bulk resistance that had an inverse relationship with the thickness. This mechanism is not likely to play an important role unless films less than 50 nm or so are used or if artificial interfaces with similar properties can be produced in the bulk of a material at the level of every 50 nm or less.

As a final note in this area, it is known from a number of studies, including a recent one at MIT[103], that thin films of YSZ can have very high residual stresses. There has not been any direct research into whether these stresses affect the transport or electrochemical properties in films. Such effects may be expected, however, based on molecular dynamics simulations of strained YSZ superlattices[104] and fairly preliminary experimental evidence from externally strained bulk YSZ ceramics[105]. This remains an unexplored area.

1.4 Impedance Spectroscopy

The measurement of electrical resistance is traditionally done with application of a voltage and measurement of the resultant steady state current response or vice-versa. This is by and large successful as an empirical, macroscopic tool, but it ignores the fact that there are generally a whole host of microscopic processes contributing to the overall resistance. Multiple charge carriers may be active within a material, internal or external interfaces may disrupt the current, samples may be inhomogeneous, chemical or electrochemical reactions may control the charge flow, etc. Impedance spectroscopy can deconvolute these processes by examining the electrical response function in the frequency domain, since each of them typically has different time constants.

Impedance is a generalization of electrical resistance. It is used for periodic signals and accounts for both magnitude and phase information with a complex representation:

$$\boldsymbol{Z}(\omega) = Z' + i \cdot Z'' \tag{43}$$

where $\boldsymbol{Z}$ is an impedance vector which depends on the frequency, ω; Z' is the real component of the impedance or resistance; Z'' is the imaginary component of the impedance or reactance; and $i \equiv \sqrt{-1}$. Measurement of impedance is typically done by applying a small amplitude, fixed frequency, sinusoidal signal and measuring the amplitude and phase of the linear response. There is some research that uses harmonic analysis to examine non-linear characteristics, but this is much less common. Impedance spectroscopy involves sweeping the frequency to measure the sample over a range of interest. Automated instruments exist that perform impedance spectroscopy over a wide frequency range, often from below 10^{-3} Hz to, in the ideal case, above 10^{7} Hz. High frequency measurement is complicated by cable inductance, stray capacitance, and the need for impedance-matched circuits at radio frequencies.

Spectra are often plotted in the imaginary plane, Z' vs. Z'', with one data point per frequency. Measurements are usually more capacitive than inductive (i.e., Z'' is negative), so the imaginary axis is often drawn negative-side up. The spectrum for a parallel resistor-capacitor circuit, perhaps the most common element in solid state impedance spectroscopy, is shown in Figure 20. In the imaginary plane, this circuit has the appearance of a semicircle centered on the real axis and with a diameter equal to the resistance. This behavior is so often observed because essentially all physical processes that give a resistance have some capacitive mechanism in parallel, at the very least a stray capacitance between the electrodes. Equally the case, any dielectric mechanism has some leakage resistance in parallel.

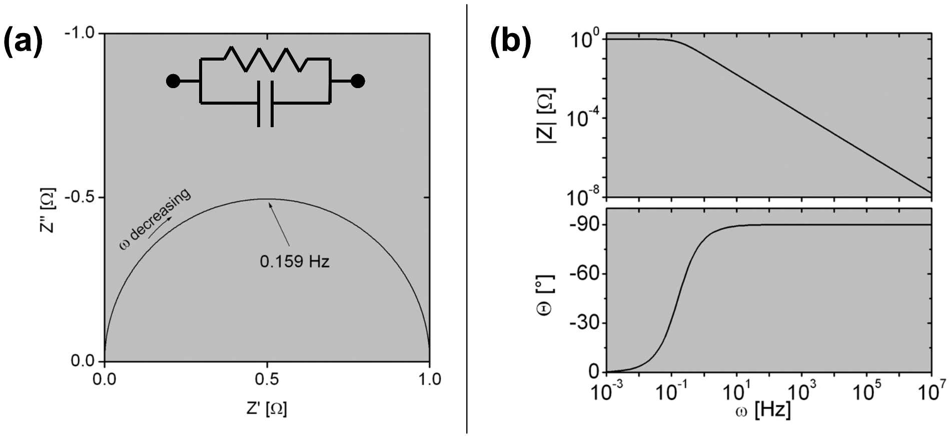

Figure 20. The impedance of a parallel resistor-capacitor circuit between 10^7 and 10^{-3} Hz, plotted (a) in the complex plane (with a circuit diagram inset) and (b) as a function of frequency, showing both the magnitude and phase. R=1 Ω; C=1 F

Often, a system can be modeled as a series of such resistor-capacitor, or RC, networks. Impedance plots in the complex plane then appear as a horizontal row of semicircles (one example can be found in Figure 23), with overlaps occurring if the peak frequencies are within about one order of magnitude. The diameter and peak frequency of each semicircle gives the resistance and capacitance of the individual RC elements, allowing the independent study of each contributor to the overall behavior.

1.4.1 Equivalent Circuit Modeling

Data reduction in impedance spectroscopy is accomplished by finding a set of circuit elements that closely match the electrical response of a sample over the measured frequency range. The ideal circuit elements: resistors, capacitors, and inductors, have frequency responses defined by

$$\begin{aligned} \boldsymbol{Z}_R(\omega) &= R \\ \boldsymbol{Z}_C(\omega) &= -i\frac{1}{\omega C} \\ \boldsymbol{Z}_L(\omega) &= i\omega L \end{aligned} \tag{44}$$

where $\boldsymbol{Z_R}$ is the impedance of a resistor, R is resistance, $\boldsymbol{Z}_C$ is the impedance of a capacitor, C is capacitance, $\boldsymbol{Z}_L$ is the impedance of an inductor and L is inductance. These elements can be combined in an infinite variety of series and parallel connections. The net impedance from a combination of two elements with individual impedance $\boldsymbol{Z}_1$ and $\boldsymbol{Z}_2$ depends on whether they are connected in series or parallel, and is found from the following equations:

$$\begin{aligned} \boldsymbol{Z}_{Series} &= \boldsymbol{Z}_1 + \boldsymbol{Z}_2 \\ \boldsymbol{Z}_{Parallel} &= \frac{1}{\dfrac{1}{\boldsymbol{Z}_1} + \dfrac{1}{\boldsymbol{Z}_2}} \end{aligned} \tag{45}$$

The impedance of combinations of larger numbers of elements can be found by recursively applying these equations. Any arbitrary $\boldsymbol{Z}(\omega)$, no matter how complicated, can be matched exactly by constructing a circuit from individual elements and adjusting the resistances, capacitances, and inductances. More typically, a reasonably approximate fit to experimental data is achieved using as few elements as possible.

Perhaps the biggest limitation of impedance spectroscopy is the ambiguity of the results. An electrical response does not have a unique equivalent circuit solution. Figure 21, for example, shows three circuits that give the same impedance at all frequencies. The choice of the equivalent circuit used to fit the data, and the determination of what constitutes a reasonable fit, lies with each investigator. An increased number of elements allows a data fitting routine to have more degrees of freedom and usually leads to less mathematical error in the regression analysis.

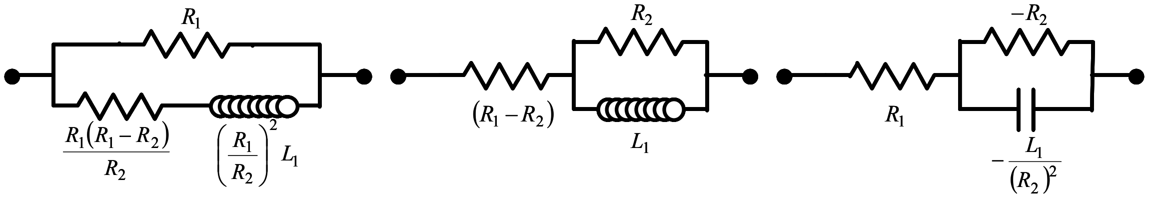

Figure 21. Three simple circuits that have the same electrical impedance at all frequencies (the negative values of the third circuit are non-physical). Adapted from reference 106.

Because the form of the equivalent circuit is chosen and not derived, the solution depends critically on the investigator's assumptions. Ideally, these assumptions come from knowledge of the system under test. Each element in an equivalent circuit used to model data from a real system should have a physical basis. A rich variable set built by changing system geometry, composition, environment, or other factors helps the investigator determine the system and can provide significantly more confidence in the equivalent circuit choice.

It is often found that the behavior of a real system is not adequately modeled with an ideal RC circuit. One reason for this is because combinations of ideal elements characteristically lead to circuit behavior with one or more discrete time constants. For example, the resistor-capacitor circuit shown in Figure 20 has a single time constant of $2\pi(R \cdot C) = 6.28\ \text{s}$, leading to a peak semicircle frequency of $(1/6.28\ \text{s}) = 0.159\ \text{Hz}$. In real systems, heterogeneities like imperfect electrode contacts or a range of temperatures in a material with a thermally activated resistance lead to a continuous distribution of time constants surrounding one or more median values[107]. To allow for such distributions, a constant phase element (CPE) can be used. This circuit element has an impedance defined as[106]

$$\boldsymbol{Z}_{CPE}(\omega) = A(i\omega)^{-\alpha} \tag{46}$$

where the exponent α determines the response characteristic. By comparison with equations 44, it can be seen that a CPE is a generalization of the ideal elements, and reduces to a resistor when α =0, a capacitor when α =1, and an inductor α =–1. It can be shown[106] that a CPE has a distribution of time constants given by

$$G(\tau) = \frac{\sin(\alpha\pi)}{\pi} A^{-1}\tau^{\alpha} \tag{47}$$

where τ is a time constant and $G(\tau)$ is the distribution function. For non-integer values of α, this function is non-zero and implies distributed time constants. CPEs are most typically used to represent non-ideal capacitors and so α values are close to 1, but are as low as 0.8. A parallel resistor-CPE circuit appears in the complex plane as a semicircle with the center of curvature depressed below the real axis, as seen in Figure 22. Other common uses for a CPE are to model semi-infinite diffusion or an infinite transmission line by setting α to 0.5.

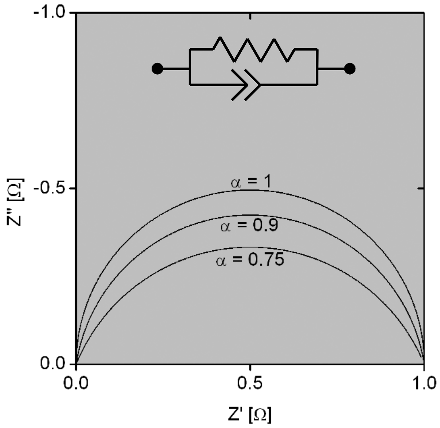

Figure 22. The impedance of parallel resistor-CPE circuits between 10^7 and 10^{-3} Hz, plotted in the complex plane. The inset is a diagram of the circuit. For each circuit R=1 Ω, A=1 $F^{-1}\cdot s^{1-\alpha}$, and α is as indicated. When α=1, it is the same as an ideal RC circuit (cf. Figure 20). As α decreases, the capacitor is less ideal and the semicircle is more depressed.

1.4.2 Impedance of Ceramic Electrolytes

The first use of impedance spectroscopy with ceramic electrolytes was by Bauerle, who studied YSZ electrolytes contacted with porous Pt electrodes[68]. Electrodes were made both by sputtering and by applying a metal paste. Bauerle found, as have many other researchers ever since, that three sources of impedance are dominant. The first two, at higher frequencies, are the impedance of charge transport through the electrolyte bulk and the electrolyte grain boundaries. The third, at lower frequencies, is the impedance of the electrode activation polarization. Bauerle used admittance plots instead of impedance plots. Admittance, $Y(\omega)$, is the inverse of the impedance and also has a semicircle in the complex plane for RC circuits of the type shown in Figure 20 (the axes are *B*, the susceptance or imaginary admittance, and *G*, the conductance or real admittance). Impedance plots are more often used now. A typical one from reference 56 is shown in Figure 23, along with an equivalent circuit model. Also indicated are the peak frequencies of each semicircle. Note that the electrode semicircle at the lowest frequencies is incomplete, since that study was only concerned with the electrolyte conductivity.

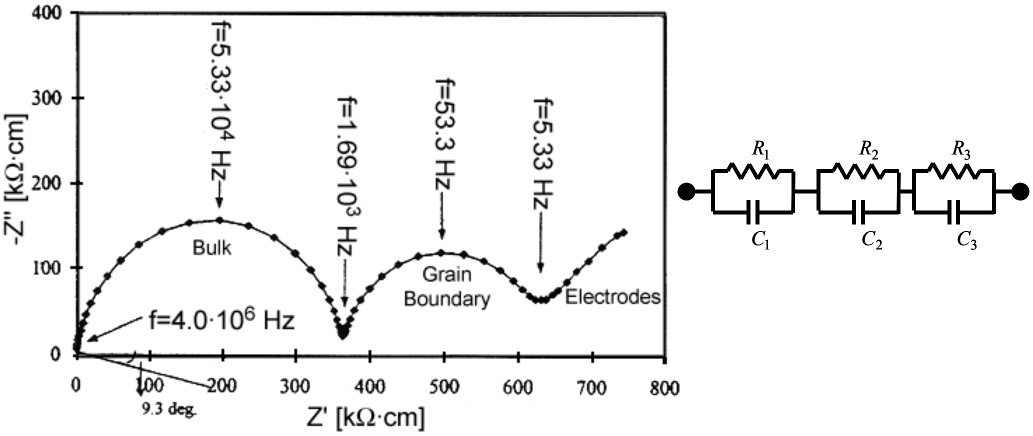

Figure 23. A typical impedance spectrum from a study of YSZ electrolyte polarization. Solid dots are raw data and lines are the fit to the equivalent circuit, shown on the side. A few frequencies are indicated. The semicircles are, as indicated, slightly depressed. Adapted from reference 56.

Bauerle used two methods to determine the meaning of the impedance results. First, samples with different geometry were measured to see how the resistances and capacitances scaled. Second, additional measurements were performed using the 4-probe dc technique, which removes electrode polarization resistance. Because $1/R_1$ and C_1 were proportional to the electrode area and disappeared with the 4-probe measurement, they were ascribed to the electrode impedance. Conversely, $1/R_2$, C_2 , and $1/R_3$ were proportional to the quotient of the electrode area to the distance between the electrodes and remained during 4-probe measurement, so they were ascribed to the electrolyte impedance.

Two rather large resistances, R_2 and R_3, were due to the electrolyte. This highlights two key differences between the impedance of solid and liquid electrolytes. Liquid electrolytes are generally highly conductive and homogeneous. Solid electrolytes, on the other hand, are often more resistive, especially at lower temperatures, and typically exhibit grain boundary behavior that is markedly different from that of the bulk. The resistance and capacitance of the electrolyte bulk are typically quite low so that the peak frequencies are usually very high. As was the case in Bauerle's work, the peak frequency for the bulk impedance is often above the instrument's capability.

In ceramic electrolytes, it is very often the case that the grain boundaries are blocking to ionic motion. This can be due to an innate resistance of the disordered region but in YSZ is often thought to be due primarily to impurity phases that segregate to the grain boundaries. The impurity phases, typically silicates, are highly resistive and the current is therefore constricted to regions of direct grain-to-grain contact. The grain boundary capacitance for such cases is found by considering the impurity phase to be the dielectric between two grains acting as electrodes. Since the grain separation is typically very small, this capacitance can be larger than the bulk capacitance by more than an order of magnitude. This explanation for the grain boundary impedance was suggested by Bauerle, based upon having similar activation energy between the grain and grain boundary resistances as well as finding reduced grain boundary resistance for a higher purity sample, and is often cited in more recent studies. The clearest method to determine whether a particular impedance feature is associated with a grain boundary is to compare the impedance of a polycrystalline sample with a single crystal.

Impedance spectroscopy of an electrolyte system necessarily includes the measurement of electrode polarization resistance. Since impedance spectra are measured with small voltages and accordingly small currents, activation polarization is expected to dominate over concentration polarization. Additionally, the activation polarization is likely to be in the linear regime so that the charge transfer resistance of equation 19 is measured. The capacitance of the electrode polarization is a double-layer or chemical capacitance and can be as large as 10 μF or possibly larger. This pushes the peak frequency to a very low range, possibly 1 mHz or even less. If more than one electrode process contributes significantly to the resistance, then it can show up as a second electrode arc in the impedance plot. Often, however, only one subreaction is significant and only one such arc is found.

1.4.3 Microelectrodes

As shown in Figure 5, the geometry of a fuel cell electrode can be quite complicated. This is necessary to obtain a large triple phase boundary length and thereby reduce the activation polarization. On the other hand, it makes the electrode resistance highly dependent upon the processing steps. This dependency complicates fundamental understanding of the reaction kinetics, since there may be unknown correlations between a variable under study like composition and the final composite geometry. The electrode resistance also becomes dependent on the procedures of a particular laboratory and perhaps even variations in purchased raw materials.

Small electrodes with finely controlled geometry, or microelectrodes, are now being used to alleviate these concerns. Through the use of simplified geometry, a more direct correlation can be made between, for example, charge transfer resistance and a well characterized triple phase boundary length. Such correlations give insight into the rate-limiting step and thus the most prudent method for optimizing electrodes. These electrodes are usually a small, dense piece of the electrode material in contact with a large, dense piece of the electrolyte. The contact size and shape are controlled.

Often, a 'working' microelectrode is used in conjunction with a much larger 'counter' electrode. By using geometrically asymmetric electrodes, the dominant polarization resistance occurs at the small electrode. The benefit is when an electrical potential is applied to the system, most of the voltage drop will be at the microelectrode, thus allowing independent study of the anodic and cathodic performance. With fully symmetric electrodes, it is unclear whether the anode or cathode is more resistive and thus which reaction is being measured. Another benefit is that a number of microelectrodes of different geometry and size can be placed on the same structure with one large counter electrode, increasing measurement speed, reproducibility, and insight.

One drawback to microelectrodes is that the small size tends to create very large resistances. This issue is compounded with solid state electrochemistry, since the electrolyte resistivities are often already rather large. Resistances greater than 1 MΩ or so can be difficult to measure using conventional impedance spectroscopy, though impedance measurement systems using calibrated amplifiers are available that are specified as capable of measuring up to 10^{15} Ω (and some DC techniques can measure even higher resistances).

Microelectrodes were first used about 25 years ago with more traditional liquid electrochemistry[108]. More recently, they have been used for a number of applications within solid state ionics[109]. Microelectrodes used in solid state systems can be produced using the tip of a needle or by pressing a wire into the electrolyte surface, but perhaps the best geometric control comes from using thin film processing and photolithography.

Microelectrodes have been used with various fuel cell systems. O'Hayre investigated Pt microelectrodes produced by focused ion beam direct writing on Nafion®, a PEM electrolyte[110]. A large platinum counter electrode was on the opposite side of the electrolyte. The electrode structures were then measured by impedance spectroscopy. Using circular electrodes, they found that an electrode's impedance was linearly proportional to its circumference, so long as the electrode was dense. This gives direct, experimental evidence that the electrochemically active sites are located at the triple phase boundary. Larger electrodes cracked during preparation, creating triple phase boundary sites within the circle. When this occurred, the electrode impedance was proportional to the area.

For SOFC applications, Bieberle, et al., investigated Ni pattern anodes on YSZ single crystals[111,112]. This work built upon similar work by Mizusaki, et al.[113], by investigating a range of electrode geometries. Dense Ni films were sputtered onto YSZ single crystal surfaces and then etched through a photolithographic resist pattern. Impedance spectroscopic characterization found only one electrode process active at near equilibrium conditions, but at high anodic bias, another electrode process was observed. Similar to the previous study mentioned, the main electrode process was found to be roughly linearly proportional to the triple phase boundary length for very fine geometry electrodes. Pores and cracks in the electrode caused a deviation from this trend for the electrodes with the least triple phase boundary length per area.

Another recent paper described using microelectrodes to study the electrode polarization of the classic SOFC cathode material, LSM, on a YSZ electrolyte[114,115]. LSM is normally thought to be a good electron conductor and a poor oxygen ion conductor, suggesting that the charge transfer resistance of LSM microelectrodes should be proportional to the perimeter length. Interestingly, this study observed that the resistance was indeed proportional to the perimeter length when an anodic bias was used but proportional to the electrode area with a cathodic bias. Under cathodic bias, the LSM microelectrodes were thought to have become conductive to oxygen ions so that the electrochemically active sites were located across the entire surface of the film. It should be emphasized that this mechanism does rely on the use of very thin LSM microelectrodes (<1 μm). The bulk path of ion transfer through the LSM occurs in parallel with the surface path at the triple phase boundary. Above some critical thickness, the ionic resistance through the LSM will exceed the resistance of the surface path and the bulk path will no longer be favorable. LSM particles used in a conventional SOFC are likely to be much thicker than the microelectrodes studied. This is an instance where the behavior of a microelectrode, due to its geometry, departed from the behavior that would be expected from bulk electrodes produced by more conventional means. Such concerns must be considered when extrapolating the behavior of microelectrodes.

Two papers from Radhakrishnan, et al., detailed impedance spectroscopic measurements of stripe pattern electrodes of LSM[116] and Pt[117] on polycrystalline YSZ discs. The results from the LSM study showed that the microelectrode resistance was proportional to the electrode perimeter length, consistent with a charge transfer reaction at the triple phase boundary. In opposition to references 114 and 115, transfer of ions through the LSM was not found. Reference 117 is one of a number of studies using microelectrodes of Pt on YSZ. Such investigations have been of interest for both SOFC and electrochemical oxygen sensor applications and are discussed in detail in section 1.5, below.

1.5 Platinum Electrodes for YSZ

The electrodes in a solid oxide fuel cell must fulfill two basic requirements: they must be conductive for electron (or hole) charge carriers and they must be stable in the chemical and thermal operating environment. Note that the chemical stability also includes chemical interaction between the electrode and electrolyte phase and the thermal stability also includes stresses arising from mismatch in the coefficient of thermal expansion between the two phases. In addition to these requirements, it is also beneficial if the electrode is catalytically active towards the half-reaction occurring on its surface. Even at the high operation temperatures of solid oxide fuel cells, many materials satisfy the basic requirements on the anodic side, since low oxygen partial pressures protect many metals from destructive oxidation. In contrast, on the cathodic side, high temperatures and high oxygen pressures prevents the use of non-noble metals. Typically, oxides that are metallic conductors of electrons, such as one of the many metallic perovskites, are used. The traditional choices for the anode and cathode are nickel and strontium doped lanthanum manganese oxide (LSM), respectively. As discussed in section 1.2.3, to increase the number of triple phase boundaries, these materials are often made into porous composites with the electrolyte.

Platinum, which is chemically stable and is catalytic towards both oxidation[118] and reduction[119] reactions, is an advantageous electrode material for many fuel cell types. Mogensen and Skaarup estimate that at 850°C, the surface exchange current density determined by $^{16}O/^{18}O$ exchange experiments are—by over two orders of magnitude—larger on platinum than on any other common electrolyte or cathode material[120]. For lower temperature fuel cells, the catalytic activity is desirable for sufficient power output. μSOFCs, because they are small, will not use nearly as much material as a large SOFC, so the cost of platinum may not be prohibitive.

The simplicity of composition and stability of platinum also makes it suitable as a model electrode. Many research groups have studied the kinetics of the Pt/YSZ system, though there is little consensus. Nearly every sub-reaction step that could conceivably be rate limiting has been identified as being lmiting, but this is likely to have arisen due to differences in composition, microstructure, and other experimental parameters[21]. A few studies have endeavored to model this system, most notably a series of papers by Mitterdorfer and Gauckler[121-123]. Unfortunately, there remain uncertainties in the values of input parameters like the triple phase boundary width as well as the sensitivity of such parameters on impurities or other experimentally uncontrolled factors. The results of a number of these studies will be summarized below, with particular attention paid to studies that use electrodes that have sufficient porosity to eliminate diffusion limitations (i.e., concentration polarization) and especially those that have well-characterized geometry.

A number of studies have used porous Pt electrodes on the surface of YSZ electrolytes and reported the polarization resistance. Included in these are papers by Bauerle[68], who used Pt paste and porous sputtered Pt electrodes; Van Herle and McEvoy[124], and Yoon, et al.[125], who used Pt paste electrodes; and Badwal, et al.[126], and Verkerk, et al.[127], who used porous sputtered Pt electrodes. Sasaki, et al. used Pt electrodes produced in a variety of ways, including sputtered, evaporated, paste (fired at low and high temperature), and solution deposited[128]. For all of these, the Pt electrodes were applied to bulk, polycrystalline YSZ that had been sintered at high temperature. After applying the electrodes, all of the samples were either heat-treated at or measured at temperatures of 800°C or higher. The values measured for polarization resistances have been normalized to the electrode area and are plotted against temperature in Figure 24. The measurements were done in air, except for references 125 and 126, which were measured in pure O_2.

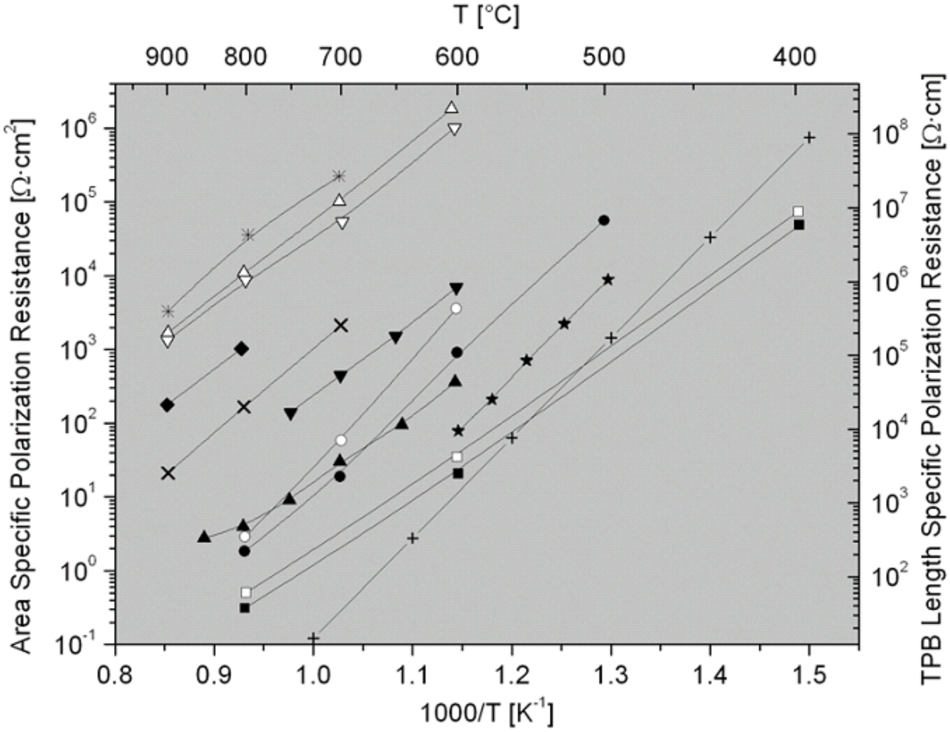

Figure 24. The area specific platinum electrode polarization resistance as reported by a number of different research groups. Using the crude estimate of 120 m·cm^{-2} TPB length per unit area of Pt electrode, the TPB length specific polarization resistance axis on the right can be used. Reference 68: (■,□) = paste, (●,○) = sputtered; ▲ = reference 124; ▼ = reference 125; ★ = reference 126; + = reference 127; and reference 128: ◆ = evaporated, × = low temperature fired paste, ✳ = 1400°C fired paste, △ = sputtered, ▽ = solution deposited.

The activation energies appear to be similar within two groups, either around 1.4-1.7 eV or 2.6-2.8 eV, for all of the electrodes in all of the studies. Badwal compiled relevant activation energies for diffusion of atomic oxygen (1.48 eV)[129] and dissociative adsorption of oxygen (2.7 eV)[130] on Pt surfaces, and these are in relatively good agreement with the sets of data above. Differences in the experimental conditions or Pt surfaces may determine whether the adsorption or diffusion is the rate limiting step. Though the activation energies are similar, the resistance values differ by nearly 6 orders of magnitude. This likely indicates uncompensated differences in geometry in addition to differences in composition and purity. Taking a goal for the area specific resistance of at most 1 $\Omega\cdot cm^2$, Figure 24 shows that a Pt electrode produced by traditional means on the surface of a dense YSZ electrolyte will not be useful until at least 600°C, and likely much higher.

The more useful parameter to which the values should be normalized is not the electrode area; however, it is the electrode triple phase boundary length. One can estimate the amount of triple phase boundary length that is found per unit of area of electrode. For Pt paste electrodes, this has been estimated as between 15-150 $m\cdot cm^{-2}$ by Mitterdorfer and Gauckler[122]. Verkerk, et al., examined the sputtered Pt electrodes used in reference 127 by microscope and estimated a value of 120 $m\cdot cm^{-2}$, in surprisingly good agreement considering the very different processing method. Taking this value, a secondary axis of triple phase boundary length specific polarization resistance is given in Figure 24; this must be considered a very crude estimate. The data taken from Sasaki, et al., is proof of this: the same Pt paste electrode increases in resistance by about two orders of magnitude when it is fired at 1400°C instead of at a lower temperature (not specified in the paper, but at least 900°C since measurements occurred at that temperature). The loss of porosity and thus triple phase boundary length is the probable cause.

Perhaps more informative is the research that used electrodes with comparatively well-defined triple phase boundary length. This has been done by Verkerk, et al., who used for the electrode a woven Pt gauze pressed into a polycrystalline YSZ electrolyte surface[127]. After measurement, the gauze was examined and the perimeter of the flattened contacts was taken as the TPB length. The authors conclude, however, that this method probably underestimated the length since it neglected TPB within the imperfectly flat contact area. Shkerin took an identical approach, but used single crystal YSZ instead[131]. Two reports used a similar approach, but with Pt wire instead of gauze: Shkerin, et al., used interdigitated Pt wire electrodes[132] while Schwandt and Weppner used a Pt wire coil[133]. Radhakrishnan attempted to have extremely well-defined electrodes by using a photolithographic process to shape stripe-pattern, thin film Pt electrodes[117]. Unfortunately, after an initial anneal step at 900°C and testing at up to 800°C, the Pt began to agglomerate, an effect seen before in other circumstances[134,135]. This created pores in the electrodes and increased the triple phase boundary length in an uncontrolled manner. Nevertheless, this was accounted for after the measurements and a reasonable estimate at the actual TPB length was made. Like the previous studies that used more poorly defined electrode geometries, all of these studies used bulk YSZ (both polycrystalline and single crystal) and all of them used very high temperature heat treatments—at least 900°C—after the electrodes were applied. All measurements were performed in air except references 132 and 133, which were performed in pure O_2.

The values measured for polarization resistance from these studies have been normalized to the given electrode TPB length and are plotted against temperature in Figure 25. Aside from reference 127, the activation energies appear to be relatively similar to those of Figure 24, at about 1.4-1.7 eV or 2.6-2.8 eV. Despite the better estimate for the TPB length, the normalized resistance values still range over about 2.5 orders of magnitude, even neglecting the values from reference 127 that likely result from a low TPB length estimate. On the positive side, the average values of Figure 24 and Figure 25, both referenced to the TPB length specific resistance, are in good agreement.

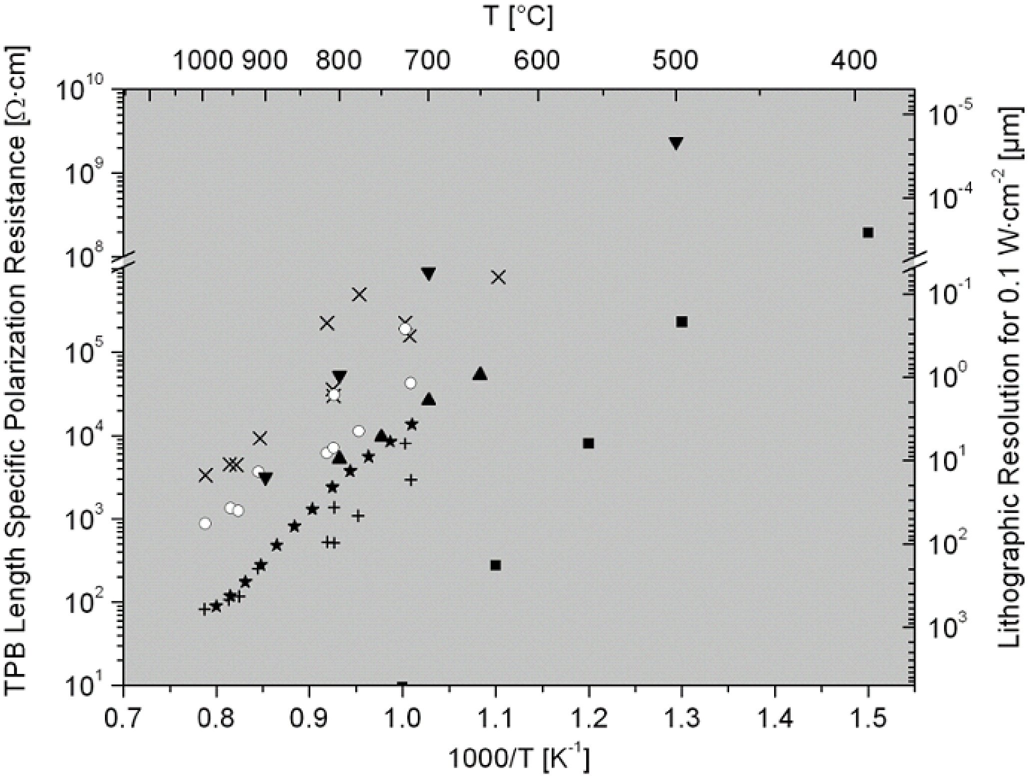

Figure 25. The triple phase boundary length specific platinum electrode polarization resistance as reported by a number of different research groups. Using a goal of 0.1 W·cm-2 for the power output from a μSOFC using these electrodes, the axis on the right, which describes the lithographic resolution needed, can be used. ▲ = reference 117; ■ = reference 127; reference 131: ✕ = (100) orientation crystal, ○ = (110) orientation crystal, + = (111) orientation crystal; ★ = reference 132; ▼ = reference 133.

Using the TPB length specific values gives predictive power to the researcher. In the context of a μSOFC, where the TPB length may come from the etching of pores into a solid Pt film on the surface of a solid YSZ film (see Figure 26a), the TPB length, l_{TPB}, in an area, A, is inversely proportional to a nominal lithographic resolution, λ

$$\frac{l_{TPB}}{A} = \frac{1}{\lambda} \tag{48}$$

Furthermore, an estimate for the power output can be made from the electrode polarization resistance. Continuing the assumptions from section 1.2.7, this is likely to be the only significant polarization mechanism. If the polarization resistance were ohmic, then the maximum power per unit area would be (see Figure 26b)

$$\mathrm{P}_{\max} = \frac{V_{OC}}{2} \cdot \frac{V_{OC}}{2R} \cdot \frac{1}{A} = \frac{V_{OC}^2}{4R \cdot A} \approx \frac{0.25}{R \cdot A} \tag{49}$$

where the R is the polarization resistance, A is the electrode area, and V_{OC} is the open circuit voltage, estimated at 1 V in the second equality. A reasonable estimate accounts for the non-linearity of the polarization resistance such that the maximum power is

$$\mathrm{P}_{\max} = \frac{V_{OC}^2}{2R \cdot A} \approx \frac{0.5}{R \cdot A} \tag{50}$$

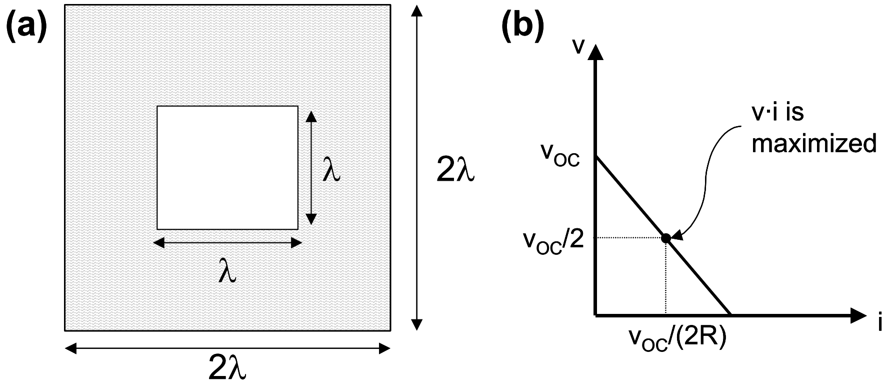

Figure 26. Graphical representations of the estimates used in equations 48 and 49. (a) Schematic diagram of dense Pt electrode etched to expose an underlying, dense YSZ electrolyte. Lithographic resolution λ is taken to mean that an array can be created of square pores with side length λ, separated by a distance λ. (b) A linear v-i curve has an intercept of V_{OC} and a slope equal to the resistance. The power output, v·i, is zero at the endpoints and maximal at the center.

Combining equations 48 and 50, the lithography needed to produce a goal power output can be correlated to the TPB length specific resistance according to

$$\lambda = \frac{0.5}{R \cdot l_{TPB} \cdot P_{\max}} = \frac{0.5}{R' \cdot P_{\max}} \tag{51}$$

where *R'* is the TPB length specific resistance. Using a casual goal of 0.1 W·cm^{-2}, the secondary axis of Figure 25 was created, showing the resolution of lithography needed. For most of the electrodes, at temperatures below 650°C, sub-micron lithography is needed and below about 500°C, physical limits are reached. This is a severe hindrance to the ability to get reasonable power from a μSOFC. Better understanding of the electrode kinetics is needed in order to be able to decrease these TPB length specific resistances and, in addition, more suitable thin film electrode microstructures must be found in order to remove the need for such fine resolution lithography.

Quite a few authors have explored the oxygen partial pressure (pO$_2$) dependence of the activation polarization. The features usually found in the resistance- pO$_2$ graphs include: a minimum in the resistance at a pO$_2$ somewhat below standard air, slopes of ±½ on either side of the minimum, a reduction in the pO$_2$ of minimum resistance as the temperature decreased, and a reduced activation energy for the resistance on the low pO$_2$ side of the minimum compared to the high side. A compilation of these results from a few different research groups is given in Figure 27. Another aspect of the pO$_2$ dependence that is occasionally reported is that the resistance becomes insensitive to pO$_2$ at low temperatures and high pO$_2$. This has been explained as the formation of stable Pt oxides on the Pt surfaces in these regimes, which has been shown to affect the polarization resistance[136]. An alternate explanation is that equilibration is slow in these conditions, and the measurements do not reflect steady state values.

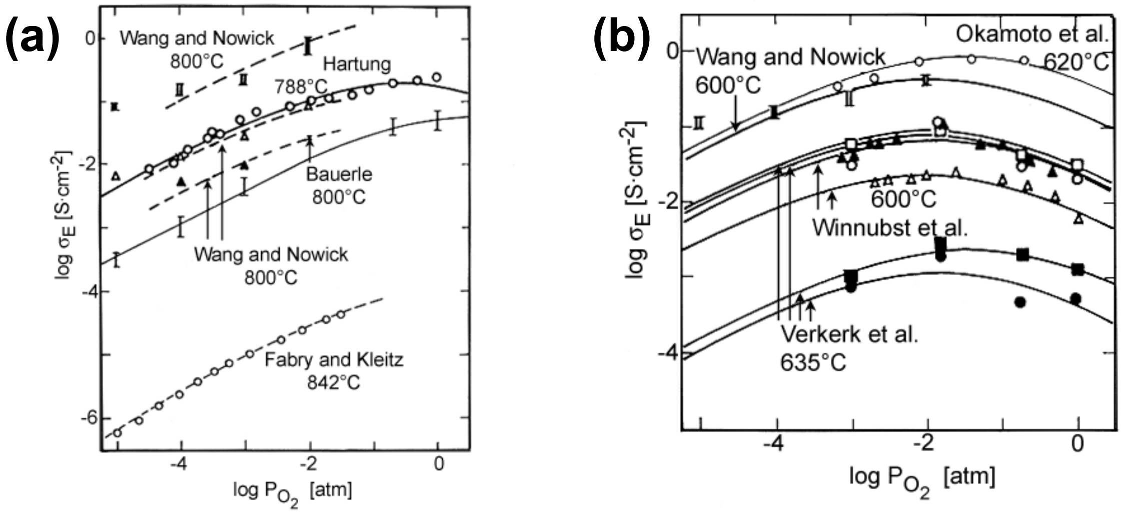

Figure 27. Dependence of the electrode polarization conductance per unit area (σ_E) upon oxygen partial pressure (pO$_2$) as reported by a number of different research groups near (a) 800°C and (b) 600°C. Adapted from reference 137. Data from references: Wang and Nowick - 138 and 139; Hartung - 140; Bauerle - 68; Fabry and Kleitz - 141; Okamoto - 142; Winnubst - 143; Verkerk - 127.

These results were explained in papers by Mizusaki, et al.[137,144], and Kuzin and Komarov[145] as relating to the concentration of oxygen atoms adsorbed on the Pt surface. Using a Langmuir isotherm, the Pt surface coverage is related to the oxygen partial pressure according to

$$\frac{\theta}{1-\theta} = \left(\frac{P_{O_2}}{P^*_{O_2}} \right)^{1/2} \tag{52}$$

where θ is the fraction of Pt surface sites that are covered by an adsorbed oxygen species and $P^*_{O_2}$ is the oxygen partial pressure where the coverage is ½. It is then reasoned that the dissociative adsorption reaction and the surface diffusion reaction each depend on the surface coverage as $\theta(1-\theta)$. Either of these could be the rate limiting step, since this dependence, combined with equation 52, yields the behaviors observed. Specifically, Mizusaki derives an equation for the diffusion reaction rate limiting step to be

$$\sigma_E = \frac{4 \cdot F^2 \cdot B \cdot \lambda \cdot c \cdot a^*_0 \cdot \left(P_{O_2}\right)^{1/2}}{\delta \cdot \left[a^*_0 + \left(P_{O_2}\right)^{1/2} \right]^2} \tag{53}$$

where σ_E is the electrode polarization conductance per unit area; B is the TPB length per unit area; λ is a constant proportional to the mobility of adsorbed oxygen; c is the concentration of adsorption sites on the surface; a^*_0 is the oxygen activity at $\theta = ½$; and δ is the average diffusion length. This equation gives a ±½ slope on either side of a conductance maximum, as required.

The fact that the activation energies for these reactions are often matched when measuring the activation energy for Pt electrode activation polarization (see Figure 24 and the discussion that follows) lends further credence to these being rate limiting steps.

Furthermore, Schwandt and Weppner argue that the diffusion reaction can be viewed as[133]

$$\mathrm{O_{ad}(Pt) + V_{ad}(ERS) \rightarrow V_{ad}(Pt) + O_{ad}(ERS)} \tag{54}$$

where $\mathrm{O_{ad}}$ are adsorbed oxygen species, $\mathrm{V_{ad}}$ is a vacant adsorption site, and the sites are located, as indicated parenthetically, on the Pt surface or the electrochemical reaction site (ERS). If the reaction sites are located only at the triple phase boundary, and the diffusion of $\mathrm{O_{ad}}$ to these sites are rate limiting, then the linear dependence of the electrode conductance upon the triple phase boundary length can be explained.

While the above discussion has centered on the resistance, impedance studies have also examined the capacitance. The capacitance of the Pt/YSZ interface has been determined by a few researchers to be between about 60 and 350 $\mu F \cdot cm^{-2}$, with little or no temperature or oxygen partial pressure dependence[68, 133,146]. This capacitance is related to not just electrical effects, such as the double layer in the electrolyte, but also chemical effects, such as boundary layer oxygen concentration changes.

Unfortunately, this complicates quantitative understanding of the phenomenon[133].

1.6 Thin Film Metal-Ceramic Composites

Composite thin films are of interest to researchers for a number of applications. As is often the case with composites, these are typically developed to create a set of properties that is difficult to find in a single-phase material. High electronic conductivity, ionic conductivity, and catalytic activity for oxidation and reduction reactions are the unique properties required for fuel cell electrodes. A key concern with composites is the degree of connectivity between the various phases. Two-phase composites typically have three structural regimes: discontinuous particles of phase A in a matrix of phase B, discontinuous particles of phase B in a matrix of phase A, and a transitional regime between these with interpenetrating, bi-continuous networks of phase A and phase B[147]. Micro solid oxide fuel cell electrodes need electron and oxygen ion access to the triple phase boundaries at the surface, and so a thin film composite of a metal and a ceramic electrolyte—a cermet—within the bi-continuous structure regime is required.

As can be seen in Figure 28, the requirement of large TPB length suggests that optimal electrodes will have a high degree of phase mixing and small grain sizes. This concept was verified for Ni-YSZ composite SOFC electrodes processed by traditional means by van Berkel, et al.[148]. Deposition methods that produce small grain sizes and, in addition, have low impurity concentrations, can be used with both metals and ceramics, have reasonable compositional and morphological control, and can coat large-area substrates are desired. Physical vapor deposition routes, and especially sputtering, fit these characteristics well.

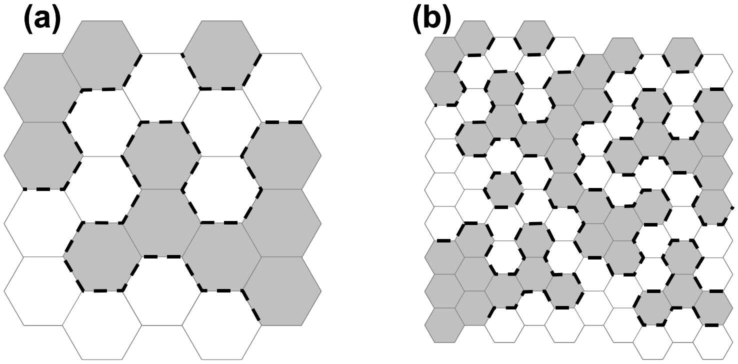

Figure 28. The triple phase boundary, the dashed line at the boundary between the white electrolyte phase and gray electrode phase, is shown for idealized composite films with (a) large grain size and (b) small grain size. In order to reduce the activation polarization, an optimal fuel cell electrode has large triple phase boundary length per area and thus small grain size.

Miller, et al., reported the first cermet film produced by co-sputtering[149,150]. Au-SiO_2 films were created by simultaneously DC sputtering a Au target and RF sputtering a SiO_2 target. The focus of the work was on films with a minority volume content of gold such that gold particles, 2-10 nm in diameter, were discontinuous within a SiO_2 matrix. Conduction of electrons by percolation of the metal species or by tunneling through the silica phase was the main focus of the work, though the structural properties were also characterized. The studies found that the gold particle diameter was larger when the proportion of gold increased, when the substrate temperature during deposition increased, and after a 2 hr, 600°C anneal in air. The particle sizes were not affected, however, by a similar anneal at 300°C.

A similar co-sputtering technique was used to produce a range of different cermets, consisting of a Ni, Pt, or Au metal with a SiO_2 or Al_2O_3 ceramic by Abeles, et al.[147]. The films were deposited by RF co-sputtering using a single sputtering gun. Small discs of the metal were placed on top of a target of the oxide material. Different compositions were deposited by changing the number of discs placed on the target. The grain sizes of the metals were similar to those in the previous work described. Similar to the previous work, much of the focus was on electron transport. This work demonstrated the ability to co-sputter a composite film from a range of immiscible source materials.

An article by Zaidi, et al., discusses co-evaporated Mn and SiO_2, though the form of the resulting film is unclear[151]. The authors refer to the film as a cermet, but it is not clear from the article whether the phases have in fact formed discrete metallic and ceramic phases. In fact, XPS results indicate that, at least on the surface, the Mn is oxidized. Since the films were processed in vacuum, the oxygen presumably came from the SiO_2 source. This finding indicates the difficulties in producing composites from solid-solution forming materials by vapor deposition methods, which involve mixing the constituents at the atomic level. Roux, et al., worked around this problem with a unique deposition method that nucleated Bi grains prior to interaction with the vapor of the oxide phase, SiO_x[152]. Bi metal was thermally evaporated and the vapor was passed through an inert gas at liquid nitrogen temperatures. The beam of Bi nanoclusters thus formed, each around 4 nm in size, is then introduced into a low-pressure chamber with an active electron beam evaporation source of SiO. A film of embedded Bi clusters within a matrix of reduced SiO_x results.

Gadenne, et al., reported the deposition and characterization of Au-Al_2O_3 and Ni-Al_2O_3 thin films as fundamental studies in percolation theory[153,154]. Transmission electron microscopy (TEM) showed the films to be 4-10 nm crystallites of the metallic phase within an amorphous matrix of the ceramic. The films were characterized using in situ macroscopic electrical conductivity measurements during the film growth as well as nanometer scale local electrical conductivity using conducting atomic force microscopy (AFM). A transition occurred in the metal concentration required to obtain percolation as the film thickness increased, since the connectivity changed from planar to 3-dimensional.

Hazra, et al., reported the growth of Pt-Al_2O_3 cermet films by co-sputtering, though the details of the deposition conditions were not given[155]. The authors used synchrotron-source, grazing incidence small angle x-ray scattering to examine the platinum nanoparticles embedded in the alumina matrix. The particles were slightly ellipsoidal, with a height of about 5 nm and width of about 4 nm.

Reactive co-sputtering was used by Zakrzewska, et al., to produce Au-TiO_2 and Ag-TiO_2 cermet films, with applications in photoelectrochemical splitting of water[156]. Mosaic targets of Ag:Ti and Au:Ti were sputtered in an Ar + O_2 gas mixture that oxidized the titanium phase but not the noble metal. Similar to the previous studies, the metals formed nanoparticulates of around 10 nm within a matrix of amorphous oxide material.

Approaching the composition of films of interest to SOFCs, Sundeen and Buchanan used spin coating from wet chemical precursors to produce Ni-ZrO_2 films (pure, un-stabilized zirconia)[157,158]. Heat treatments, necessary to remove organics, were combined with high temperature anneal steps. The result of these were, unlike in the papers described above, crystallization of the oxide phase as well as somewhat larger grain sizes, 30 nm - 70 nm for the ZrO_2 and 50 nm - 250 nm for the Ni.

Though the application was not for SOFCs, YSZ was used as the ceramic phase in co-sputtered Au-YSZ films reported by Sirinakis, et al.[159]. Separate targets of Au and YSZ were used. The substrates were not heated during deposition, but were subsequently annealed at temperatures ranging from 600°C to 1000°C. As indicated by x-ray diffraction and transmission electron microscopy, the Au and YSZ phases were crystalline as deposited, and the grain sizes grew with increasing anneal temperature. Au grains on the film surface were found to agglomerate and grew in size substantially more then the grains within the bulk of the material.

A few authors have reported thin film cermets for solid oxide fuel cell applications. Barnett's group has been particularly active in this field. In one report, the co-sputtering of Ag-YSZ cermet films was detailed[160]. Separate targets of Ag and Y-Zr metal were used. Substrates were either unheated, though the temperature quickly rose to a steady-state value of 70°C during deposition, or were heated up to 350°C. When deposited on an unheated substrate, the films were nearly amorphous. After annealing at 600°C for 1 hr, both Ag and YSZ x-ray diffraction peaks were visible. The electrical conductivity of films with varying Ag content was measured, and a transition was found at a volume fraction of Ag of 0.4. Metallic conduction at concentrations greater than 40% indicated a continuous network of Ag had formed. Measurement of the electrochemical performance of the films was not reported. μSOFC devices that used co-deposited Ag-YSZ and Ni-YSZ cermet films were patented[161,162].

The group has also reported and patented the co-sputtering of cermets consisting of Ag and either

$La_{0.7}Sr_{0.3}CoO_3$ (LSC) or $La_{0.7}Sr_{0.3}MnO_3$ (LSM) for a thin film cathode[163,164]. The interfacial polarization resistances of these films placed on a Bi_2O_3-based electrolyte were reported, and the cermets showed better performance than films of pure Ag, pure LSC, or pure LSM. The lowest resistance was obtained with a Ag-LSC cermet having 30% Ag by volume. A value of 0.3 $\Omega \cdot cm^2$ was obtained at 750°C, though it rose to nearly 10 $\Omega \cdot cm^2$ at 500°C.

Hayashi, et al., investigated the growth of Ni-YSZ cermet films for use as a SOFC anode[165]. Reactive, RF co-sputtering in 50/50 mixtures of Ar and O_2 using nickel and YSZ targets resulted in NiO-YSZ films. These films were then annealed at 1000°C for 3 hr in 4% H_2 – 96% N_2 forming gas. This procedure reduced the NiO throughout the bulk of the film to Ni. Grain sizes, as measured by atomic force microscopy, were around 40 nm before reduction, but increased greatly to around 800 nm after reduction. Pore formation was also found after reduction, likely due to the decrease in volume between the NiO and Ni phase. The Ni-YSZ film was electrochemically characterized on the surface of a bulk YSZ pellet in an 97% H_2 – 3% H_2O atmosphere. The total anodic overpotential at 0.1 $A \cdot cm^{-2}$ was 45 mV at 900°C and 72 mV at 800°C, which the authors state is less than a slurry-based Ni-YSZ composite. The same group also produced a ceramic-ceramic composite of LSM and YSZ by co-sputtering for use as a SOFC cathode[166]. X-ray diffraction indicated that the composite formed separate grains of LSM and YSZ, which is surprising since the materials are known to react and form $La_2Zr_2O_7$ and $SrZrO_3$[167]. The films had low overpotential at 1 $A \cdot cm^{-2}$, 100 mV at 1000°C, but rapidly increased to nearly 200 mV at 900°C and much higher (value not given) at 800°C.

Two studies have described the fabrication of Pt-YSZ films, both with electrochemical device electrode applications. The first, while described in the paper as a composite film, was a more-or-less layered structure. A YSZ substrate was covered with a sputtered Pt layer followed by a sputtered YSZ layer[168]. This arrangement has a number of disadvantages, since the top YSZ film would tend to block gas access to the triple phase boundary and the Pt film would tend to prevent any ions that enter the top YSZ film from reaching the electrolyte. Nevertheless, after a 1000°C anneal step, these films were used as an electrode. The electrode presumably had a better, more mixed-phase morphology than dense, stacked layers, possibly because the films were porous when deposited or because of material relocation during the anneal step. The performance of the composite film was better than a Pt film without the top YSZ film, though that may have been because the Pt agglomerated less when stabilized by the zirconia. Films with a thinner top YSZ film generally performed better, possibly because thicker top layers blocked the TPB sites.

The second study involves composite cermets with more suitable microstructures, fabricated using a MOCVD technique[169]. Films of Pt-YSZ, IrO_2-YSZ, and Pt-IrO_2-YSZ were fabricated. Grain sizes were in the range 15-35 nm, as measured by x-ray diffraction. Impedance spectroscopy was used to determine the polarization resistance of the Pt-YSZ films when deposited on polycrystalline YSZ pellets. The resistance compared well with Pt paste below 700°C and had an activation energy of 1.76-1.86 eV.

1.7 Conclusions of the Literature Review

While there have been numerous studies characterizing the polarization resistance of platinum electrodes on YSZ electrolytes, the conclusions have varied widely and few—perhaps none—have been done with the rigor required to make accurately predictive models. The few studies that characterized the TPB length-specific resistance have left significant outstanding questions. First, the measurements have all been taken at high temperature (>900°C) or after a high temperature processing step. It has been clearly shown that at these temperatures silicates and other impurities quickly contaminate the grain boundaries and surfaces of YSZ. Moreover, even in the absence of impurities, segregation of the Y dopant has been shown to create a vastly different surface structure and it is unclear to what degree the measurements are affected by these changes. Also, no studies to date have measured the electrode polarization on YSZ films, and the effects of small grain sizes, high residual stresses, and other phenomena associated with thin film processing are unknown.

The difficulties in producing electrodes for SOFCs that remain highly kinetically active at low operating temperatures have been demonstrated. This is especially the case for μSOFC electrodes that are most likely thin and homogeneous, single phase films. A more fundamental understanding of the parameters that control the kinetics of the electrode reaction is needed and the microelectrode approach has been shown to be successful in this regard. Platinum and YSZ make a good model system for the study of these kinetics because of their stability, simplicity, and past and possible future application in solid state electrochemical systems. The study of platinum microelectrode on YSZ bulk and thin film surfaces is needed in order to reach a fundamental understanding of and, hopefully, the ability to improve the kinetic rate of the electrode reaction per unit of triple phase boundary length.

As a parallel, mutually beneficial complement to this approach, the amount of triple phase boundary length per unit of area can also be increased. Co-sputtering of cermet films looks promising in this regard. The small grain sizes achieved by others with similar composition films, down to single nanometer diameters, suggest very long TPB lengths. Tailoring of the composition and grain size appears possible by adjusting the relative sputtering powers and substrate temperature. One possible issue arises in trying to obtain a bi-continuous network of the two phases, since most thin film cermets to date have indicated microstructures with a discontinuous metal phase. It is also unclear whether the increased TPB length per unit area on the surface of a dense cermet film can make up for the loss in TPB length that comes from not having a thick, porous composite.

Outside of the two brief reports described, platinum-based thin film composites have not been extensively studied for this application, despite many advantages. Platinum is highly catalytically active for both the cathode and anode reactions and so the same composite could be used for both electrodes. This holds the advantages of increasing the reaction rates, simplifying the device processing by reducing the number of materials needed to create a complete device, and allowing a fuel cell stack with a coefficient of thermal expansion that is symmetric through the thickness. This last advantage is important for a thin film stack since it mitigates a significant source of thermomechanical stress, namely a bimetal strip-like bending moment. Platinum and YSZ are also both highly chemically stable, and so should pose little concern for microelectronics processing necessary to produce the device, subsequent to the film deposition. Outstanding questions include whether such films can be produced with the requisite microstructure and whether the electrode polarization resistances of these films are sufficiently low.

1.8 Objectives of the Research

- Determine the effects of sputtering process parameters of YSZ on the conductivity
- Use platinum microelectrodes with stable, well-defined geometry to define a triple phase boundary length specific electrode polarization resistance
- Determine the effects of the sputtering process parameters of YSZ on the polarization resistance of platinum microelectrodes and compare with bulk YSZ
- Identify the rate limiting step in the electrode reaction by examining the dependence of the polarization resistance upon electrode geometry, temperature, oxygen partial pressure, and sample process parameters
- Establish ways to decrease the polarization resistance per unit of triple phase boundary length for platinum electrodes on YSZ surfaces
- Find co-sputtering methods to produce composite films with interpenetrating, bi-continuous networks of platinum and YSZ
- Characterize the electrochemical performance of the composite films to determine their efficacy as SOFC electrodes
- Establish ways to decrease the polarization resistance of μSOFC electrodes by using platinum-YSZ thin film composites to increase the amount of triple phase boundary length per unit area

CHAPTER 2. EXPERIMENTATION

2.1 Yttria Stabilized Zirconia Deposition

Yttria stabilized zirconia films were produced for this study by sputtering. High purity yttrium-zirconium metal alloy targets, 5.08 cm in diameter and 0.635 cm thick were custom made by ACI Alloys (San Jose, CA). The impurity concentrations of the yttrium and zirconium raw materials are given in Table 2 below, though the levels in the targets may have increased or decreased from these during the arc-melting and machining into target form. Two target compositions were used: 9%Y-91%Zr and 16%Y-84%Zr. Films from these targets will be referred to as YSZ9 and YSZ16, respectively.

Table 2. The quoted elemental concentrations of the raw materials used to produce the yttrium-zirconium targets and the assumed net final concentrations in the target. All units are parts per million by weight, except for percent by weight where noted. Only elements contributing over 1 ppm to the total are included.

	16%Y-84%Zr			9%Y-91%Zr		
	Y Raw material	Zr Raw material	Total	Y Raw material	Zr Raw material	Total
Al		120	100		0.10 %	910
B		0.47 %	0.39 %			
C	330	221	240		100	91
Ca	420	<10	<76	40		3.6
Ce	38		6.1	10		0.9
Cr		115	97			
Cu		54	45			
Dy	430		69	80		7.2
Fe	140	550	480	200	760	709
Hf		120	100		100	91
La	160		26	30		2.7
Mg	100	<10	<25	10		0.9
Mn		37	31			
N	0.200 %	72	380		100	91
Nd	66		11			
O	590		94		<0.15 %	<0.14 %
S	300		48			
Si				40		3.6
Tb	45		7.2			
V					300	273
W	400		64			
Y	Bal.		16 %	Bal.		9 %
Zr		Bal.	84 %		Bal.	91 %

Oxidized YSZ films were deposited from these targets by reactive, radio frequency, balanced magnetron sputtering in a Kurt J. Lesker (Clairton, PA) sputtering machine. Targets were indirectly water cooled through a copper backing plate. The sputtering gun was a Torus 2C model held at an angle of 30° to the vertical. An Advanced Energy (Fort Collins, CO) RFX-600 power supply provided 200 watts of power at 13.56 MHz. The substrates were at an uncontrolled, floating bias and were rotated to create radially uniform film thickness. Substrates were situated horizontally at a distance of about 10 cm from the target.

Targets were cleaned immediately prior to deposition by sputtering at full power for about 10 minutes with a target shutter closed. This procedure removed the surface layer of the target before any film was deposited on the substrates. After this process, the target shutter was opened and a deposition timer started. After reaching a desired film thickness (determined using the calibrated deposition rate as described in section 2.3), always between 100 nm and 1 μm, the target shutter was closed and the power supply switched off.

The sputtering chamber was evacuated to a background pressure of $<2 \cdot 10^{-4}$ Pa ($2 \cdot 10^{-6}$ Torr) using a CTI Cryogenics (Chelmsford, MA) model Cryotorr 8 cryogenic pump and as measured with an ionization gauge. The pump down time required to reach this pressure was about 12 hr. In order to create oxidized films, an oxygen – argon ratio of 1:9 was introduced into the chamber using MKS Instruments (Wilmington, MA) model 1179A mass flow controllers, operated with a model 647C process controller. The mass flow controllers were connected to nominally pure oxygen and argon sources. The total flow rate was around 20 sccm but was actively adjusted in order to maintain a working pressure of 1.33 Pa (10 mTorr).

Halogen lamps behind the substrate were used for depositions at 300°C or 600°C. Additional depositions were made on unheated substrates. A thermocouple mounted near the substrate provided feedback to a Watlow (St. Louis, MO) Series 96 temperature controller. Substrates were brought to the deposition temperature using a ramp rate of about 5°C per minute and allowed to equilibrate for at least 15 minutes before beginning deposition. After deposition was complete, heated substrates were set to cool at a similar rate, though the rate of cooling decreased near room temperature.

Amorphous, fused silica substrates, roughly 100 mm in diameter and 500 μm thick, from Mark Optics (Santa Ana, CA) were used. Fused silica was chosen because it is electrically insulating, stable at high temperatures, available in large diameters, and inexpensive. The films were deposited on a side of the substrate that was polished by the manufacturer to less than 20 Å RMS roughness. Before loading the substrates into the sputtering chamber, they were cleaned with two sequences of successive rinses with acetone, methanol, and isopropyl alcohol and then blown dry with filtered dry air.

Single crystal YSZ substrates from Coating and Crystal Technology (Kittanning, PA) were also used on occasion. These substrates were square, 15 mm to a side, and roughly 500 µm thick. Substrates with (100) and (111) orientations were used and were cleaned before deposition in an identical manner to the silica substrates.

2.2 Platinum – Yttria Stabilized Zirconia Composite Deposition

Composite films of platinum and YSZ were produced by co-sputtering in the same sputtering machine used to produce the YSZ films. Two separate targets were used, each loaded in an individual Kurt J. Lesker model Torus 2C sputtering gun. A 99.99% pure platinum target, 5.08 cm in diameter by 0.3175 cm thick, produced by Birmingham Metal (Birmingham, UK), was connected to an Advanced Energy MDX-500 DC power supply, while the 9% Y – 91 % Zr target was connected to the RF power supply described in section 2.1. The composition was varied by adjusting the relative sputtering powers used with each target. The co-sputtering procedure took advantage of the noble character of the platinum by using a somewhat oxidizing sputtering environment in order to oxidize the YSZ phase and yet keep the platinum phase metallic. The sputtering atmosphere was either 1:9 or 5:95 oxygen – argon, always at a pressure of 1.33 Pa (10 mTorr).

The substrate was optionally heated during deposition to 300ºC or 600ºC to improve the crystallization of the separate phases and adjust the grain sizes. Heating and cooling rates were about 5°C per minute and the substrates were allowed to equilibrate for at least 15 min. before deposition.

The film surface is expected to be the electrochemically active area, containing all of the gas-accessible triple phase boundary sites. Therefore, depending on how the sample is constructed, the first or last few nanometers of the deposition are where the compositional control is paramount. Film deposition began and ended by toggling a shutter above the targets. All attempts were made to open and close the shutters above the separate targets simultaneously, always within one or two seconds of each other. At the steady-state deposition rates measured, this interval equates to less than one atomic monolayer of deposition, however it is not known whether the opening of the shutter creates any longer timescale transient of film deposition and therefore any uncontrolled compositional variation at the beginning of film deposition. To try to combat this issue, full sputtering power was supplied for about ten minutes before the shutters were opened with the intent of reaching steady state before deposition began. It is unknown, though, if any amount of deposition occurred with the shutters closed and if there was thereby any uncontrolled deposition either before the shutters were opened or after they were closed to end the deposition.

2.3 Deposition Calibration

The deposition rate for a particular set of conditions was determined by sputtering a film onto a shadow-masked sample. For low temperature depositions, a glass slide substrate was masked with Kapton tape. High temperature depositions used a Si substrate with stripes made from office supply-type liquid paper as a shadow mask. After deposition for about 1 hr, the shadow mask was removed. The step height of the film at the edge of the shadowed region was then measured in six different locations using a Tencor (San Jose, CA) P-10 surface profilometer. The diamond-tipped stylus had a vertical force of 6 mg and was scanned at $20\mu m{\cdot}s^{-1}$. The accuracy is specified at about 0.8 nm. The thickness values were averaged and then divided by the total time of deposition to reach a deposition rate. This rate was then used to achieve a desired film thickness during subsequent depositions. The radial uniformity of deposition was calibrated using a similar technique on a 100 mm diameter Si wafer with a series of shadow masks placed outward from the center.

In addition to the purposeful heating of substrates during deposition, there can be substantial heating due to the bombardment of ions and electrons that is inherent to a sputtering process[170]. The latent temperature rise during a YSZ deposition was measured in this system by a collaborator, Dave Quinn[103]. A type K thermocouple was bonded to the backside of a 100 mm diameter Si wafer using an electrically insulating, thermally conductive paste. The thermocouple was connected to a vacuum feed-through and the temperature was recorded at various times during the sputtering process.

2.4 Physical Characterization

2.4.1 Scanning Electron Microscopy

Samples were viewed in a scanning electron microscope to image the edge definition of the electrode patterns and to look for cracks and other microstructural features. An environmental scanning electron microscope (ESEM) was used because charging effects on electrically insulating samples can be avoided without applying a conductive coating to the sample. The microscope was an FEI/Phillips (Hillsboro, OR) model XL30 field emission gun ESEM. A gaseous secondary electron detector collected the image. Generally, the highest resolution was achieved using 30 kV accelerating voltage and around 333 Pa (2.5 Torr) sample chamber pressure; however, these conditions were adjusted as needed to improve resolution. Minimal working distances improved the resolution considerably, and generally a distance of around 5 mm was used. Samples in the ESEM were held to an aluminum stub using carbon tape.

Cross-section samples were made by fracture. The backside of a sample was first scribed with a diamond tip. The sample was then placed on the edge of a glass slide and pressure was applied with tweezers to opposite ends of the sample until it fractured. One piece was then stuck, fracture edge up, onto an aluminum stub using carbon tape.

2.4.2 Atomic Force Microscopy

Atomic force microscopy was used to image the grain sizes of the YSZ films. The grain sizes were too small to be visualized easily by other means, and x-ray diffraction methods of determining grain size can be inaccurate for thin films, due to both anisotropic grain dimensions and strain effects. A Veeco Metrology (Santa Barbara, CA) Dimension 3000 microscope with a Nanoscope IIIa controller was operated in Tapping Mode. The cantilevers used were model TESP, produced by Veeco Probes (Santa Barbara, CA). These silicon cantilevers have a nominal tip radius of less than 10 nm, spring constant of 40 $N{\cdot}m^{-1}$, and resonant frequency of around 300 kHz. Samples were measured in open air, with no physical preparation. Both height and phase images were collected, with the latter useful for discerning grain boundaries. Micrographs were analyzed and manipulated using Veeco's Nanoscope software, version 5.12r3.

2.4.3 X-ray Diffraction

To determine the crystallinity, phase, and texture of the films, they were measured in a Rigaku (Tokyo, Japan) RU300 x-ray diffractometer. Samples were measured in a theta-two theta reflection arrangement. The divergence and scattering slits were 1° while the receiving slit was 0.3 mm. A 185 mm diffractometer was used. X-rays were produced with a rotating, water-cooled copper anode, operating at 300 mA and 60 kV, and were monochromated to select the Cu Kα wavelength (λ=1.541Å). A continuous sweep of diffraction angle at a rate of about 2° per minute was used, with intensities integrated over a 0.02° step. Diffraction patterns were analyzed using the software package Jade, version 7, from Materials Data, Inc. (Livermore, CA) and compared against standards from the ICCD powder diffraction file.

2.4.4 X-ray Photoelectron Spectroscopy

The chemical composition and bonding state of the sample surfaces were measured in a Kratos Analytical (Manchester, UK) model Axis Ultra x-ray photoelectron spectrometer. A monochromated aluminum x-ray source, emitting at 1486.6 eV, was used at a power of 150 W. For survey spectra, a pass energy of 160 eV was used. For high resolution scans of narrow energy ranges, a pass energy of 10 eV was used. Binding energy values were calibrated by setting the peak energy of the 1s electron in carbon, found as a surface contaminant on most materials kept in open air, to 285.0 eV. For depth-dependent composition determination, angle resolved measurements were performed. Spectra were measured at take-off angles relative to the surface normal of 0°, 35°, and 70°. Larger angles are more surface sensitive, with the analyzed sample depth roughly estimated at 10 nm at 0° and 2 nm at 70°. Spectra were analyzed using Casa Software's CasaXPS software, version 2.3.13Dev9. The machine was operated with the assistance of Ms. Libby Shaw and Dr. Joseph Bullard.

2.5 Platinum Microelectrode Fabrication

Dense platinum interdigitated electrodes were microfabricated on the surface of the YSZ thin films (on both the fused silica and single crystal YSZ substrates) as well as directly on the surfaces of single crystal YSZ substrates and tapecast, polycrystalline YSZ substrates. Wideband ultraviolet photolithography was used to produce interdigitated photoresist patterns as described below and diagrammed in Figure 29.

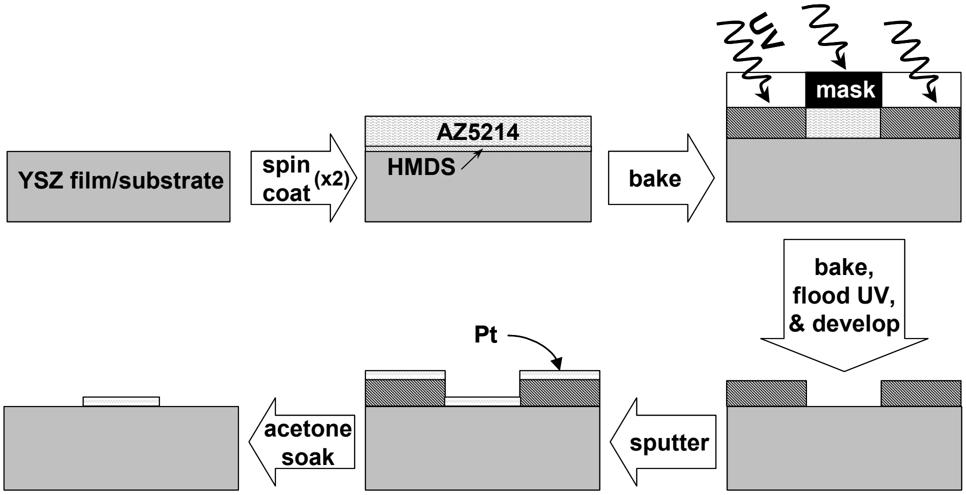

Figure 29. Process flow for producing the platinum microelectrodes. All images shown in cross-section.

Samples were first cleaned with two sequences of successive rinses with acetone, methanol, and isopropyl alcohol and then blown dry with filtered dry air. Samples were then dried in an oven held at 200°C for at least 15 minutes. Hexamethyldisilazane (HMDS), an adhesion promoter for the photoresist, was then coated on the substrates by spin coating at a speed of around 500 RPM for 30 seconds. Samples were then placed in a 130°C oven for around 10 minutes in order to evaporate excess HMDS.

Clariant Corporation (Somerville, NJ) AZ-5214E image reversal photoresist was then spin coated onto the sample surface. This photoresist is designed to give a negative vertical wall profile, which is beneficial for lift-off processes. A rotation speed of 2000 RPM was used to produce a nominal, final photoresist thickness of 1.98μm. Samples were then placed in a 90°C oven for 30 minutes to evaporate the solvents from the photoresist.

The samples were then exposed to broadband ultraviolet light for 4 seconds through a chrome photolithography mask that had a number of different interdigitated electrode designs. Since this was a negative photoresist process, chrome features in the mask defined areas of the photoresist that would later be removed by the developer. Each electrode consisted of a contact pad, approximately 1 mm × 1 mm; a spine, 100 µm wide by approximately 8 mm long; and a set of fingers emanating from the spine, each approximately 7.8 mm long and of varying width (see Figure 30a). The geometric parameters for the different electrode patterns are tabulated in Table 3. Each design was about 8 mm × 8 mm, designed to fit on a 10 mm × 10 mm die. The 100 mm wafers had 8 different electrode patterns on the mask exposed simultaneously. Smaller samples of 15 mm × 15 mm to allow for edge defects in the photolithography were centered under and exposed to just one electrode pattern.

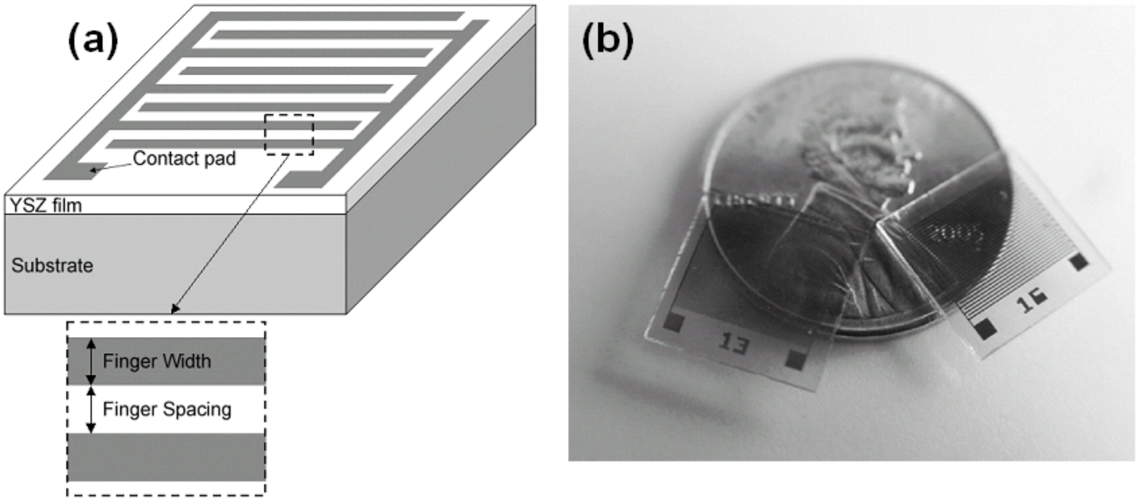

Figure 30. Interdigitated electrode devices in a (a) schematic view and (b) photographed with a penny to indicate size. Platinum electrodes in pattern 13 and 16, which appear dark in the photograph, are on the surface of transparent silica substrates with a 1 µm thick YSZ film.

Table 3. The geometric parameters for the interdigitated electrode patterns used in this study.

	Pattern number							
	16	15	14	13	12	11	10	9
Finger width [µm]	100	50	25	15	10	10	5	5
Finger spacing [µm]	100	50	25	15	10	5	5	3
Number of fingers [-]	16	33	66	110	165	220	330	412
Nominal total electrode perimeter [cm]	25.3	51.8	103	172	258	344	515	643
Nominal electrode area [cm^2]	0.246	0.256	0.257	0.257	0.257	0.343	0.257	0.321

An image reversal bake was then done for 26 minutes. The timing of this step to within 1 minute was the most crucial for successful development of the photoresist. Following this, the samples were allowed to cool for a few minutes and then flood exposed to ultraviolet light for around 30 seconds. To finish the patterning, the samples were soaked in Clariant Corporation AZ422 developer until the electrode patterns were completely developed, as determined by visual inspection. To prevent further developing of the pattern, the samples were then rinsed in deionized water, blown dry with filtered nitrogen, and then packaged in a dust-proof container until further processing.

Flaws in the developed photoresist pattern were not uncommon due to particles in the photoresist or airborne dust in the processing laboratory. After developing the patterns, the samples were examined by optical microscope. If critical flaws, such as scratches connecting the two interdigitated electrodes patterns, were found then the samples were cleaned and another attempt at the photolithography could be made. The cleaning involved two sequences of successive rinses with acetone, methanol, and isopropyl alcohol and then a blow-dry with dust-filtered nitrogen. Some of the flaws came from stuck photoresist or other particles on the chrome mask. To remove these, the mask was cleaned in piranha solution, a 3:1 mixture of concentrated sulfuric acid and hydrogen peroxide, after every few uses.

Dense platinum films were then sputtered onto the photoresist patterns using the same machine as the previous films. The sputtering atmosphere was argon, maintained at 0.67 Pa (5.0 mTorr) with a flow rate of roughly 15 sccm. No substrate heating or bias was used. 50 watts of DC power were used. As was done with the YSZ deposition, the target surface was first cleaned by sputtering with the shutter closed. The shutter was then opened for 8 minutes, which produced a roughly 150 nm thick film. This thickness was used because thinner films may not be fully dense or impermeable to oxygen and thicker films were difficult to lift-off with the roughly 2 μm thick photoresist pattern used.

To complete the lift-off patterning, the samples were soaked in acetone in a covered dish. After a few hours, the photoresist was completely dissolved, giving the platinum above it a wrinkled appearance. Mild agitation of the dish gently lifted off most of the platinum, leaving behind the electrodes. The samples, still soaking in acetone, were then placed in an ultrasonic bath for a few seconds to remove any remnant flecks of platinum stuck to the electrode edges. The samples were then rinsed one more time sequentially in acetone, methanol, and isopropyl alcohol and dried with filtered dry air. Two devices produced by this method are pictured in Figure 30(b).

A circular die-saw separated the dies produced on 100 mm wafers. To protect the samples from dust and projectiles produced by the saw, the wafers were first coated with AZ5214 photoresist by spin coating followed by baking at 90ºC. The spin speeds and baking times were not important for this step, but were generally about 1000 RPM and 30 minutes, respectively. A Disco Abrasive Systems (Tokyo, Japan) Model DAD-2H/6T programmable die saw cut the wafer at 10 mm intervals in the x and y directions, using a visual alignment of the cut path to the features. The oxide substrates were prone to cracking, and so a very slow vertical cut speed of 18 $\mu m \cdot s^{-1}$ was used.

Samples produced by the above method are symmetric Pt/YSZ/Pt structures with both electrodes of the same composition and geometry, at the same temperature, and in the same environment. The electrodes are also closely spaced on the same side of the electrolyte, meaning surface conduction may become an interfering, low resistance current path. In order to test this possibility, a large back electrode was made by applying Engelhard (East Newark, NJ) type 6082 platinum paste to the backside of single crystal YSZ substrates samples. A platinum mesh current collector with a platinum lead wire welded to it was embedded within the paste. Comparisons were then made between measurements taken with the two top electrodes spaced only microns apart and with a top electrodes and the back electrode spaced more then 2.5 mm apart. A diagram of this structure is given in Figure 31.

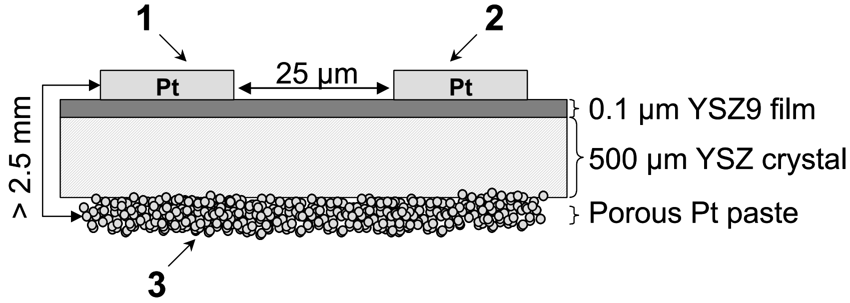

Figure 31. A diagram of the Pt paste back electrode samples used to test the presence of surface conduction. Comparisons are made between the impedance measured from electrode 1 to electrode 2 and the impedance measured from electrode 1 to electrode 3.

2.6 Platinum-YSZ Composite Microelectrode Fabrication

Microelectrodes of Pt-YSZ were used to study the polarization resistance of the electrodes. It was desirable to perform the depositions at substrate temperatures exceeding the stable region of photoresist. Therefore, lift-off processes could not be used to shape the electrodes. In addition, platinum and YSZ are both difficult to chemically etch, and so a wet chemical method to etch the composite films would have been difficult. For these reasons, shadow masking was used to form the microelectrodes. A significant disadvantage of this method is that the film thickness decreases gradually near the edge of the mask, creating an edge area that may exhibit characteristics different from the center.

Double side polished YSZ single crystals, 10 mm × 10 mm square, were used as the electrolyte. A large area back electrode was formed by depositing the Pt-YSZ composite on one side of the crystal through a shadow mask that blocked only the outer ~1 mm border of the crystal. Working microelectrodes were then formed by depositing the composite film through a stainless steel plate that was machined with five through-holes of different sizes: 1.5 mm, 2 mm, 2.5 mm, 3 mm, and 4 mm in diameter. A photograph of a measured sample is given in Figure 32. The counter electrode was contacted with platinum paste, mesh, and wire similar to the back electrode depicted in Figure 31.

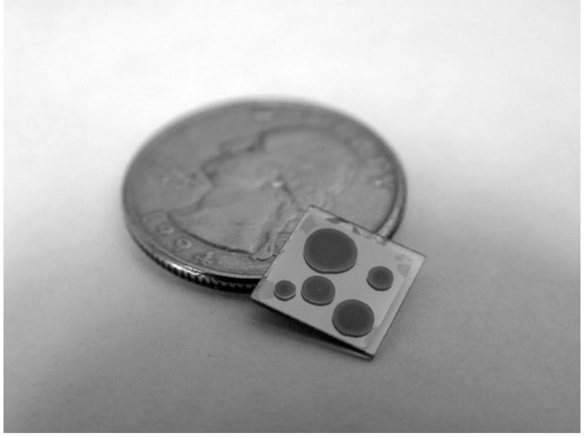

Figure 32. A photograph of a Pt-YSZ composite microelectrode device. Five microelectrodes, which appear dark in the photograph, can be seen on the top surface while the large counter electrode, which appears brighter, is visible through the transparent YSZ substrate.

2.7 Impedance Spectroscopy

The chief electrical characterization method used in this research was electrochemical impedance spectroscopy (EIS). Impedance spectra were collected by a Solartron Analytical (Farnborough, UK) model 1260 impedance analyzer, controlled by a computer running Scribner Associates' (Southern Pines, NC) ZPlot software, version 2.8d. Measurements were made from high frequency to low frequency, 10^7 Hz to 10^{-3} Hz, stepped logarithmically. A few techniques were employed to reduce the data collection times. First, if a spectrum appeared to be sufficiently complete by 10^{-2} Hz, the last decade of frequency was not collected. Second, at frequencies $>10^{-2}$ Hz, 20 data points per decade were collected, while at lower frequencies only 10 data points per decade were collected. Third, the duration of data integration, expressed as the number of cycles, was decreased, from 20 cycles at the highest frequencies (subject to a minimum time of 1 s) down to 3 at the lowest. Finally, each time the frequency was stepped, a delay was used before the integration to avoid measurement of transients; 6

cycles of delay were used at the highest frequencies and only 1 at the lowest. Even with these methods, full spectra, down to 10^{-3} Hz, took approximately 8 hours to collect, while the shortened spectra, down to 10^{-2} Hz, took just under 1 hour. Signal amplitudes were 20 mV RMS, centered about 0 V DC bias.

Spectra were analyzed, including least-squares regression analysis of equivalent circuit elements, using the Scribner Associates' ZView software, version 2.8d. An equivalent circuit similar to the one shown in Figure 33 was used, though one of the R-CPE elements was removed for samples using a YSZ single crystal substrate. Small subsections of the data were first fit crudely to single R-C elements, and these values were used as initial guesses to the equivalent circuit describing the entire spectrum. When a number of sequential spectra were obtained, such as during a temperature ramp, an automated batch fitting routine was used. First, the equivalent circuit values for one of the spectra were found. These values were then used as the initial guesses for next spectrum, and so on.

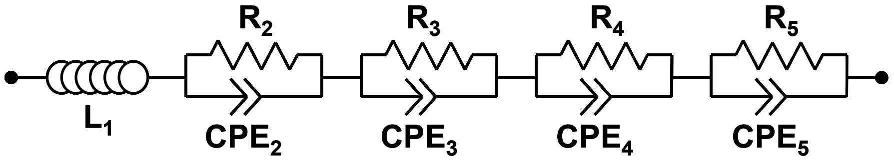

Figure 33. The equivalent circuit that was fit to the impedance spectra of interdigitated Pt electrode samples. Samples with a single crystal YSZ substrate electrolyte had one of the R-CPE elements removed. Pt-YSZ composite electrode samples had two of the R-CPE elements removed.

From the resistance values derived, conductivity values were calculated. The sample geometries were far from a traditional parallel plate arrangement, so the standard formula for conversion of resistance to conductivity could not be used. A numerical, finite element solution was written in MATLAB version 7.0.4 from The Mathworks (Natick, MA), using the Partial Differential Equation Toolbox version 1.0.6. This code determined the multiplier needed to convert the measured resistance into a conductivity for each sample's known electrode geometry and electrolyte thickness. Details of the method and the code developed are given in Appendix A.

Samples were measured in two different probe stations. The first station was an open-air system, Suss MicroTec (Waterbury Center, VT) model SOM4, modified by the addition of a small hot stage, Linkam Scientific Instruments (Tadworth, UK) model TS1500. The heated portion of this stage is built into a 7 mm diameter cup. Since the samples used in this study were too large to fit in that cup, a titanium stub was machined, with a stem sized to just fit inside the cup and a 4 mm thick, 16 mm diameter top portion on which the sample sat. Samples were contacted with 250 μm diameter, 99.99% pure platinum wire from Birmingham Metal. The wires were formed into a loop and mounted in a Suss MicroTec PH150 manual XYZ positioner. The wires then made pressure contact to the electrodes, as determined by visual inspection through the probe station microscope.

Measurements were done at temperatures between 150°C and 500°C, the goal operating temperature of a μSOFC. The actual temperature of the sample was measured with a thermocouple pressed onto the sample. To improve thermal contact, the thermocouple bead was flattened with a hammer and one of the flattened faces kept in contact with the sample using mechanical pressure. Even so, repeatability of the contact was sub-optimal, and experimental error in the temperature measurement may have been significant. The size of the hot stage was also just a little bigger than the samples. A significant radial gradient in temperature was thus expected. In order to have consistency in the temperature measurement, the samples were centered on the hot stage and thermocouple bead placed halfway between the contact pads. Finally, the air above the sample was not directly heated and so there was likely a thermal gradient through the thickness of the sample, with the thermocouple again measuring the colder portion of that gradient. Temperatures probably erred by being measured as too low. In order to eliminate the measurement of transient effects during heating, such as evaporation of condensates from the surface, samples were generally first brought to the highest measurement temperature, equilibrated for 15 minutes, measured, and then equilibrated and measured at lower and lower temperatures. A Labview program automated the hot stage temperature control, sample temperature measurement, and timing of the equilibration and measurement cycles.

The second probe station, designed and assembled by Dr. Avner Rothschild and McAllister Technical Systems (Coeur d'Alene, ID), was fully enclosed so that the gaseous environment surrounding the samples could be controlled. Four MKS 1359C mass flow controllers, connected to ultra high purity nitrogen, ultra high purity oxygen, and calibrated oxygen – nitrogen mixtures, were controlled with a MKS 647C mass flow programmer. By adjusting the flow rates of these gases into the chamber, the oxygen partial pressure was adjusted from approximately $3 \cdot 10^{-7}$ atm – 1 atm, with total pressure remaining approximately 1 atm (a one-way flow valve was used at the outlet to prevent backflow from the exhaust, thus creating a very small overpressure inside the chamber). The oxygen – nitrogen mixtures were necessary to accurately reach the entire range of oxygen partial pressures, since the mass flow controllers were accurate to only about 0.5% of full-scale flow, or ±8 sccm. Extremely dilute mixing of pure oxygen with pure nitrogen could thus not be accurately maintained. Instead, pure oxygen was used and diluted with pure nitrogen to reach levels of 100% to >1%, a certified 1% oxygen in nitrogen mixture was used and diluted for levels of 1% to >100 ppm, and so forth until an unmixed ultra high purity nitrogen gas was used and gave about 0.3 ppm oxygen. Total flow rate was kept constant at 300 sccm, which yielded an atmospheric turnover time of roughly 30 min for the entire system, including a premixing tank, the pipes, and the measurement chamber. Oxygen partial pressure inside the chamber was measured in real time with a Bosch automotive oxygen sensor. The sensor was calibrated using the steady state voltage output when flowing the undiluted, certified oxygen – nitrogen gas mixtures.

It took hours for oxygen to be purged out of the system to below levels of 0.1%, so samples were measured by loading them in to the probe station, purging the chamber with ultra high purity nitrogen flowing at the maximum rate for a long period of time, and then introducing oxygen as needed in order to measure at progressively higher oxygen partial pressures. Samples were equilibrated for 1 hour after oxygen partial pressure changes before any measurements occurred. For reasons discussed above, generally samples were first brought to the highest measurement temperature and then measured at decreasing temperatures. When gas and temperature were both controlled, samples were brought to a new oxygen partial pressure, equilibrated for 1 hour, then brought to the highest measurement temperature, equilibrated for 20 minutes, measured, and then equilibrated and measured at lower and lower temperatures before increasing the oxygen partial pressure again and repeating the cycle. A Labview program was written to automate all of these operations and allowed real time and programmed control both at the local computer and over the Internet.

The samples in the second probe station were pressed with metal clips onto a 5.08 cm diameter hot stage made by HeatWave Labs (Watsonville, CA) in the center of the chamber. Measurements were done between 150°C and 500°C. Temperature was measured with a thermocouple pressed into a silica substrate of the same thickness as the sample being measured, similarly held by metal clips at the same distance from the center of hot stage. Neither this substrate nor the thermocouple was moved between measurements, so that the temperature measurement was more consistent from sample to sample. Similar to the other probe station, there was a gradient in temperature through the thickness of the sample since the surface of the hot stage was hotter than the surrounding air.

System calibration and assumptions about high and low resistance paths were tested by measuring impedance spectra for off-the-shelf resistor and capacitor combinations, platinum microelectrodes created directly on a fused silica substrate, platinum wire leads short-circuited by direct contact with each other, and leads contacting opposite ends of the same microfabricated platinum electrode. The latter two tests were useful to quantify the series inductance present in the cables and leads, the resistance of the leads and the thin film platinum electrodes, and the parallel capacitance of the test setup as a whole.

CHAPTER 3. RESULTS

3.1 Yttria Stabilized Zirconia Film Deposition

Deposition rates at the conditions described in section 2.1 were calibrated by measuring the thickness after various deposition times. These are plotted in Figure 34 along with a linear fit that was forced to run through the origin. The slope of the line gives a deposition rate of 30.2 Å·min^{-1}. The values were re-confirmed occasionally to check for drift. The time between the first and last measurement in the graph was nearly 2.5 years, so the deposition rate appears to be quite stable. The deposition rate also does not seem to depend on the substrate temperature. Unheated depositions are plotted as filled circles, while depositions at 600°C are the open circles. The two sets of data appear to be collinear.

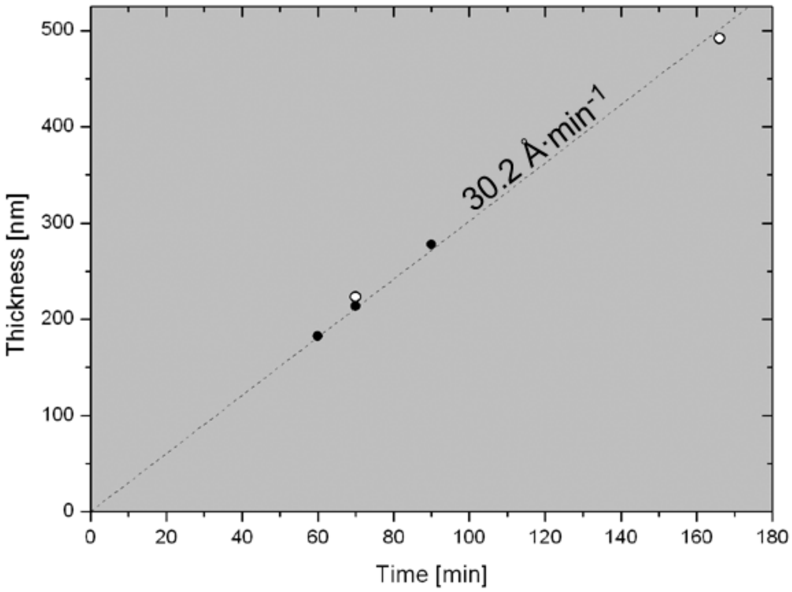

Figure 34. Thickness of YSZ9 films measured after various deposition times. ● = unheated deposition and ○ = 600°C deposition. Dashed line is a linear fit forced to cross the origin.

The deposition rates were measured always very close to the center of the substrate. For the 100 mm diameter substrates, radially uniform interference fringes were visible away from the center of the wafer, indicating thickness non-uniformity. This was expected, since the targets were only 50.8 mm in diameter. The thickness non-uniformity was not especially important to this study, since all of the characterization was done on the central ~60 mm diameter region. In this region, the thickness was measured to be uniform, within experimental error of the value at the center[103].

The temperature during nominally unheated depositions was characterized by a collaborator, Dave Quinn[103]. The substrate temperature over the course of the deposition is plotted in Figure 35. It was found that after igniting the plasma, but before even opening the shutter to begin deposition, the substrate quickly rose to around 115°C. After opening the shutter, the substrate temperature rose to around 185°C, and was stable at that value during the entire deposition. This value is consistent with what others have found during YSZ sputter deposition[170]. The minimum deposition temperatures must be considered to be 185°C.

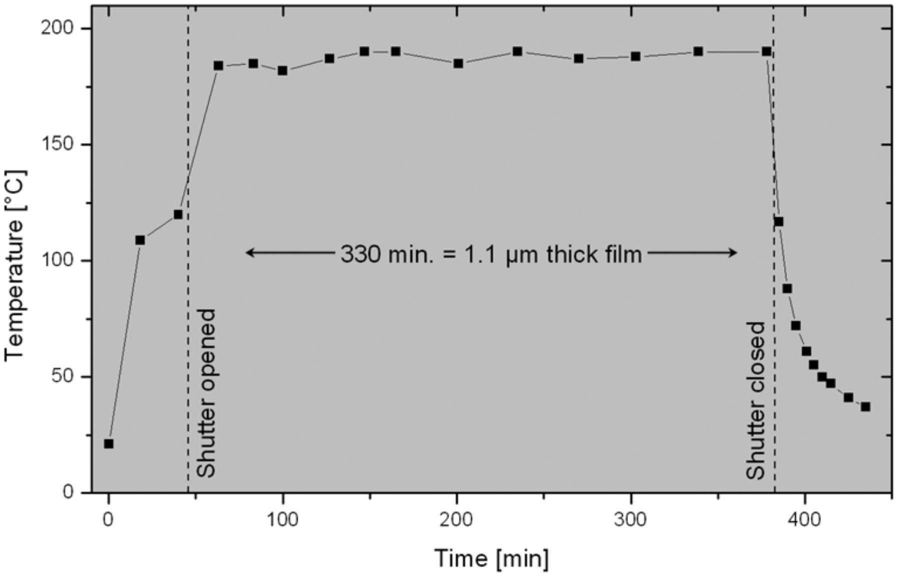

Figure 35. The temperature during deposition on an unheated substrate. Data courtesy Dave Quinn, first published in reference 103.

3.2 Yttria Stabilized Zirconia Physical Characterization

Atomic force microscope images for various films are presented in Figure 36(a)-(g). The lateral dimensions all span 1μm. An image of the as received, polished surface of a YSZ single crystal substrate is presented in Figure 36(h). The lateral dimension of this image spans 10 μm. The vertical dimension for all of the images is indicated by the color: black for the baseline and progressively whiter for increasing height. The range of the vertical dimension is different in each image, in order to enhance contrast. The range is indicated as "Z-scale" at the bottom of each image. All of the scans have been normalized using a plane fit routine. A 3rd order, X-Y plane fit was used, meaning a surface with cubic curvature in both lateral dimensions was subtracted from the data.

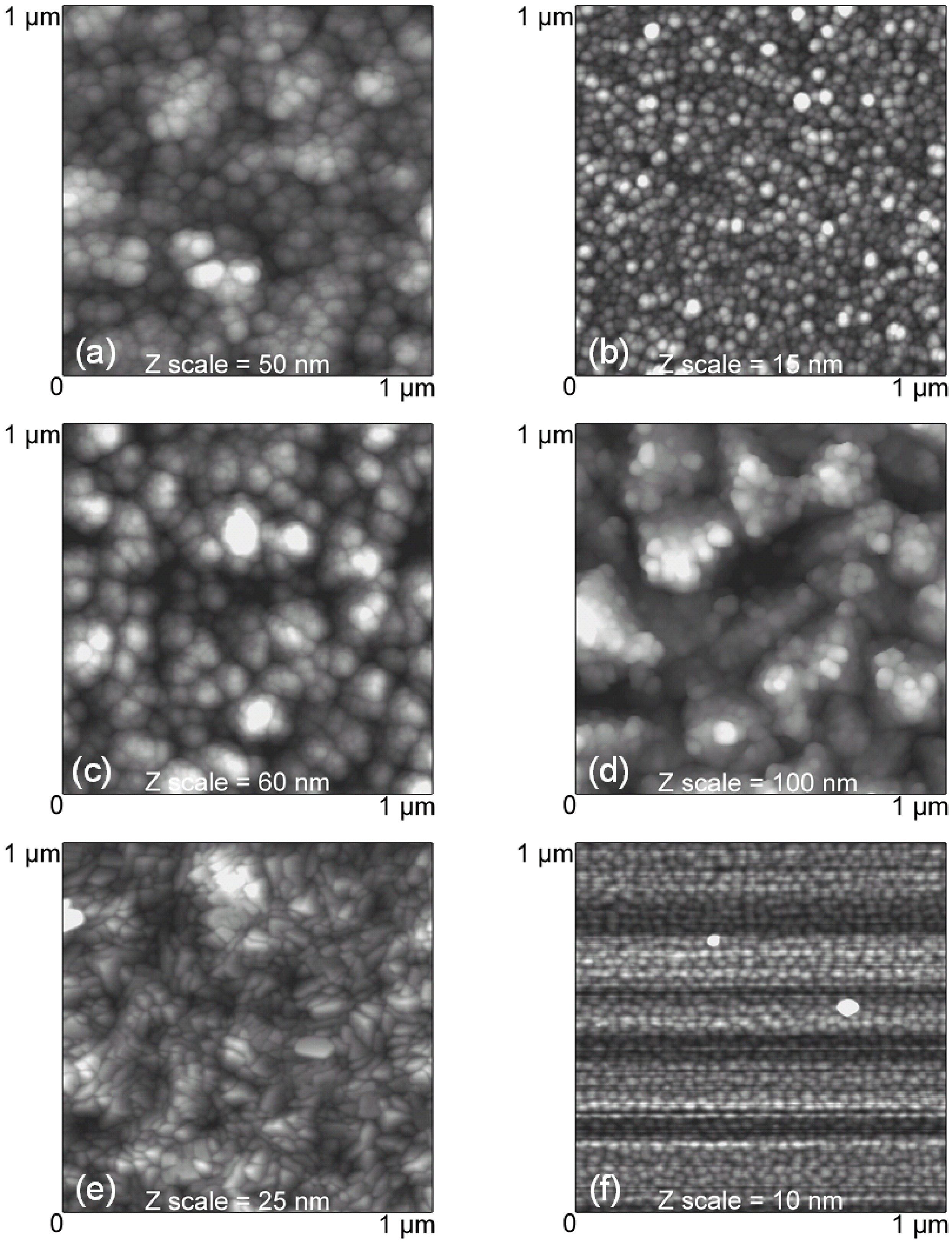
1 µm
(a)
Z scale = 50 nm
0
1 µm
1 µm
(b)
Z scale = 15 nm
0
1 µm
1 µm
(c)
Z scale = 60 nm
0
1 µm
1 µm
(d)
Z scale = 100 nm
0
1 µm
1 µm
(e)
Z scale = 25 nm
0
1 µm
1 µm
(f)
Z scale = 10 nm
0
1 µm

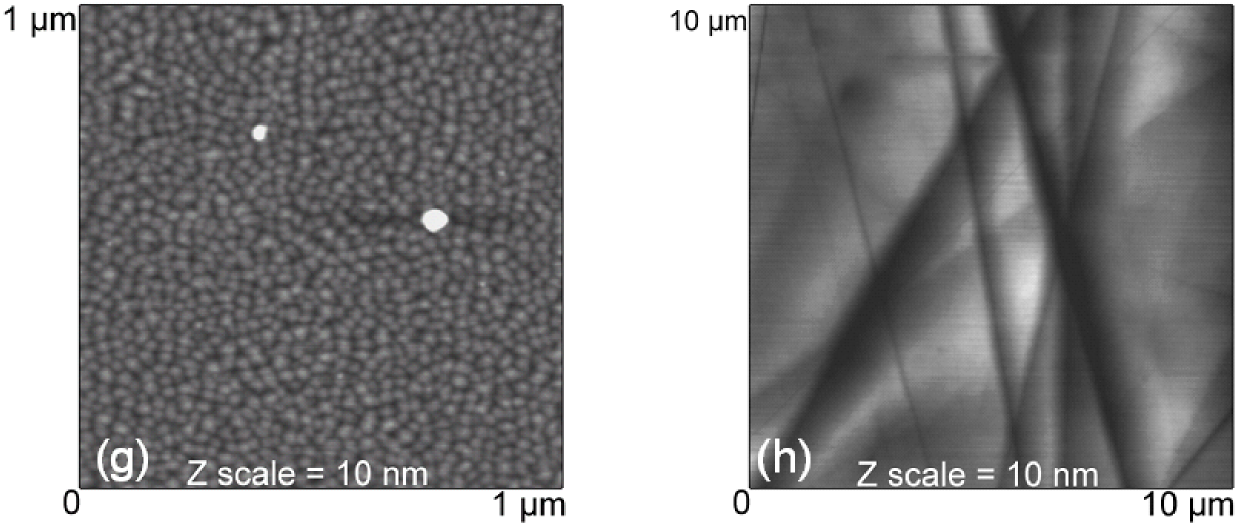

Figure 36. Atomic force micrographs of YSZ samples. The films are: (a) YSZ9 film, deposited on an unheated SiO_2 substrate; (b) YSZ9 film, deposited on an unheated single crystal YSZ substrate; (c) YSZ16 film, deposited on an unheated SiO_2 substrate; (d) YSZ9 film, deposited on a 300°C SiO_2 substrate; (e) YSZ9 film, deposited on a 600°C SiO_2 substrate; (f) YSZ9 film, deposited on a 600°C single crystal YSZ substrate; and (g) same as image f, but image flattened by software (see text for details). Plot (h) is the as-received, polished surface of a YSZ single crystal.

The YSZ9 film deposited at 600°C onto a YSZ single crystal substrate, depicted in Figure 36(f), is extremely flat (Z scale = 10 nm). Such a narrow range of values exposed the noise in the AFM signal due to mechanical vibration of the instrument and other irregularities. In order to correct for this a 3rd order "flatten" routine was performed with the software. This routine is more aggressive in the height normalization, subtracting cubic fits to individual rows and columns of data. It therefore removes both noise and the true, physical meaning of the height scale. The resultant image after flattening is provided in Figure 36(g). The single crystal sample of Figure 36(h) has been similarly flattened.

Other than the single crystal, the AFM images appear to show individual grains of YSZ formed during deposition. Grains appear to have a more monodisperse grain size when deposited on single crystal YSZ substrates compared to silica. The film deposited at 600°C onto a silica substrate (Figure 36e) has angular grains that indicate well-formed crystal planes at the surface. The film deposited at 600°C onto a single crystal YSZ substrate (Figure 36f) shows features that may not actually represent grains. The roughness of this film is on the order of only two unit cells and preliminary x-ray diffraction results from the sample indicated a high degree of epitaxy. These features may thus represent adatoms or other topographic features not related to grains and grain boundaries. The grains are very likely to be columnar, since they are deposited so far below the melting temperature[171]. The grain boundaries that are found on the surface and thus can participate at the triple phase boundary are important for this study. For this reason, the grain size in the vertical dimension was not explored.

The single crystal sample shows linear features that are depressed 5-10 nm below the surface. These are most likely scratches from the polishing process.

The tapecast YSZ was best imaged by SEM, since AFM scans could only contain a region too small to be meaningful for this sample. A scanning electron micrograph of a tapecast specimen is given in Figure 37. The grain boundaries are clearly visible.

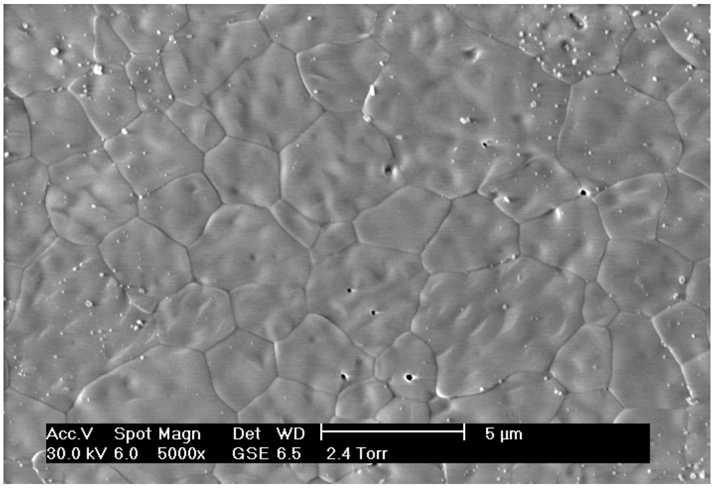

Figure 37. Scanning electron micrograph of tapecast YSZ.

From the micrographs, the grain size and roughness values were determined. All of these values are compiled in Table 4. Grain size determination from the AFM images took advantage of Tapping Mode phase images, not shown, which displayed increased grain boundary contrast. The grain size of the tapecast YSZ was determined from the unmodified SEM image; roughness could not be determined from this image. The linear intercept method was used to determine the grain size for all of the samples, using the average of 10 intercept lines for each. This method may have overestimated the grain sizes of the film samples, since extremely small grains (less than about 15 nm) can be difficult to visualize by AFM. The grain size, as expected, increased with increased deposition temperature. Roughness values were determined after only a 1^{st} order plane fitting, except for the highly smooth images of Figure 36(g) and (h). A 1^{st} order flatten routine was performed on these images, which were otherwise too noisy to obtain reasonable data. Unfortunately, this procedure in some ways makes comparison with these roughness values non-quantitative. The two bright white spots on Figure 36(g) are probably dust or another non-representative surface flaw. These features were excluded from the roughness determination. The only discernible trend to the roughness data is that films deposited on YSZ single crystal substrates are smoother than those deposited on silica substrates. There does not seem to be any trend with deposition temperature.

Table 4. The grain size and roughness values for YSZ films and bulk samples, as determined by AFM and SEM. Units are nm, except where indicated.

Figure	Target Composition	Deposition temperature	Substrate	Grain Size [nm]	RMS Roughness [nm]
36a	$Y_{0.09}Zr_{0.91}$	Unheated	SiO_2	28.9	8.86
36b	$Y_{0.09}Zr_{0.91}$	Unheated	YSZ single crystal	24.8	2.99
36c	$Y_{0.16}Zr_{0.84}$	Unheated	SiO_2	26.0	15.23
36d	$Y_{0.09}Zr_{0.91}$	300°C	SiO_2	32.5	23.85
36e	$Y_{0.09}Zr_{0.91}$	600°C	SiO_2	35.2	11.05
36f,g	$Y_{0.09}Zr_{0.91}$	600°C	YSZ single crystal	28.6[a]	1.02
36h	--	--	YSZ single crystal	--	1.95
45	--	--	HF-etched YSZ single crystal[b]	--	25.42
37	--	--	Tapecast YSZ	2.33 µm	--

[a] May not represent a true grain size. See text for details.
[b] Discussed later in the text.

To determine the phase, x-ray diffraction patterns were collected for the YSZ films. Patterns for YSZ9 films deposited on amorphous silica substrates at various temperatures are shown in Figure 38. Except for the broad substrate peak, all of the peaks could be matched with a cubic phase YSZ peak from PDF card #30-1468. Though peaks are found at all deposition temperatures, indicating crystallization occurred, the possibility of some amount of amorphous material in the films cannot be eliminated.

Comparing the patterns in Figure 38, the peaks become sharper as deposition temperature is increased. This indicates improved crystallization and larger grain sizes. The peak heights for the films deposited without substrate heating are at about the ratio expected from the PDF card. This is indicative of random grain orientation. On the other hand, the films deposited at 600°C have highly exaggerated (200) and (400) peaks. These denote tendency towards growth in the [100] direction at higher temperatures. Very similar results are obtained from the films with higher dopant composition. The higher doping content favors the presence of cubic phase instead of tetragonal phase YSZ.

No monoclinic zirconia is believed to be present in the films since no monoclinic peaks (PDF card #37-1484) could be found. On the other hand, the presence of tetragonal phase zirconia (PDF card #48-0224) can not be eliminated. There is little difference in diffraction pattern between the cubic and tetragonal phases—some of the cubic peaks are split into two closely spaced, smaller peaks for the tetragonal phase. This peak splitting may be concealed because, due to small grain sizes, the peaks in the film diffraction patterns are quite broad. Nevertheless, the peak widths in each pattern were compared and the peaks that would be split if the films were tetragonal phase were no more broad than those peaks that would be single peaks. This is an indicator that the films are predominantly cubic phase. There are a few small, additional peaks for the tetragonal phase that are not found for the cubic phase. One is indicated in Figure 38 by a 't'. There does appear to be a very small peak at this location for the YSZ9 films, particularly the films deposited at 300°C and 600°C. This conveys the presence of tetragonal phase, however the peak is hardly visible, and it is difficult to make a positive assessment based on it.

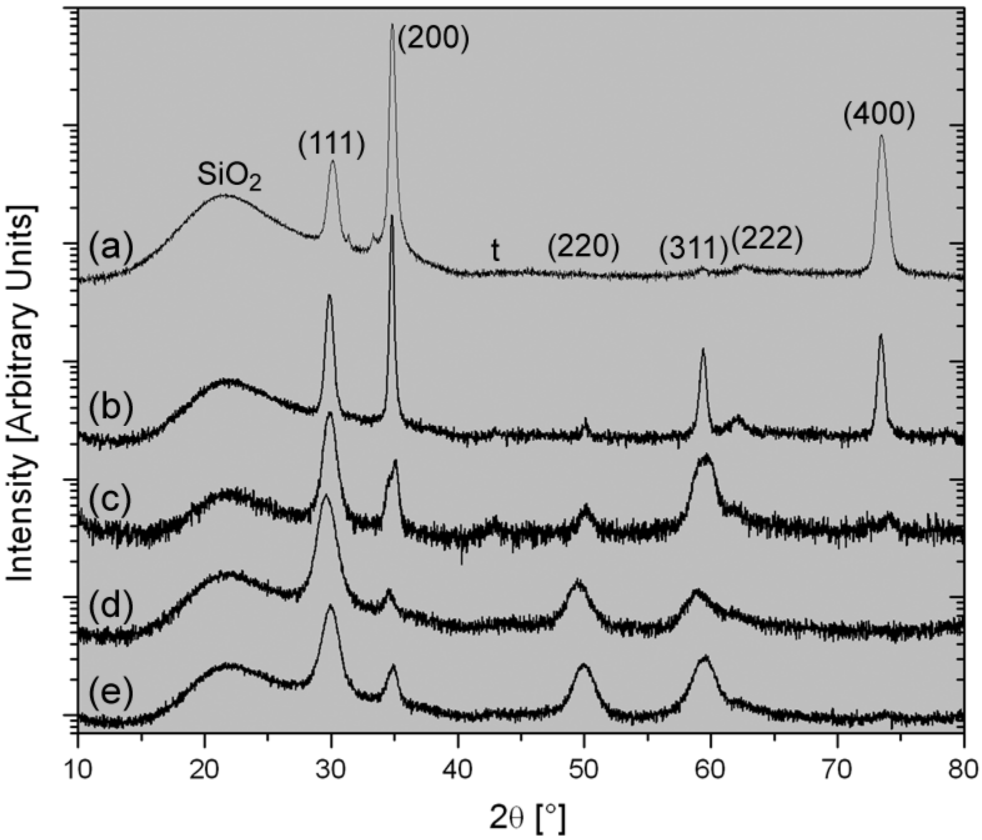

Figure 38. X-ray diffraction patterns from YSZ films deposited on amorphous silica substrates: (a) YSZ16 film at 600°C, (b) YSZ9 film at 600°C, (c) YSZ9 film at 300°C, (d) YSZ16 film deposited without substrate heating, and (e) YSZ9 film deposited without substrate heating. Terms in parenthesis are the Miller indices of the diffraction planes of cubic YSZ. The 't' indicates the location of the (102) peak of tetragonal YSZ. Note that intensity is in logarithmic scale.

X-ray diffraction patterns were collected for a YSZ9 film deposited without substrate heating onto a silica substrate both before and after a 1 hr anneal at 500°C in an alumina tube furnace. This was done to see if grain growth or phase changes occur when these films first encounter high temperatures. In Figure 39, the two patterns are shown. There is not much difference between the two patterns, though the peaks do appear to become a little sharper. This suggests that either a small amount of grain growth is occurring or non-uniform stresses are being relieved. One new peak at about 45° appears after the anneal. There is no cubic or tetragonal YSZ peak at this location and monoclinic peaks near this location are very small. The peak location also does not appear to be related to Y, Zr, or Si metal phases. This peak may be due to nucleation of crystals within the amorphous substrate or the pickup of contaminants from the furnace. To the naked eye, the sample did not change in appearance. Many common metals with the FCC crystal structure, such as nickel and cobalt, have major peaks in this area and are known to have been used previously in the annealing furnace.

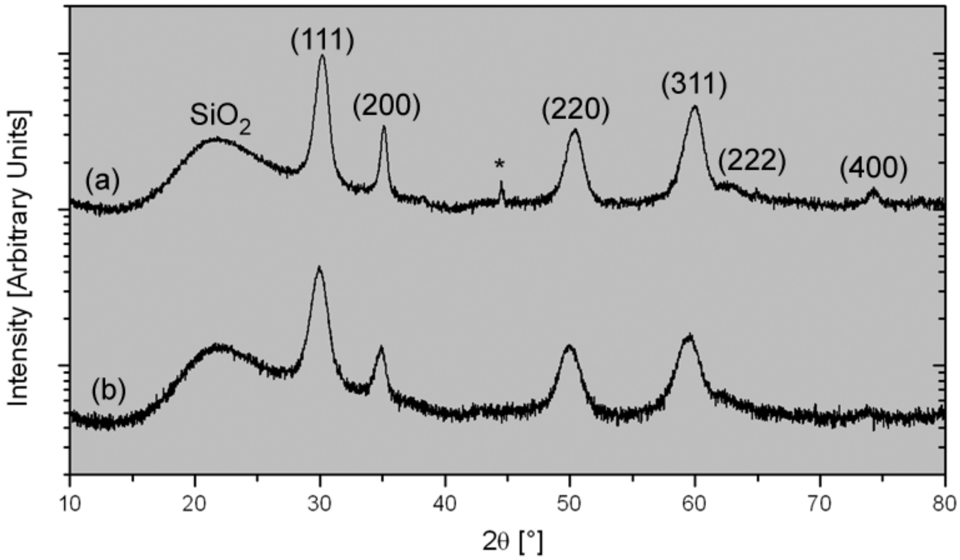

Figure 39. X-ray diffraction pattern from a YSZ9 film deposited without heating on an amorphous silica substrate (a) after a 1 hr anneal at 500°C and (b) as deposited. Terms in parenthesis refer to the Miller indices of the diffraction planes of cubic YSZ. The asterisk indicates an unidentified phase. Note that intensity is in logarithmic scale.

A similar measurement was done for a YSZ9 film deposited at 600°C onto an amorphous silica substrate, both before and after 1 hr at 500°C. These patterns are presented in Figure 40. There is very little difference between the two spectra, indicating the film is stable in phase and grain size. The exception is the appearance of a small, sharp peak at about 45°. As in the previous figure, this may be due to nucleation of crystallites in the substrate or pickup of contaminants from the furnace.

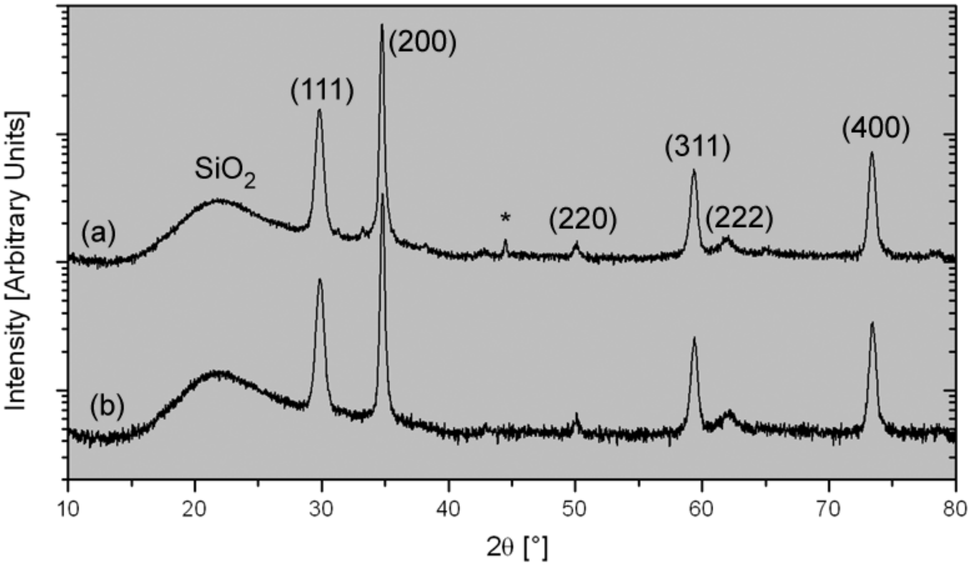

Figure 40. X-ray diffraction pattern from a YSZ9 film deposited at 600°C on an amorphous silica substrate (a) after a 1 hr anneal at 500°C and (b) as deposited. Terms in parenthesis refer to the Miller indices of the diffraction planes of cubic YSZ. The asterisk indicates an unidentified phase. Note that intensity is in logarithmic scale.

The Y/Zr ratios on the sample surfaces were determined by x-ray photoelectron spectroscopy (XPS). This measurement was especially important for the films in order to determine how well their composition matched the targets. Due to the nature of XPS, the results collected in Table 5, must be considered somewhat approximate. The Y/Zr ratio is presented along with the more common reference of the dopant percent on an oxide basis. The conversion between the two is

$$\%\text{ by oxide} = \frac{1}{1+\dfrac{2}{(\text{Y/Zr ratio})}} \tag{55}$$

Table 5. The Y/Zr ratio on the surface of YSZ films and bulk samples, as determined by XPS.

Target Composition	Target Y/Zr ratio	Deposition temperature	Substrate	Measured Y/Zr ratio	Dopant level as % by oxide
$Y_{0.09}Zr_{0.91}$	0.0989	Unheated	SiO_2	0.0968	4.62
$Y_{0.16}Zr_{0.84}$	0.190	Unheated	SiO_2	0.189	8.63
$Y_{0.09}Zr_{0.91}$	0.0989	300°C	SiO_2	0.0875	4.19
$Y_{0.09}Zr_{0.91}$	0.0989	600°C	SiO_2	0.0864	4.14
--	--	--	YSZ single crystal	0.230	10.3
--	--	--	Tapecast YSZ	0.314[a]	13.6[a]

[a] May be in error. See text for details.

It appears that the target composition is matched quite well by the film composition. There may be a slight decrease in the Y content at increased substrate temperature, but the measured difference is probably within experimental error. The single crystal dopant level is a little higher than the expected value of 8-9.5%. The Y concentration measured for the tapecast sample is surprisingly high. This result likely comes from two sources. First, this sample was sintered at high temperature, and so there is probably Y segregation to the surface, as described in section 1.3.3. Thus, the Y content measured at the surface by XPS is probably not characteristic of the bulk content. Second, there appears to be overlapping Y and Si peaks. The peak near 100 eV indicates Si contamination at the surface of the bulk YSZ. A Si peak overlaps the main Y peak at about 150 eV, and this is likely leading to an incorrectly large area measured for the Y peak.

Survey spectra for a series of samples were collected after the Pt electrodes were microfabricated on to their surface. This was done in order to capture the chemistry of surfaces in the same state in which they were electrically characterized. Survey spectra to look for unknown surface contaminants, are presented in Figure 41. The x-ray beam was roughly 500 µm in diameter, which was large enough to strike both the Pt electrode fingers and the YSZ surface between the fingers. The spectra therefore generally contain information about both the YSZ and Pt. The only exception is the spectra of the tapecast YSZ (Figure 41g), where the beam unfortunately did not hit any of the Pt. As is commonly done with XPS results, the energy values are displayed in order of decreasing electron binding energy, since this is increasing electron kinetic energy as measured in the instrument.

The survey spectra indicate the presence of a few contaminants. All of the spectra had peaks for carbon, however this is found for nearly any sample measured by XPS after being in open air and represents carbonaceous adsorbates. The single crystal YSZ and the YSZ9 film deposited at 600°C onto the single crystal YSZ both showed some amount of phosphorous. The source of this contaminant is believed to be the Alconox cleaning solution used as the final inorganic cleaning step by the crystal manufacturer[172]. This detergent is 7.3% phosphorous, by weight[173]. The YSZ9 film deposited at 600°C onto the single crystal YSZ indicated the presence of sodium. This is possibly also from the Alconox, though since no other sample had sodium peaks, is more likely to have come from accidental skin or other contact to this sample.

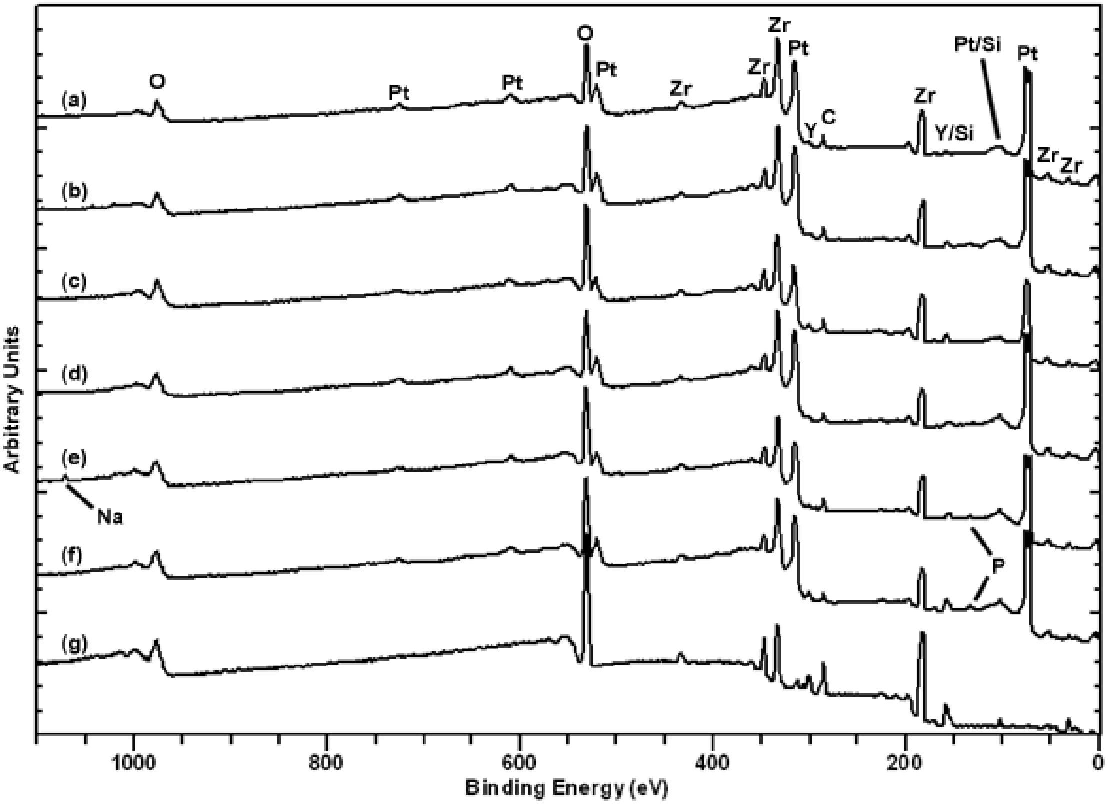

Figure 41. Survey x-ray photoelectron spectra for post-processed samples with the electrolyte consisting of: (a) YSZ9 film, deposited on an unheated SiO_2 substrate; (b) YSZ9 film, deposited on an unheated single crystal YSZ substrate; (c) YSZ16 film, deposited on an unheated SiO_2 substrate; (d) YSZ9 film, deposited on a 600°C SiO_2 substrate; (e) YSZ9 film, deposited on a 600°C single crystal YSZ substrate; (f) single crystal YSZ substrate; and (g) tapecast YSZ substrate. Peak positions for the elements found are as indicated.

A number of samples appeared to display contamination from Si. This was difficult to detect from the survey spectra, since Si peaks overlap with the expected Pt and Y peaks. In order to more carefully distinguish the Si peaks and to obtain information on the O bonding state, high resolution spectra were obtained. Angle resolved measurements were done to obtain depth information. These spectra, measured at three take-off angles, are presented for a number of samples in Figure 42. The samples are the same as those in Figure 41, and so represent the chemistry of the sample surfaces after platinum microelectrode processing. Two energy ranges are shown: 537-528 eV, a region containing the O1s peak, and 167-145 eV, a region containing the Y3d doublet peaks and the Si2s peak. The energy values for each spectrum were individually calibrated using a high resolution spectrum of the 281-292 eV energy region (not shown). This region contained a C1s peak that was set to 285.0 eV. Based on their unusual shape and small peak height, some spectra appear to have had error in collection; these are indicated by question marks.

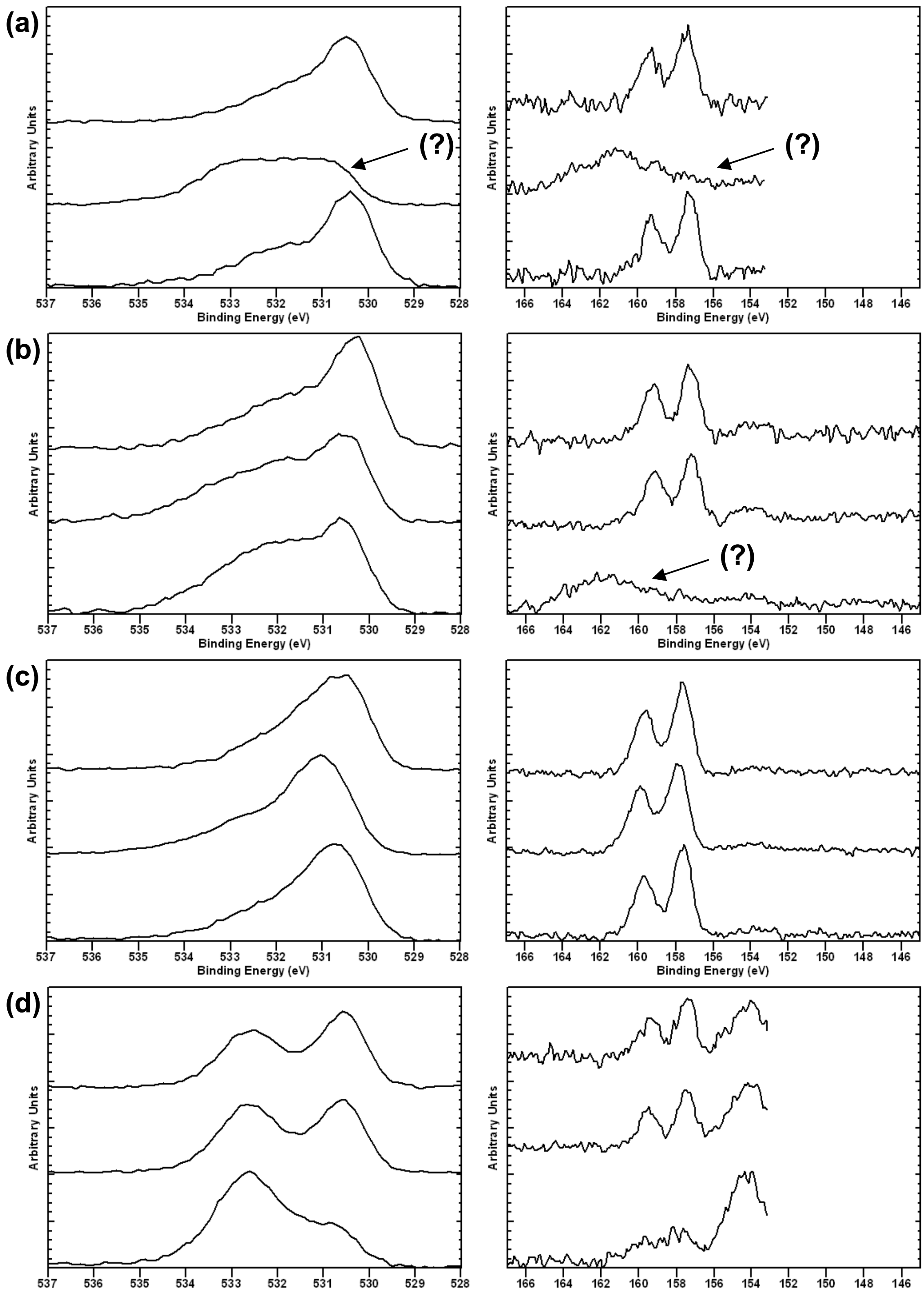
(a)
(b)
(c)
(d)
(?)
(?)
(?)
Arbitrary Units
Binding Energy (eV)
537
536
535
534
533
532
531
530
529
528
166
164
162
160
158
156
154
152
150
148
146

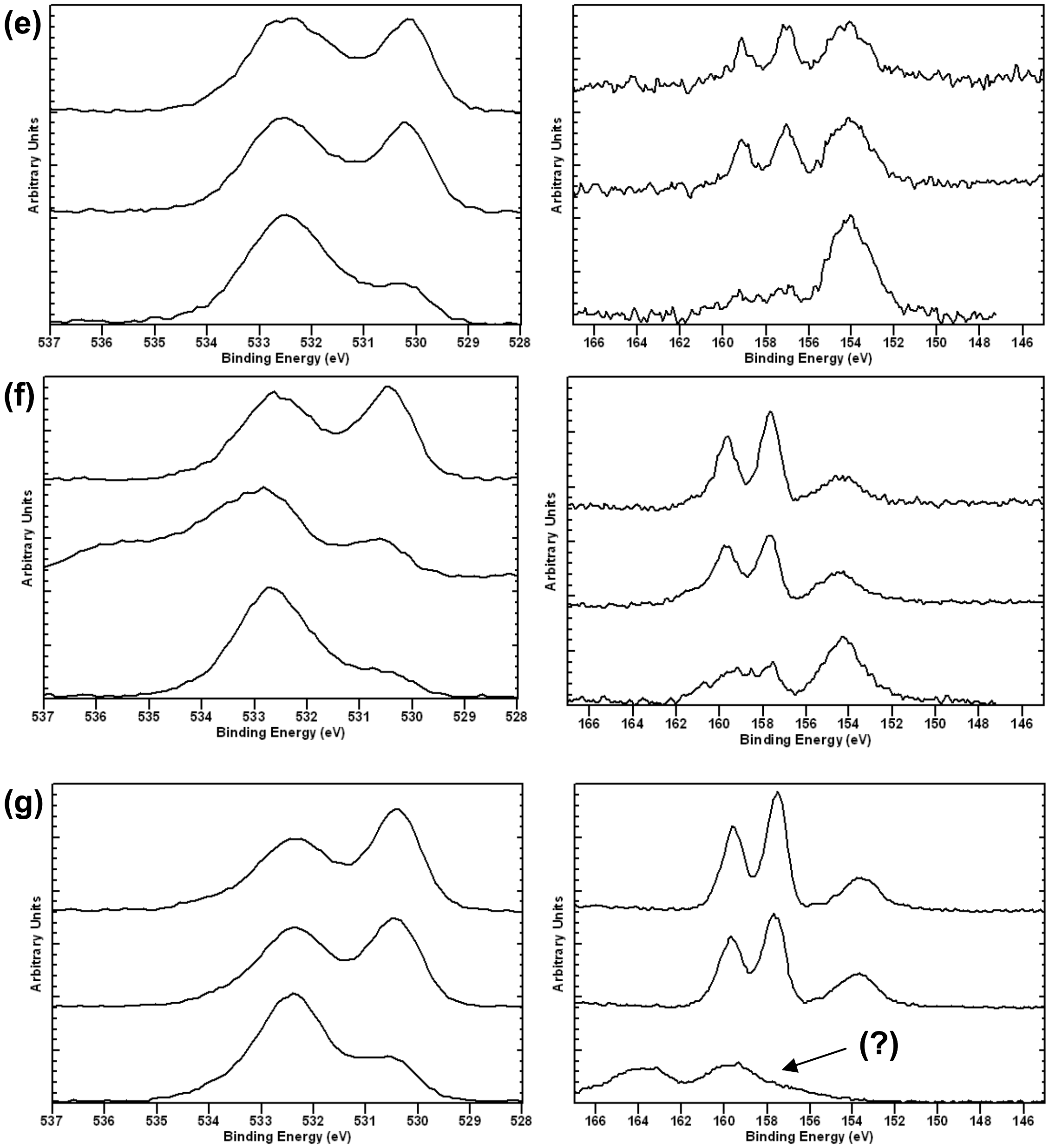

Figure 42. High resolution x-ray photoelectron spectra for post-processed samples with the electrolyte consisting of: (a) YSZ9 film, deposited on an unheated SiO_2 substrate; (b) YSZ9 film, deposited on an unheated single crystal YSZ substrate; (c) YSZ16 film, deposited on an unheated SiO_2 substrate; (d) YSZ9 film, deposited on a 600°C SiO_2 substrate; (e) YSZ9 film, deposited on a 600°C single crystal YSZ substrate; (f) single crystal YSZ substrate; and (g) tapecast YSZ substrate. Each graph includes spectra from 3 different take-off angles. The top spectrum was measured at 0° (least surface sensitive), the middle spectrum at 35°, and the bottom spectrum at 70° (most surface sensitive). The spectra in the left column show O1s electron energies while the spectra on the right show electron energies from Y3d at 157-160 eV and, if present, Si2s near 154 eV. Graphs that appear to have had error in collection are indicated with question marks.

Two findings are immediately apparent when comparing the spectra of Figure 42. First, the samples in spectra (d)-(g) have, in addition to the expected Y3d doublet peaks at about 157 and 159 eV, a Si2s peak near 154 eV. This peak increases in intensity as the take-off angle increases, revealing that the Si impurities are preferentially located on the outer one or two nanometers of the sample. At the same time that the Si peak is increasing, the Y peak is decreasing. The Si peak position is in the area expected for an oxygen-bonded Si. The samples in spectra (a)-(c) have small Si peaks that are difficult to distinguish from the background, even at the highest take-off angles.

The second finding concerns the oxygen peaks. There appears to be two main components of the peaks, a high binding energy (HBE) peak at about 532.5 eV and a low binding energy (LBE) peak at 530.5 eV. These binding energies were correlated in section 1.3.3 with O bonded to Si and Zr, respectively, and it appears here that the area of the HBE peak correlates well with the area of the Si peak. This correlation holds both between samples as well as during the angle-resolved measurements of a particular sample. The O bonding state on the surface appears to be with Zr on the surfaces of samples (a)-(c) and with Si on the surfaces of samples (d)-(g). Taken together, these two findings indicate that the surface of the samples in spectra (a)-(c) are fairly pure, while those in spectra (d)-(g) have a coating, perhaps as thin as 1 atom thick, of silica or a silicate. The "pure" samples were the films deposited at low temperatures, while the Si contaminated samples are the films deposited at high temperature as well as the polycrystalline and single crystal bulk samples.

To determine the source of the Si contamination, a few spectra were measured from single crystal YSZ samples subject to different processing techniques. Figure 43 shows the high resolution spectra for these samples. Figure 43(a) shows a YSZ single crystal, as received from the supplier and before any processing whatsoever. There is a very small amount of Si found at the highest take-off angle—none can be detected at 0° and 35°—and the O bonding state shows only a weak HBE peak. Figure 43(b) shows comparable results for a similar crystal after being annealed at 600°C for 2 hr. These results show that at the temperatures used to process and measure the samples, Si does not segregate to the surface of the YSZ single crystals. One suspected source of the Si was the HMDS (a silicon-based metalorganic) used in the microprocessing of the Pt electrodes as an adhesion promoter for the photoresist. A sample with Pt electrodes microfabricated on the surface of a YSZ single crystal was processed without using the HMDS. Other than skipping the HMDS spin coat, the microfabrication was identical. Figure 43(c) shows that after this alternate processing route, there is no Si found on the surface of this sample. Angle resolved measurements could not be performed on this sample and only a 0° take-off angle spectrum is shown.

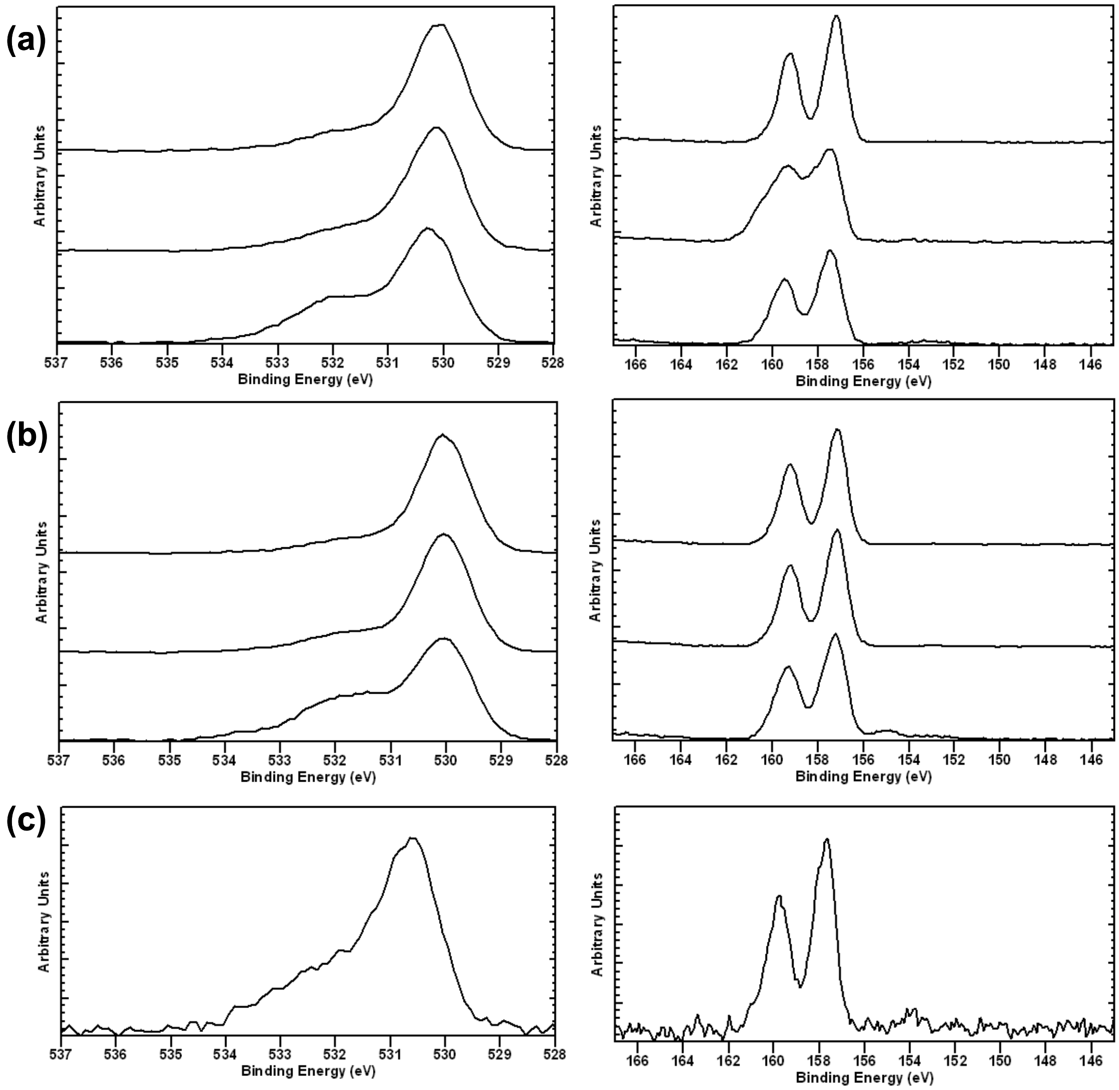

Figure 43. High resolution x-ray photoelectron spectra of (a) a single crystal YSZ substrate, as received from the supplier; (b) a single crystal YSZ substrate after annealing in a tube furnace at 600°C for 2 hr.; and (c) a single crystal YSZ substrate after microfabricating Pt electrodes on the surface without the use of HMDS adhesion promoter. Graphs (a) and (b) include spectra from 3 different take-off angles. The top spectrum was measured at 0° (least surface sensitive), the middle spectrum at 35°, and the bottom spectrum at 70° (most surface sensitive). Graph (c) only includes data from a take-off angle of 0°.

An attempt to remove the silicon contamination layer from a single crystal sample, after microfabrication of the Pt electrodes, was performed. The sample was placed in a Teflon beaker with concentrated hydrofluoric acid for about 5 minutes, then removed, rinsed with deionized water, and dried. The sample was electrically characterized, as will be described in section 3.4, and examined by XPS and SEM. Both survey and high resolution XPS spectra are presented in Figure 44. The spectra show that the Si layer was, to some degree, successfully etched away. There is only a small Si2s peak in the high resolution spectrum and the O1s peaks consist predominately of the LBE peak. The survey spectra also indicate that the Y/Zr ratio on the surface was also affected by the etching, increasing to approximately 1 (i.e., equal amounts of Y and Zr). Using HF presents the risk of fluorinating the surface, however no fluorine can be found in the survey spectrum. Since the XPS was performed after electrically characterizing the sample, the fluorine may have been removed at the elevated measurement temperatures.

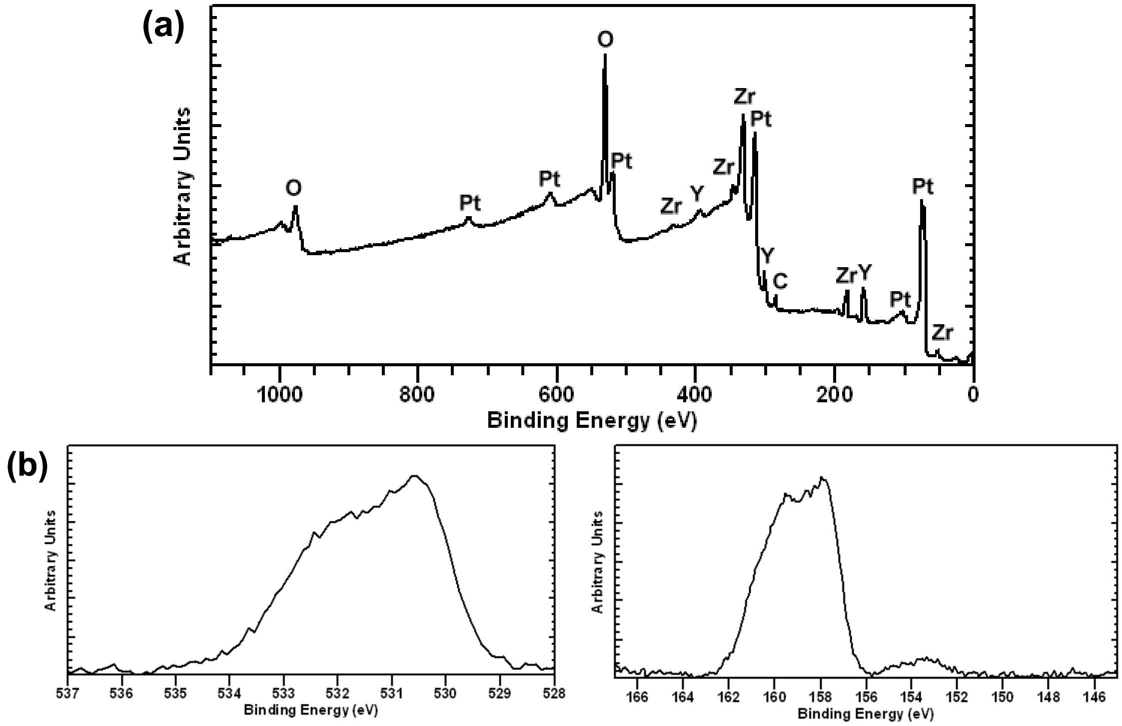

Figure 44. (a) Survey and (b) high resolution x-ray photoelectron spectra of a single crystal YSZ sample after microfabricating Pt electrodes on the surface as normal and then washing in HF. The high resolution spectrum on the left shows the O1s region while the spectrum on the right shows the Y3d doublet at 155-162 eV, with the two peaks overlapping, and a small Si2s peak just below 154 eV. Graphs only include data from a take-off angle of 0°.

The scanning electron micrograph of the etched sample is shown in Figure 45. The YSZ surface appears to have been roughened by the treatment. Features roughly 100 nm wide and in random shapes can be seen scattered across the surface. AFM showed these features to be raised from the surface. The roughness measured by AFM is included in Table 4. From the untreated single crystal surface, with a roughness of less than 2 nm, the etching increases the roughness more than tenfold to over 25 nm. The Pt electrode surfaces on the sample were examined by SEM and did not appear to have been affected by the HF.

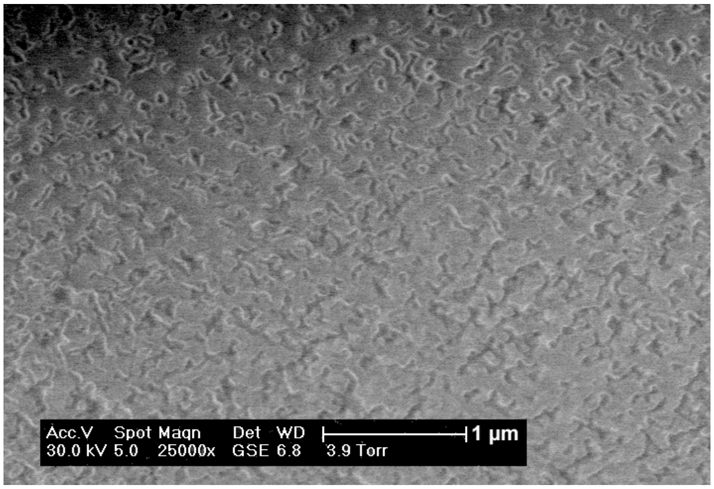

Figure 45. Scanning electron micrograph of a single crystal YSZ sample after microfabricating Pt electrodes on the surface as normal and then washing in HF. The surface is visibly roughened.

3.3 Platinum Microelectrode Physical Characterization

Due mainly to dust, the microfabrication processes employed in the study were not successful for very high resolution lithography. Patterns 13-16, which had features 15 μm and larger, were successfully created most of the time. The electrode patterns that had finer features were very often riddled with short circuits and were, unfortunately, unusable. An interdigitated electrode design is unfortunate in this regard, since just one flaw that connects two adjacent fingers creates a short circuit that makes the entire pattern unusable. Two typical flaws are shown in Figure 46(a) and (b). The first is a short circuit contact between two adjacent electrode fingers. The second is a non-catastrophic flaw where two adjacent electrode fingers are misshapen yet do not make contact.

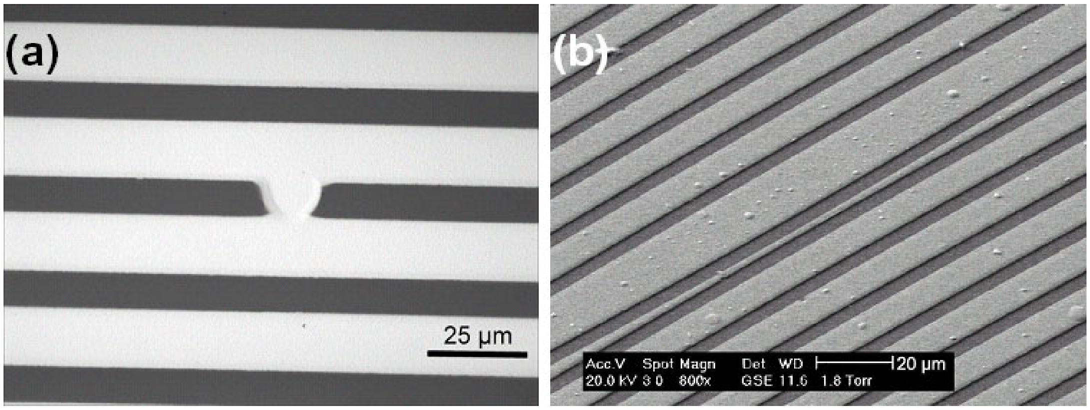

Figure 46. Occasional flaws in the electrodes produced by photolithography include (a) short circuits between electrodes, shown in an optical micrograph and (b) misshapen fingers, shown in a scanning electron micrograph. In both images, Pt electrodes appear brighter than the dark substrate upon which they are placed.

The thickness and lateral dimensions of the electrodes were confirmed by profilometry, as seen in Figure 47. This figure is the profilometer trace of an electrode that was designed to be 250 nm thick, with 15 µm wide electrode fingers and 10 µm spacing between the fingers. This pattern has been realized with high fidelity.

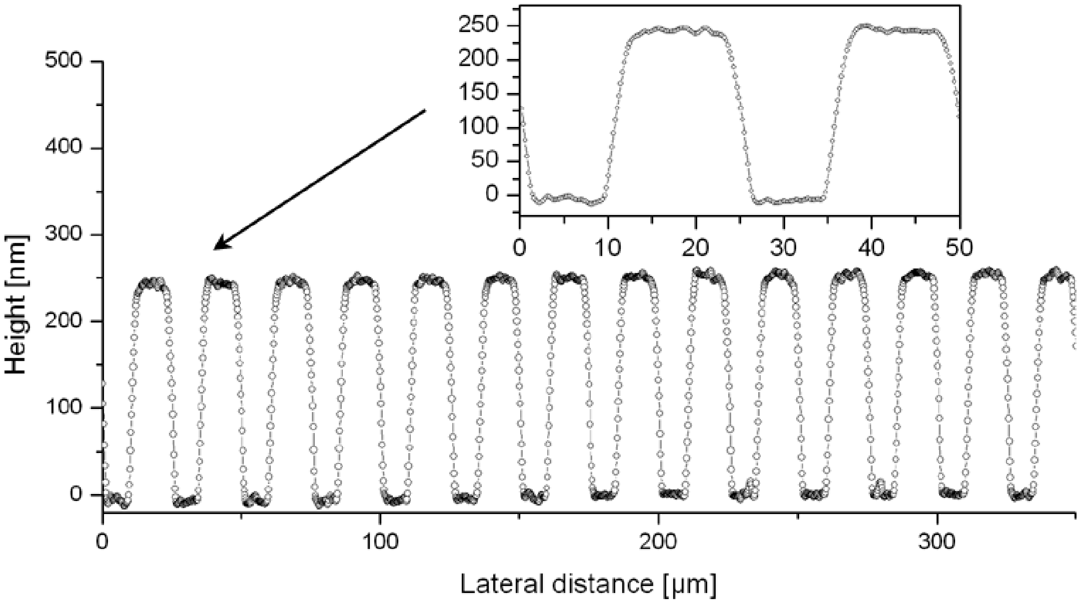

Figure 47. Profilometer trace of a 250 nm thick, interdigitated platinum electrode with 15 µm wide fingers, spaced 10 µm apart. Note that lateral units are µm while vertical units are nm.

Of high importance to this work is the lateral roughness in the electrode edge, since this defines the triple phase boundary length. In general, there was very little roughness seen at the millimeter-scale. The micron- to submicron-scale roughness was characterized by scanning electron microscopy. The edge of the electrode in Figure 48 was traced on a computer to determine the total edge length. This was compared against the direct path length between the two endpoints to determine the overall increase in TPB length from the macroscopic or expected length. The electrode length is found to be about 11% larger than the expected value due to the lateral roughness. This value was assumed to hold for all of the samples because it was assumed that the edge roughness at this size scale was derived from the microfabrication processes, which were the same for all samples. Specifically, it was assumed to be uninfluenced by the out-of-plane roughness of the underlying substrate, which was orders of magnitude smaller by comparison.

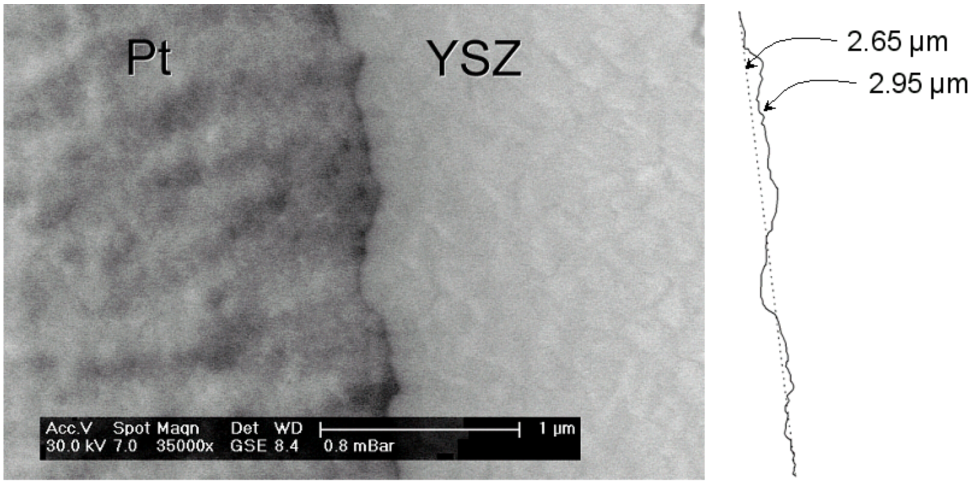

Figure 48. Scanning electron micrograph of the edge of a microfabricated Pt electrode. Also shown is a trace of the electrode (solid line), which is 11% larger than the direct path (dotted line).

The nm-scale electrode roughness, in both the lateral and out-of-plane dimensions, was not considered. As discussed in section 1.2.3, the TPB has a non-zero width and depth. This blurs the delineation of the TPB away from the electrode edge over the distance of at least a few unit cells. Differences between samples in the nm-scale roughness are therefore unlikely to have any effect. In addition, surface tension effects will probably eliminate such small roughness in the Pt edge.

The electrode morphology was not entirely stable after long term, high temperature anneals. This is a serious problem, found also in previous studies[117], since it can lead to unaccounted for increases in the triple phase boundary length. A scanning electron micrograph is shown in Figure 49, showing the beginnings of agglomeration of the electrode: roughening of the edges and pore creation in the interior. Pores are visible as darkened spots within the electrode. Fortunately for this study, agglomeration was found to have occurred after annealing at 600°C, and did not occur during the temperatures and hold times normally used for electrical testing.

It is not believed that pores in the Pt layer could have contributed to any changes in the electrical characterization. Pores could not be found on electrodes on the surface of multiple samples after the standard electrical characterization process. These include samples with both very high and very low electrode performance.

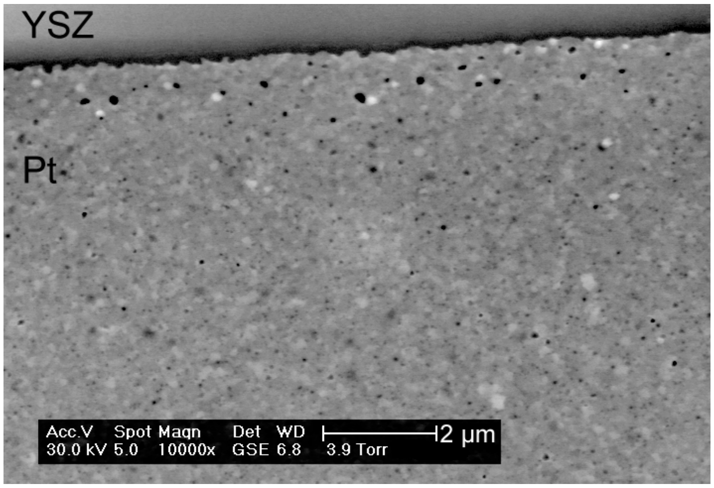

Figure 49. Scanning electron micrograph of the edge of a microfabricated Pt electrode after annealing at 600°C for 100 hr, showing pore formation and edge roughening.

Samples with patterned Pt electrodes were characterized by XRD to determine whether the sputtered Pt was affected by the structure underneath. These patterns are plotted in Figure 50. The Pt electrode deposited on a single crystal YSZ substrate only showed (111) plane diffraction, and so grew with preferred orientation. The electrodes deposited on YSZ films grown at 600°C or without substrate heating showed preference for (111) orientation, but also had a significant (200) plane reflections. An identical x-ray diffraction pattern to Figure 50(a) was found after annealing for 100 hr. at 600°C, indicating that the Pt electrodes were stable with regard to orientation and phase.

High resolution XPS of the Pt peaks was done to determine if the oxidation state depended on the structure underneath. The main peak is the Pt4f doublet, shown in Figure 51 for electrodes deposited on YSZ9 films deposited on silica substrates at 600°C and unheated. Only one set of peaks is found for each sample, however the peak widths seem slightly different. Increased peak width probably indicates the formation of Pt-O bonds. The lower energy peak of pure Pt is expected to be at 71-72 eV, with peaks for O-bonded Pt shifted to 74-75 eV[174]. Though the difference in the Pt peaks between the two samples is small, the Pt deposited on the unheated substrate appears to be slightly more oxidized. Another finding is that the Pt peaks for both samples appear to become slightly broader at increased take-off angle, though the difference is again very slight. This result means that the Pt-O bonds are found preferentially at the surface.

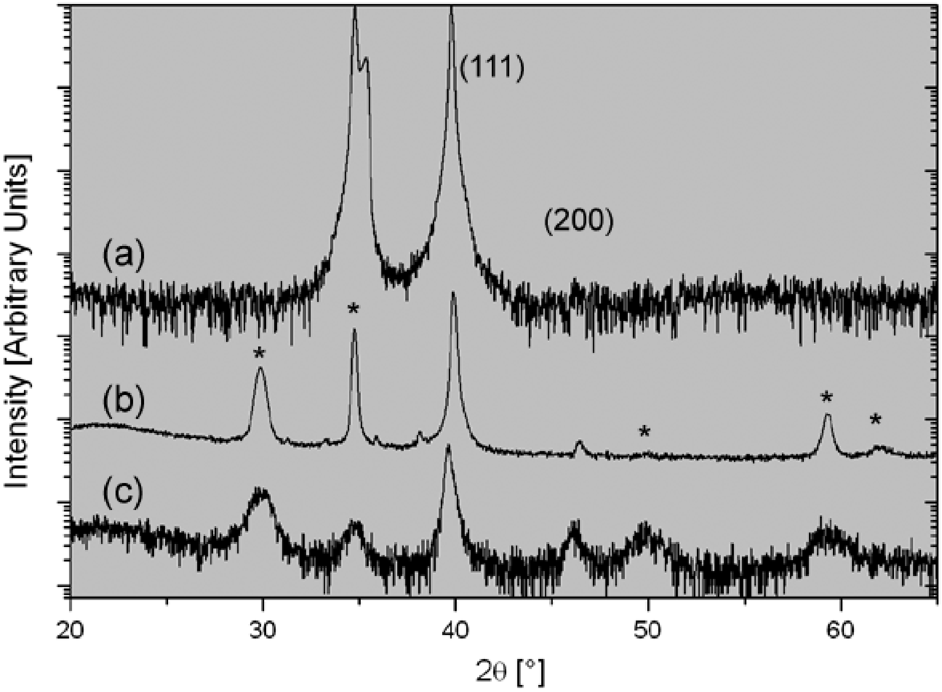

Figure 50. X-ray diffraction pattern for Pt electrodes microfabricated on the surface of (a) single crystal YSZ with (100) orientation, (b) YSZ9 film deposited on an unheated silica substrate, and (c) YSZ9 film deposited on a 600°C silica substrate. Terms in parenthesis refer to the Miller indices of the diffraction planes of Pt. Locations indicated with asterisks are from the YSZ. Note that intensity is in logarithmic scale.

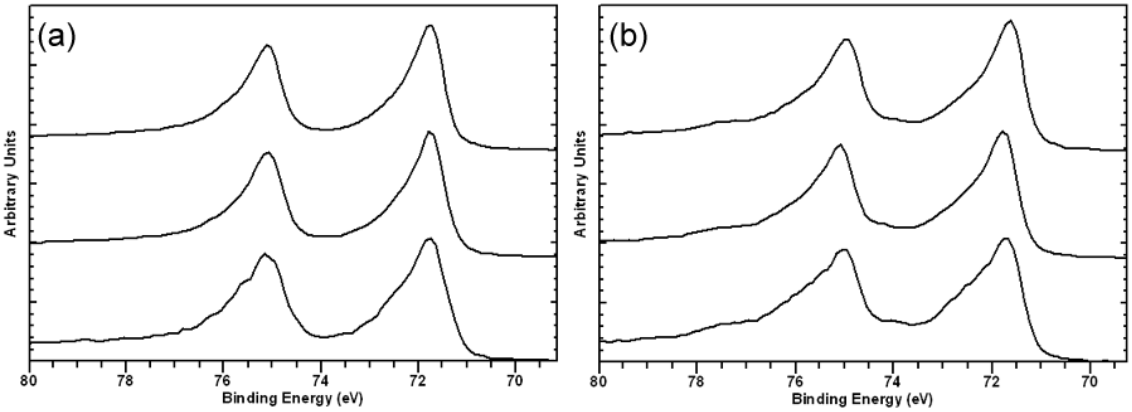

Figure 51. High resolution x-ray photoelectron spectra for Pt electrodes microfabricated on the surface of (a) YSZ9 film deposited on a 600°C silica substrate and (b) YSZ9 film deposited on an unheated silica substrate. Each graph includes spectra from 3 different take-off angles. The top spectrum was measured at 0° (least surface sensitive), the middle spectrum at 35°, and the bottom spectrum at 70° (most surface sensitive).

3.4 Electrical Characterization of YSZ using Platinum Microelectrodes

Impedance spectra collected from the calibration runs measured the series inductance of the system to be 3.0 µH, the series resistance of the cabling and leads to be 0.50 Ω, and the series resistance of the Pt electrodes to be between 40 – 50 Ω. A series inductor was included in the equivalent circuit (Figure 33) and used as a variable for every data fit, though the value changed little. Over the course of over 650 impedance spectra, measuring a wide range of samples, temperatures, and oxygen partial pressures, the minimum inductance measured was 1.5 µH and the maximum was 21 µH. Changes in the cabling, leads, and electrode geometry probably led to this small variance. The resistances of the leads and the Pt electrodes were insignificant compared to the other resistances measured and could not be successfully determined from the impedance spectra of samples.

Electrodes placed directly on a fused silica substrate were difficult to measure because the resistances were very high. At 405°C the sample had a resistance of $4.45 \cdot 10^7$ Ω, while at 499°C the resistance was $7.01 \cdot 10^6$ Ω. As will be seen, these were much higher resistances than measured for YSZ films deposited on the silica substrates. Conductance through the silica substrates was thus considered insignificant.

A typical impedance spectrum for a thin film YSZ sample deposited on a silica substrate is given in Figure 52. Both the raw data and the fit from the equivalent circuit are shown, and the match seems acceptable. There is one dominant arc, labeled IV, at low frequencies and three impedance arcs, labeled I, II, and III, at the high frequency portion of the spectrum. The four arcs all overlap to some extent, and the third arc is quite depressed below the real axis. All four of these arcs had a resistance that rapidly decreased as the temperature increased, meaning the peak frequencies increased with temperature. Usually, not all four arcs were visible in the same spectrum because the high frequency arcs had peak frequencies above the measurable range at high temperatures and the low frequency arc had a peak frequency below the measured range at low temperatures. In fact, the impedance plot in Figure 52 does not give much confidence in the fit to arc IV since only the first third or so of the semicircle is visible. Ordinarily a more complete arc was required to achieve acceptable confidence in the equivalent circuit fit. The quantitatively significant arc IV data collected have been derived from more complete arcs. The impedance spectra of tapecast, bulk YSZ samples looked qualitatively very similar to those from the films deposited on silica: 4 impedance arcs, with the three at high frequencies and the fourth extending to very low frequencies. The single crystal YSZ samples and those that used single crystal YSZ as a substrate for a YSZ film had similar impedance diagrams except that arc II was not present.

The equivalent circuit element values were compiled so that the resistance and capacitance values between different samples and temperatures could be compared. Arcs I-IV were assigned to the different impedance spectra based on similar capacitances, temperature dependences of resistance, and dependences on sample geometry. These behaviors for each of the arcs will be detailed below. When the constant phase elements approximate a capacitor (i.e., $\alpha \geq 0.8$), the term capacitance will be used. The units, however, will be correctly stated as $F \cdot s^{\alpha-1}$.

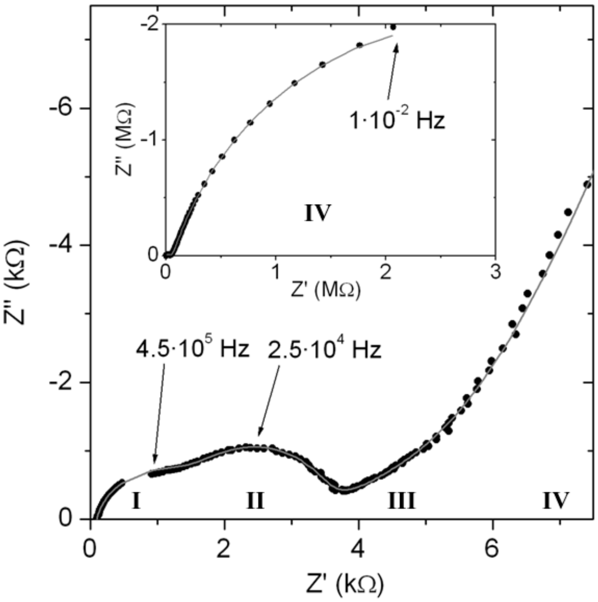

Figure 52. A typical impedance spectrum for a thin film YSZ deposited on a silica substrate. Points are raw data, line is the fit from the equivalent circuit. The main portion of the graph displays the high frequency portion of the spectrum while the inset shows the complete spectrum (note the change in units). The frequency at selected point is given.

3.4.1 Electrolyte Conductivity

Arc I was not depressed much below the real axis, so the CPE element very nearly matched ideal capacitor behavior. The measured capacitances were quite low, typically between $10^{-11} – 10^{-10}$ $F \cdot s^{\alpha-1}$. This is probably nearing the smallest capacitance that can be measured in the system, due to stray capacitances and instrumental limitations. The resistances scaled roughly linearly with the electrolyte geometry, as shown in Figure 53 for a few of the film on silica samples.

An alternate way of demonstrating the dependence of the arc I resistance upon geometry is shown in Figure 54. The measured resistance values for YSZ9 films deposited at 600°C on silica substrates using a few different electrode geometries are displayed in Figure 54(a). Using the numerical solution routine detailed in Appendix A, the arc I resistance values are converted into an electrolyte conductivity. For the film on silica samples, most of the voltage drop occurs between the electrodes. Thus, the conversion of resistance to conductivity is numerically very similar to the simple parallel plate model with the cross sectional area being the length of the electrode finger multiplied by the electrolyte thickness and the current path length being the electrode finger spacing. These values are displayed in Figure 54(b). Though the resistance at a constant temperature varies between samples by nearly 2 orders of magnitude, the conductivity values derived are consistent.

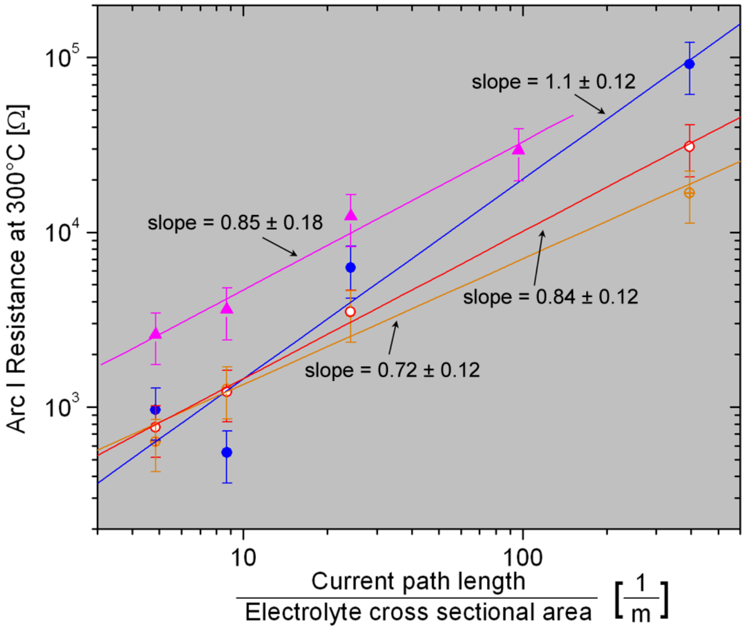

Figure 53. Arc I resistance at 300°C, plotted as a function of the conduction path length divided by the cross-sectional area of the electrolyte. ● = YSZ9 film deposited unheated; ⊕ = YSZ9 film deposited at 300°C; ○ = YSZ9 film deposited at 600°C; ▲ = YSZ16 film deposited unheated.

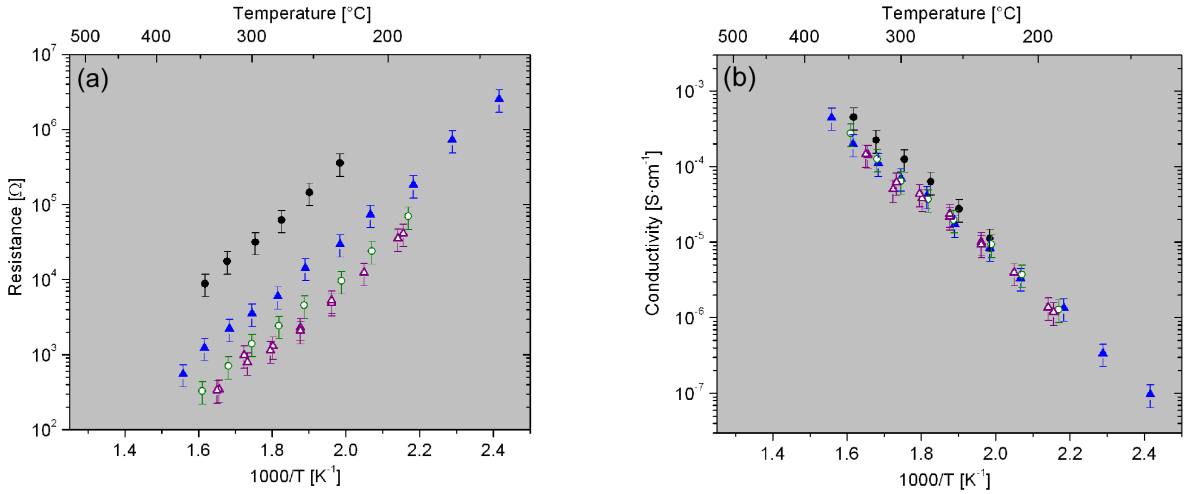

Figure 54. The arc I (a) resistance and (b) conductivity as a function of temperature for YSZ9 films deposited at 600°C onto silica substrates. The spacing between the electrodes are: ● = 100 µm, ▲ = 25 µm, ○ = 15 µm, and △ = 10 µm.

The magnitudes and activation energies for arc I resistance are similar to those from the literature. These resistances did not depend on the oxygen partial pressure, within the range measured. These results, combined with the low capacitance values and the fact that the resistances, which are orders of magnitude apart, can be normalized to a consistent conductivity value, form a strong indication that arc I is due to electrolyte grain resistance. The conductivity values derived from the arc I resistance will be called the grain conductivity for the remainder of this thesis.

The temperature-grain conductivity product is plotted in Figure 55 for all of the samples measured in this study. For most of the data sets, samples with a wide range of electrode and electrolyte geometries were measured and are graphed. There is a fair amount of scatter in all of the data, which is believed to be due mainly to error in temperature measurement and flaws in the photolithography that created electrodes with incorrect geometry. In the background of each plot is a white stripe that approximates the range of literature values compiled in Figure 16. Arrhenius-type data fit lines are plotted for all of the samples except for the films deposited on single crystal YSZ substrates. The activation energies derived are compiled in Table 6.

The tapecast sample depicted in plot (a) had a conductivity near the average of the literature data, which is a good check on the legitimacy of the measurements. As can be seen, the activation energy also closely matches the literature values. The single crystal YSZ samples, shown in plots (b) and (c), had conductivities that are near the upper end and in some cases exceed the literature values. The same plots show the conductivities measured for the bare substrates and those in which a YSZ film was deposited on the surface. The resistances measured were relatively similar for these samples, which proves that—for the YSZ substrates, in opposition to the silica substrates—the current traveled mainly through the thick substrate and not the much thinner film on the surface. For this reason, all of these samples used the substrate geometry to normalize and find the conductivity. Plots (d), (e), and (f) show the grain conductivities for the YSZ9 films. These conductivities average a fair bit higher than the bulk samples and the literature values. As expected from the lower dopant content, the conductivity is particularly improved at low temperatures due to lower activation energies. Within the limits of experimental error, there is no difference between films deposited at different temperatures. Finally, plots (g) and (h) cover the YSZ16 films deposited on silica. These values are very similar to those for the single crystal samples and with a similar activation energy.

At the measurement temperatures used, the conductivity of YSZ is a strong function of the dopant content. The literature data covers a range of dopant concentration, including some fairly high concentrations of 12 % by oxide or greater. The single crystal YSZ samples and, especially, the YSZ films have dopant concentrations near the lower end of the spectrum. It is therefore not surprising that the conductivity values are near the upper end of the literature values.

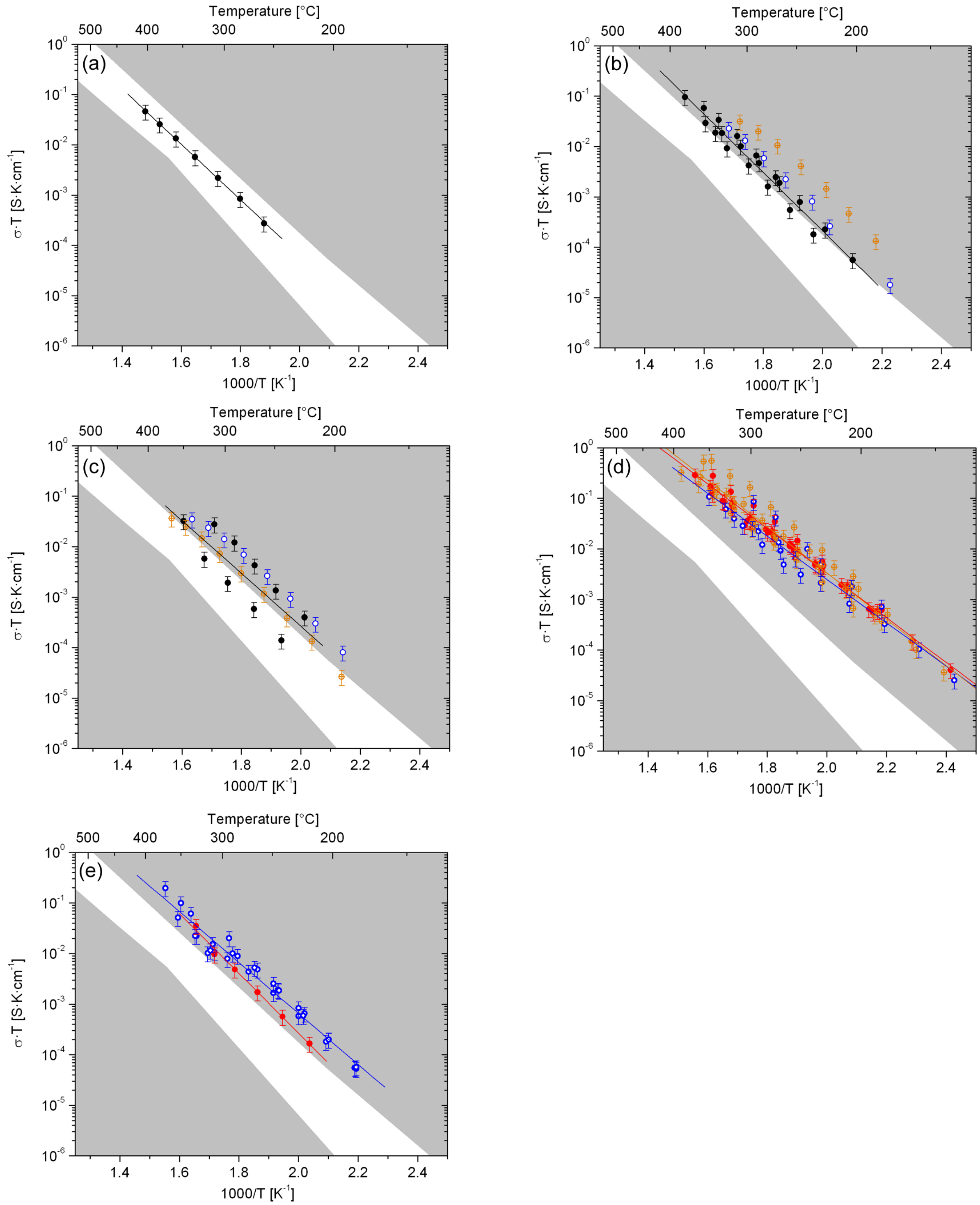

Figure 55. The grain conductivity for the samples measured in this study. The samples are: (a) tapecast YSZ; (b) (100) orientation YSZ single crystal samples; (c) (111) oriented YSZ single crystal samples; (d) YSZ9 films deposited on silica substrates; (e) YSZ16 films deposited on silica substrates at 300°C. The lines are best fits to an Arrhenius dependence. For the single crystal samples ● = bare substrate, ○ = substrate with 100 nm thick YSZ9 film deposited unheated on the surface, and ⊕ = substrate with 100 nm thick YSZ9 film deposited at 600°C on the surface. For the film on silica samples, ○ = film deposited unheated, ⊕ = film deposited at 300°C, and ● = film deposited at 600°C. The white stripe in the background approximates the range of literature values displayed in Figure 16.

Arc II was similar in behavior to arc I. It was usually not very depressed, with capacitance values that were low, but always larger than those of arc I. Typically, for an individual sample at a given temperature, the arc II capacitance was about one order of magnitude larger than the arc I capacitance. The arc II resistances scaled with the electrolyte geometry in the same way as arc I, as can be seen in Figure 56. Arc II, like arc I, did not depend on the oxygen partial pressure.

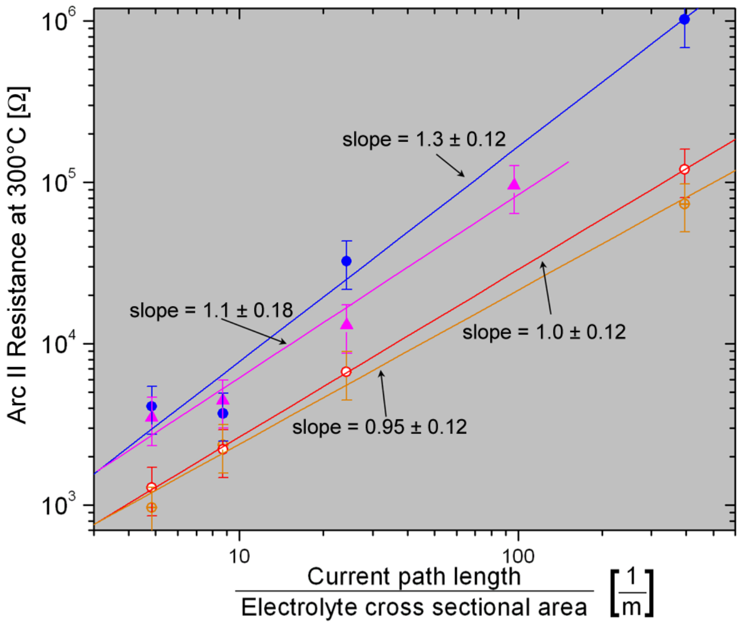

Figure 56. Arc II resistance at 300°C, plotted as a function of the conduction path length divided by the cross-sectional area of the electrolyte. ● = YSZ9 film deposited unheated; ⊕ = YSZ9 film deposited at 300°C; ○ = YSZ9 film deposited at 600°C; ▲ = YSZ16 film deposited unheated.

As mentioned previously, arc II was not found on any of the single crystal YSZ samples. Based on these results, arc II is assigned to the grain boundary impedance. The combined arc I and arc II therefore represents the total electrolyte impedance. Accordingly, the sum of the arc I and arc II resistances also scales with the electrolyte geometry. The temperature-grain boundary conductivity product is plotted in Figure 57 for all of the non-single crystal samples measured in the study. The conductivity is normalized to the overall electrolyte geometry without regard to the grain size or grain boundary geometry.

There is a great deal of scatter in the grain boundary conductivity for the YSZ9 films deposited unheated on silica (filled blue circles in plot b). This is believed to be because these films experienced significant cracking during thermal cycles. The cracks presumably occurred along grain boundaries, so they affected the grain boundary impedance. The extent of cracking was dependent on the film thickness and the thermal history, and so was an uncontrolled increase in the resistance.

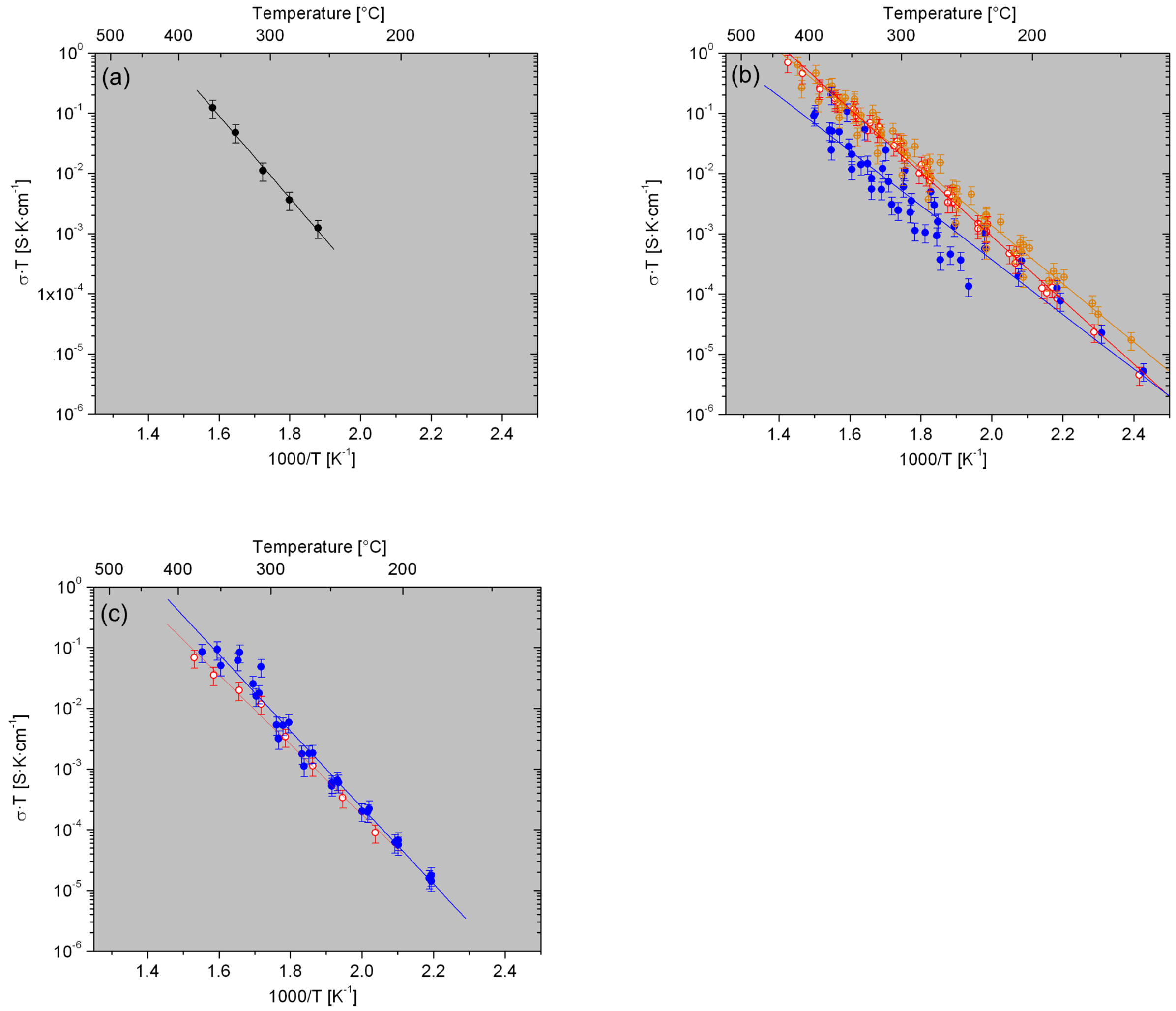

Figure 57. The grain boundary conductivity for the samples measured in this study. The samples are: (a) tapecast YSZ; (b) YSZ9 films, deposited on silica substrates; and (c) YSZ16 films, deposited on silica substrates. For the film samples, ● = unheated deposition, ⊕ = 300°C deposition, and ○ = 600°C deposition.

The grain boundary conductivity of the YSZ9 films deposited at 300°C was higher than those deposited at 600°C. The activation energy for the YSZ16 films was higher because of larger dopant content. This reduced the conductivity of the YSZ16 films to below that of the YSZ9 films at the temperatures measured.

The activation energies of grain and grain boundary conduction for all of the samples are given in Table 6. Two trends can be seen. First, the activation energies of grain boundary conduction are slightly more than those for grain conduction. Second, the activation energies of grain and grain boundary conduction increase with increased dopant concentration.

Table 6. The activation energies of grain and grain boundary conduction for the samples measured in this study.

Film	Deposition temperature	Substrate	Activation energy of grain conduction [eV]	Activation energy of grain boundary conduction [eV]
YSZ9	Unheated	SiO_2	0.85 ± 0.035	0.90 ± 0.024
YSZ16	Unheated	SiO_2	1.0 ± 0.033	1.3 ± 0.034
YSZ9	300°C	SiO_2	0.91 ± 0.022	0.96 ± 0.019
YSZ9	600°C	SiO_2	0.88 ± 0.027	1.1 ± 0.023
YSZ16	600°C	SiO_2	1.2 ± 0.11	1.1 ± 0.074
--	--	(100) YSZ single crystal	1.2 ± 0.053	--
--	--	(111) YSZ single crystal	1.0 ± 0.091	--
--	--	Tapecast YSZ	1.1 ± 0.096	1.4 ± 0.15

3.4.2 Constriction Resistance

The highly depressed arc III is not normally seen in impedance studies of solid electrolyte systems. The α parameter was very low each time, around 0.5. Such a value is indicative of a diffusion process or transmission line. Arc III overlapped quite a bit with arc IV, which made equivalent circuit fitting more difficult. A significant amount of scatter is in the data for this reason.

An Arrhenius plot of the arc III resistance is given in Figure 58. Error bars are not provided in the figure for the sake of intelligibility. Clearly, the non-normalized resistances vary widely, even between samples with the same type of electrolyte. No simple relationship between the sample geometry and the arc III resistance can be found. The activation energies derived from the figure are in Table 7. Comparing Table 6 and Table 7, the activation energy of the arc III resistance was very similar to that of the grain and grain boundary resistance.

Table 7. The activation energies of the arc III resistance for the samples measured in this study.

Film	Deposition temperature	Substrate	Activation energy of arc III resistance [eV]
YSZ9	Unheated	SiO_2	0.97
YSZ16	Unheated	SiO_2	1.4
YSZ9	300°C	SiO_2	0.97
YSZ9	600°C	SiO_2	0.97
YSZ16	600°C	SiO_2	1.1
--	--	(100) YSZ single crystal	1.3
--	--	Tapecast YSZ	1.3[a]

[a] Average of high temperature and low temperature regimes.

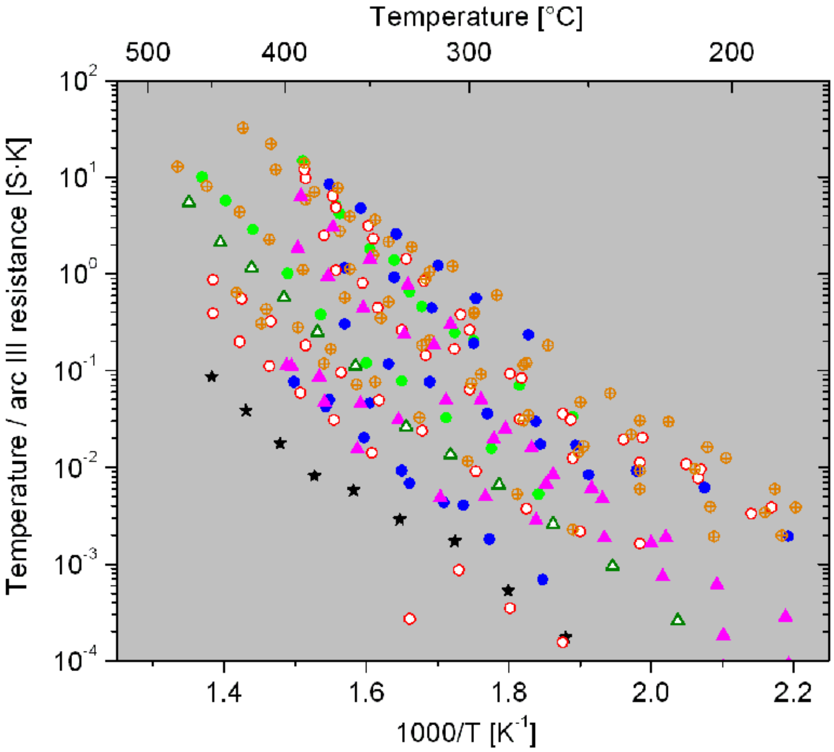

Figure 58. An Arrhenius plot of the arc III resistance for the samples measured in this study. ★ = tapecast YSZ, ● = (100) oriented YSZ single crystal, ● = YSZ9 film deposited unheated on silica, ⊕ = YSZ9 film deposited at 300°C on silica, ○ = YSZ9 film deposited at 600°C on silica, ▲ = YSZ16 film deposited unheated on silica, △ = YSZ16 film deposited at 600°C on silica.

For each sample, the resistance values were comparable to the grain and grain boundary conductivity. The ratio of the arc III resistance to the sum of the grain and grain boundary resistances is plotted for a few select samples as a function of temperature in Figure 59. Because the activation energies are similar, the ratio did not significantly depend on temperature. For the film on silica samples, the ratio was between about 0.1-1. For the YSZ bulk samples and the film samples with YSZ single crystal substrates—in other words, the samples with thick electrolytes—the ratio was between about 1-30. The figure shows that, in general, thinner electrolytes and wider electrode fingers produce a higher resistance ratio.

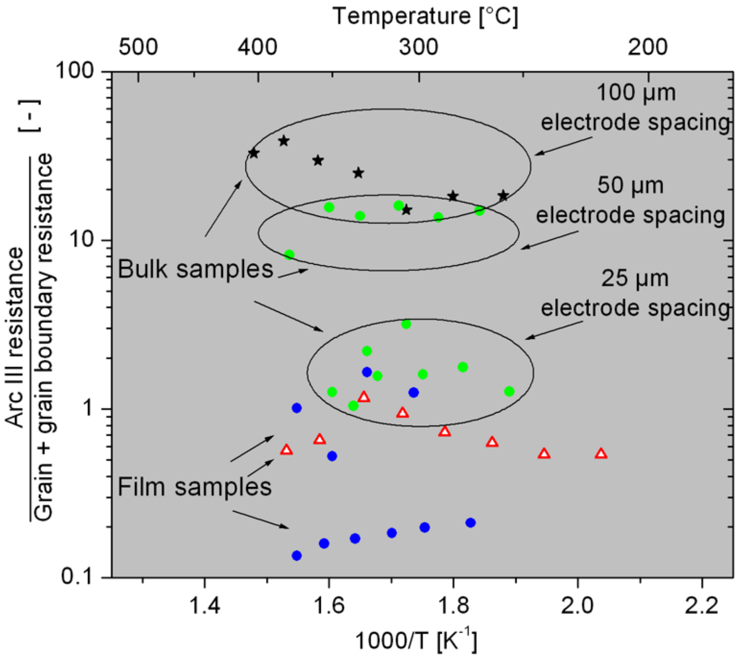

Figure 59. The ratio of the arc III resistance to the sum of the grain and grain boundary resistance is plotted as a function of temperature for a few selected samples. Symbols carry the same meaning as in Figure 58.

Many of the features of arc III are explained by considering it to be a constriction resistance near the triple phase boundary. This can be understood by considering the interface between the electrode and electrolyte. At high frequencies, the interface is expected to have the ability to store a finite amount of ions and ionic defects. It thus electrically behaves as a capacitor. As the frequency decreases, the capacitor is charged and there is additional resistance as the current path is constricted to the vicinity of the triple phase boundary. At the triple phase boundary, chemical exchange with the atmosphere can occur. The constricted current path is within the electrolyte, so it is expected that the activation energy is similar to that of the grain and grain boundary resistances. The capacitance is interfacial, so the very large capacitances measured also are expected. Finally, a constriction resistance successfully explains the severe depression of the semicircle. The electrode-electrolyte interface behaves electrically like a transmission line, as shown in Figure 60. This situation creates a very wide distribution of time constants and thus, as discussed in section 1.4.1, a highly depressed semicircle. The arc III resistance will be referred to as a constriction resistance for the remainder of this dissertation. A more detailed discussion of the constriction resistance will be given in section 4.1.2 and numerical modeling of the constriction term is described in Appendix A.

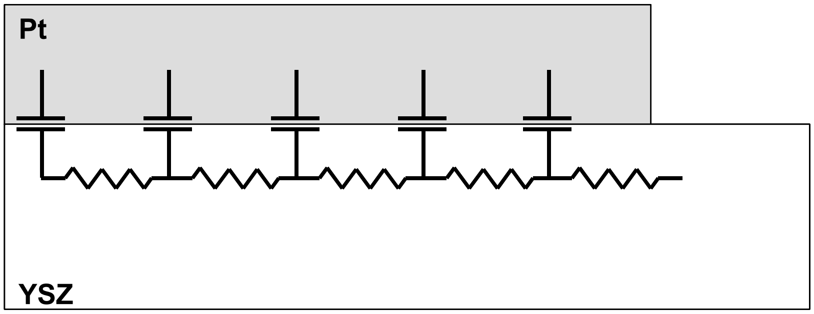

Figure 60. The electrode-electrolyte interface modeled as a transmission line.

3.4.3 Electrode Polarization Resistance

The lowest frequency arc, arc IV, was generally somewhat depressed with an α parameter of between 0.8 - 0.9. The capacitance was quite large, typically on the order of 10^{-5} $F\cdot s^{\alpha-1}$. The resistance values scaled roughly inversely with the perimeter length of the electrodes and were highly dependent upon the oxygen partial pressure. Based upon these findings, this impedance was ascribed to the electrode activation polarization resistance.

Further evidence suggesting that this arc is due to electrode polarization comes in finding the same impedance for electrodes with different spacing on the electrolyte surface. This is shown in Figure 61. Single crystal samples with Pt paste back electrodes were used for this experiment in order to vary the inter-electrode spacing by a factor of over 500. Impedance spectra were collected between the two interdigitated electrodes on the top surface and then between one of the interdigitated electrodes and the back electrode. A diagram of the structure was given in Figure 31. Though the electrolyte resistance was different, Figure 61 shows that the arc IV resistance is the same for both electrode configurations. These two findings are consistent with the different current path through the electrolyte yet the same amount of electrochemically active sites for the electrode reaction. This result proves, in particular, that the arc IV impedance is not due to surface conduction between the electrodes. As can be seen, this result holds true for electrodes placed on YSZ9 films deposited both unheated and at 600°C on a YSZ single crystal substrate.

The electrode polarization resistance at 400°C is plotted as a function of triple phase boundary length for a number of samples in Figure 62. All of these samples are based on a 1 μm thick YSZ9 film electrolyte, deposited on silica substrates. Unfortunately, the difficulties in producing fine lithographic features prevented the creation of as wide a range of TPB lengths as originally intended. Though few data points could be produced, the fitted slope for each of these lines is about -1. A normalized conductance (inverse resistance) per unit of TPB length can thus be determined for the various sample geometries. This value is plotted in Figure 63 for the samples measured in air.

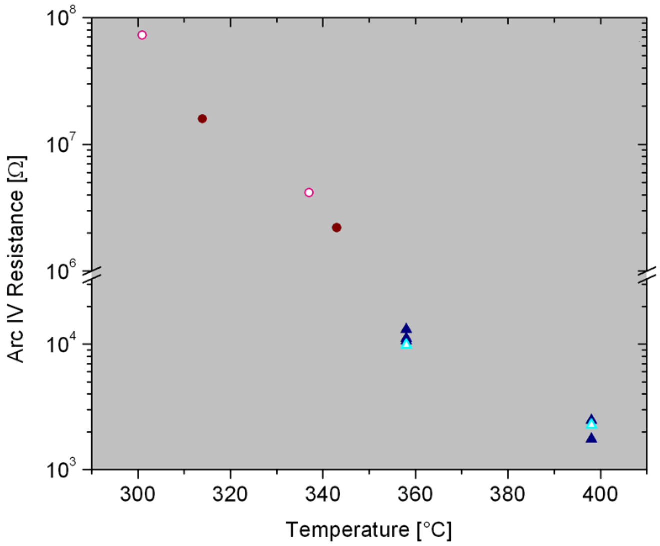

Figure 61. The arc IV resistance for single crystal substrate samples, comparing the impedance between two closely spaced electrodes on the same side of the substrate and between widely spaced electrodes on opposite sides of the substrate. (●,○) = YSZ9 film deposited at 600°C on a YSZ single crystal substrate, (▲,△) = YSZ9 film deposited on an unheated YSZ single crystal substrate. Closed symbols were measured between electrodes on the same side of the substrate; open symbols were measured between electrodes on opposite sides.

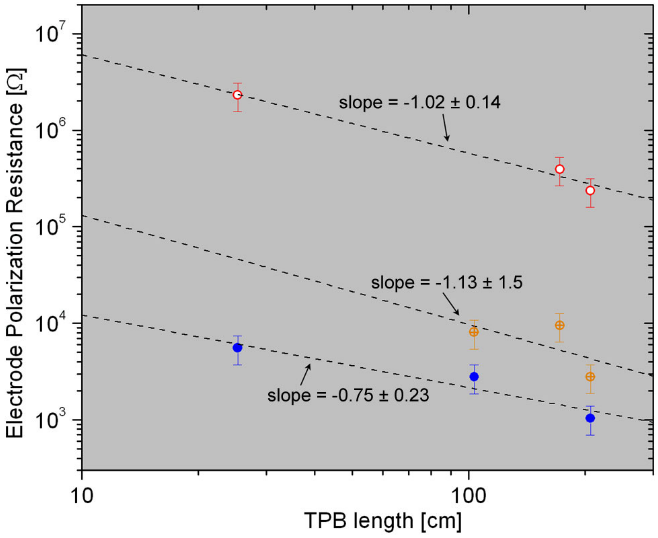

Figure 62. The electrode polarization resistance at 400°C, as a function of the triple phase boundary length. ● = YSZ9 film deposited on an unheated silica substrate, ⊕ = YSZ9 film deposited on a 300°C silica substrate, and ○ = YSZ9 film deposited on a 600°C silica substrate. Dashed lines are linear fits with a slope as indicated. Note that the uncertainty in the slope of the YSZ9 film deposited on a 300°C silica substrate is essentially too large to specify.

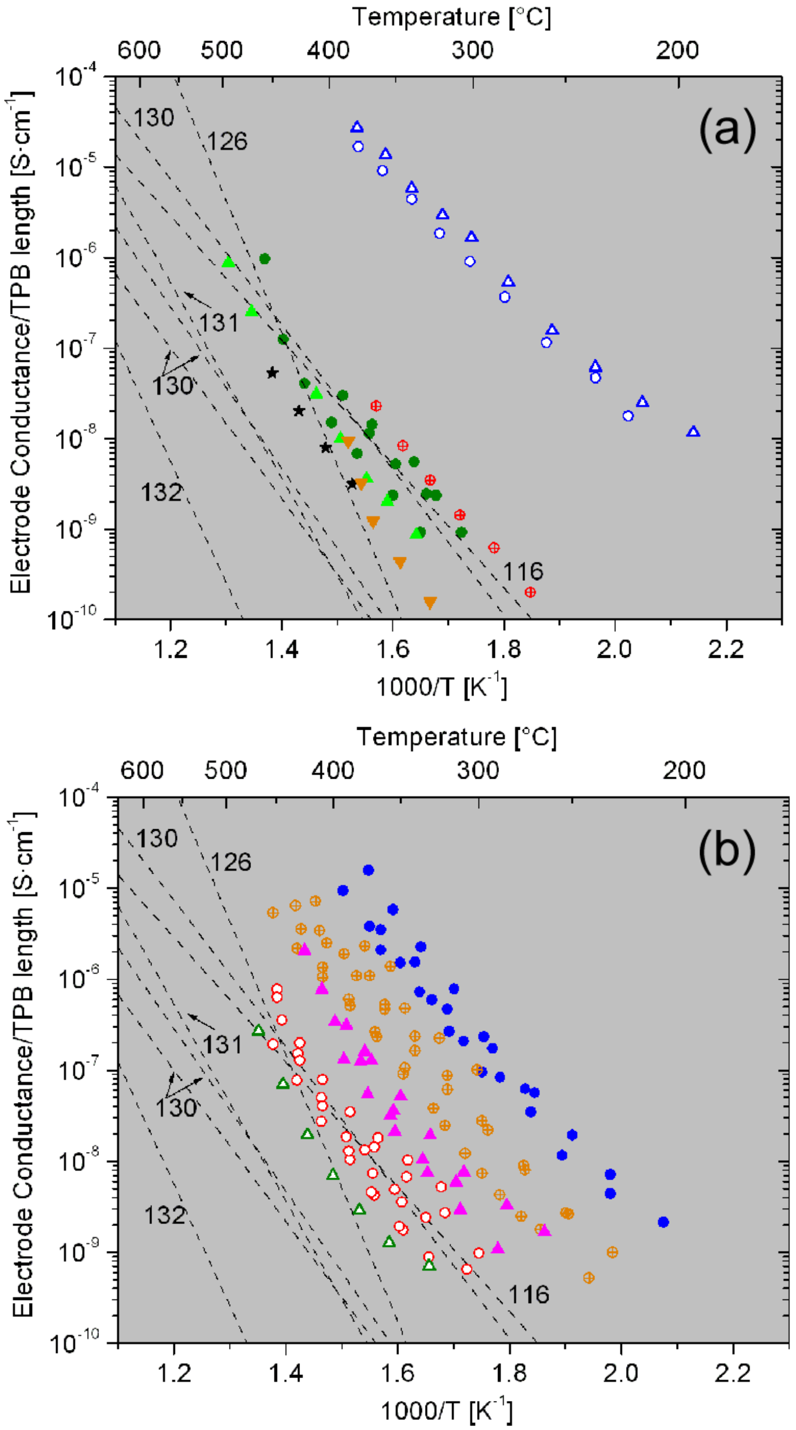

Figure 63. The electrode polarization conductance normalized to the triple phase boundary length. Dashed lines are fits to the literature values plotted in Figure 25; numbers indicate the reference. (a) Bulk samples: ● = (100) oriented single crystal YSZ; ○ = YSZ9 film deposited on an unheated (100) oriented single crystal YSZ; ⊕ = YSZ9 film deposited on a 600°C (100) oriented single crystal YSZ; ▲ = (111) oriented single crystal YSZ; △ = YSZ9 film deposited on an unheated (111) oriented single crystal YSZ; ▼ = YSZ9 film deposited on a 600°C (111) oriented single crystal YSZ; ★ = tapecast YSZ. (b) Film on silica samples: ● = YSZ9 film deposited unheated; ⊕ = YSZ9 film deposited at 300°C; ○ = YSZ9 film deposited at 600°C; ▲ = YSZ16 film deposited unheated; △ = YSZ16 film deposited at 600°C.

Though the activation energy for all of the samples is similar—about 1.55 eV—the magnitudes at a given temperature are enormously different. There is a slight trend towards lower activation energy for the highest conductance samples, reducing from about 1.6 eV to 1.4 eV. Though little data could be collected at low temperatures, there also seems to be a reduction in the activation energy below about 250°C.

As can be seen in the figure, the normalized conductances of electrodes placed on YSZ single crystals of both orientations, tapecast YSZ, and films of both compositions when deposited at 600°C are on par with the best values reported in literature. Electrodes placed on YSZ9 films deposited without heating on either silica or YSZ single crystal substrates have nearly 300 times higher electrode polarization conductance while the YSZ16 films deposited without heating showed a more modest improvement. The YSZ9 films deposited at 300°C were only slightly worse than the unheated deposition, which is consistent with the finding that unheated depositions actually occurred at around 200°C.

The fact that the polarization conductance is critically dependent upon the electrolyte surface is demonstrated by comparing the YSZ single crystal samples. Electrodes placed directly on the single crystal surface had low polarization conductance. By inserting a YSZ9 film deposited without substrate heating between the single crystal surface and the electrode, the polarization conductance increased nearly 2.5 orders of magnitude. Inserting the same composition film deposited at 600°C provided no such benefit. Another demonstration of the control of the electrolyte surface upon the electrode polarization conductance is that the conductances for the YSZ9 films did not change whether the substrate is silica or a YSZ single crystal. The electrolytic resistances were vastly different in these situations, since in one case the substrate was conductive and in the other it was insulating, however the electrode polarization conductance was nearly the same in both situations.

The electrode conductance as a function of the oxygen partial pressure is plotted in Figure 64. The behavior was qualitatively similar for all of the samples measured. At every temperature, a maximum in the conductance was found at a certain pO_2. On either side of the maximum, the slope of log pO_2 vs. log conductance was roughly ± ½. The pO_2 of maximum conductance was reduced at lower temperatures. The activation energy at the low pO_2 side of the maximum was less than the high pO_2 side. The trends described were found for a (100) oriented YSZ single crystal sample, a YSZ9 film deposited on an unheated (100) and (111) oriented YSZ single crystal, and a YSZ9 film deposited on a silica substrate at 300°C. These samples cover the entire range of polarization conductances displayed in Figure 63: the low conductance electrodes on single crystals, the high conductance electrodes on unheated deposition films, and the average conductance of the 300°C deposited films.

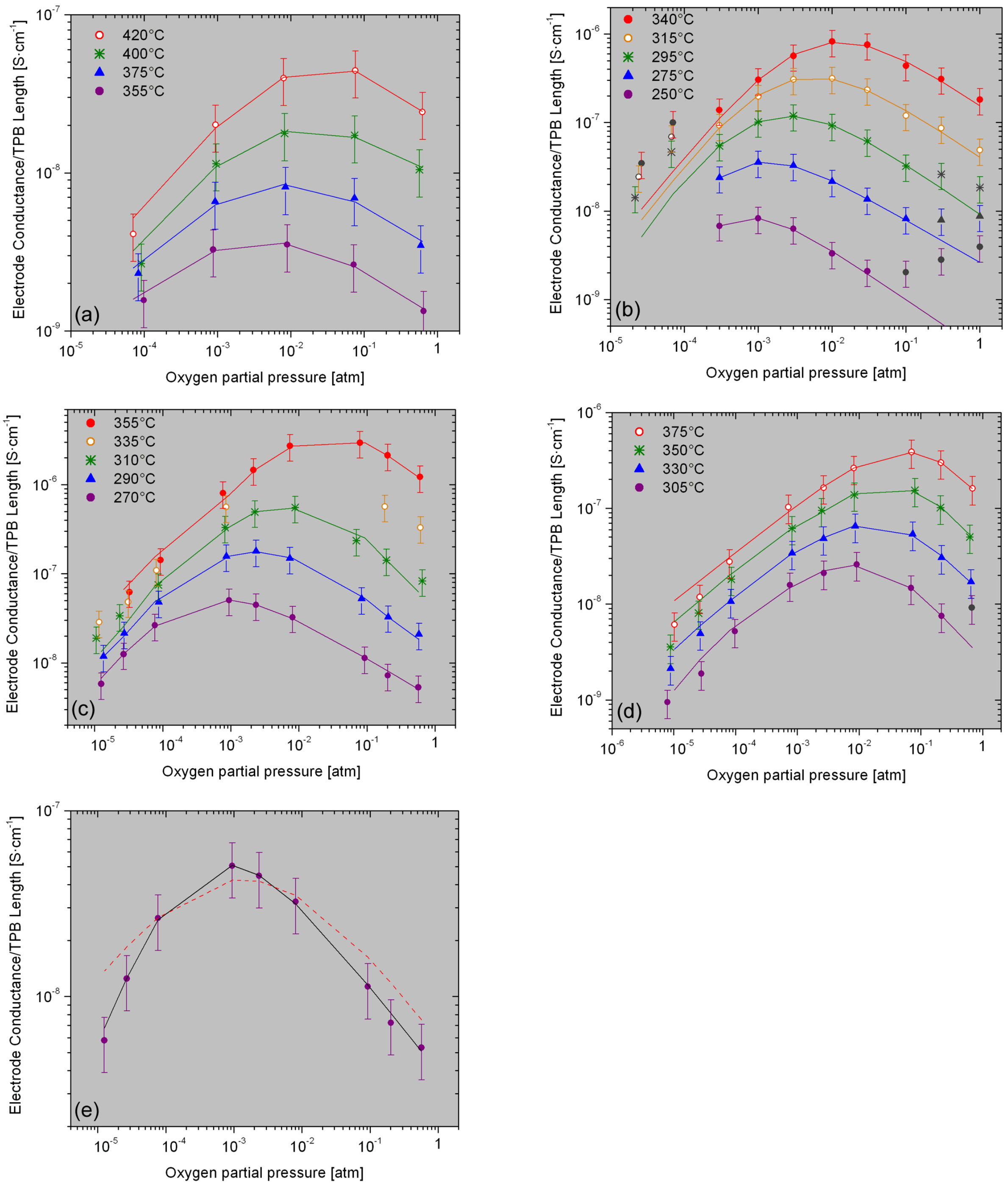

Figure 64. The normalized, isothermal electrode polarization conductance as a function of oxygen partial pressure for: (a) (111) oriented single crystal YSZ; (b) YSZ9 film deposited on an unheated (100) oriented YSZ single crystal substrates; (c) YSZ9 film deposited on an unheated (111) oriented YSZ single crystal substrates; and (d) YSZ9 film deposited on a silica substrate at 300°C. Data points colored black were excluded from the fitting routine. Lines are fits to equation 56. Plot (e) compares the fit to equation 56 (solid black line) and 53(dashed red line) for the data set of plot (c), 270°C.

The lines in Figure 63 represent fits to a modified form of equation 53. The equation was modified to allow the slopes to vary slightly from exactly ± ½. As can be seen in Figure 63(e), the slopes tended to be slightly larger than +½ at low pO_2 and slightly smaller than -½ at high pO_2. In addition, there was generally some asymmetry in the slopes, with a steeper slope at low pO_2 than high pO_2. To account for this, equation 53 was modified to allow the slopes to vary. The equation used was

$$\sigma_E = \frac{4 \cdot F^2 \cdot B \cdot \lambda \cdot c \cdot a_0^* \cdot \left(P_{O_2}\right)^a}{\delta \cdot \left[a_0^* + \left(P_{O_2}\right)^b\right]^2} \tag{56}$$

where *a* and *b* are used as additional parameters to set the slope of the graph away from the conductance maximum. By inspection, the slope of the log-log plot is equal to *a* at $pO_2 \ll pO_2^*$ and $(a-2b)$ at $pO_2 \gg pO_2^*$, where pO_2^* is the pO_2 of maximum conductance. Equation 53 sets $a=b=½$. The average values for the fitting parameters were 0.76 ± 0.011 for *a* and 0.73 ± 0.033 for *b*, translating to an average slope of +0.76 on the low pO_2 side and -0.70 on the high pO_2 side.

At the lowest temperatures and highest pO_2, a third regime broke away from the -½ slope expected, and an increase in the conductance with increasing pO_2 was found. This regime includes the pO_2 of normal air. Therefore, this effect may account for a slight reduction in activation energy that seems to be present in measurements performed in air below 250°C. This can be seen, for example, in the YSZ9 film on an unheated (111) oriented single crystal YSZ plotted in Figure 63(a). As discussed in section 1.5 and reference 175, this may indicate the creation of stable platinum oxide phases on the surface.

3.4.4 Si-free Single Crystal Samples

To specifically examine the role of the Si impurities, the two samples of single crystal YSZ that had reduced Si contamination on the surface were electrically characterized. First was the single crystal sample that had Pt electrodes microfabricated without the use of HMDS photoresist adhesion promoter. This sample was shown in Figure 43(c) to not have Si on the surface. Comparison is made with the identical sample made with HMDS. As seen in Figure 65, the electrode polarization was similar for the two samples, but slightly better for the sample made without HMDS. This shows that the mere presence or lack of Si is not entirely sufficient to explain the difference in electrode polarization behavior. Though not shown, the electrolyte resistance was the same for these samples.

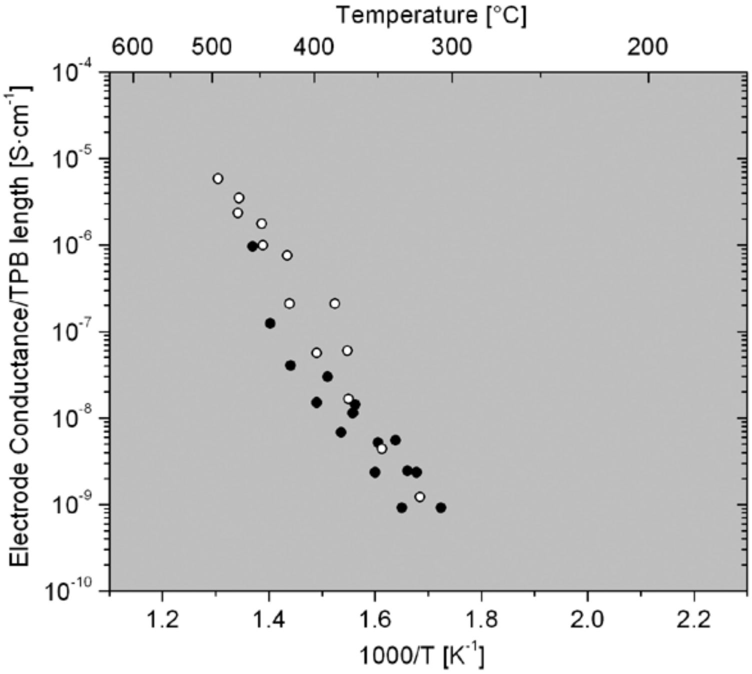

Figure 65. The normalized electrode polarization conductance of single crystal YSZ samples using electrodes microfabricated with and without HMDS adhesion promoter. ● = Si-contaminated YSZ single crystal with electrodes microfabricated with HMDS, ○ = Si-free YSZ single crystal with electrodes microfabricated without HMDS.

The polarization resistance of the single crystal sample cleaned in HF is plotted in Figure 66. This sample was shown in Figure 44 to have had much of the Si on the surface successfully etched away. Though the electrolyte resistance did not change after the etching, the electrode polarization conductance did. Some transient behavior was found in the polarization conductance during the initial heating cycle, but during subsequent heating cycles the conductance was repeatable and showed the same activation energy as before etching. The polarization conductance during the second measurement after etching is nearly 2 orders of magnitude improved compared to the same sample before etching. The conductance is not as high as the unheated deposition YSZ9 film, but was better than the unheated deposition YSZ16 film. The XPS results showed no fluorine on the surface, however that characterization was performed after the electrical characterization. Therefore, the transient behavior may have been due to fluorine leaving the surface as the sample was first heated.

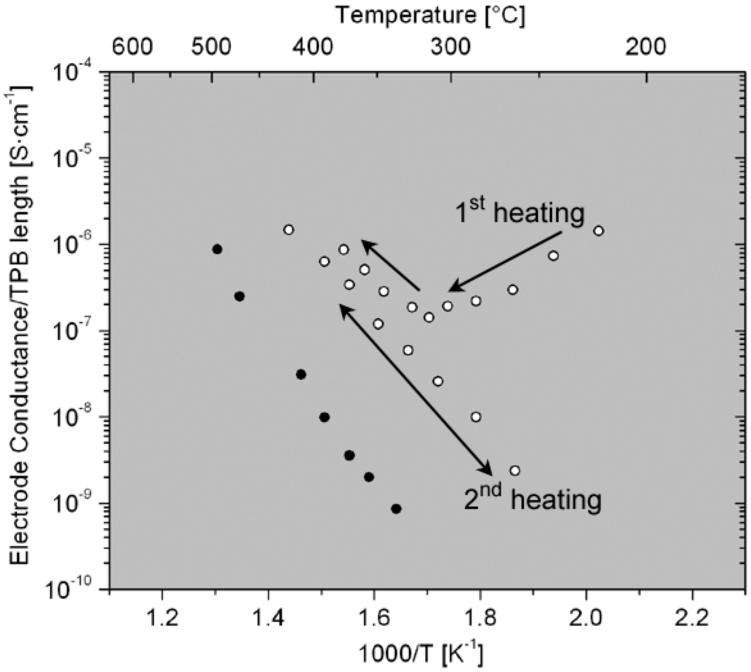

Figure 66. The normalized electrode polarization conductance of a single crystal YSZ sample before and after etching in HF. ● = YSZ single crystal before etching in HF (high Si content on surface) and ○ = YSZ single crystal after etching in HF (low Si content on surface).

3.5 Composite Platinum – Yttria Stabilized Zirconia Thin Films

3.5.1 Film Deposition and Physical Characterization

The composition of the Pt-YSZ films were determined using the Pt:Zr atomic ratio found by XPS. The Pt:Zr ratio of films deposited with various conditions is compiled in Table 8. As expected, the Pt composition increases with increased relative Pt sputtering power. To a first approximation, a volumetric ratio of 1:1 for the Pt and YSZ phases was desired in order to have percolated phases and maximal triple phase boundary length. Accounting for the different atomic densities of the Pt and YSZ phases, the Pt:Zr atomic ratio that achieves the 1:1 volume ratio is 2.47:1.

Table 8. The Pt-Zr atomic ratio of Pt-YSZ composite films deposited under a range of conditions.

Film Number	Pt sputtering power [W]	Y-Zr sputtering power [W]	Deposition temperature [°C]	$Ar:O_2$ ratio in sputtering gas [-]	Pt:Zr atomic ratio in film [-]
1	0	200	630	95:5	0
2	10	200	630	95:5	1.08:1
3	20	200	630	95:5	1.64:1
4	30	200	630	95:5	1.73:1
5	50	150	500	90:10	2.54:1
6	50	100	500	90:10	3.56:1
7	50	50	500	90:10	7.09:1

The deposition rates and Pt/(Pt+Zr) atomic ratio were found to be non-correlated for the series of films deposited with the Y-Zr target sputtering power kept constant. The values are plotted in Figure 67. Their non-linearity may signify a non-trivial interaction between the plasmas above the targets. Another possibility is that the volumes of the Pt or YSZ phases were changing their atomic densities. This is most likely to have occurred if one or both phases were changing oxidation state, however XPS indicated no change in oxidation states and XRD found no evidence of metallic Zr or Y phases.

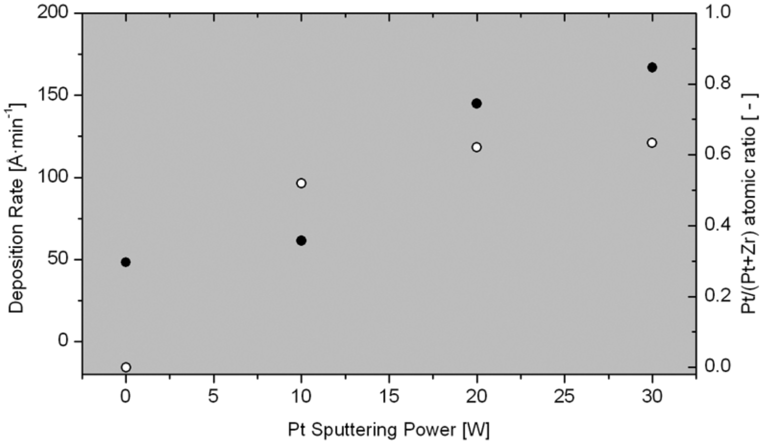

Figure 67. The deposition rate and Pt:Zr atomic ratio of Pt-YSZ composite films deposited with different Pt sputtering powers. All samples deposited with a Y-Zr target sputtering power of 200W, a substrate temperature of 630°C, and an Ar:O$_2$ ratio of 95:5. ● = Deposition rate and ○ = Pt:(Pt+Zr) atomic ratio.

X-ray diffraction revealed that crystallization of the Pt and YSZ phases was difficult and was dependent on the deposition temperature and relative sputtering powers. In Figure 68 is the diffraction data for low Pt content films deposited on single crystal Si substrates. Deposition at 300°C resulted in a completely amorphous film, with no Pt or YSZ peaks. Even after annealing this film at 600°C, no peaks were visible. Deposition at 600°C or above resulted in a film with distinct peaks for both Pt and YSZ phases. Based on the relative peak heights, there appeared to be some preferred orientation to both the Pt and YSZ phases. Figure 69 shows the X-ray diffraction spectra for high Pt content films deposited on silica substrates. Deposition at both 300°C and 500°C resulted in moderate Pt peaks and very small YSZ peaks. The Pt phase seemed to be easier to crystallize, consistent with its lower melting temperature (1769°C) compared to YSZ (2680°C). The YSZ peaks are very small for both deposition temperatures, so most of it was amorphous. Though the presence of peaks indicate individual, crystalline phases of Pt and YSZ, some Pt dissolved in the YSZ phase and vice-versa cannot be determined from these results. Sputtering is not an equilibrium process, so the concentrations may exceed equilibrium solubility limits.

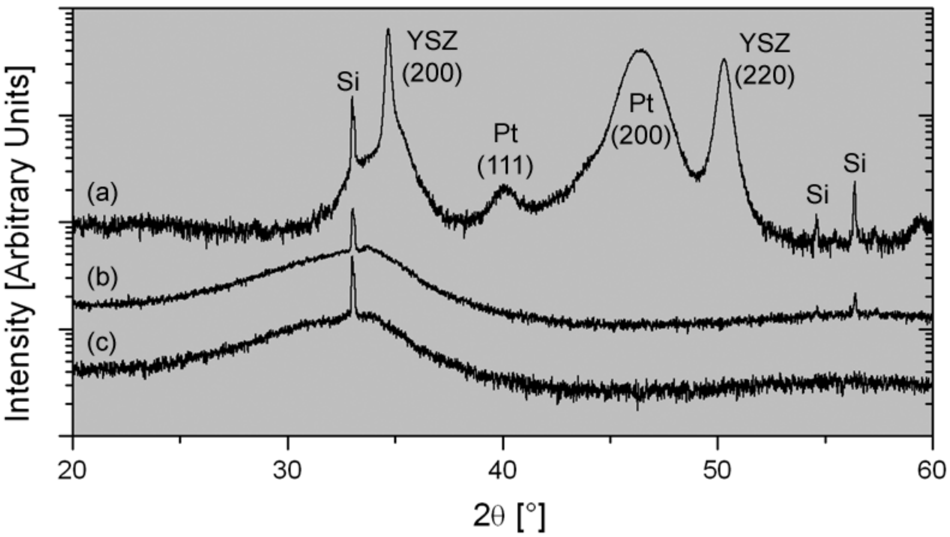

Figure 68. X-ray diffraction spectra for Pt-YSZ films deposited at (a) 630°C and (b) 300°C onto single crystal Si substrates. Plot (c) is the diffraction pattern for the same film as plot (b), after annealing at 600°C for 1 hour. The sputtering powers were Pt: 10 W and Y-Zr: 200 W.

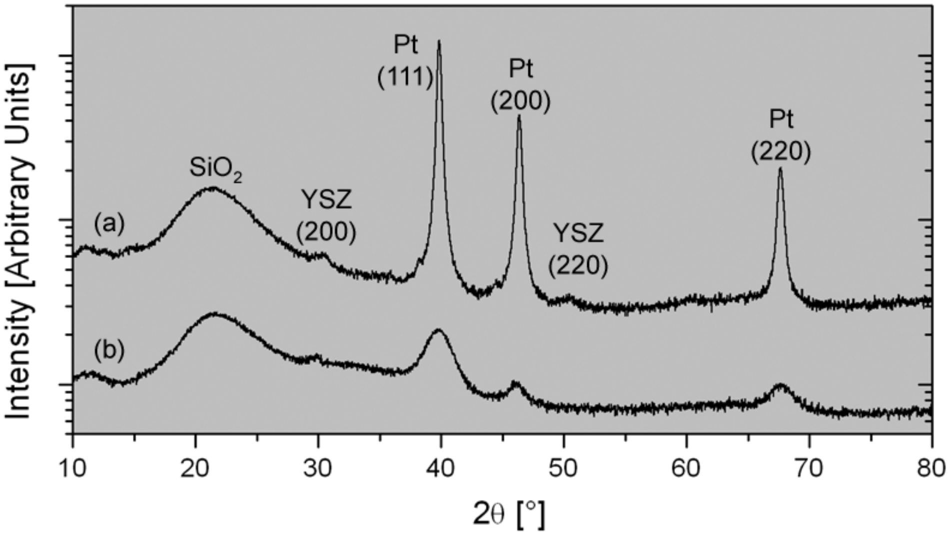

Figure 69. X-ray diffraction spectra for Pt-YSZ films deposited at (a) 500°C and (b) 300°C onto silica substrates. The sputtering powers were Pt: 50 W and Y-Zr: 150 W.

A scanning electron micrograph of the film 3 Pt-YSZ composite is given in Figure 70. There appears to be grains of 50 nm or less in size. Unfortunately, the resolution of the SEM did not allow any finer detail to be visualized. Any grains of size less than 50 nm or so cannot be distinguished from this micrograph.

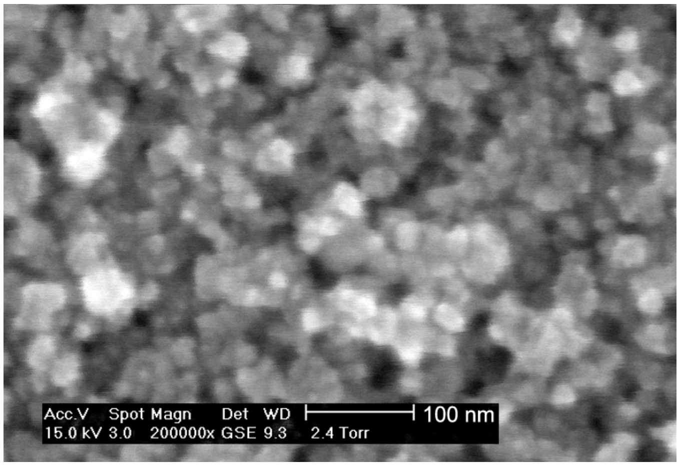

Figure 70. Scanning electron micrograph of a Pt-YSZ film deposited at 600°C.

3.5.2 Electrical Characterization

The Pt-YSZ films were first tested for percolation of electronically conducting Pt grains. Two points separated by a few centimeters on the surfaces of the films were contacted in the probe station. A multimeter then tested for electrical continuity, with a successful test indicating percolating grains. The amorphous films depicted in Figure 68(b) and (c) were non-conducting, despite being 52% Pt on an atomic basis. The film depicted in Figure 68(a) had the same amount of Pt; this film was electrically conductive because the higher deposition temperature allowed the Pt to form distinct, crystalline grains. The films depicted in Figure 69, which had higher Pt content with crystalline peaks, were both electrically conductive.

Two films were electrically characterized: films 3 and 5 as listed in Table 8. Film 3 had a composition of about 40:60 volume ratio of Pt:YSZ, while film 5 had a composition near the 50:50 volume ratio of Pt:YSZ. Both films had distinct Pt crystalline diffraction peaks; in film 3 there were also large and well-defined YSZ peaks while in film 5 there were only very weak YSZ peaks. Impedance plots for these samples consisted of two semicircles, as seen in Figure 71. The equivalent circuit of Figure 33, leaving out two of the R-CPE pairs, was used to model the data. The R-CPE pairs excluded were those associated with grain boundary and constriction impedances.

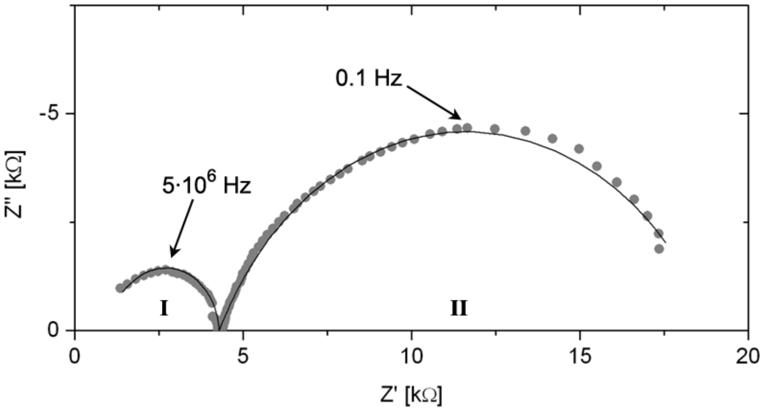

Figure 71. Typical impedance spectrum of a Pt-YSZ microelectrode on a YSZ single crystal. Points are raw data; line is the fit to the equivalent circuit. The semicircle peak frequencies are given.

Arc I, the high frequency semicircle, is believed to be due to the impedance of the YSZ single crystal electrolyte. The behavior of this semicircle was quantitatively very similar for the film 3 and film 5 samples. The semicircle was not very depressed and the capacitance was very low, around 10^{-11} F·s$^{\alpha-1}$. The resistance and capacitance were both roughly proportional to the microelectrode area. Normalized to the electrolyte geometry, the conductivity closely matches values measured with the interdigitated platinum electrodes. This can be seen in Figure 72.

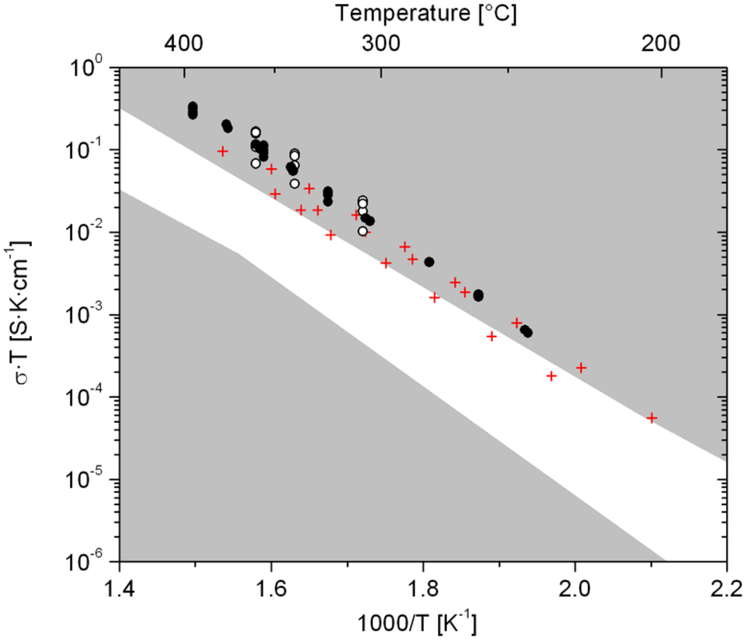

Figure 72. Conductivity of the YSZ single crystal electrolyte, as measured by Pt-YSZ microelectrodes. ● = film 3 microelectrodes and ○ = film 5 microelectrodes. ✚ = values determined with interdigitated Pt electrodes. The white stripe in the background approximates the range of literature values displayed in Figure 16.

No grain boundary semicircle was found for these samples, since the electrolyte was a single crystal. The lack of a constriction resistance semicircle suggests that ionic charge injection occurred across the entire surface of the composite film. An interesting observation was that dense Pt microelectrodes produced with the same geometry as the Pt-YSZ microelectrodes *did* display a constriction resistance. This gives strong supporting evidence to the notion of a TPB-related constriction resistance term.

Arc II, the low frequency semicircle, is believed to be due to the electrode activation polarization. While films 3 and 5 were qualitatively similar for this arc, they exhibited quantitative differences. The arc was fairly depressed for both films, with an α parameter close to 0.7. The capacitance was very large at around 10^{-4} $F\cdot s^{\alpha-1}$ for the film 3 samples and about 1 order of magnitude smaller for the film 5 samples. The resistances are plotted as a function of the electrode radius for film 3 and film 5 in Figure 73(a) and (b), respectively. At each temperature, the slope of the log-log plots are slightly larger than 2.

The electrode polarization conductance normalized to the electrode area is plotted for both films as a function of temperature in Figure 74. Though these films are composites, they are believed to be dense. A single plane of triple phase boundaries is thus present on the top surface. Comparison can be made between these conductances per area and the values from literature for single-phase, porous Pt electrodes on a YSZ surface. These literature values also have a single plane of triple phase boundaries, though they are located at the bottom surface of the electrode. The polarization conductances per area are 1-2 orders of magnitude larger than the best reported values from literature. Converse to the capacitance data, the conductance of a film 3 microelectrode was about one order of magnitude larger than the conductance of a film 5 microelectrode of the same size. The activation energy was 1.32 ± 0.10 eV for film 3 and 1.54 ± 0.15 eV for film 5. This closely matches the activation energy found in this study with interdigitated, single-phase Pt electrodes on YSZ as well as much of the literature data with Pt electrodes on YSZ.

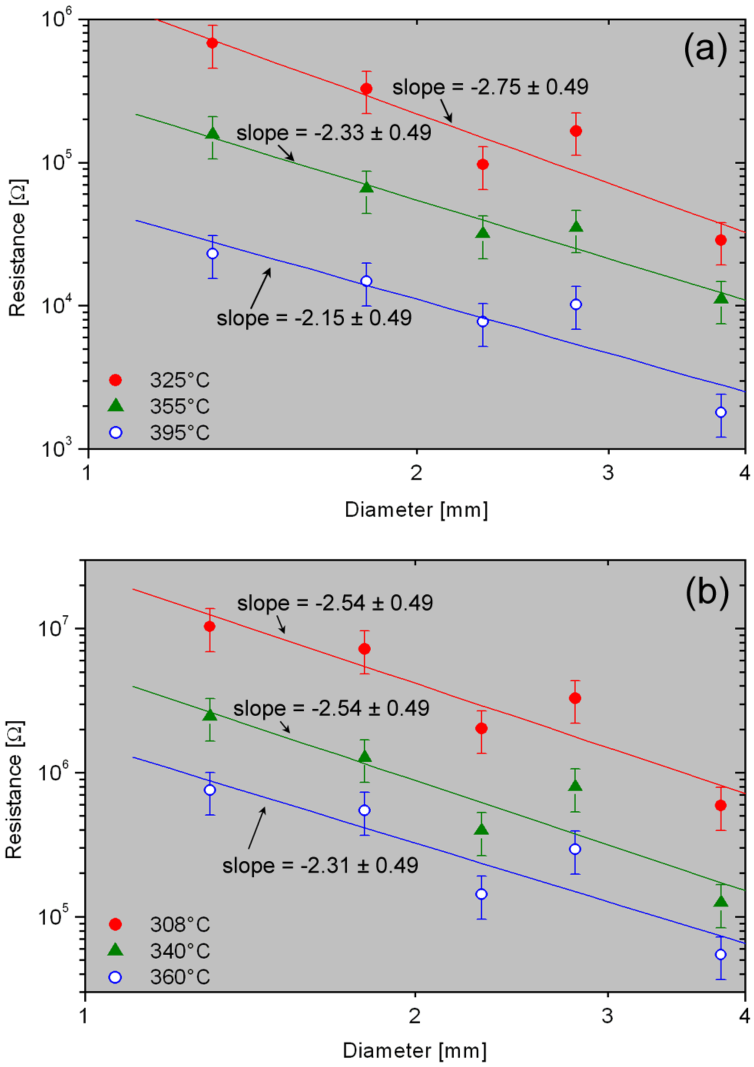

Figure 73. Electrode polarization resistance as a function of electrode radius for Pt-YSZ microelectrodes of (a) film 3 and (b) film 5.

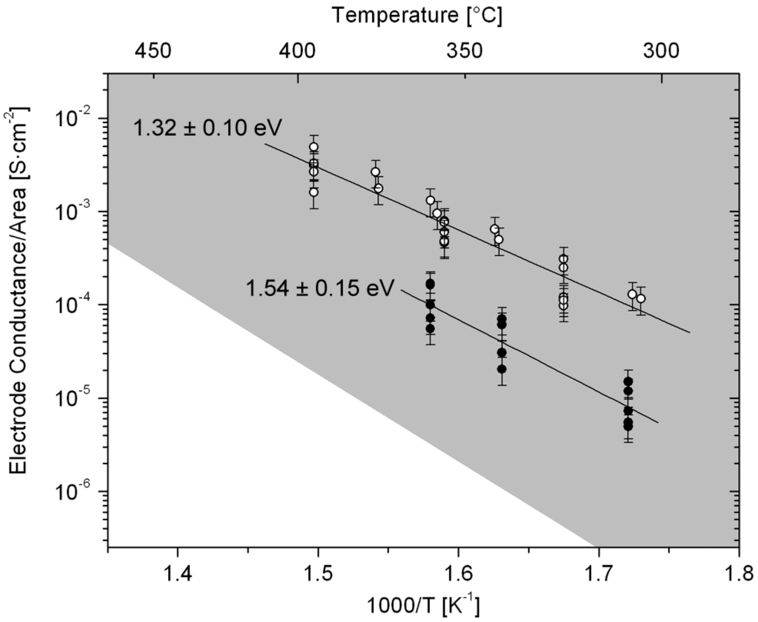

Figure 74. Arrhenius plot of electrode polarization conductance per unit area for Pt-YSZ microelectrodes. ● = film 5 microelectrodes and ○ = film 3 microelectrodes. The white portion in the lower-left approximates the upper range of literature values displayed in Figure 24.

CHAPTER 4. DISCUSSION

4.1 Performance of Single-Phase Platinum Electrodes on YSZ Surfaces

4.1.1 Electrolyte Resistance

The measurements made in this work confirm that, ignoring constriction effects, the electrolytic resistance of a thin film electrolyte will not be the dominant loss mechanism in a microfabricated solid oxide fuel cell. This assumption was originally made in chapter 1 using conductivity values of bulk YSZ as reported in the literature. In fact, the conductivities determined here for the YSZ thin films exceeded both the literature values and the measured bulk samples. According to the arguments made in section 1.2.7, this makes the ohmic resistance all but insignificant.

Despite the reduced conductivity of YSZ compared to other oxygen ion conductors (e.g., gadolinia doped ceria), YSZ films of moderate thickness appear suitable for inclusion in μSOFCs. If a limit of 0.5 $\Omega\cdot\text{cm}^2$ is placed on the electrolyte area specific resistance, then a maximum thickness can be determined from the conductivity values. For even the lowest conductivity film—YSZ16 deposited at 600°C—the conductivity allows a thickness of up to roughly 50 nm at 300°C and 500 nm at 400°C. In reality, the area specific resistances of the electrode activation polarization are larger than this 0.5 $\Omega\cdot\text{cm}^2$ by orders of magnitude, and thicker electrolyte films will still contribute insignificantly to the total device resistance.

One exception to this behavior is the YSZ9 film deposited unheated on a silica substrate. These had a larger grain boundary resistance than the other films, due to mechanical cracking. The overall conductivity still results in an insignificant contribution to the overall resistance of a μSOFC, however the lack of mechanical integrity might prohibit their use. On the other hand, the films did not crack when deposited on YSZ single crystal substrates. Thus, these films may still be of use if the μSOFC is constructed on a substrate with similar coefficient of thermal expansion.

The grain conductivities of the YSZ9 films were found to be greater than those of the bulk samples, especially the tapecast specimen. This is, in part, due to the difference in dopant concentration. As described in section 1.3.1, increased dopant levels in YSZ lead to increased activation energy of conduction below about 800°C. Generally, below about 400°C, this results in the conductivity of lower Y-content YSZ to surpass that of more standard Y-content materials. This is shown explicitly in Figure 75, where the dashed line represents the grain conductivity of bulk YSZ with composition similar to the YSZ16 films in this study and the solid line represents that of bulk YSZ with composition similar to the YSZ9 films. Included in this graph are the corresponding data for the films deposited on silica. The results are qualitatively similar, with the conductivity of the

YSZ9 films surpassing those of the YSZ16 films. However, the YSZ9 films have conductivities as much as two orders of magnitude higher than those reported for bulk YSZ. This is especially the case for the film deposited at 600°C (Figure 75b).

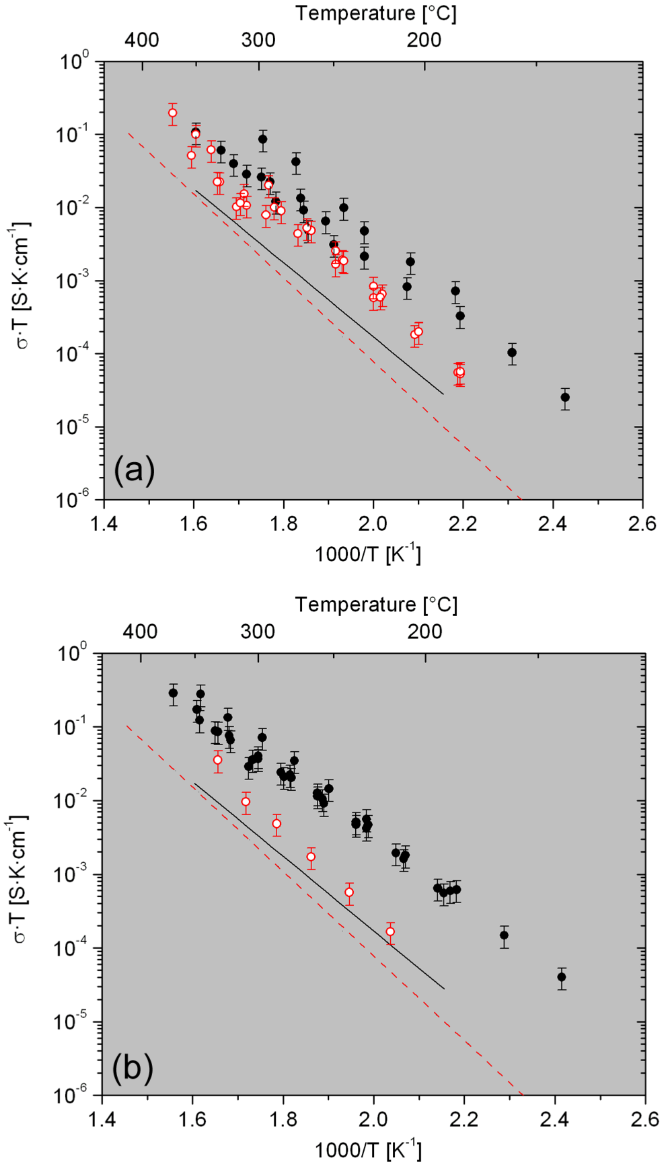

Figure 75. Arrhenius plot of YSZ grain conductivity, comparing compositions of roughly $Y_{0.09}Zr_{0.91}O_{2-x}$ (●, solid line) and $Y_{0.16}Zr_{0.84}O_{2-x}$ (○, dashed line). Points are the values measured for films in this study; lines are linear fits to data from reference 56. Films in plot (a) were deposited without substrate heating, while those in plot (b) were deposited at 600°C.

Generally, the largest conductivity in YSZ is found at compositions very close to the morphotropic phase boundary, essentially the minimum required to obtain fully cubic material. In these films, it appears from the x-ray diffraction data that cubic YSZ was stabilized at the much reduced dopant concentrations of the YSZ9 films. Similar results have been seen before, with even pure zirconia adopting cubic morphology at very small particle sizes[93,176]. Thus, the Y concentration needed to obtain the metastable cubic phase appears to have been appreciably reduced in thin YSZ films produced in this study, leading to significantly enhanced ionic conductivity.

As mentioned in section 1.3.4, enhanced conductivities have been reported before for YSZ films. Most notably, this was reported by Kosacki, et al., in reference 100. Only total conductivities (grain + grain boundary) were reported in this reference. Plotted in Figure 76 is the conductivity data from this reference for standard, bulk material and the nanocrystalline grain size enhanced conductivity films. Compared against these is the total conductivity of the YSZ9 and YSZ16 films from this study, deposited at 600°C. Similar comparison could not be done with the unheated deposition films, since the cracking led to unreliable grain boundary conductivity results in the unheated deposition YSZ9 films. As can be seen, the total conductivity values from the YSZ16 film in this study are only slightly larger than the bulk values from the literature, while the YSZ9 film is, at the lowest measurement temperatures, enhanced from this value by about 2 orders of magnitude. Nevertheless, at these low temperatures, the enhanced conductivity of reference 100 is larger still by an order of magnitude. Such extraordinarily high conductivities were not found in this study.

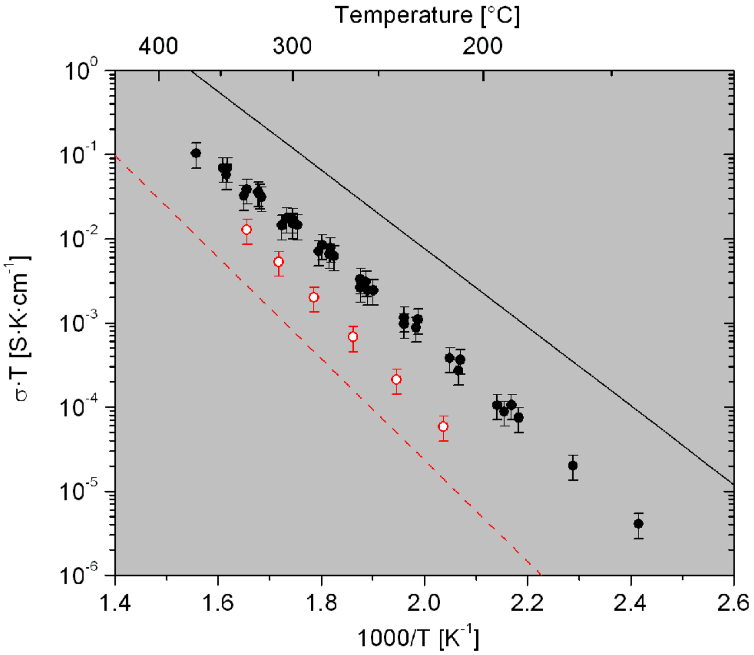

Figure 76. Comparison of the total (grain + grain boundary) conductivity of YSZ9 (●) and YSZ16 (○) films deposited at 600°C with the results of bulk specimen (dashed line) and nanocrystalline films (solid line) from reference 100. Reference data has been extrapolated from measurement between 450°C – 900°C and are from specimen with similar composition to the YSZ16 film.

Kosacki also reported a reduction in the activation energy of conduction for the nanometric films compared to the bulk material. A reduction in activation energy was not found for the films in this study when compared to bulk specimens with equivalent Y contents (the YSZ9 films had a reduced activation energy, however this is attributed to the reduced dopant levels yielding decreased vacancy ordering, as discussed in section 1.3.1). The source of enhanced conductivity and reduced activation energy in Kosacki's results remains unclear. On the other hand, if the films in Kosacki's work had an unexpectedly low dopant concentration, then perhaps favorable comparison can be made between those results and the results reported here. Decreased dopant concentration could be expected to lead to decreased activation energy of conduction, at least at the lower measurement temperatures. As posited here, perhaps cubic phase material was achieved in Kosacki's films despite lower dopant levels, leading to the enhanced conductivity. It is not known whether the actual dopant concentration in Kosacki's films were measured, however they were produced by a polymer precursor route. These routes are often excellent at preserving the stoichiometry of a film from that of the precursors.

Comparing the conductivity of single crystal samples with and without a YSZ film on the surface shows that the samples with the appropriate YSZ film had improved net conductivity. It is at first rather surprising that the film can cause a measurable increase in conductivity, since the film is only 100 nm thick while the single crystal is 500 µm thick. On the other hand, by having the electrodes closely spaced on the top surface, the current does not penetrate very deep into the substrate—loosely speaking, only about as deep as the distance between the electrodes.

We have shown that YSZ films on insulating silica substrates can have conductivities 10-100 times higher than that of the single crystals. The net resistance of the coated crystal can be modeled with a slight alteration of the code described in Appendix A. The original model, used to convert measured resistances to conductivity values, assumed a homogeneous conductivity. For this case, the model was modified to have a heterogeneous conductivity, with one value for the bottom 499.9 µm thickness of the electrolyte and a different value for the top 100 nm. The electrode geometry used was that of pattern 14, since that was the geometry for all of the samples of this type measured. The results of this model are plotted in Figure 77. At relative conductivity values between 10 and 100, as observed for the films and single crystals in this study, an overall relative reduction in resistance of the sample between 0.95 and 0.75 can indeed be expected. Unfortunately, the uncertainty in the results reported here prevent quantitative comparison with this model.

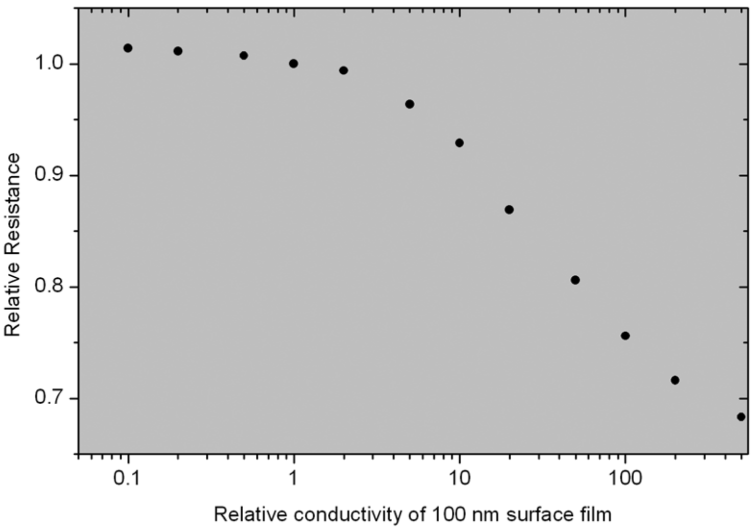

Figure 77. Net resistance of a single crystal that has a 100 nm thick film with a different conductivity on the surface. The resistance is relative to the case where the film has the same conductivity as the single crystal (i.e., homogeneous conductivity). The electrode geometry is that of pattern 14.

The grain boundary conductivity reported in Figure 57 is an effective conductivity, normalized to the sample geometry but not to the grain boundary geometry. More properly, one should compare a grain boundary area specific resistance, $\hat{R}$, given by

$$\hat{R} = \frac{d_G}{\sigma_{GB}} \tag{57}$$

where d_G is the average grain size and σ_{GB} is the grain boundary conductivity. This value represents the resistance of a unit cross-sectional area of a single grain boundary. If the grain boundary thickness were known, then the real or specific grain boundary conductivity could be determined[72]. Often, this thickness can be estimated from the relative capacitance of the grain and grain boundary semicircles according to

$$\delta_{GB} = \frac{C_G}{C_{GB}} d_G \tag{58}$$

where δ_{GB} is the grain boundary thickness, C_G is the grain capacitance, and C_{GB} is the grain boundary capacitance. The assumption inherent in this equation is that the relative permittivity of the grain and grain boundary is the same. Aoki, et al., used this technique and determined the grain boundary thickness in YSZ to be between 1-2 nm[72].

In this study, the sample geometries created very low grain capacitances. These capacitances were smaller than the parasitic capacitances of the substrates and the testing chamber. Thus, reliable values for C_G were not obtained. This prevents using the estimate of equation 58 to determine the real grain boundary conductivity. For this reason, the area specific grain boundary resistance is the main axis plotted in Figure 78. On the other hand, an estimate for the grain boundary conductivity is given in the secondary axis. This estimate is made using a thickness of 1 nm for the boundary thickness, roughly what was determined in reference 72. The unheated deposited YSZ9 films are not included in the figure, since cracking in the films led to a large amount of scatter in the data.

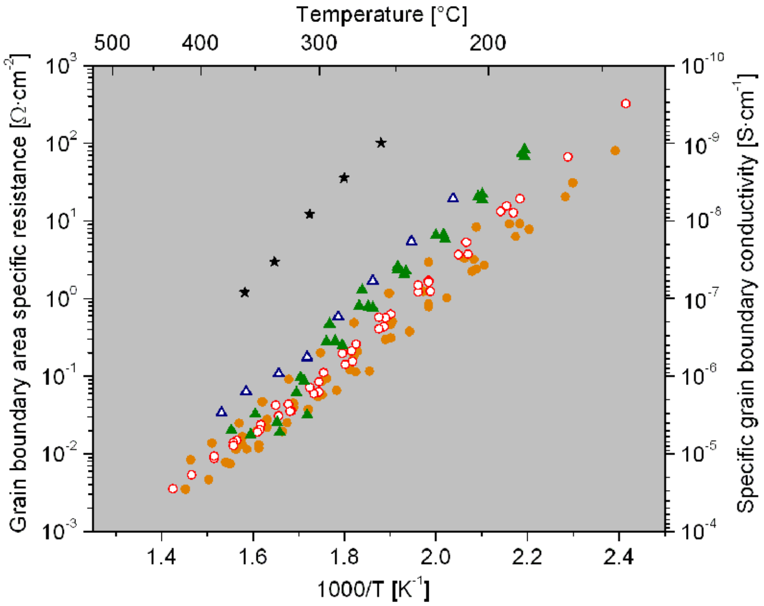

Figure 78. Arrhenius plot of the grain boundary area specific resistance. The specific grain boundary conductivity axis assumes a grain boundary thickness of 1 nm. ● = YSZ9 film deposited at 300°C; ○ = YSZ9 film deposited at 600°C; ▲ = YSZ16 film deposited unheated; △ = YSZ16 film deposited at 600°C; ★ = tapecast YSZ.

The grain boundary area specific resistance of the tapecast YSZ is much greater than that of the films. This is probably due to the fact that the tapecast specimen was sintered at high temperature and was not of high purity. Thus, the grain boundaries are likely to be highly impure and blocking to ionic conduction. In contrast, the films were made from high purity materials and never saw very high temperatures. Thus, their grain boundaries are likely to be highly pure and conductive.

As discussed in section 1.3.2, the grain boundary conductivity in highly pure YSZ is about a factor of 100-300 less than the conductivity of the grain. Using the estimated values from the secondary axis of Figure 78, the ratio of the grain boundary conductivity to the grain conductivity is plotted in Figure 79. The films have a grain boundary conductivity less than the grain conductivity by a factor of about 100, in good agreement with the results of reference 72. On the other hand, the tapecast specimen has a grain boundary conductivity less than the grain conductivity by a factor of about 500, consistent with reduced purity grain boundaries.

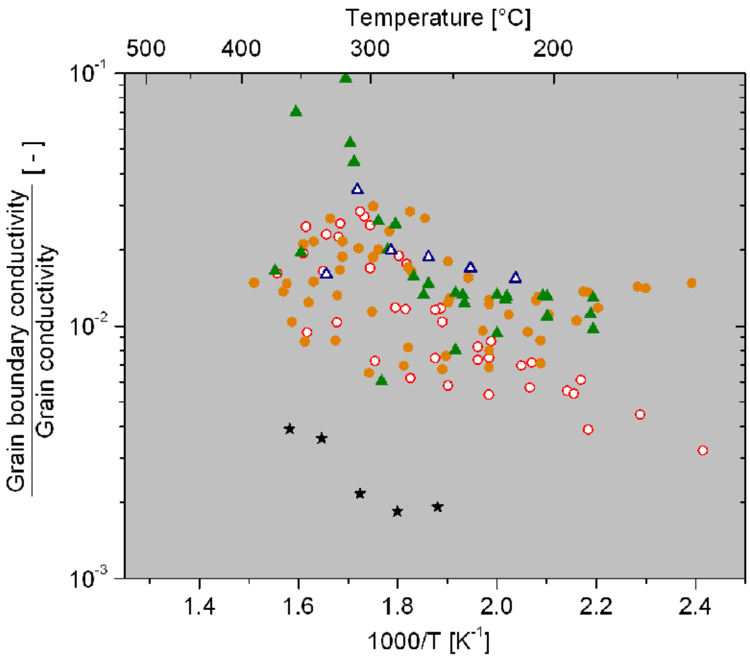

Figure 79. Ratio of the grain boundary conductivity to the grain conductivity of the films and polycrystalline bulk specimen. Symbols have the same meaning as in Figure 78.

Comparing the films, the grain boundary specific resistance of the YSZ9 films was less than that of the YSZ16 films below 400°C. This is the same behavior as the grain conductivity. It further indicates that lower dopant levels in the films are beneficial to higher conduction at reduced temperatures.

4.1.2 Constriction Resistance

The large constriction resistances seen in this work are not normally observed when characterizing bulk specimens. In some sense, the constriction resistance is rather large here only because the electrodes were intentionally sub-optimal for performance. The degree of constriction must be related to the ratio of the triple phase boundary width to the average electrode contact width. Electrode contact sizes are normally defined by the particle diameter of a granular electrode phase. These may be on the order of 1 μm or even less. In this study, the contact sizes were defined by lithography to be up to 100 times this size. Therefore, the observed large constriction resistance is expected in this situation.

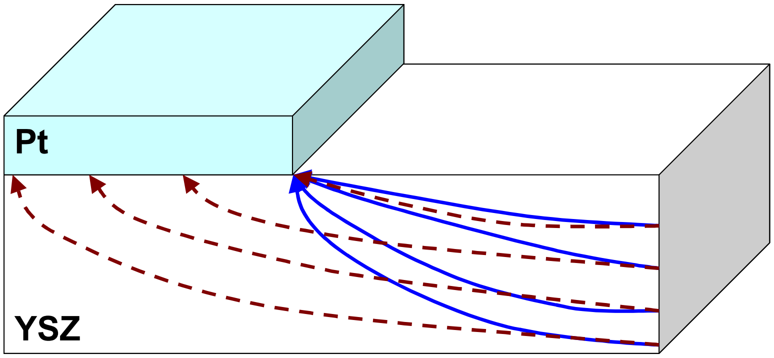

Figure 80. Schematic picture of the constriction resistance. The unconstricted current path is shown with dashed lines; the constricted current path is in solid lines.

The amount of constriction resistance can be estimated from the sample geometry. Fleig, et al., has estimated the resistance of thin electrolytes measured with dense, non-ionically conducting electrodes on the surfaces in a geometry nearly identical to those used in this study[36]. The equation derived, in slightly modified form to fit the definitions of the geometric terms used here, is

$$R \approx \frac{1}{\sigma \cdot x}\left[\frac{s}{t} + \frac{2}{\pi}\ln\left(\frac{t}{w_{TPB}}\right)\right] \tag{59}$$

where σ is the conductivity, x is the triple phase boundary length, s is the electrode spacing, t is the electrolyte thickness, and w_{TPB} is the radius of a semi-cylindrical triple phase boundary. The first term of the equation is the conventional, lateral resistance through the electrolyte film and the second term is the constriction resistance term. When $s >> t$, the first term dominates and constriction effects are minimized. This finding correlates well with the results found in this study, where the thin film on silica samples had relatively small constriction resistances.

The constriction term was derived with the assumption that the electrolyte is much thinner than the electrode spacing. An improvement to the equation can be made by allowing the thickness to be larger than the electrode spacing. In place of the thickness, the smaller of the thickness and the spacing can be used. The resulting equation is

$$R \approx \frac{1}{\sigma \cdot x}\left[\frac{s}{t} + \frac{2}{\pi}\ln\left(\frac{\min(t,s)}{w_{TPB}}\right)\right] \tag{60}$$

where min(y,z) is the smaller value of y and z. When $s < t$, signifying relatively thick electrolytes, the second term in this equation explicitly shows how the ratio of the triple phase boundary width to the electrode contact size affects the amount of constriction.

The predictions of these equations can be compared to more exact finite element calculations of the resistance. The finite element calculations were done as described in Appendix A. The comparisons are plotted in Figure 81. The resistance values are given in terms of a unit-less "geometric resistance," which is described in Appendix A. In plot (a), the finite element results for a 500 µm thick electrolyte across a range of electrode spacings are compared to equations 59 and 60. Equation 59 is expected to be a very poor prediction of this geometry, since the derivation assumed an electrolyte much thinner than the electrode spacing. The prediction of equation 60 is highly satisfactory. In plot (b), equation 60 is compared to the finite element calculations for a few electrolyte thicknesses. A very good match is found for the thin electrolytes, where equations 59 and 60 are identical and the constriction effects are less significant. As can be seen in the small electrode spacing region of the 5 µm electrolyte thickness line, the equation becomes less acceptable when the electrolyte thickness is similar to the electrode spacing. Nevertheless, the equations are instructive in gaining a qualitative understanding of the effects detailed in Figure 59.

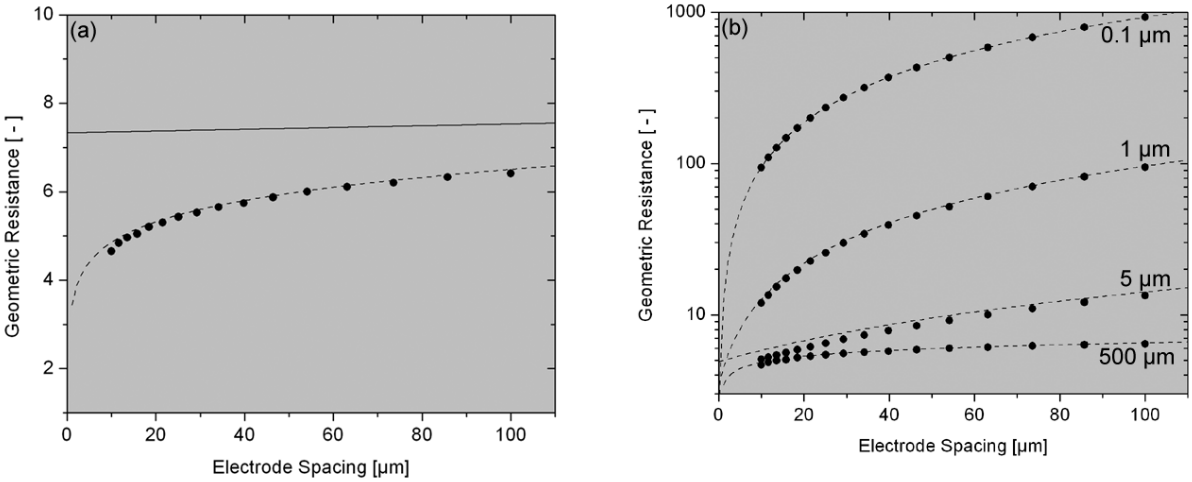

Figure 81. The calculated and predicted resistances of the electrolyte geometries employed in this study after accounting for constriction effects. Points are the finite element calculated resistance and dashed lines are the predictions from equation 60. The assumed triple phase boundary width was always 5 nm. (a) 500 µm thick electrolyte; the prediction from equation 59 is the solid line. (b) A range of thicknesses.

To achieve a more quantitative understanding, the finite element calculations can be compared to the measured constriction resistances. For a proper comparison, the ratio of the "total constricted resistance" (grain + grain boundary + constriction resistance) to the "unconstricted resistance" (grain + grain boundary resistance) is compared to the ideal ratio calculated from the finite element model. Three different triple phase boundary widths are used in the finite element calculation. These values are determined for a few relevant geometries in Table 9.

Table 9. The ratio of the total constricted resistance to the unconstricted resistance as measured and as calculated from the finite element model. Three different TPB widths are used in the models.

Electrolyte	Electrolyte thickness [μm]	Electrode Spacing [μm]	Measured resistance ratio [-]	Calculated resistance ratio [-]		
				w_{TPB} = 1 nm	w_{TPB} = 5 nm	w_{TPB} = 10 nm
Tapecast	500	100	26.4	3.73	3.22	3.00
Single crystal	500	50	14.7	3.55	3.03	2.81
Single crystal	500	25	2.74	3.29	2.78	2.56
YSZ film	1	100	1.32	1.01	1.01	1.01
YSZ film	1	25	1.61	1.08	1.06	1.05

Other than the single crystal with 25 μm electrode spacing, the measured resistance ratios are significantly higher than those calculated from the finite element model. This could be because the triple phase boundary widths assumed in the model are too large. This explanation is highly unlikely, however, since the smallest width modeled, 1 nm, is already nearing the size of a single unit cell. A more likely explanation is that the resistance is constricted in both lateral dimensions. This would be the case if not all of the triple phase boundary length was capable of current injection. Specifically, there may be only certain sites on the electrolyte surface that are capable of oxygen exchange with the electrode. Modeling this additional constriction would require a more complex 3-dimensional model.

Ideally, one could use the measured resistance ratios to derive an estimate for the triple phase boundary width. Determining this width has not been accomplished before, despite its importance for complete understanding of fuel cell performance. If there is 3-dimensional constriction, then the more complex model should allow determination of both the size and the average distribution of the active sites along the triple phase boundary length. This could prove extremely valuable in correlating the active sites with atomic or microstructural features.

The constriction resistance may be an important component of the ohmic polarization losses in a μSOFC. As demonstrated here, when the electrode reactions are limited to the triple phase boundaries, the actual electrolyte resistance can be much increased. Thus, electrodes that are structured natively or by lithography to the sub-micron level are needed not only for decreased activation polarization but potentially also for decreased ohmic polarization.

4.1.3 Electrode Activation Polarization

Combining the results of the physical and electrical characterization of Pt microelectrodes on YSZ surfaces, we can attempt to identify the rate limiting reaction step. The two most important results regarding the electrode activation polarization conductance were that the conductances were linearly proportional to the triple phase boundary length and the conductances of electrodes placed on unheated deposited films were orders of magnitude less than those on other electrolyte surfaces.

The large difference in activation polarization conductance can be largely but not completely explained through the presence or lack of silicon contamination on the surface. Both the single crystals and the very small grain sized films deposited at 600°C had a high electrode polarization resistance, so the cause cannot be merely the presence of grain boundaries on the surface. The cause also cannot be crystallographic orientation of the electrolyte, since both the low polarization resistance, unheated deposited YSZ9 films and the high polarization resistance, tape cast bulk YSZ had random orientation.

It can be concluded that the major source of surface silicon in this study is the HMDS photoresist adhesion promoter. This is deduced by comparing the XPS results of the as received YSZ single crystal, where there is no Si present; the YSZ single crystal after photolithography without using HMDS, where there is again no Si present; and the YSZ single crystal after photolithography using HMDS, where there is Si present. Photolithographic processing was successfully accomplished without the HMDS photoresist adhesion promoter, so removing the contamination is an easy problem to fix in the context of the processing route used in this study. It does not remove the generality of the results, however, since it was shown in section 1.3.3 that YSZ surfaces subject to standard, high temperature processing conditions are nearly always covered with Si.

The reason that the films deposited without substrate heating are not contaminated with silicon is unclear. The photolithographic process used with these films was the same as the rest, including the use of HMDS. It has been suggested that the silation of metal oxide surfaces by HMDS is accomplished by the reaction of HMDS with surface hydroxyl ions[177]. It is possible that the films sputtered onto an unheated substrate are in a non-equilibrium state that inhibits surface hydration. For example, the surface may be slightly nonstoichiometric with regard to oxygen.

Surface passivation by HMDS exposure has been shown to reduce the catalytic activity of Pt[178]. It should be emphasized, however, that in this work the HMDS exposure occurred well before the Pt was sputtered onto the substrate. For the Si to have poisoned the Pt surface would have required the silicate to travel from the YSZ surface onto the Pt at temperatures of only 450°C or below. This is unlikely. In addition, the Si contamination was commensurate with a change in the bonding state of oxygen. By XPS, the Pt was found to be largely unoxidized, thus the silicate must be on the oxide electrolyte surface.

The finding that the Si contamination correlated with changes in the oxygen bonding on the electrolyte surface is especially telling. Whatever effect the electrolyte surface has upon the electrode activation polarization, it almost certainly is due to the bonding state of surface oxygen ions and vacancies. The triple phase boundary exchange reaction can be considered as transfer of an oxygen and a vacancy between the Pt and YSZ surfaces:

$$O''_{ad}(Pt, TPB) + V_O^{\bullet\bullet}(YSZ, TPB) \leftrightarrow V_{ad}(Pt, TPB) + O_O^{\times}(YSZ, TPB) \quad (61)$$

with the forward direction describing the cathodic reaction and the reverse direction describing the anodic reaction. Si bonds strongly with oxygen and has few intrinsic vacancies. Therefore, a change in the oxygen bonding from Y/Zr-O to Si-O likely results in a drastic reduction in the number of oxygen surface vacancies.

The dependence of the activation polarization upon temperature and oxygen partial pressure is very similar for all of the samples measured. This is a strong indication that the effect of the silicon contamination is merely to serve as a blocking layer on the electrolyte surface. If the silicon participated in the exchange reaction, then a change in the activation energy and possibly also the oxygen partial pressure dependence would be expected.

As discussed in section 1.5, an activation energy of around 1.4 eV and a pO_2 dependence of ±½ are commonly found for the activation polarization resistance of Pt electrodes on YSZ surfaces. These values are similar to what was found in this study. The explanation for these values is that the rate limiting reaction step is the diffusion of oxygen on the Pt surface. This is not necessarily inconsistent with the results here, even though the Pt surfaces appeared to be nearly the same for all samples.

The rate limiting reaction step is believed to be either the triple phase boundary exchange reaction or the diffusion on the Pt electrode surfaces of oxygen to the electrochemical reaction sites at the triple phase boundary. As discussed above, Si contamination partially covers the surface of the YSZ and blocks the oxygen from accessing these reaction sites. The reduction in active sites would thus lead to both decreased triple phase boundary exchange reaction rate, and decreased diffusivity of oxygen adsorbed on the Pt surface. The decreased diffusivity occurs because the diffusion path would be limited to occur towards (and away from) the few remaining reaction sites. Effectively, the cross-sectional area of the diffusion path on the Pt surface is limited, and the resistance increases. This situation is given schematically in Figure 82. In fact, these two reaction steps are quite similar in the sense that both involve the breaking of a Pt-O bond and motion of the freed O to a neighboring vacant site. In that regard, a similar activation energy can be expected for these two situations. The pO_2 dependence found in this study was used in previous studies as proof of the rate limiting step being adsorbed oxygen diffusion. However, similar reasoning can also yield the dependence to be due to the TPB exchange reaction as the rate limiting step. This is because both reactions involve the exchange of $O_{ad}(Pt)$ for a $V_{ad}(Pt)$ and thus both reactions should have a $\theta(1-\theta)$ type dependence on the pO_2, where θ is the surface coverage of O on Pt. Essentially, the θ dependence comes from the cathodic reaction and the $(1-\theta)$ dependence comes from the anodic reaction.

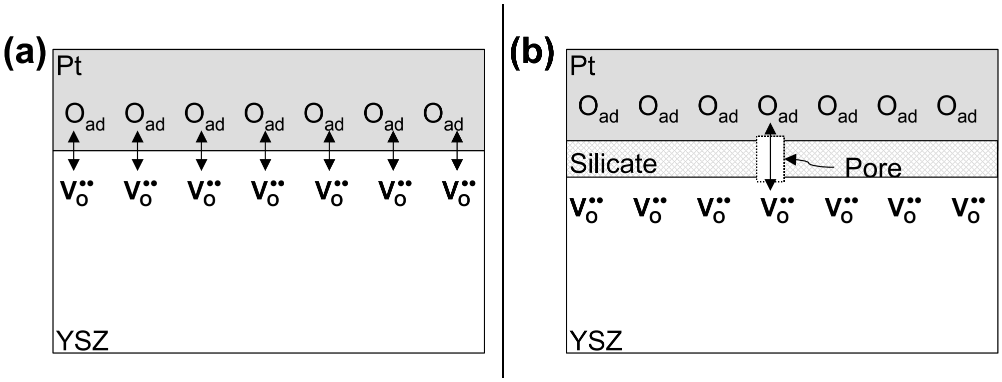

Figure 82. Diagram of the (a) high number of TPB reaction sites and wide cross section for O_{ad}(Pt) diffusion next to a clean YSZ surface and (b) low number of TPB reaction sites and narrow cross section for O_{ad}(Pt) diffusion next to a YSZ surface covered with a silicate. The term pore is used loosely, since the silicate is expected to be only an atomic monolayer in thickness and the pore might represent a gap between two silicate islands.

It is not entirely determined from this work which of these two reactions is rate limiting. On the other hand, if the rate limiting reaction step is oxygen diffusion on the platinum surface, then the impedance feature associated with it would likely not appear as a semicircle or be well-simulated by a pseudo-R-C circuit. Specifically, at high frequencies, a linear region with a 45° slope to the real axis should be found. Processes of exactly this type are described in detail by Adler as being technically co-limited by the adsorption and diffusion reactions[18]. This is termed Cottrell behavior, and is very similar to the Warburg behavior found with purely diffusional processes. Neither of these behaviors was witnessed in this study, thus the TPB exchange reaction, equation 61, is believed to be the rate limiting step.

The mere presence or lack of Si contamination is not fully sufficient to explain the obtained results. Though all of the samples with Si contamination on the surface had a low polarization conductance, not all of the samples without Si contamination had equally high conductance. For example, the single crystal sample that was etched in HF indeed shows an increased polarization conductance by a factor of nearly 100, however the single crystal sample produced without HMDS—also a Si free surface—exhibited only a small increase in conductance. Another comparison can be made between the YSZ9 and YSZ16 films deposited unheated. The films are both randomly oriented, have similar grain sizes, and lack Si contamination. Yet, the activation polarization conductance is different by a factor of about 30.

An explanation for these effects may be that there are preferential electrochemical reaction sites on the YSZ surface. These are possibly found at surface structural defects like corners, edges, kinks and steps. By this argument, the Si contamination increased the activation polarization resistance not so much because it blocked the YSZ surface generally, but because it blocked the access to these highly active sites.

Such surface features have recently been correlated with the catalytic activity of YSZ for N_2O decomposition[179]. The same study also found that oxygen at these sites desorbed at lower temperatures than at sites with higher coordination number. Unfortunately, little is known about the surface structure of YSZ (see reference 180 for an ab initio structure determination of the primary surfaces), and furthermore it is unknown to what degree the data that has been presented in the past is compromised by surface segregation and contamination.

In this work, the unetched single crystal was highly smooth and thus likely had very few surface states like corners, edges, etc. On the other hand, the etched single crystal was found to be highly roughened and likely had more of these features. A difference in concentration of surface defects may explain why the etched crystal had such higher polarization conductance.

Similarly, the difference in electrode polarization between the YSZ9 and YSZ16 films may be due to a difference in the concentration of surface defects. Since these concentrations are close to the morphotropic phase boundary, the small change in dopant concentration may have changed the growth mechanism and altered the surface structure.

Another possible explanation for this difference is that the concentration of mobile oxygen vacancies on the surfaces are different. At the measurement temperatures used, the higher dopant concentration in the YSZ16 is known to lead to vacancy ordering. This fact is demonstrated in the increased activation energy of grain conductivity for these films. It should be noted, however, that the HF etched single crystal, with a polarization resistance between that of the YSZ9 and YSZ16 films, had a higher surface dopant concentration on the surface than either one.

The notion that only certain sites along the triple phase boundary are active is consistent with the finding that the constriction resistances were larger than a simple 2-dimensional constriction can account for. If the exchange reaction can only occur where the triple phase boundary intersects a surface ledge, for example, than the degree of current constriction would be much larger—in some way correlated with the inverse of the surface ledge concentration. Consistent with this, the etched single crystal had a ratio of constricted to unconstricted resistance of about 1.6 compared to a ratio of about 2.3 for the unetched single crystal processed without HMDS. By this theory, this result indicates a lower concentration of electrochemically active defects on the surface of the unetched crystal.

4.1.4 Power Output from a SOFC with Pt Electrodes

The power output expected from a fuel cell with YSZ electrolyte and Pt electrodes can be estimated from the electrode polarization resistances. The estimates made in Figure 25 can be extended to include this electrode data for the samples measured in this study. These estimates allow an approximation of the resolution of lithography needed to achieve 0.1 W·cm^{-2} using dense Pt electrodes on YSZ surfaces. This is plotted in Figure 83 for the electrolyte surfaces in this study that exhibited the highest and lowest polarization resistance. As mentioned in section 1.5, even the best values from the literature have little chance of being capable of sufficient power output at 400°C. The lithographic resolution required is simply too fine: at best 100 nm, but in the worst case below physical limits. The close agreement found between the tapecast standard measured here and the best literature values are comforting as a validity check on the results, though not as a solution to this problem. On the other hand, the much increased conductance measured with electrodes placed on the YSZ9 films deposited on an unheated YSZ single crystal suggest a promising solution. At 400°C, the results suggest that lithography at the level of 1-2 μm should be sufficient to obtain 0.1 W·cm^{-2} and patterning at the 100-200 nm level should prove sufficient for 1 W·cm^{-2}.

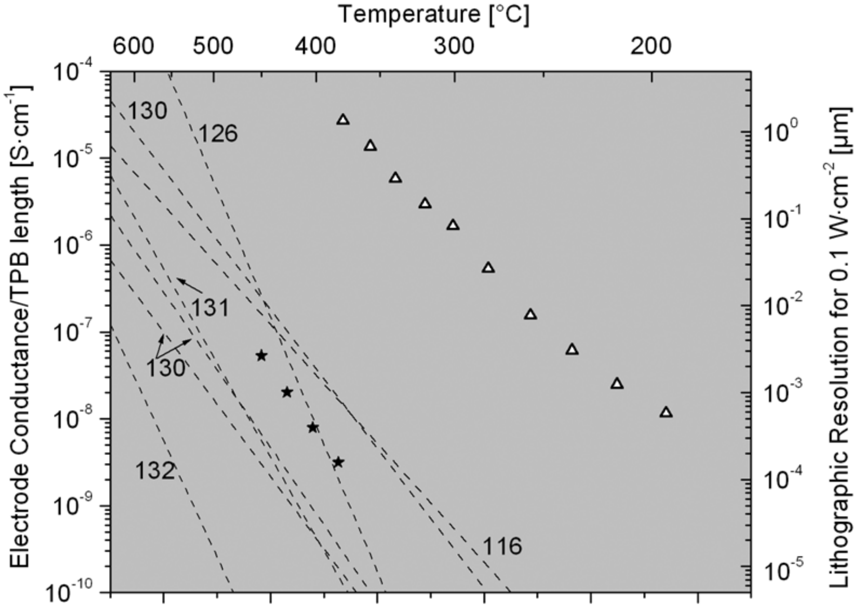

Figure 83. The electrode polarization conductance normalized to the triple phase boundary length for the best and worst electrolyte surfaces measured in this study. Dashed lines are fits to the literature values plotted in Figure 25; numbers indicate the reference. ★ = tapecast YSZ; △ = YSZ16 film deposited at 600°C.

These results can be plotted in an alternate fashion—instead of determining the temperature at which a set power level is possible, one can examine the power outputs possible at a set temperature.

Interpolating all of the data to a constant temperature, 400°C, the measured polarization conductance is plotted as a function of the triple phase boundary length in Figure 84. The triple phase boundary axis is extended from the very small values used in this study to the large values that are useful in a real device. Plotting in this manner allows comparison with the complex, composite electrodes more typically used in SOFCs. The right axis relies upon the estimate of equation 49 while the top axis uses the estimate of equation 48. Two of the best cathodes processed by traditional means reported in the literature are included as the horizontal dashed lines. The triple phase boundary length of these electrodes is determined by the processing conditions, and so is not capable of being directly modified. Because these are thick, porous electrodes, they are presumed to have very high triple phase boundary length per unit of projected surface area. The lines are placed at the reported conductance per cm^2. Both papers report the power output per cm^2 for fuel cells constructed with these cathodes. These values agree fairly well with the estimate used to construct the right axis. Also included is the data reported by Radhakrishnan, et al., for Pt and LSM cathodes with defined triple phase boundary lengths. These are plotted with a slope of one since triple phase boundary length specific conductances were determined in these studies.

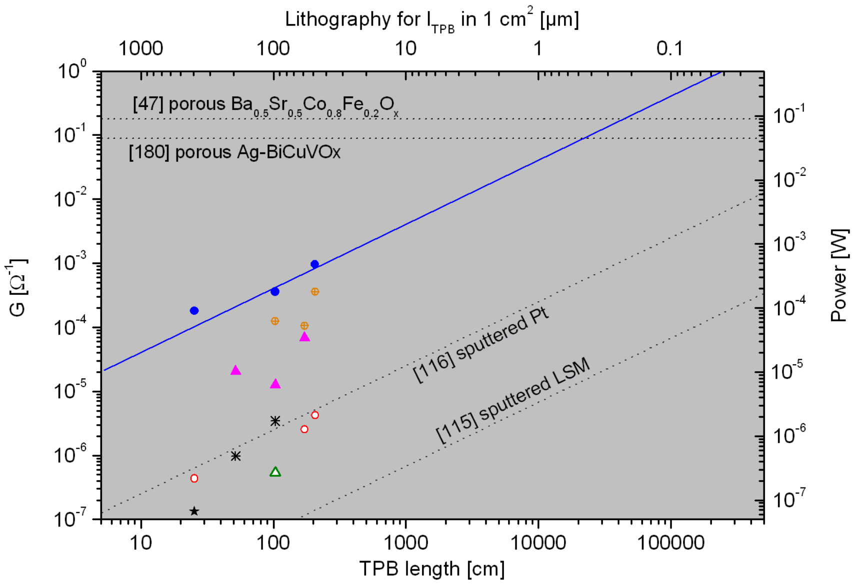

Figure 84. The electrode activation polarization conductance at 400°C as a function of triple phase boundary length. Dotted lines correspond to literature data (number indicates the reference). The diagonal dotted lines are for Pt and LSM electrodes with controlled TPB length. The horizontal dotted lines are two of the best reported cathodes produced by traditional means. The solid line is a linear fit to the best performance electrodes in this study. ● = YSZ9 film deposited on an unheated silica substrate, ⊕ = YSZ9 film deposited on a 300°C silica substrate, ○ = YSZ9 film deposited on a 600°C silica substrate, ▲ = YSZ16 film deposited on an unheated silica substrate, △ = YSZ16 film deposited on a 600°C silica substrate, ✱ = (100) oriented single crystal YSZ, ★ = tapecast YSZ.

Figure 84 suggests that 1 μm lithography can create Pt electrodes with 10,000 cm of triple phase boundary length in 1 cm^2 area. If this electrode is placed on a YSZ9 film deposited on an unheated silica wafer, then a fuel cell can be expected to achieve around 0.01 W·cm^{-2}. At a lithographic resolution of 0.25 μm, which is achievable in relatively conventional processing, this single layer electrode is expected to perform as well as the best composite cathode reported in literature. Finally, power outputs approaching 1 W·cm^{-2} may be achieved at only 400°C before physical limits are reached.

One must be careful when extrapolating trends, as done in Figure 84. For this extrapolation to be valid, the rate limiting step must be the same across the entire range. Literature measurements were nearly always collected with electrodes having orders of magnitude greater triple phase boundary length per unit area. Thus, similarities between the activation energies and pO_2 dependences of the electrode activation polarization measured here and reported in much of the literature suggests that the rate limiting step is indeed the same at higher triple phase boundary length densities.

The use of lithography to create the triple phase boundaries is a bit heavy-handed. In truth, such well-defined electrode geometries are not needed in a device. A simpler and cheaper processing method may suffice. In that regard, simple processing routes to create porous platinum films with sub-micron pore sizes are of interest (e.g., reference 182). Processing in this way is highly promising to not only reduce cost but also to obtain triple phase boundary lengths that match or exceed what can be produced via photolithography. If such a film can be produced with grain and pore sizes of about 100 nm, Figure 83 suggests that YSZ9 films grown on unheated substrates can enable 0.1 W·cm^{-2} at less than 300°C.

4.2 Performance of Composite Platinum – Yttria Stabilized Zirconia Electrodes

The electrode polarization resistances of the composite platinum-YSZ thin film microelectrodes placed on single crystal YSZ substrates were roughly proportional to the inverse of the electrode radius squared. As discussed in section 1.4.3, this strongly indicates that the electrode reaction is occurring over the entire surface area of the electrode, and not just at the perimeter. Thus, the processing method was successful in creating bi-continuous networks of Pt and YSZ, with triple phase boundaries distributed over the surface.

The performance of the composite electrodes can be compared to the dense Pt electrodes used in the other part of this work. Figure 85 repeats Figure 84, but adds the conductance (per 1 cm^2) of the Pt-YSZ films. These are plotted as horizontal lines, since the triple phase boundary length is set by the processing conditions and could not be changed by trivial means. The polarization conductance of film 3 approaches that of the best reported cathodes. This is somewhat remarkable, since the cathodes in the literature are thick and porous, with the capability of extending the triple phase boundary away from the planar interface with the electrolyte. On the other hand, the Pt-YSZ composite films only have a single plane in which to support triple phase boundaries on the surface, since they are dense.

Nevertheless, the films significantly under-perform relative to expectations. The expected electrode polarization conductance from the Pt-YSZ films can be estimated by taking the grain size of the films as the lithographic resolution in Figure 85. The surfaces are Si free, thus they should fall on the solid line extrapolated from the YSZ9 films deposited without substrate heating. The grains are around 30 nm, leading to an expected conductance about 2.5-3 orders of magnitude larger than what was observed (and an expected power output capability of nearly 1 W·cm^{-2} at 400°C). The similarity in activation energy between the composite electrodes and the dense Pt electrodes suggest that the rate limiting process is the same in both, and thus the extrapolation should be valid.

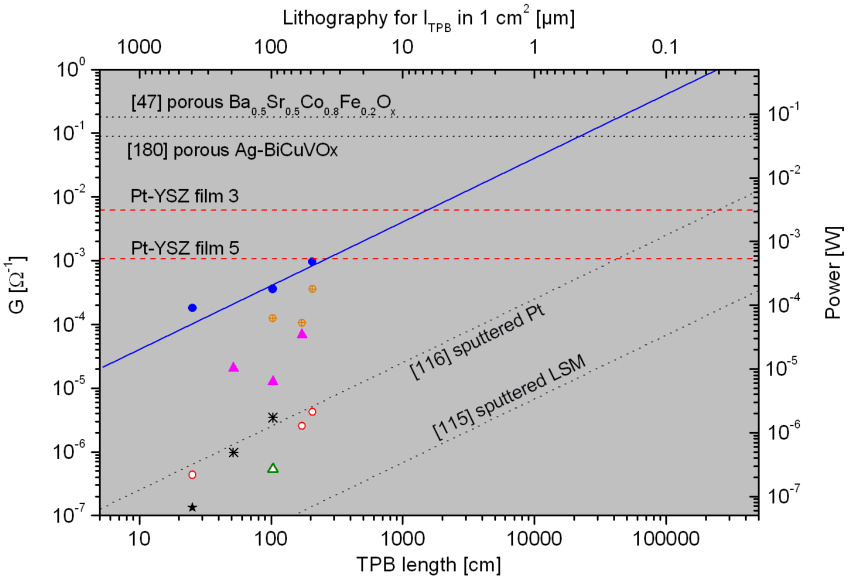

Figure 85. The electrode activation polarization conductance at 400°C, including the Pt-YSZ composite films. The lines and symbols carry the same meaning as in Figure 84.

One reason the films so seriously under-perform is because the microstructure needs to be optimized. Proof of this comes from comparing film 5 and film 3. The composition of the film 5 electrodes was nearly 50% Pt and 50% YSZ, by volume. The film 3 electrodes were around 40% Pt and 60% YSZ. Therefore, one would expect that the film 5 electrodes would have longer triple phase boundary length and thus higher polarization conductance than film 3. Unfortunately, this was not the case.

This likely indicates that the either the percolation of the YSZ phase was a problem or that Pt impurities in the YSZ phase interrupted the charge transfer at the triple phase boundary. The first possibility implies by percolation theory that the YSZ phase forms into larger grains, and thus a higher proportion of the film volume must be YSZ to ensure YSZ percolation. In film 5 then, there is less YSZ and some of the triple phase boundaries are effectively inaccessible because they involve YSZ islands. This argument, however, runs counter to the finding that the XRD peaks in film 5 show well crystallized Pt and very small grained (nearly amorphous) YSZ.

It is more likely the case that the YSZ is interrupted by the presence of Pt. One drawback to the co-sputtering technique is that the phases are essentially atomically mixed in the vapor phase. The technique relies on the surface diffusion of arriving species to create phase segregation during deposition. This process appears to be frustrated in film 5, since the YSZ has difficulty segregating and crystallizing even at 500°C. In contrast, the Pt and YSZ phases in film 3 appears to be well crystallized. It is therefore believed that the YSZ surface is riddled with Pt species that decrease the amount of electrochemically active sites at the triple phase boundary. This is similar to the effects of Si found in the previous part of this dissertation. A solution to this problem might be found in either increasing the deposition temperature or lowering the deposition rate. Either of these will give the species arriving at the substrate a larger mean diffusion distance. This will increase the purity of the YSZ surface and increase the triple phase boundary exchange rate.

Finally, the films created in this study can be used in conjunction to create, in a single deposition run, a microfabricated solid oxide fuel cell. Such a thin film stack is shown in cross section in Figure 86. The entire stack is just over 1 μm thick, making it likely the thinnest fuel cell ever produced. The results given above suggest significant power outputs can be expected from this device.

One of the benefits of this device is that the Pt-YSZ film can be used as both anode and cathode, since these materials are stable in both oxidizing and reducing environment. Indeed, Pt is known to be catalytic to both oxidation and reduction reactions. With the same material on both sides of the electrolyte film, the thermal expansion coefficient of the stack is symmetric. This is important because, in order to allow gas access to both electrodes, the stack must be made into a freestanding membrane. If there is a gradient in thermal expansion coefficient, bending stress may lead to high stresses and possibly fracture. Testing of the mechanical and electrochemical properties of integrated μSOFC devices employing these membranes is ongoing[183].

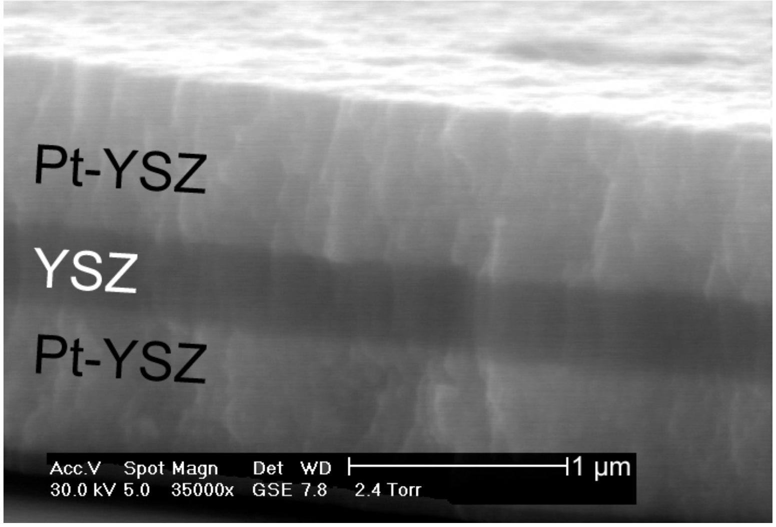

Figure 86. Scanning electron micrograph of a cross section of an anode-electrolyte-cathode µSOFC stack produced by sequential deposition of the films created in this study.

CHAPTER 5. CONCLUSIONS

5.1 Summary

This dissertation described research into methods of understanding and, ultimately, improving the solid oxide fuel cell reaction using microfabricated films and structures. The application of the work was in improving the power output from solid oxide fuel cells of both traditional and portable size scales. For both of these devices, reduced operating temperatures are desirable to reduce operating costs and improve device lifetime. Microfabrication methods were used not just to improve the electrode kinetics, but also to systematically quantify them. This information can be used to design optimal electrodes that can be used at reduced temperature and thereby allow solid oxide fuel cells to be an economically competitive energy solution at both stationary and portable size scales.

The first microfabrication method used dense platinum thin film electrodes with well controlled geometry on the surface of bulk YSZ standards and YSZ thin films. Sputter deposition was used to produce the dense YSZ thin films. These samples were electrically characterized using impedance spectroscopy to determine not only the electrolyte conductivity but also the triple phase boundary length-specific electrode activation polarization resistance.

YSZ films of composition $Y_{0.09}Zr_{0.91}O_{2-x}$ were found to have an enhanced ionic conductivity by as much as a factor of 20-30. This is believed to be due to nanometric grain sizes creating metastable cubic morphology and leading to reduced defect interactions. All of the films were found to have significantly reduced grain boundary resistance compared to the bulk polycrystalline sample. This was believed to be due to very low impurity content of the film grain boundaries. In all cases, the electrolytic resistance of a thin film electrolyte is expected to be insignificant compared to the electrode polarization resistances in a SOFC.

A constriction resistance was found for all of the samples at low frequencies. This resistance was due to the very large electrode contacts compared to the triple phase boundary width. The dependence of the constriction resistance could be qualitatively understood from finite element modeling. The amount of constriction was consistently larger than theoretically calculated, however. This is believed to indicate a 3-dimensional constriction, with only certain sites along the triple phase boundary being active for the exchange reaction.

Concerning the electrode polarization resistance, it was found that the electrodes placed on bulk standards and films deposited at high temperatures matched the best values from the literature. The resistance decreased further by a factor of up to 300 when the electrolyte surface was a film deposited at reduced temperature. X-ray photoelectron spectroscopy revealed the cause of this to be silicon contamination on the surface of the electrolyte. In this study, the source of the silicon was a chemical used in the photolithographic processing of the platinum electrodes, but silicon contamination on the surface of YSZ electrolytes is a known and common phenomenon after high temperature sintering of the ceramic. These measurements are possibly the first electrochemical characterization of nearly silicon-free YSZ surfaces.

The rate limiting step in the electrode reaction is believed to be the exchange of adsorbed oxygen on the platinum surface with an oxygen vacancy on the YSZ surface. This determination was based upon the activation energy and pO_2 dependence of the electrode polarization resistance and the shape of the impedance curve. Diffusion of adsorbed oxygen on the Pt surface is another possibility for the rate limiting step. Electrochemically active sites are believed to be non-uniformly present on the YSZ surface. Rather, they are believed to occur at surface defects such as ledges, kinks, etc. This explains the larger than expected constriction resistance and the decrease in electrode polarization resistance following the etching-induced roughening of a single crystal surface.

The second microfabrication method used was reactive co-sputtering to produce composite Pt-YSZ thin films with a bi-continuous network morphology and grain sizes on the order of 30 nm. Such intimate mixing of the electronic and ionic conducting phases created an effective mixed ionic-electronic conductor with the entire surface of the film electrochemically active to the electrode reaction. The composition of the films, in terms of Pt to YSZ ratio, was successfully controlled by adjusting the sputtering powers used on the targets. The best processing conditions resulted in electrodes with an area specific polarization resistance less than 500 $\Omega\cdot cm^2$ at 400°C and, by extrapolation, 10 $\Omega\cdot cm^2$ at 511°C and 1 $\Omega\cdot cm^2$ at 608°C. These films may enable operation of a micro-solid oxide fuel cell at intermediate temperatures (400-500°C). On the other hand, the composite films under-performed their expectation by 2.5-3 orders of magnitude, based upon predictions from the Pt microelectrode data of the first portion of this dissertation. There is likely a great deal of microstructural optimization still possible with these films.

5.2 Recommendations for Future Work

There are a number of questions raised by this work. Some of the more promising avenues that are recommended for future study are:

- Examine the dopant concentration effects on film conductivity and electrode activation polarization by measuring films with a range of dopant levels, especially lower levels since in this study YSZ9 had better performance than YSZ16.
- Examine the effects of the high stress state within the sputtered films upon the electrical and

electrochemical properties by, for example, undertaking measurements at controlled temperature and applied stress in a high temperature Instron machine.

- Confirm the meaning of the pO_2 measurements by blocking the O_{ad}(Pt) sites. This could be done by introducing into the measurement chamber CO or another gas species that strongly adheres to the Pt surface. This should shift the $\theta = ½$ point to higher pO_2.
- Determine the triple phase boundary width and/or distribution of electrochemically active sites on the surface of YSZ by combining constriction resistance measurements with more complete and detailed modeling. Perhaps more optimal electrode geometries for this purpose could be determined. The key to the approach is the combination of impedance spectroscopy and electrodes that have low triple phase boundary length per unit area. The former enables the deconvolution of the constricted from the unconstricted resistance while the latter ensures that the constricted resistance is significantly larger than the unconstricted resistance.
- Optimize the Pt-YSZ composite films for microstructure, phase composition, and grain sizes. Estimating the triple phase boundary lengths of the composite films, and comparing to the expected performance per unit of triple phase boundary length as found with the interdigitated Pt electrodes, suggest that the performance of the composite films can be vastly improved.
- Examine other potential applications for the composite films. These films may be useful not just as fuel cells for solid oxide fuel cells, but also in gas sensors or as thin film oxygen permeation membranes.
- Improve the performance of co-sputtered composite film electrodes by incorporating materials with better catalytic activity and/or conductivity. For example, Mazanec suggests $In_{0.95}Pr_{0.025}Zr_{0.025}O_x$ -YSZ can support a very high oxygen flux[184].

APPENDIX A. NUMERICAL SOLUTION OF RESISTANCE

A.1 Theory

Typical samples used to measure the conductivity of a solid material have a parallel plate or bar geometry. Either of these situations yields a simple relationship between the resistance and conductivity:

$$\sigma = \frac{l}{R \cdot A} \tag{62}$$

where σ is the conductivity, l is the path length of the current, R is the resistance, and A is the cross-sectional area of the current path. This relationship can be derived analytically. Similar expressions can be derived for other geometries, especially when symmetry arguments reduce the geometry to a simple form. A few important examples of these relationships for other geometries are derived in reference 185. Interdigitated geometries have been examined by a few studies[186-188], but none could be directly applied to the samples used here. Samples with less symmetric geometries and/or heterogeneous material properties are often incapable of yielding an analytic expression similar to equation 62. In these situations, numerical methods must be used.

One such method is finite elements[189-191]. First, the sample geometry and boundary conditions are expressed in a format understood by the computer. The geometry is then broken into a mesh of small, usually triangular elements. On each of these elements, a discretized and simplified form of the governing partial differential equation is solved. Continuity is forced at the edges of neighboring elements to create a solution that is continuous over the whole geometry. Solutions at element edges on the border of the geometry are set by the boundary conditions. The partial differential equation used for electrical conductivity is Poisson's equation:

$$-\nabla \cdot \sigma \nabla \phi = 0 \tag{63}$$

where ϕ is the spatially-varying potential. This equation is an alternate expression of Ohm's law, $J = \sigma \cdot E$.

To determine a structure's electrical resistance, Poisson's equation is solved to determine the steady state electrical potential as a function of position within the structure. The current density at any point is then found by multiplying the gradient of the voltage by the conductivity. The total current flowing through the structure is determined by integrating the current density over an equipotential line. Thus the voltage and current through the structure is found, and the resistance is calculated from their ratio.

The finite element method used in this dissertation was implemented in MATLAB, using the partial differential equation toolbox. A parallel plate arrangement was first used as a validity check for the method. The resistances of structures with various conductivities and parallel plate geometries were calculated with MATLAB code similar to what is presented below. The resistances derived successfully matched the known relationship of equation 62.

The geometry of samples in this dissertation is interdigitated electrodes, shown schematically in Figure 87(a). Ignoring edge effects, this can be reduced to a 2-dimensional geometry by slicing down the dashed line shown in this figure. The cross-section is shown in Figure 87(b) with + and – signs indicating electrodes of alternating polarity. This structure is further reduced by the translational symmetry of the electrodes, slicing again down the dashed lines. The resultant single +/- electrode junction is shown in Figure 87(c). Finally, the anti-symmetry of the voltage can be exploited by solving only half of this arrangement to reach the structure shown in Figure 87(d).

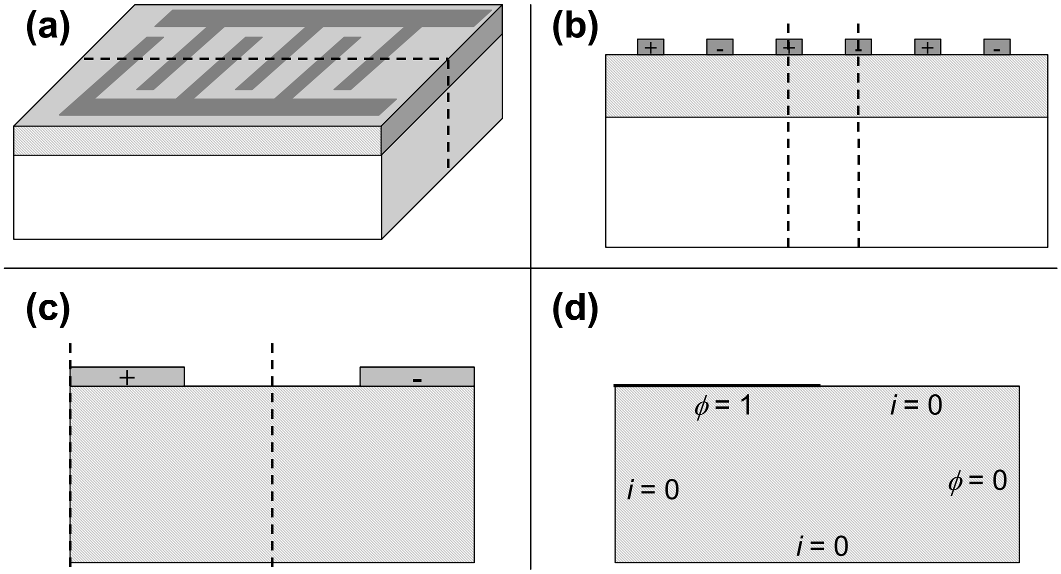

Figure 87. The geometry used to model the resistance of interdigitated electrode samples, in successive stages of reduction by symmetry. (a) The complete sample geometry, (b) geometry reduced to a cross-section, (c) geometry reduced by the mirror symmetry of the voltage, and (d) geometry reduced by anti-symmetry of the voltage. In parts (a) – (c), the dashed lines border the section shown in the subsequent part of the figure. In part (d), the boundary conditions for the unconstricted resistance are given. *i* refers to the current normal to the boundary.

Figure 87(d) shows the boundary conditions used for the unconstricted resistance. At the bottom edge of the electrolyte, the current normal must be zero. This is the case for both the bulk samples, where this edge is the bottom of the sample, and for the films on silica substrates, where there is assumed to be zero current in the substrate. The normal current also must be zero on the left edge due to the symmetry of the electrode. The left half of the upper edge represents the electrode/electrolyte interface. It is held at a voltage of 1 V for this model. The electrolyte/air interface found on the right half of the upper edge must have a normal current of zero. Finally, the right edge is the line of anti-symmetry in the voltage, and so must have a voltage of 0 V. Since the electrode was given a voltage of +1 V, the antisymmetric electrode, not shown, must have a voltage of -1 V. Thus, a total voltage of 2 V is applied in this model.

The electrolyte thickness and the electrode spacing defined the geometry of the sample. For the sample geometries important to this study, the electrode spacing was equal to the electrode finger width. Given a particular geometry and a nominal conductivity of 1 $S\cdot cm^{-1}$, the code given in section A.3 derived the spatially varying voltage and thus the current.

Dividing the total 2 V applied by the resultant current gave a 2-dimensional "geometric resistance." To convert this value back to a 3-dimensional form, the geometric resistance had to be divided by the total length of the sample in the direction perpendicular to the cross-section. The conductivity of a real sample could then found by dividing this value by the measured resistance:

$$\sigma = \frac{R_{geom}}{x \cdot R_{meas}} \tag{64}$$

where R_{geom} is the 2-dimensional geometric resistance derived from the model, x is the triple phase boundary length of the electrode, and R_{meas} is the measured sample resistance. This model was run for the film and bulk electrolyte thicknesses across the range of electrode geometries employed. The geometric resistances derived were then used to convert the measured resistances to the grain and grain boundary conductivity values reported.

To examine the effects of constriction resistance, the boundary conditions were slightly modified. The electrode/electrolyte interface in this situation can no longer support current flow and so was maintained $i = 0$. Instead, a small triple phase boundary region was added at the electrode edge. It was made semicircular in shape and the radius was examined as a third geometric input variable. This is implemented in the code in section A.4.

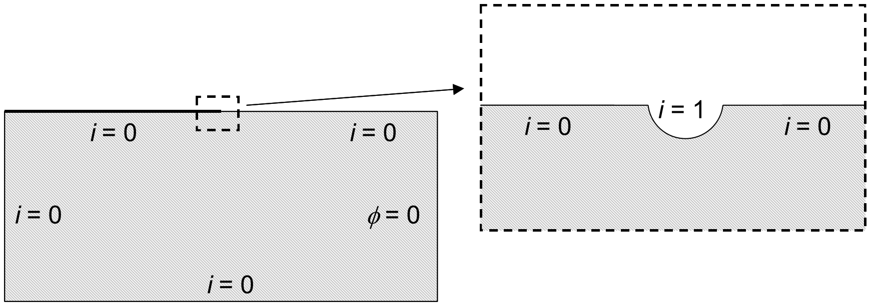

Figure 88. The boundary conditions used to model the constricted resistance. *i* refers to the current normal to the boundary.

A.2 Results

In all finite element modeling, there is a trade-off between accuracy and computation time. Often, this trade-off is determined by the size of the elements. The code below employed an adaptive meshing scheme. This scheme first derived a solution on a coarse mesh, meaning large elements and thus poor accuracy but quick calculation. It then refined the mesh into smaller elements only in locations of high solution gradients. These locations are expected to contain the largest errors. A solution was then found with this refined mesh, the mesh was further refined, and so on. This technique significantly reduced processing time but the number of mesh refinement generations still had to be controlled. To determine the number of generations needed, a resistance was calculated as a function of the number of mesh generations employed. A constricted geometry was chosen, since large voltage gradients made it more susceptible to discretization error.

Figure 89 shows the results of this experiment. The resistance calculated with the finest mesh (21 refinement generations) was taken as the standard value. The error in the other calculations, relative to the standard resistance, is plotted. As can be seen, convergence was achieved rapidly. In order to err on the side of caution, 15 refinement generations were used for all calculations. This typically resulted in a calculation time of about 1 minute per geometry.

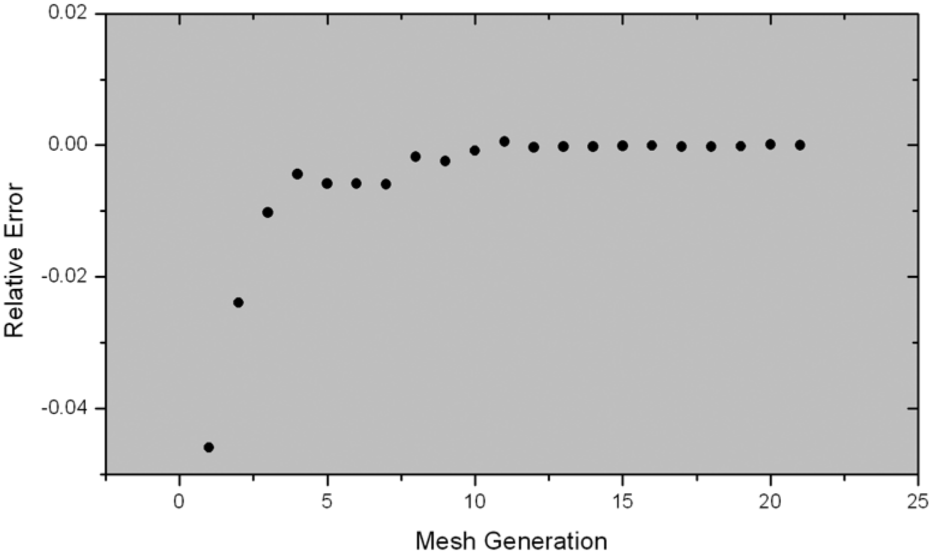

Figure 89. The relative error in the resistance of a constricted geometry, calculated as a function of the number of adaptive mesh refinement generations. The standard resistance value, from which the errors are calculated, is the resistance at mesh generation 21.

Figure 90 shows the voltage as a function of position for two different geometries within the portion of the electrolyte displayed in Figure 87(c). The "electrodes" are on the top surface, +1 V on the right side and –1 V on the left. The geometry plotted in (a) and (b) is more typical of the bulk samples while that plotted in (c) and (d) are similar to the thin films on silica substrates. The color indicates the voltage; red is +1 V and blue is –1 V. Arrows plotted indicate the direction of current and, by their length, the local current density. Unconstricted resistances are shown in parts (a) and (b), while constricted resistances are shown in parts (c) and (d). A few comparisons can be made. First, the current flows mainly through the top portion of the thick samples, whereas the thin samples have fairly uniform current density throughout the thickness. Second, the effect of the constriction resistance is fairly severe for the thick electrolyte, less so for the thin electrolyte. Most of the electrolyte in plot (b) is at a moderate voltage, with the bulk of the voltage drop (i.e., color gradient) found in the local vicinity of the triple phase boundary. In comparison, plot (d) is fairly similar to the unconstricted plot (c), with the bulk of the voltage drop remaining between the electrodes.

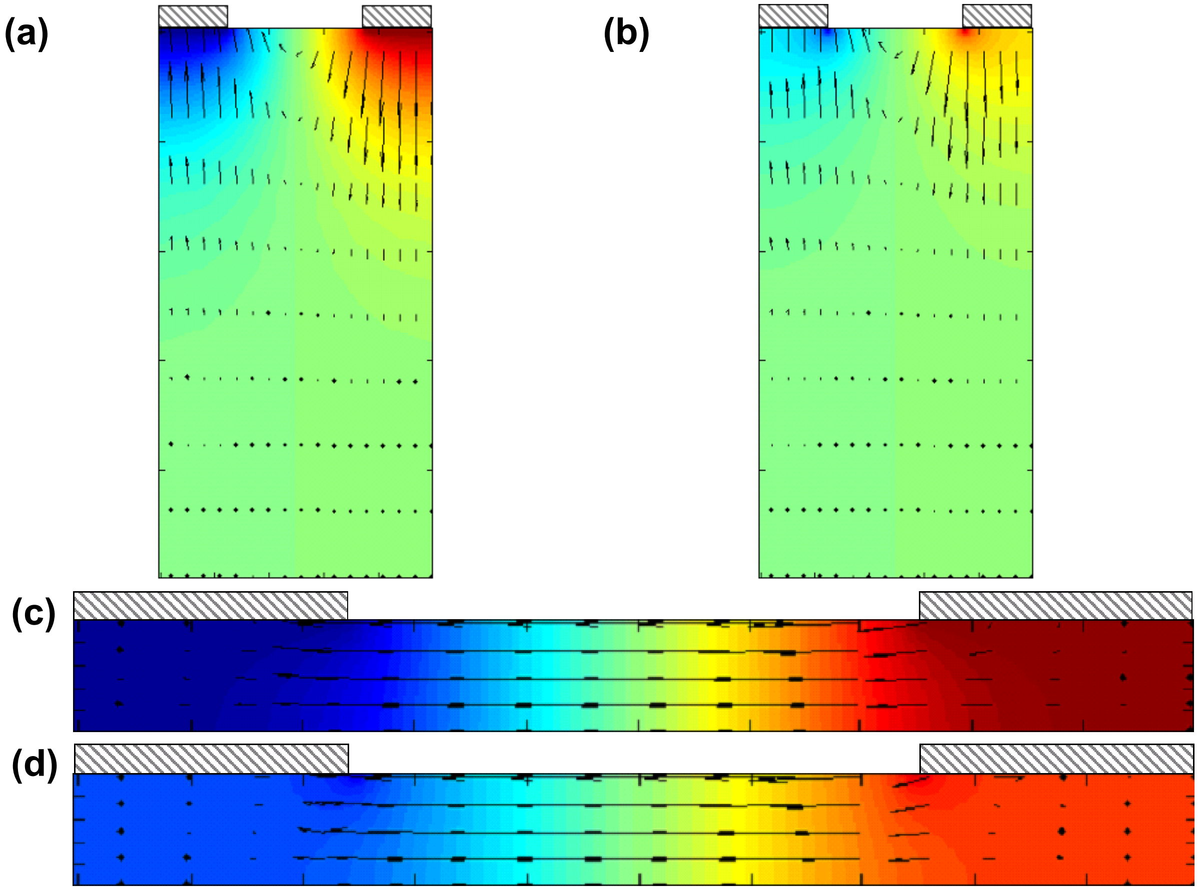

Figure 90. Spatially variant voltage within the portion of the electrolyte displayed in Figure 87(c), as calculated by the finite element method. The hashed areas represent the electrodes. Color represents the voltage. Arrows show the direction and the density of current. Plotted are (a) and (c) unconstricted current paths and (b) and (d) constricted current paths. Plots (a) and (b) have a geometry more alike the bulk samples, while plots (c) and (d) are more like the thin film on silica substrate samples.

The geometric resistances calculated for a few example geometries are shown in Table 10. As may be expected from the Figure 90 (c), the unconstricted resistance is similar to what is calculated from a simple parallel plate geometry when the electrolyte thickness is much less than the electrode spacing. In these situations, most of the current enters and exits the electrolyte near the inner edges of the electrodes and the current is fairly uniform through the film cross section. It also can be seen in the table as in the figure that the effects of constriction are keener for the thick electrolytes and wider electrodes. This behavior matches what was observed experimentally in Figure 59. Further results from this modeling can be found in the discussion of the constriction resistances, section 4.1.2.

Table 10. The geometric resistances calculated for a few sample geometries, including both constricted and unconstricted cases.

Electrolyte thickness [μm]	Electrode Spacing [μm]	Triple phase boundary radius [nm]	Constricted geometric resistance [-]	Unconstricted geometric resistance [-]
1	10	5	12.60	10.84
1	100	5	101.4	100.65
500	100	5	6.367	1.993
"	"	1	7.381	"

A.3 MATLAB Code for Unconstricted Interdigitated Electrode Resistance

```
function [R,S,T]=IDE_u(varargin);
%%%%%%%%%%%%%%%%%%%%%%%%%%%%%%%%%%%%%%%%%%%%%%%%%%%%%%%%%%%%%%%%%%%%%%%%%%%%
% This function requires 2,3,4, or 6 input arguments.
%
% 2 or 3 arguments specify one particular geometry to be solved for:
% IDE_u(electrode spacing, electrolyte thickness, *mesh refines)
%
% 4 or 6 arguments specify a range of geometries to solve for:
% IDE_u(initial spacing, final spacing, initial thickness, final...
%   thickness, *variable resolution, *mesh refines)
%
% *these input variables are optional:
% mesh refines: the number of mesh generations to use.  High number means
%    a finer mesh and thus greater accuracy and longer computation times.
%    Default is 15.
% variable resolution: the number of electrode spacing and thicknesses per
%    decade to solve for.  Default is 15.
%
% The outputs are the resistance, spacing, and thickness (arrays).
% If one or no output is specified, the output is the resistance(s).
% Using 2 or 3 arguments also outputs a graphical voltage map.
%%%%%%%%%%%%%%%%%%%%%%%%%%%%%%%%%%%%%%%%%%%%%%%%%%%%%%%%%%%%%%%%%%%%%%%%%%%%
% Further details:
% This function calculates the resistance of a dense IDE structure on top
% of a conductor, where charge injection occurs across the entire
% electrode interface.  The symmetric geometric unit is one half of a
```

```
% crosssection.  The ElectrodeSpacing and the FilmThickness are varied.
% The variables are spaced logarithmically, with VarRes steps per decade.
% The mesh is adaptively refined MeshRef number of times.  A voltage of 1
% is held along the electrode, and the right side boundary (the line of
% symmetry between two physical electrodes) is kept at a voltage of zero.
% All other edges have zero normal current boundary condition.  The
% overall voltage difference in the IDE structure is thus two volts, since
% symmetry would give a voltage of -1 for the opposite electrode. The
% resistance of the structure, R, is given by R = V/I.  Since V = 2 and
% I = the sum of the difference in V at every point along the electrode
% surface, then: R=2/I
% This is solved as a function of ElectrodeSpacing & FilmThickness.
% Conductivity is in S/nm, but R is linearly proportional to its inverse,
% so it isn't a variable.  I is per nanometer in the 'Z' direction, which
% projects into the cross-section (and R is thus ohm-nm).
% To find the resistance of a real IDE structure, take the resistance
% output from this function and divide by the total length of one
% electrode (or the length per finger times the number of fingers).
%%%%%%%%%%%%%%%%%%%%%%%%%%%%%%%%%%%%%%%%%%%%%%%%%%%%%%%%%%%%%%%%%%%%%%%%%%

%%%%%%%%%%
%Variables are initialized
if (nargin == 4 | nargin == 6)
    InitElectrodeSpacing = max(varargin{1}(1), varargin{2}(1));
    FinalElectrodeSpacing = min(varargin{1}(1), varargin{2}(1));
    InitFilmThickness = max(varargin{3}(1), varargin{4}(1));
    FinalFilmThickness = min(varargin{3}(1), varargin{4}(1));
elseif (nargin == 2 | nargin == 3)
    InitElectrodeSpacing = varargin{1}(1);
    FinalElectrodeSpacing = varargin{1}(1);
    InitFilmThickness = varargin{2}(1);
    FinalFilmThickness = varargin{2}(1);
else
    error('Incorrect syntax.  See m-file for details.');
end

if (nargin == 3 | nargin == 6)
    VarRes = varargin{nargin-1}(1);
    MeshRef = varargin{nargin}(1);
else
    VarRes = 15;
    MeshRef = 15;
end

size(1)=floor(log10(InitElectrodeSpacing/FinalElectrodeSpacing)*VarRes)+1;
size(2)=floor(log10(InitFilmThickness/FinalFilmThickness)*VarRes)+1;
Resistance = zeros(size(1),size(2));
Spacing = zeros(size(1),1);
Thickness = zeros(size(2),1);
Conductivity='1';
%%%%%%%%%%

%%%%%%%%%%
%Nested for loops are used to vary the geometric parameters.

ElectrodeSpacing = InitElectrodeSpacing;
for j=1:size(1)
```

```
FilmThickness = InitFilmThickness;
for i=1:size(2)

    %%%%%%%%%%
    %This sets up the geometry and boundary condition matrices.
    ES=ElectrodeSpacing; FT=FilmThickness;

    g = [2     2     2     2      2
         0     0     -ES   -ES    -ES/2
         0     -ES   -ES   -ES/2  0
         FT    0     0     FT     FT
         0     0     FT    FT     FT
         0     0     0     0      0
         1     1     1     1      1];

    b = [1     1     1     1      1
         1     0     0     1      0
         1     1     1     1      1
         1     1     1     1      1
         1     48    48    1      48
         1     48    48    1      48
         48    48    48    48     48
         48    48    48    48     48
         49    49    49    49     49
         48    48    48    49     48];
    %%%%%%%%%%


    %%%%%%%%%%
    %If range of geometries is to be solved for, display current one.
    if (nargin == 4 | nargin == 6)
        fprintf('\n(%d, %d): ES=%d, FT=%d\n',j,i,ES,FT);
    end
    %%%%%%%%%%


    %%%%%%%%%%
    % initmesh has errors with sufficiently weird geometries.
    % Thus, this code is in a try/catch loop, which breaks nicely.
    try
        warning off all
        [p,e,t] = initmesh(g,'hgrad',1.99999,'hmax',max(ES,FT)/10);
        warning on all
    catch
        fprintf('*Geometry Error* Solution not computed.\n');
        Resistance(j,i) = NaN;
        Thickness(i) = FilmThickness;
        FilmThickness = round(FilmThickness/(10^(1/VarRes)));
        continue
    end
    %%%%%%%%%%


    %%%%%%%%%%
    %This command forms the PDE solution on an adaptive mesh
    [u,p,e,t] = adaptmesh_quiet(...
```

```
                    g,b,Conductivity,0,0,'Mesh',p,e,t,'Ngen',MeshRef);
        %%%%%%%%%%


        %%%%%%%%%%
        %If only 1 geometry is solved for, voltage map is plotted
        if (nargin == 2 | nargin == 3)
            pdeplot(p,e,t,'xydata',u,'colormap','jet');
            daspect([1 1 1]);
        end
        %%%%%%%%%%

        x=[-ES:ES/250:0];
        y=[0:FT/250:FT];
        cgux=pdeprtni(p,t,cgux);
        cguy=pdeprtni(p,t,cguy);
        jx=tri2grid(p,t,cgux,x,y);
        jy=tri2grid(p,t,cguy,x,y);
        ix=-sum(jx(:,end))*FT/250;
        Resistance(j,i) = 2/ix;

        Thickness(i) = FilmThickness;
        FilmThickness = round(FilmThickness/(10^(1/VarRes)));
    end

    Spacing(j) = ElectrodeSpacing;
    ElectrodeSpacing = round(ElectrodeSpacing/(10^(1/VarRes)));
end

%%%%%%%%%%

R=Resistance;
S=Spacing;
T=Thickness;
End
%%%%%%%%%%%%%%%%%%%%%%%%%%%%%%%%%%%%%%%%%%%%%%%%%%%%%%%%%%%%%%%%%%%%%%%%%%
```

Please see the note at the end of section A.4 regarding the function `adaptmesh_quiet`.

A.4 MATLAB Code for Constricted Interdigitated Electrode Resistance

```
function [R,S,T]=IDE_c(varargin);
%%%%%%%%%%%%%%%%%%%%%%%%%%%%%%%%%%%%%%%%%%%%%%%%%%%%%%%%%%%%%%%%%%%%%%%%%%
%
% This function requires 3,4,6, or 8 input arguments.
%
% 3 or 4 arguments specify one particular geometry to be solved for:
% IDE_c(3PB radius, electrode spacing, electrolyte thickness, *mesh...
% refines) and gives a voltage map of the result.
%
% 6 or 8 arguments specify a range of geometries to solve for:
% IDE_c(initial radius, final radius, initial spacing, final spacing,...
% initial thickness, final thickness, *variable resolution,...
% *mesh refines)
```

```
%
% *these input variables are optional:
% mesh refines: the number of mesh generations to use.  High number means
%    a finer mesh and thus greater accuracy and longer computation times.
%    Default is 15.
% variable resolution: the number of electrode spacing and thicknesses per
%    decade to solve for.  Default is 15.
%
% The outputs are the resistance, spacing, and thickness (arrays).
% If one or no output is specified, the output is the resistance(s).
% Using 2 or 3 arguments also outputs a graphical voltage map.
%%%%%%%%%%%%%%%%%%%%%%%%%%%%%%%%%%%%%%%%%%%%%%%%%%%%%%%%%%%%%%%%%%%%%%%%%%
%
% Further details:
% This function calculates the resistance of a dense IDE structure on top
% of an electrolyte, where charge injection can only occur at the triple
% phase boundary.  The symmetric geometric unit is one half of a cross-
% section with the TPB modeled as a semicircle in the center of the top
% surface of an electrolyte.  The semicircle model thus breaks down when
% the radius is nearly the same size as the other parameters. The TPB
% radius (named TriplePhaseBoundary) is varied, as is the ElectrodeSpacing
% and the electrolyte FilmThickness.  The variables are spaced
% logarithmically, with VarRes steps per decade.  The mesh is adaptively
% refined MeshRef number of times.  A current input of 1 amp per unit
% length of TPB is input along the TPB, and the right side boundary (the
% line of symmetry between two physical electrodes) is kept at a voltage
% of 0.  All other edges have zero normal current boundary condition.  The
% overall voltage difference in the IDE structure is thus twice the
% maximum voltage found, since symmetry would give a voltage of -max for
% the opposite electrode. The resistance of the structure, R, is given by
% R=V/I.  Since V=2*max(u) and I=1*arclength(TPB)=pi*TriplePhaseBoundary,
% then: R=2*max(u)/(pi*TriplePhaseBoundary)
% This is solved as a function of TPB, ElectrodeSpacing & FilmThickness.
% Conductivity is in S/nm, but R is linearly proportional to its inverse,
% so it isn't a variable.  I is per nanometer in the 'Z' direction, which
% projects into the cross-section (and R is thus ohm-nm).
% To find the resistance of a real IDE structure, take the resistance
% output from this function and divide by the total length of one
% electrode (or the length per finger times the number of fingers).
%%%%%%%%%%%%%%%%%%%%%%%%%%%%%%%%%%%%%%%%%%%%%%%%%%%%%%%%%%%%%%%%%%%%%%%%%%

%%%%%%%%%%
%Variables are initialized
if (nargin == 6 | nargin == 8)
    InitTriplePhaseBoundary = max(varargin{1}(1), varargin{2}(1));
    FinalTriplePhaseBoundary = min(varargin{1}(1), varargin{2}(1));
    InitElectrodeSpacing = max(varargin{3}(1), varargin{4}(1));
    FinalElectrodeSpacing = min(varargin{3}(1), varargin{4}(1));
    InitFilmThickness = max(varargin{5}(1), varargin{6}(1));
    FinalFilmThickness = min(varargin{5}(1), varargin{6}(1));
elseif (nargin == 3 | nargin == 4)
    InitTriplePhaseBoundary = varargin{1}(1);
    FinalTriplePhaseBoundary = varargin{1}(1);
    InitElectrodeSpacing = varargin{2}(1);
    FinalElectrodeSpacing = varargin{2}(1);
    InitFilmThickness = varargin{3}(1);
    FinalFilmThickness = varargin{3}(1);
```

```
else
    error('Incorrect syntax.  See m-file for details.');
end

if (nargin == 4 | nargin == 8)
    VarRes = varargin{nargin-1}(1);
    MeshRef = varargin{nargin}(1);
else
    VarRes = 15;
    MeshRef = 15;
end

size(1)=floor(log10(InitTriplePhaseBoundary/FinalTriplePhaseBoundary)*...
 VarRes)+1;
size(2)=floor(log10(InitElectrodeSpacing/FinalElectrodeSpacing)*VarRes)+1;
size(3)=floor(log10(InitFilmThickness/FinalFilmThickness)*VarRes)+1;
Resistance = zeros(size(1),size(2),size(3));
Width = zeros(size(1),1);
Spacing = zeros(size(2),1);
Thickness = zeros(size(3),1);
Conductivity='1';
%%%%%%%%%%


%%%%%%%%%%
%Nested for loops are used to vary the geometric parameters.
TriplePhaseBoundary = InitTriplePhaseBoundary;
for k=1:size(1)

  ElectrodeSpacing = InitElectrodeSpacing;
  for j=1:size(2)

    FilmThickness = InitFilmThickness;
    for i=1:size(3)

      %%%%%%%%%%
      %This sets up the geometry and boundary condition matrices.
      ES=ElectrodeSpacing; FT=FilmThickness; TPB=TriplePhaseBoundary;

      g = [2     2     2     2         2         1         1
           0     0     -ES   -ES       -ES/2+TPB -ES/2-TPB -ES/2
           0     -ES   -ES   -ES/2-TPB 0         -ES/2     -ES/2+TPB
           FT    0     0     FT        FT        FT        FT-TPB
           0     0     FT    FT        FT        FT-TPB    FT
           0     0     0     0         0         0         0
           1     1     1     1         1         1         1
           0     0     0     0         0         -ES/2     -ES/2
           0     0     0     0         0         FT        FT
           0     0     0     0         0         TPB       TPB];

      b = [1     1     1     1         1         1          1
           1     0     0     0         0         0          0
           1     1     1     1         1         1          1
           1     1     1     1         1         1          1
           1     48    48    48        48        48         48
           1     48    48    48        48         49          49
           48    48    48    48        48         48          48
```

```
          48    48    48    48        48          48           48
          49    49    49    49        49          49           49
          48    48    48    48        48          48           48];
    %%%%%%%%%%


    %%%%%%%%%%
    %If a range of geometries is to be solved for, display current one.
    if (nargin == 6 | nargin == 8)
        fprintf('\n(%d, %d, %d): TPB=%2.3f, ES=%d, ...
                FT=%d\n',k,j,i,TPB,ES,FT);
    end
    %%%%%%%%%%


    %%%%%%%%%%
    % initmesh has errors with sufficiently weird geometries.
    % Thus, this code is in a try/catch loop, which breaks nicely.
    try
        warning off all
        [p,e,t] = initmesh(g,'hgrad',1.99999,'hmax',max(ES,FT)/10);
        warning on all
    catch
        fprintf('*Geometry Error*  Solution not computed.\n');
        Resistance(k,j,i) = NaN;
        Thickness(i) = FilmThickness;
        FilmThickness = round(FilmThickness/(10^(1/VarRes)));
        continue
    end
    %%%%%%%%%%


    %%%%%%%%%%
    %This command forms the PDE solution on an adaptive mesh
    [u,p,e,t] = adaptmesh_quiet(...
                g,b,Conductivity,0,0,'Mesh',p,e,t,'Ngen',MeshRef);
    %%%%%%%%%%


    %%%%%%%%%%
    %If only 1 geometry is solved for, voltage map is plotted
    if (nargin == 3 | nargin == 4)
        pdeplot(p,e,t,'xydata',u,'colormap','jet');
        daspect([1 1 1]);
    end
    %%%%%%%%%%

    Resistance(k,j,i) = 2*max(u)/(pi*TriplePhaseBoundary);

    Thickness(i) = FilmThickness;
    FilmThickness = round(FilmThickness/(10^(1/VarRes)));
  end

  Spacing(j) = ElectrodeSpacing;
  ElectrodeSpacing = round(ElectrodeSpacing/(10^(1/VarRes)));
end
```

```
  Width(k) = TriplePhaseBoundary;
  TriplePhaseBoundary =
round(1E3*TriplePhaseBoundary/(10^(1/VarRes)))/1E3;
end
%%%%%%%%%%

R=Resistance;
W=Width;
S=Spacing;
T=Thickness;
End
%%%%%%%%%%%%%%%%%%%%%%%%%%%%%%%%%%%%%%%%%%%%%%%%%%%%%%%%%%%%%%%%%%%%%%%%%%%%%%%%
```

Note: The function `adaptmesh_quiet`, used in the codes above, is identical to the function `adaptmesh` that is part of the pde toolbox except for three alterations. The changes merely compact the screen output and in no way change the mathematics.

Line 244 of `adaptmesh`

```
fprintf('Number of triangles: %g\n',size(t,2))
```

is replaced with

```
fprintf('(%2.0f) Number of triangles: %g',gen,size(t,2))
told=size(t,2);
```

Line 275 of `adaptmesh`

```
fprintf('\nMaximum number of refinement passes obtained.\n');
```

is replaced with

```
fprintf('\nMax # of refinement passes.\n',size(t,2));
```

and above Line 290 of `adaptmesh` should be inserted

```
for qlp=1:26+ceil(log10(told+0.1))
    fprintf('\b')
end
```

APPENDIX B. THERMAL STABILITY OF YSZ FILMS

B.1 Purpose and Experimental Methods

This thesis presented results that showed superior properties of YSZ films that were processed at vastly reduced temperatures compared to standard ceramic processing routes. In some applications, these low processing temperatures may be less than the intended operating temperature. A question that arises, therefore, is whether the properties of the films are stable during prolonged time at elevated temperature.

To test for any degradation, a few samples were set aside after electrical characterization and annealed in a tube furnace at 600°C for 10 or 100 hours. The same sputtered platinum electrodes were on the sample surface for the entire process. These samples were then re-characterized by X-ray diffraction and impedance spectroscopy, as described in Chapter 2. The samples treated in this manner were: a YSZ9 film deposited at 600°C on a silica substrate, a YSZ9 film deposited at 300°C on a silica substrate, and a YSZ9 film deposited unheated on a YSZ single crystal substrate.

A YSZ9 film deposited unheated on a silica substrate could not be used in this experiment because these films delaminated during the heat treatment. This thermomechanical degradation indicates one way that the unheated deposited films may be unstable at potential operating temperatures. On the other hand, this degradation likely results from the large difference in thermal expansion coefficient between the YSZ film ($\alpha = 10 \cdot 10^{-6}\ K^{-1}$)[9] and the fused silica substrate ($\alpha = 5.5 \cdot 10^{-7}\ K^{-1}$)[50] and so may be solved by substitution of a more complementary substrate.

B.2 Results

X-ray diffraction patterns for the samples with silica substrates are shown in Figure 91 and Figure 92 both before and after annealing for 100 hours. In both figures, little difference is seen the YSZ or Pt peaks, even after the full annealing cycle. Similarly, the electrolyte conductivities were essentially unchanged after 10 or even 100 hours of 600°C annealing. This is shown for the grain conductivity of all three samples in Figure 93 and for the grain boundary conductivity of the non-single crystal substrate samples in Figure 94. Any evolution that occurred in the crystallinity and electrolytic conductivity of the films appear to be within experimental error. It is perhaps not surprising that the samples change little at 600°C, since the melting points of the fused silica substrate (1713°C), YSZ electrolyte (2680°C), and Pt electrodes (1769°C) are so far removed from the annealing temperature used. These first results bode well for the utility of these films at temperatures of at least 600°C.

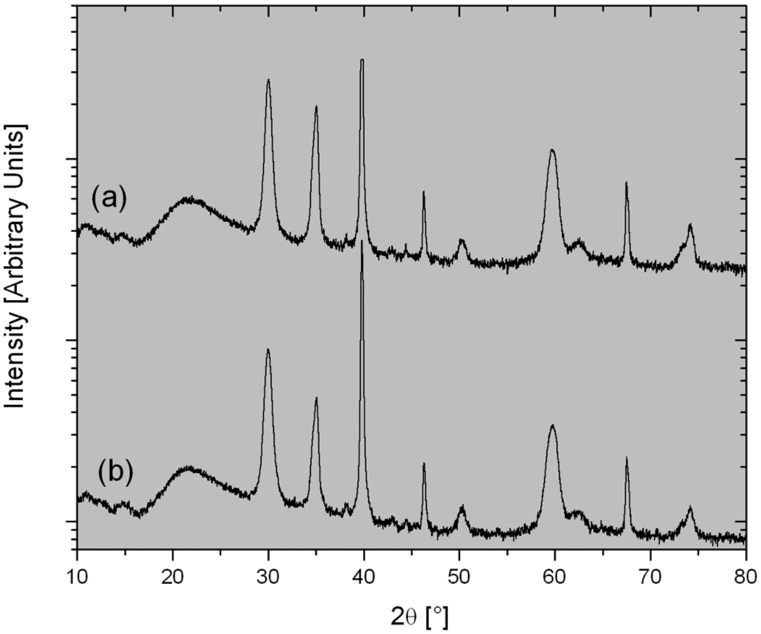

Figure 91. X-ray diffraction patterns of a sample consisting of platinum interdigitated electrodes on a YSZ9 film deposited onto a silica substrate at 300°C. Patterns shown are (a) after annealing at 600°C for 100 hours and (b) before any heat treatment. Note that intensity is in logarithmic scale.

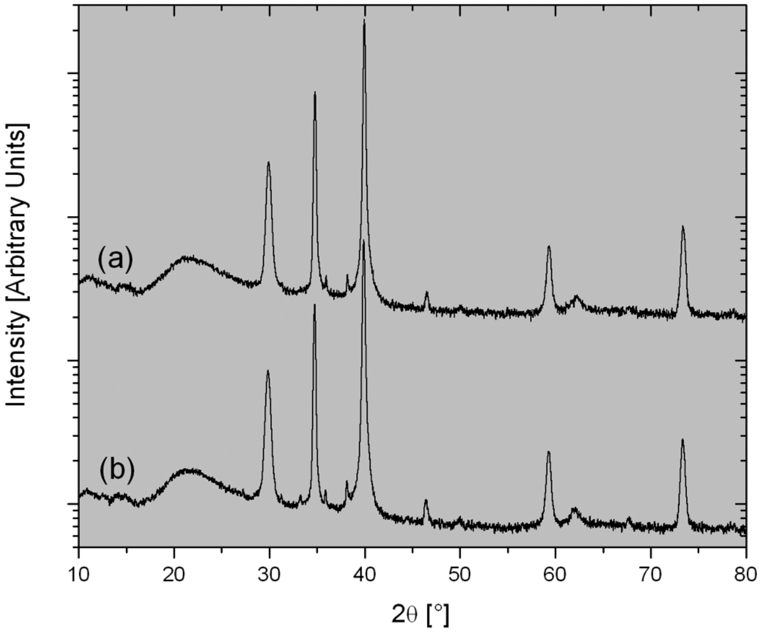

Figure 92. X-ray diffraction patterns of a sample consisting of platinum interdigitated electrodes on a YSZ9 film deposited onto a silica substrate at 600°C. Patterns shown are (a) after annealing at 600°C for 100 hours and (b) before any heat treatment. Note that intensity is in logarithmic scale.

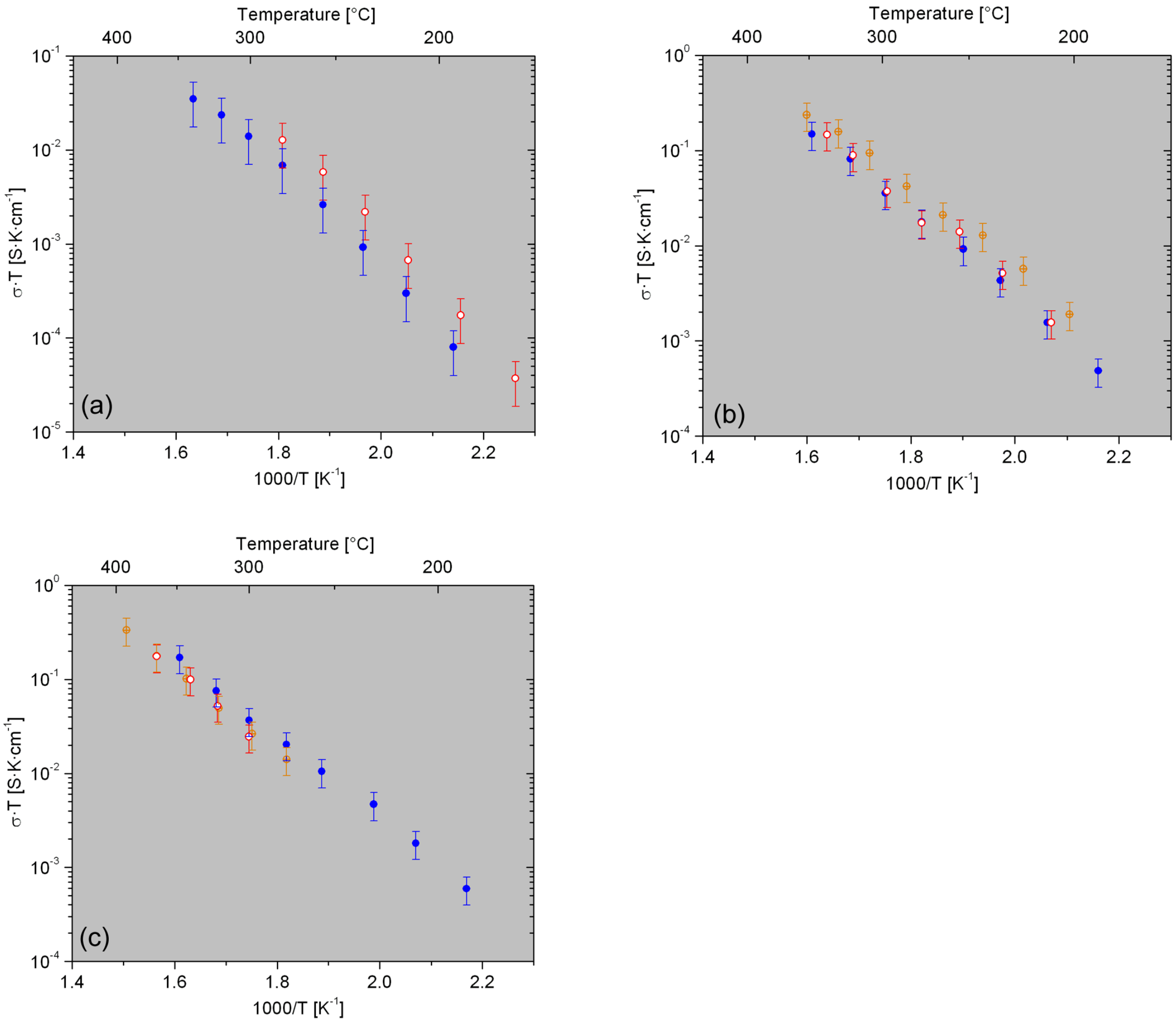

Figure 93. The grain conductivity of (a) (111) oriented YSZ single crystal with a YSZ9 film deposited unheated on the surface; (b) YSZ9 film deposited on a silica substrate at 300°C; and (c) YSZ9 film deposited on a silica substrate at 600°C. In each graph, ● = sample as initially created, ⊕ = after 10 hr. anneal at 600°C, and ○ = after 100 hr. anneal at 600°C.

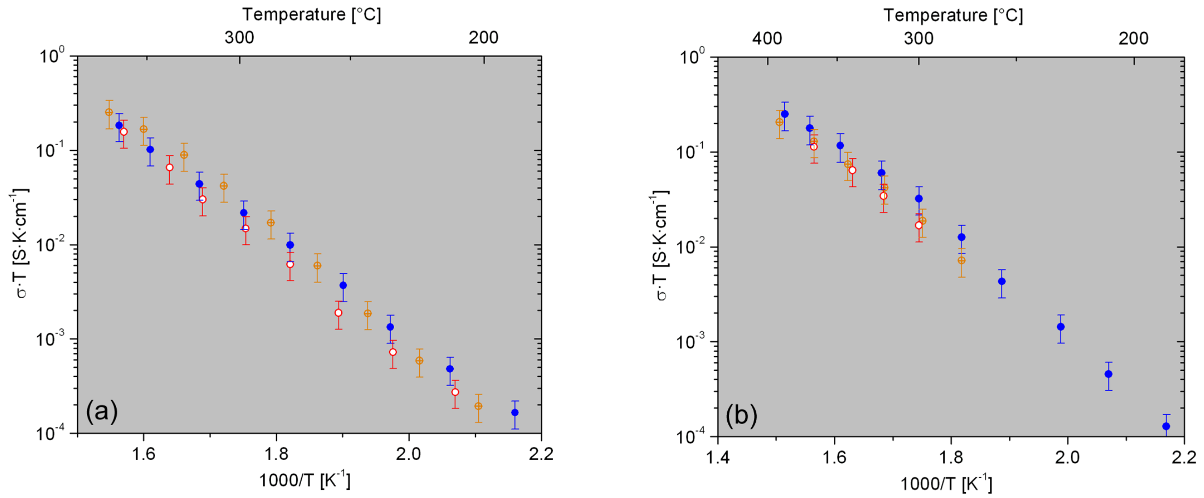

Figure 94. The grain boundary conductivity of (a) YSZ9 film deposited on a silica substrate at 300°C and (b) YSZ9 film deposited on a silica substrate at 600°C. In both graphs, ● = sample as initially created, ⊕ = after 10 hr. anneal at 600°C, and ○ = after 100 hr. anneal at 600°C.

Figure 95 shows the electrode activation polarization conductance per triple phase boundary length for the samples before and after annealing. While the high electrochemical conductance electrodes placed on the unheated deposited film surface showed no degradation, the electrodes placed on the 300°C and 600°C deposited films did show degradation during annealing. There appeared to have been a slight decrease in activation energy for the unheated deposited film, though the cause of this is unclear. The polarization conductance of the 300°C deposited film degraded by approximately half of an order of magnitude after 10 hours and continued to degrade by another half of an order of magnitude after 100 total hours. The conductance of the 600°C deposited film degraded by a factor of about 3 during the first 10 hours and then did not degrade further during the next 90 hours.

There probably was not a change in the platinum electrodes themselves, since the degradation behavior was different for each sample. Presumably, the electrodes would have changed in a similar manner for each sample. Rather, the decrease in activation polarization conductance is likely due to motion of surface silica to triple phase boundary sites. The driving force for this motion is capillary action pulling the silica to the corner between the planar YSZ electrolyte and the Pt electrode edge that rises from the surface. The surface of the unheated deposited film had no silica, and no degradation was found. The 600°C deposited film was severely contaminated, and degradation occurred rapidly as silica quickly filled in any gaps along the triple phase boundary. The 300°C deposited film appears to require silica to diffuse from farther away on the electrolyte surface, accounting for the continual nature of the degradation (and possibly the $\approx\sqrt{t}$ dependence). This would be consistent with reduced silica contamination on the surface, albeit the contamination levels of the 300°C deposited film were not directly measured. After very long annealing times, it is presumed that the enough silica on the surface of the 300°C film would diffuse to the triple phase boundaries to degrade the polarization to the level of the 600°C film.

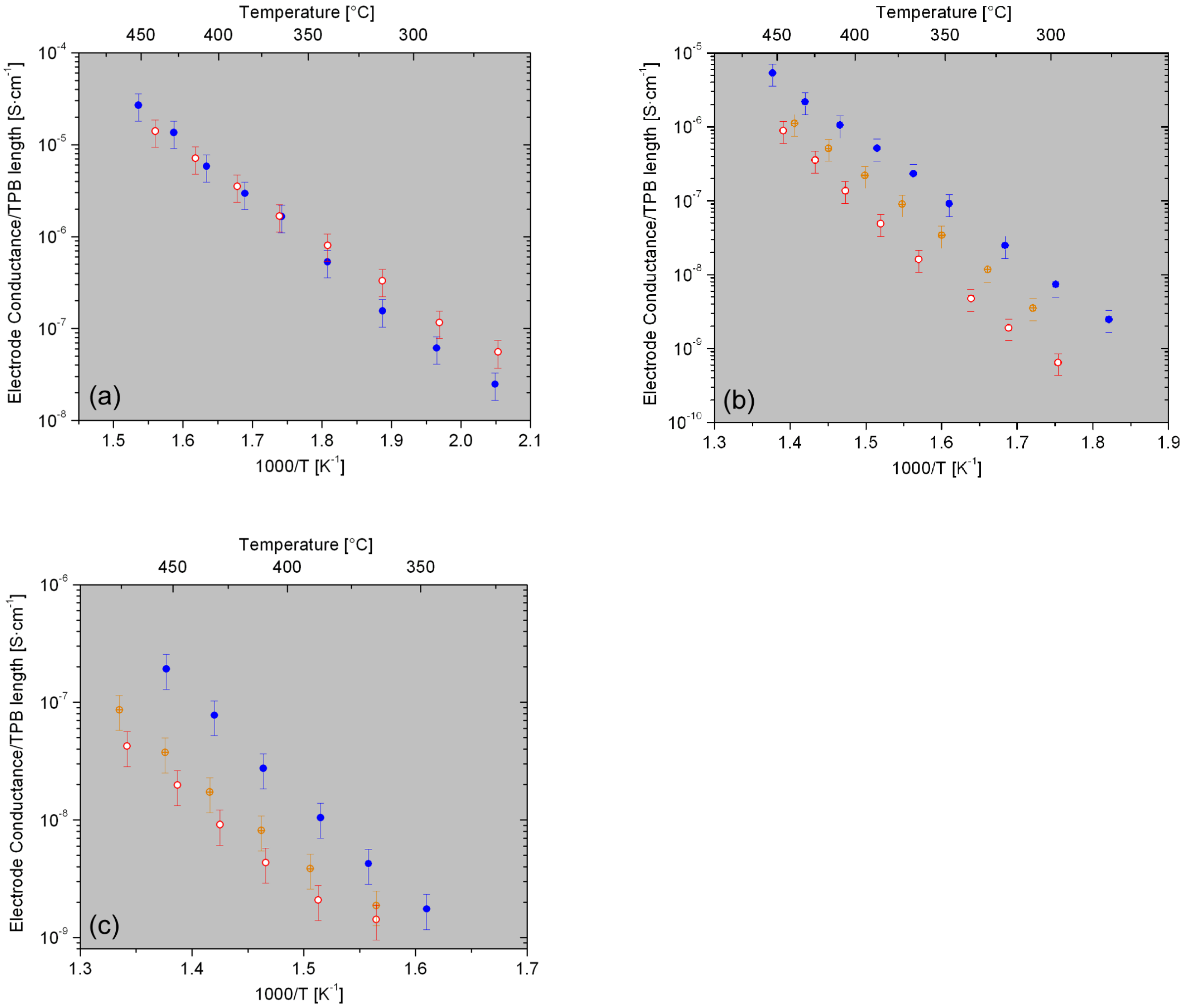

Figure 95. The electrode activation polarization conductance normalized to the triple phase boundary length of (a) (111) oriented YSZ single crystal with a YSZ9 film deposited unheated on the surface; (b) YSZ9 film deposited on a silica substrate at 300°C; and (c) YSZ9 film deposited on a silica substrate at 600°C. In each graph, ● = sample as initially created, ⊕ = after 10 hr. anneal at 600°C, and ○ = after 100 hr. anneal at 600°C.

REFERENCES

1. Hubbert, M.K., "Energy from fossil fuels," *Science*, **109**, 103-109 (1949).

2. Intergovernmental Panel on Climate Change, *Climate Change 2001: The Scientific Basis. Contribution of Working Group I to the Third Assessment Report of the Intergovernmental Panel on Climate Change*, Houghton, J.T., Ding, Y., Griggs, D.J., Noguer, M., van der Linden, P.J., Dai, X., Maskell, K. & Johnson, C.A., eds. (Cambridge University Press, New York, NY) 2001.

3. Zemansky, M.W. and Dittman, R.H., *Heat and Thermodynamics*, 7th ed. (McGraw Hill, New York, NY) 1997.

4. Patil, A.S., Dubois, T.G., Sifer, N., Bostic, E., Gardner, K., Quah, M. and Bolton, C., "Portable fuel cell systems for America's army: technology transition to the field," *J. Power Sources*, **136**, 220-225 (2004).

5. Jankowski, A.F., Hayes, J.P., Graff, R.T. and Morse, J.D., "Testing of solid oxide fuel cells for micro to macro power generation," in *Solid Oxide Fuel Cells VI*, Dokiya, M. and Singhal, S., eds., **99-19**, 932-937 (Electrochemical Society Proceedings, Pennington, PA) 1999.

6. Chen, X., Wu, N.J., Smith, L. and Ignatiev, A., "Thin-film heterostructure solid oxide fuel cells," *Appl. Phys. Lett.*, **84**, 2700-2702 (2004).

7. Shao, Z., Haile, S.M., Ahn, J., Ronney, P.D., Zhan, Z. and Barnett, S.A., "A thermally self-sustained micro solid-oxide fuel-cell stack with high power density," *Nature*, **435**, 795-798 (2005).

8. Mogensen, M., Jensen, K.V., Jørgensen, M.J. and Primdahl, S., "Progress in understanding SOFC electrodes," *Solid State Ionics*, **150**, 123-129 (2002).

9. Srikar, V.T., Turner, K.T., Ie, T.Y.A. and Spearing, S.M., "Structural design considerations for micromachined solid-oxide fuel cells," *J. Power Sources*, **125**, 62-69 (2004).

10. Tang, Y., Stanley, K., Wu, J., Ghosh, D. and Zhang, J., "Design considerations of micro thin film solid-oxide fuel cells," *J. Micromech. Microeng.*, **15**, S185-192 (2005).

11. Baertsch, C.D., Jensen, K.F., Hertz, J.L., Tuller, H.L., Vengallatore, S.T., Spearing, S.M. and Schmidt, M.A., "Fabrication and structural characterization of self-supporting electrolyte membranes for a micro-solid oxide fuel cell," *J. Mater. Res.*, **19**, 2604-2615 (2004).

12. Grove, W.R., "On voltaic series and the combination of gases by platinum," *Philos. Mag.*, **14**, 127-130 (1839).

13. Srinivasan, S., Mosdale, R., Stevens, P. and Yang, C., "Fuel cells: reaching the era of clean and efficient power generation in the twenty-first century," *Annu. Rev. Energy Environ.*, **24**, 281-328 (1999).

14. Brandon, N.P., Skinner, S. and Steele, B.C.H., "Recent advances in materials for fuel cells," *Annu. Rev. Mater. Res.*, **33**, 183-213 (2003).

15. Maier, J., "Interaction of oxygen with oxides: how to interpret effective rate constants," *Solid State Ionics*, **135**, 575-588 (2000).

16. Nowotny, J., Bak, T., Nowotny, M.K. and Sorrell, C.C., "Charge transfer at oxygen/zirconia interface at elevated temperatures, part 2: oxidation of zirconia," *Adv. Appl. Ceram.*, **104**, 154-164 (2005).

17. Bard, A.J. and Faulkner, L.R., *Electrochemical Methods: Fundamentals and Applications*, 2nd ed. (John Wiley & Sons, Singapore) 2004.

18. Adler, S.B., "Factors governing oxygen reduction in solid oxide fuel cell cathodes," *Chem. Rev.*, **104**, 4791-4843 (2004).

19. Tuller, H.L., "Mixed conduction in nonstoichiometric oxides," in *Nonstoichiometric Oxides*, Sorensen, O.T., ed., 271-335 (Academic Press, New York) 1981.

20. United States Department of Energy, *Fuel Cell Handbook*, 6th ed. (Morgantown, WV) 2002.

21. Minh, N., "SECA Solid Oxide Fuel Cell Program," presented at Solid State Energy Conversion Alliance 3rd Annual Workshop Proceedings, March 2002; reprinted in United States Department of Energy, *Fuel Cell Handbook*, 6th ed. (Morgantown, WV) 2002.

22. Steele, B.C.H. and Heinzel, A., "Materials for fuel-cell technologies," *Nature*, **414**, 345-352 (2001).

23. Baur, E. and Preis, H., "Über Brennstoff-Ketten mit Festleitern," *Z. Elektrochem.*, **43**, 727-732 (1937).

24. Ralph, J.M., Schoeler, A.C. and Krumpelt, M., "Materials for lower temperature solid oxide fuel cells," *J. Mater. Sci.*, **36**, 1161-1172 (2001).

25. Minh, N.Q., "Ceramic fuel cells," *J. Am. Ceram. Soc.*, **76**, 563-588 (1993).

26. Mogensen, M. and Kammer, K., "Conversion of hydrocarbons in solid oxide fuel cells," *Annu. Rev. Mater. Res.*, **33**, 321-331 (2003).

27. Goodenough, J.B., "Oxide-ion electrolytes," *Annu. Rev. Mater. Res.*, **33**, 91-128 (2003).

28. Larminie, J. and Dicks, A., *Fuel Cell Systems Explained*, 2nd ed. (John Wiley & Sons, UK) 2003.

29. Dyer, C.K., "Replacing the battery in portable electronics," *Sci. Am.*, 88-93, July 1999.

30. Lide, D.R., ed., *CRC Handbook of Chemistry and Physics*, 74th ed. (CRC Press, Boca Raton, FL) 1993.

31. Cowey, K., Green, K.J., Mepsted, G.O. and Reeve, R., "Portable and military fuel cells," *Curr. Op. in Sol. State and Mater. Sci.*, **8**, 367-371 (2004).

32. Mason, J., "Micro fuel cells headed to market, and a showdown," *Small Times*, 27 May 2004.

33. Park, Y.-I., Su, P.C., Cha, S.W., Saito, Y. and Prinz, F.B., "Thin-film SOFCs using gastight YSZ thin films on nanoporous substrates," *J. Electrochem. Soc.*, **153**, A431-A436 (2006).

34. Charpentier, P., Fragnaud, P., Schleich, D.M. and Gehain, E., "Preparation of thin film SOFCs working at reduced temperature," *Solid State Ionics*, **135**, 373-380 (2000).

35. de Souza, S., Visco, S.J. and De Jonghe, L.C., "Reduced-temperature solid oxide fuel cell based on YSZ thin-film electrolyte," *J. Electrochem. Soc.*, **144**, L35-L37 (1997).

36. Fleig, J., Tuller, H.L. and Maier, J., "Electrodes and electrolytes in micro-SOFCs: a discussion of geometrical constraints," *Solid State Ionics*, **174**, 261-270 (2004).

37. Chachuat, B., Mitsos, A. and Barton, P.I., "Optimal design and steady-state operation of micro power generation employing fuel cells," *Chem. Eng. Sci.*, **60**, 4535-4556 (2005).

38. Xu, X., Xia, C., Huang, S. and Peng, D., "YSZ thin films deposited by spin-coating for IT-SOFCs," *Ceram. Int.*, **31**, 1061-1064 (2005).

39. Mogensen, M., Primdahl, S., Jørgensen, M.J. and Bagger, C., "Composite electrodes in solid oxide fuel cells and similar solid state devices," *J. Electroceram.*, **5**, 141-152 (2000).

40. Arana, L.R., Schaevitz, S.B., Franz, A.J., Schmidt, M.A. and Jensen, K.F, "A microfabricated suspended-tube chemical reactor for thermally efficient fuel processing," *J. Microelectromech. S.*, **12**, 600-612 (2003).

41. Jankowski, A.F., Hayes, J.P., Graff, R.T. and Morse, J.D., "Micro-fabricated thin-film fuel cells for portable power requirements," in *Materials for Energy Storage, Generation and Transport*, Schwarz, R.B., Ceder, G. and Ringel, S.A., eds., **730**, V4.2.1-V4.2.6 (Materials Research Society Proceedings, Warrendale, PA) 2002.

42. Morse, J. and Jankowski, A., "A MEMS-based fuel cell for microscale energy conversion," (Lawrence Livermore National Laboratory Technical Reports, Livermore, CA) 2002. Accessed 7 May 2006 at http://www.llnl.gov/tid/lof/documents/pdf/243986.pdf

43. Jankowski, A.F. and Morse, J.D., "MEMS-based thin-film fuel cells," United States Patent 6,638,654.

44. Company and product information found at http://www.ultracellpower.com. Accessed 7 May 2006.

45. Jankowski, A.F. and Hayes, J.P., "Sputter deposition of metallic sponges," *J. Vac. Sci. Technol., A*, **21**, 422-425 (2002).

46. Dyer, C.K., "A novel thin-film electrochemical device for energy conversion," *Nature*, **343**, 547-548 (1990).

47. Stefan, I.C., Jacobson, C.P., Visco, S.J. and De Jonghe, L.C., "Single chamber fuel cells: flow geometry, rate, and composition considerations," *Electrochem. Solid- State Lett.*, **7**, A198-A200 (2004).

48. Shao, Z. and Haile, S.M., "A high-performance cathode for the next generation of solid-oxide fuel cells," *Nature*, **431**, 170-173 (2004).

49. "High-candlepower Nernst Lamps," *Western Electrician*, **28**, 353 (1901); excerpted in The University at Buffalo Libraries, "Electricity and technology at the Pan-American exposition," http://ublib.buffalo.edu/libraries /exhibits/panam/sel/nernst.html. Accessed 7 May 2006.

50. ASM International Handbook Committee, *Engineered Materials Handbook*, vol. 4, *Ceramics and Glasses*, Schneider, S.J., tech. chmn. (ASM International, USA) 1991.

51. Vaßen, R., Czech, N., Malléner, W., Stamm, W. and Stöver, D., "Influence of impurity content and porosity of plasma-sprayed yttria-stabilized zirconia layers on the sintering behaviour," *Surf. Coat. Technol.*, **141**, 135-140 (2001).

52. Cutler, R.A., Reynolds, J.R. and Jones, A., "Sintering and characterization of polycrystalline monoclinic, tetragonal, and cubic zirconia," *J. Am. Ceram. Soc.*, **75**, 2173-2183 (1992).

53. Kingery, W.D., Bowen, H.K. and Uhlmann, D.R., *Introduction to Ceramics*, 2nd ed. (John Wiley & Sons, New York, NY) 1976.

54. Scott, H.G., "Phase relationships in the zirconia-yttria system," *J. Mater. Sci.*, **10**, 1527-1535 (1975).

55. Hull, S., "Superionics: crystal structures and conduction processes," *Rep. Prog. Phys.*, **67**, 1233-1314 (2004).

56. Luo, J., Almond, D.P. and Stevens, R., "Ionic mobilities and association energies from an analysis of electrical impdance of ZrO_2-Y_2O_3 alloys," *J. Am. Ceram. Soc.*, **83**, 1703-1708 (2000).

57. Badwal, S.P.S., "Electrical conductivity of single crystal and polycrystalline yttria-stabilized zirconia," *J. Mater. Sci.*, **19**, 1767-1776 (1984).

58. Abelard, P. and Baumard, J.F., "Study of the dc and ac electrical properties of an yttria-stabilized zirconia single crystal [$(ZrO_2)_{0.88}$-$(Y_2O_3)_{0.12}$]," *Phys. Rev. B: Condens. Matter Mater. Phys.*, **26**, 1005-1017 (1982).

59. Manning, P.S., Sirman, J.D., De Souza, R.A. and Kilner, J.A., "The kinetics of oxygen transport in 9.5 mol % single crystal yttria stabilised zirconia," *Solid State Ionics*, **100**, 1-10 (1997).

60. Park, J.-H. and Blumenthal, R.N., "Electronic transport in 8 mole percent Y_2O_3-ZrO_2," *J. Electrochem. Soc.*, **136**, 2867-2876 (1989).

61. Joo, J.H. and Choi, G.M., "Electrical conductivity of YSZ film grown by pulsed laser deposition," *Solid State Ionics*, **177**, 1053-1057 (2006).

62. Petrovsky, T., Anderson, H.U. and Petrovsky, V., "Impedance spectroscopy and direct current measurements of YSZ films," in *Solid-State Ionics—2002*, Knauth, P., Tarascon, J.-M., Traversa, E. and Tuller, H.L., eds., **756**, EE4.7.1-EE4.7.6 (Materials Research Society Proceedings, Warrendale, PA) 2003.

63. Thiele, E.S., Wang, L.S., Mason, T.O. and Barnett, S.A., "Deposition and properties of yttria-stabilized zirconia thin films using reactive direct current magnetron sputtering," *J. Vac. Sci. Technol., A*, **9**, 3054-3060 (1991).

64. Chen, C.C., Nasrallah, M.M. and Anderson, H.U., "Synthesis and characterization of YSZ thin film electrolytes," *Solid State Ionics*, **70/71**, 101-108 (1994).

65. Ingo, G.M. and Padeletti, G., "Segregation aspects at the fracture surfaces of 8 wt.% yttria-zirconia thermal barrier coatings," *Surf. Interface Anal.*, **21**, 450-454 (1994).

66. Hughes, A.E., "The identification of intergranular impurity phases in zirconia based ionic conductors," *Mater. Sci. Forum*, **34-36**, 243-247 (1988).

67. Badwal, S.P.S., "Grain boundary resistivity in zirconia-based materials - effect of sintering temperatures and impurities," *Solid State Ionics*, **76**, 67-80 (1995).

68. Bauerle, J.E., "Study of solid electrolyte polarization by a complex admittance method," *J. Phys. Chem. Solids*, **30**, 2657-2670 (1969).

69. Guo, X., Sigle, W., Fleig, J. and Maier, J., "Role of space charge in the grain bounday blocking effect in doped zirconia," *Solid State Ionics*, **154-155**, 555-561 (2002).

70. Steele, B.C.H., "Appraisal of $Ce_{1-y}Gd_yO_{2-y/2}$ electrolytes for IT-SOFC operation at 500°C," *Solid State Ionics*, **129**, 95-110 (2000).

71. Badwal, S.P.S., Drennan, J., Hughes, A.E. and Sexton, B.A., "A study of impurity phase segregation in full stabilized yttria-zirconia," *Mater. Sci. Forum*, **34-36**, 195-199 (1988).

72. Aoki, M., Chiang, Y.-M., Kosacki, I., Lee, L. J.-R., Tuller, H. and Liu, Y., "Solute segregation and grain-boundary impedance in high-purity stabilized zirconia," *J. Am. Ceram. Soc.*, **79**, 1169-1180 (1996).

73. Guo, X. and Ding, Y., "Grain boundary space charge effect in zirconia experimental evidence," *J. Electrochem. Soc.*, **151**, J1-J7 (2004).

74. Hughes, A.E. and Badwal, S.P.S., "Impurity and yttrium segregation in yttria-tetragonal zirconia," *Solid State Ionics*, **46**, 265-274 (1991).

75. Hughes, A.E. and Badwal, S.P.S., "Impurity segregation study at the surface of yttria-zirconia electrolytes by XPS," *Solid State Ionics*, **40-41**, 312-315 (1990).

76. Hughes, A.E., "Segregation in single-crystal fully stabilized yttria-zirconia," *J. Am. Ceram.Soc.*, **78**, 369-378 (1995).

77. Damyanova, S., Grange, P. and Delmon, B., "Surface characterization of zirconia-coated alumina and silica carriers," *J. Catal.*, **168**, 421-430 (1997).

78. Matsuoka, M., Isotani, S., Miyake, S., Setsuhara, Y., Ogata, K. and Kuratani, N., "Effects of ion energy and arrival rate on the composition of zirconium oxide films prepared by ion-beam assisted deposition," *J. Appl. Phys.*, **80**, 1177-1181 (1996).

79. Bernasik, A., Kowalski, K. and Sadowski, A., "Surface segregation in yttria-stabilized zirconia by means of angle resolved x-ray photoelectron spectroscopy," *J. Phys. Chem. Solids*, **63**, 233-239 (2002).

80. Whalen, P.J., Reidinger, F., Correale, S.T. and Marti, J., "Yttria migration in Y-TZP during high-temperature annealing," *J. Mater. Sci.*, **22**, 4465-4469 (1987).

81. Theunissen, G.S.A.M., Winnubst, A.J.A. and Burggraaf, A.J., "Surface and grain boundary analysis of doped zirconia ceramics studied by AES and XPS," *J. Mater. Sci.*, **27**, 5057-5066 (1992).

82. Zhu, J., van Ommen, J.G., Knoester, A. and Lefferts, L., "Effect of surface composition of yttrium-stabilized zirconia on partial oxidation of methane to synthesis gas," *J. Catal.*, **230**, 291-300 (2005).

83. de Ridder, M., van Welzenis, R.G., Denier van der Gon, A.W., Brongersma, H.H., Wulff, S., Chu, W.-F. and Weppner, W., "Subsurface segregation of yttria in yttria stabilized zirconia," *J. Appl. Phys.*, **92**, 3056-3064 (2002).

84. de Ridder, M., van Welzenis, R.G., Brongersma, H.H., Wulff, S., Chu, W.-F. and Weppner, W., "Discovery of the rate limiting step in solid oxide fuel cells by LEIS," *Nucl. Instrum. Methods Phys. Res., Sect. B*, **190**, 732-735 (2002).

85. de Ridder, M., Vervoort, A.G.J., van Welzenis, R.G. and Brongersma, H.H., "The limiting factor for oxygen exchange at the surface of fuel cell electrolytes," *Solid State Ionics*, **156**, 255-262 (2003).

86. de Ridder, M., van Welzenis, R.G., Brongersma, H.H. and Kreissig, U., "Oxygen exchange and diffusion in the near surface of pure and modified yttria-stabilised zirconia," *Solid State Ionics*, **158**, 67-77 (2003).

87. Mogensen, M., Vels Jensen, K., Jørgensen, M.J. and Primdahl, S., "Progress in understanding SOFC electrodes," *Solid State Ionics*, **150**, 123-129 (2002).

88. Vels Hansen, K., Norrman, K. and Mogensen, M., "H2-H2O-Ni-YSZ electrode performance – effect of segregation to the interface," *J. Electrochem. Soc.*, **151**, A1436-A1444 (2004).

89. Norrman, K., Vels Hansen, K. and Mogensen, M., "Time-of-flight secondary ion mass spectrometry as a tool for studying segregation phenomena at nickel-YSZ interfaces," *J. Eur. Cer. Soc.*, **26**, 967-980 (2006).

90. Zhang, X., Ohara, S., Mukai, K., Ogawa, M. and Fukui, T., "Effect of chemically etched electrolyte on solid oxide fuel cell performance," *Electrochemistry (Tokyo, Jpn.)*, **68**, 11-16 (2000).

91. De Jonghe, L.C., Jacobson, C.P. and Visco, S.J., "Supported electrolyte thin film synthesis of solid oxide fuel cells," *Annu. Rev. Mater. Res.*, **33**, 169-182 (2003).

92. Grove, W.R., "On the electro-chemical polarity of gases," *Phil. Trans. Roy. Soc. London*, **142**, 87-101 (1852).

93. Kao, A.S., "Comparison of zirconia thin films sputtered from metal and compound targets by reactive ion-beam process," *J. Appl. Phys.*, **69**, 3309-3315 (1991).

94. Boulouz, M., Boulouz, A., Giani, A. and Boyer, A., "Influence of substrate temperature and target composition on the properties of yttria-stabilized zirconia thin films grown by r.f. reactive magnetron sputtering," *Thin Solid Films*, **323**, 85-92 (1998).

95. Gao, P., Meng, L.J., dos Santos, M.P., Teixeira, V. and Andritschky, M., "Study of ZrO_2-Y_2O_3 films prepared by rf magnetron sputtering," *Thin Solid Films*, **377-378**, 32-36 (2000).

96. Hobein, B., Tietz, F., Stöver, D., Čekada, M. and Panjan, P., "DC sputtering of yttria-stabilised zirconia films for solid oxide fuel cell applications," *J. Eur. Cer. Soc.*, **21**, 1843-1846 (2001).

97. Thiele, E.S., Wang, L.S., Mason, T.O. and Barnett, S.A., "Deposition and properties of yttria-stabilized zirconia thin films using reactive direct current magnetron sputtering," *J. Vac. Sci. Technol., A*, **9**, 3054-3060 (1991).

98. Jankowski, A.F. and Hayes, J.P., "Sputter deposition of yttria-stabilized zirconia onto a porous Au substrate," *J. Vac. Sci. Technol., A*, **13**, 658-661 (1995).

99. Jankowski, A.F. and Hayes, J.P., "Reactive sputter deposition of yttria-stabilized zirconia," *Surf. Coat. Technol.*, **76-77**, 126-131 (1995).

100. Kosacki, I., Suzuki, T., Petrovsky, V. and Anderson, H.U., "Electrical conductivity of nanocrystalline ceria and zirconia thin films," *Solid State Ionics*, **136-137**, 1225-1233 (2000).

101. Tuller, H.L., "Ionic conduction in nanocrystalline materials," *Solid State Ionics*, **131**, 143-157 (2000).

102. Kosacki, I., Rouleau, C.M., Becher, P.F., Bentley, J. and Lowndes, D.H., "Nanoscale effects on the ionic conductivity in highly textured YSZ thin films," *Solid State Ionics*, **176**, 1319-1326 (2005).

103. Quinn, D.J., "Microstructure, Residual Stress, and Mechanical Properties of Thin Film Materials for a Microfabricated Solid Oxide Fuel Cell," M.S. thesis, Massachusetts Institute of Technology, 2006.

104. Suzuki, K., Kubo, M., Oumi, Y., Miura, R., Takaba, H., Fahmi, A., Chatterjee, A., Teraishi, K. and Miyamoto, A., "Molecular dynamics dimulation of enhanced oxygen ion diffusion in strained yttria-stabilized zirconia," *Appl. Phys. Lett.*, **73**, 1502-1504 (1998).

105. M'Peko, J.-C., Spavieri, D.L. and de Souza, M.F., "In situ characterization of th grain abd grain-boundary electrical responses of zirconia ceramics under uniaxial compressive stresses," *Appl. Phys. Lett.*, **81**, 2827-2829 (2002).

106. Macdonald, J.R., *Impedance Spectroscopy Emphasizing Solid Materials and Systems*, (John Wiley & Sons, New York, NY) 1987.

107. MacDonald, J.R., "Linear relaxation: distributions, thermal activation, structure, and ambiguity," *J. Appl. Phys.*, **62**, R51-R62 (1987).

108. Wightman, R.M., "Microvoltammetric electrodes," *Anal. Chem.*, **81**, 1125A-1134A (1981).

109. Fleig, J., "Microelectrodes in solid state ionics," *Solid State Ionics*, **161**, 279-289 (2003).

110. O'Hayre, R. and Prinz, F.B., "The air/platinum/Nafion triple-phase boundary: characteristics, scaling, and implications for fuel cells," *J. Electrochem. Soc.*, **151**, A756-A762 (2004).

111. Bieberle, A. and Gauckler, L.J., "Reaction mechanism of Ni pattern anodes for solid oxide fuel cells," *Solid State Ionics*, **135**, 337-345 (2000).

112. Bieberle, A., Meier, L.P. and Gauckler, L.J., "The electrochemistry of Ni pattern anodes used as solid oxide fuel cell model electrodes," *J. Electrochem. Soc.*, **148**, A646-A656 (2001).

113. Mizusaki, J., Tagawa, H., Saito, T., Yamamura, T., Kamitani, K., Hirano, K., Ehara, S., Takagi, T., Hikita, T., Ippommatsu, M., Nakagawa, S. and Hashimoto, K., "Kinetic studies of the reaction at the nickel pattern electrode on YSZ in H_2-H_2O atmospheres," *Solid State Ionics*, **70/71**, 52-58 (1994).

114. Brichzin, V., Fleig, J., Habermeier, H.-U. and Maier, J., "Geometry dependence of cathode polarization in solid oxide fuel cells investigated by defined Sr-doped $LaMnO_3$ microelectrodes," *Electrochem. Solid-State Lett.*, **3**, 403-406 (2000).

115. Brichzin, V., Fleig, J., Habermeier, H.-U., Cristiani, G. and Maier, J., "The geometry dependence of the polarization resistance of Sr-doped $LaMnO_3$ microelectrodes on yttria-stabilized zirconia," *Solid State Ionics*, **152-153**, 499-507 (2002).

116. Radhakrishnan, R., Virkar, A.V. and Singhal, S.C., "Estimation of charge-transfer resistivity of $La_{0.8}Sr_{0.2}MnO_3$ cathode on $Y_{0.16}Zr_{0.84}O_2$ electrolyte using patterned electrodes," *J. Electrochem. Soc.*, **152**, A210-A218 (2005).

117. Radhakrishnan, R., Virkar, A.V. and Singhal, S.C., "Estimation of charge-transfer resistivity of Pt cathode on YSZ electrolyte using patterned electrodes," *J. Electrochem. Soc.*, **152**, A927-A936 (2005).

118. Aryafar, M. and Zaera, F., "Kinetic study of the catalytic oxidation of alkanes over nickel, palladium, and platinum foils," *Catal. Lett.*, **48**, 173-183 (1997).

119. Erning, J.W., Hauber, T., Stimming, U. and Wipperman, K., "Catalysis of the electrochemical processes on solid oxide fuel cell cathodes," *J. Power Sources*, **6**, 205-211 (1996).

120. Mogensen, M. and Skaarup, S. "Kinetic and geometri adpects of solid oxide fuel cell electrodes," *Solid State Ionics*, **86-88**, 1151-1160 (1996).

121. Mitterdorfer, A. and Gauckler, L.J., "Identification of the reaction mechanism of the Pt, O_2(g)|yttria-stabilized zirconia system – part I: general framework, modelling, and structural investigation," *Solid State Ionics*, **117**, 187-202 (1999).

122. Mitterdorfer, A. and Gauckler, L.J., "Identification of the reaction mechanism of the Pt, O_2(g)|yttria-stabilized zirconia system – part II: model implementation, parameter estimation, and validation," *Solid State Ionics*, **117**, 203-217 (1999).

123. Mitterdorfer, A. and Gauckler, L.J., "Reaction kinetics of the Pt, O_2(g)|*c*-ZrO_2 system: precursor mediated adsorption," *Solid State Ionics*, **120**, 211-225 (1999).

124. Van Herle, J. and McEvoy, A.J., "Impedance characteristics of platinum electrodes on yttria-stabilized zirconia," *Ber. Bunsenges. Phys. Chem.*, **97**, 470-474 (1993).

125. Yoon, S.P., Nam, S.W., Kim, S.-G., Hong, S.-A. and Hyun, S.-H., "Characteristics of cathodic polarization at Pt/YSZ interface without the effect of electrode microstructure," *J. Power Sources*, **115**, 27-34 (2003).

126. Badwal, S.P.S., Bannister, M.J. and Murray, M.J., "Non-stoichiometric oxide electrodes for solid state electrochemical devices," *J. Electroanal. Chem.*, **168**, 363-382 (1984).

127. Verkerk, M.J., Hammink, M.W.J. and Burggraaf, A.J., "Oxygen transfer on substituted ZrO_2, Bi_2O_3, and CeO_2 electrolytes with platinum electrodes - I. electrode resistance by D-C polarization," *J. Electrochem. Soc.*, **130**, 70-78 (1983).

128. Sasaki, J., Mizusaki, J., Yamauchi, S. and Fueki, K., "Studies on electrode processes of stabilized zirconia cells by the complex impedance method," *Solid State Ionics*, **¾**, 531-535 (1981).

129. Lewis, R. and Gomer, R., "Adsorption of oxygen on platinum," *Surf. Sci.*, **12**, 157-176 (1968).

130. Weinberg, W.H. and Merrill, R.P., "Crystal field surface orbital-bond energy bond order (CFSO-BEBO) calculation of adsorption - II. Carbon monoxide, oxygen and carbon dioxide on platinum (111) and oxygen on nickel (111)," *Surf. Sci.*, **39**, 206-236 (1973).

131. Shkerin, S.N., "Model gauze electrode O_2,Pt/O^{2-}: effect of the cell's pretreatment and the single-crystal electrolyte orientation," *Russ. J. Electrochem.*, **39**, 863-866 (2003).

132. Shkerin, S.N., Gormsen, S. and Mogensen, M., "Studying the O_2, metal/O^{2-} (solid electrolyte) electrode system on model electrodes: the electrolyte surface layer properties," *Russ. J. Electrochem.*, **40**, 136-142 (2004).

133. Schwandt, C. and Weppner, W., "Kinetics of the oxygen, platinum/stabilized zirconia and oxygen, gold/stabilized zirconia electrodes under equilibrium conditions," *J. Electrochem. Soc.*, **144**, 3728-3738 (1997).

134. Firebaugh, S.L., Jensen, K.F. and Schmidt, M.A., "Investigation of high-temperature degradation of platinum thin films with an *in situ* resistance measurement apparatus," *J. Microelectromech. S.*, **7**, 128-135, (1998).

135. Jiran, E. and Thompson, C.V., "Capillary instabilities in thin, continuous films," *Thin Solid Films*, **208**, 23-28 (1992).

136. Stancovski, V., Sridhar, S. and Pal, U.B., "Thermodynamc stability and interfacial impedance of solid electrolyte cells with noble-metal electrodes," *J. Electroceram.*, **3**, 279-299 (1999).

137. Mizusaki, J., Amano, K., Yamauchi, S. and Fueki, K., "Electrode reaction at Pt,O_2(g)/stabilized zirconia interfaces – part I: theoretical consideration of reaction model," *Solid State Ionics*, **22**, 313-322 (1987).

138. Wang, D.Y. and Nowick, A.S., "Diffusion-controlled polarization of Pt, Ag, and Au electrodes with doped ceria electrolytes," *J. Electrochem. Soc.*, **128**, 55-63 (1981).

139. Wang, D.Y. and Nowick, A.S., "Cathode and anodic polarization phenomena at platinum electrodes with doped CeO_2," *J. Electrochem. Soc.*, **126**, 1155-1165 (1979).

140. Hartung, R., "Polarisationverhalten und Wechselstrombehandlung einer Pt/$Zr_{0.82}Y_{0.10}Mg_{0.08}O_{1.87}$, O_2-Elektrode," *Z. Phys. Chem. (Leipzig)*, **260**, 259-272 (1979).

141. Fabry, P. and Kleitz, M., "Influence of the metal and the electrolyte composition on the characteristics of the oxygen electrode reaction on solid oxide electrolyte," *J. Electroanal. Chem. Interface. Chem.*, **57**, 165-177 (1974).

142. Okamoto, H., Kawamura, G. and Kudo, T., "Study of oxygen adsorption on platinum through observation of exchange current in a solid electrolyte concentration cell," *Electrochim. Acta*, **28**, 379-382 (1983).

143. Winnubst, A.J.A., Scharenborg, A.H.A. and Burggraaf, A.J., "The electrode resistance of ZrO_2-Y_2O_3(-Bi_2O_3) solid electrolytes with Pt electrodes," *Solid State Ionics*, **14**, 319-327 (1984).

144. Mizusaki, J., Amano, K., Yamauchi, S. and Fueki, K., "Electrode reaction at Pt,O_2(g)/stabilized zirconia interfaces – part II: electrochemical measurements and analysis," *Solid State Ionics*, **22**, 323-330 (1987).

145. Kuzin, B.L. and Komarov, M.A., "Adsorption of O_2 at Pt and kinetics of the oxygen reaction at a porous Pt electrode in contact with a solid oxide electrolyte," *Solid State Ionics*, **39**, 163-172 (1990).

146. Verkerk, M.J. and Burggraaf, A.J., "Oxygen transfer on substituted ZrO_2, Bi_2O_3, and CeO_2 electrolytes with platinum electrodes - II. A-C impedance study," *J. Electrochem. Soc.*, **130**, 78-84 (1983).

147. Abeles, B., Sheng, P., Coutts, M.D. and Arie, Y., "Structural and electrical properties of granular metal films," *Adv. Phys.*, **24**, 407-461 (1975).

148. van Berkel, F.P.F., van Heuveln, F.H. and Huijsmans, J.P.P., "Characterization of solid oxide fuel cell electrodes by impedance spectroscopy and I-V characteristics," *Solid State Ionics*, **72**, 240-247 (1994).

149. Miller, N.C. and Shirn, G.A., "Co-sputtered Au-SiO_2 cermet films," *Appl. Phys. Lett.*, **10**, 86-88 (1967).

150. Miller, N.C., Hardiman, B. and Shirn, G.A., "Transport properties, microstructure, and conduction model of cosputtered Au-SiO_2 cermet films," *J. Appl. Phys.*, **41**, 1850-1856 (1970).

151. Zaidi, S.Z.A., Beynon, J., Steele, C.B. and Orton, B.R., "Thermoelectric power and d.c. conductivity of co-evaporated Mn/SiO_x cermet thin films," *Thin Solid Films*, **256**, 120-123 (1995).

152. Roux, J.F., Cabaud, B., Treilleux, M., Hoareau, A. and Fuchs, G., "Synthesis of size controlled nanoparticles in an insulating matrix," *Nanostruct. Mater.*, **6**, 525-528 (1995).

153. Gadenne, M., Gadenne, P., Martin, J.C. and Sella, C., "Composition and electrical properties of Au-Al_2O_3 cermet thin films: a critical study," *Thin Solid Films*, **221**, 183-190 (1992).

154. Gadenne, M., Schneegans, O., Houzé, F., Chrétien, P., Desmarest, C., Sztern, J. and Gadenne, P., "First AFM observations of thin cermet films close to the percolation threshold using a conducting tip," *Phys. B*, **279**, 94-97 (2000).

155. Hazra, S., Gibaud, A., Désert, A., Sella, C. and Naudon, A., "Morphology of nanocermet thin films: x-ray scattering study," *Phys. B*, **283**, 97-102 (2000).

156. Zakrzewska, K., Radecka, M., Kuk, A. and Osuch, W., "Noble metal/titanium dioxide nanocermets for photoelectrochemical applications," *Solid State Ionics*, **157**, 349-356 (2003).

157. Sundeen, J.E. and Buchanan, R.C., "Electrical Properties of nickel-zirconia cermet films for temperature and flow-sensor applications," *Sens. Actuators, A*, **63**, 33-40 (1997).

158. Sundeen, J.E. and Buchanan, R.C., "Thermal sensor properties of cermet resistor films on silicon substrates," *Sens. Actuators, A*, **90**, 118-124 (2001).

159. Sirinakis, G., Siddique, R., Dunn, K.A., Efstathiadis, H., Carpenter, M.A., Kaloyeros, A.E. and Sun, L., "Spectroellipsometric characterization of Au-Y2O3-stabilized ZrO2 nanocomposite films," *J. Mater. Res.*, **20**, 3320-3328 (2005).

160. Wang, L.S., Thiele, E.S. and Barnett, S.A., "Sputter deposition of yttria-stabilized zirconia and silver cermet electrodes for SOFC applications," *Solid State Ionics*, **52**, 261-267 (1992).

161. Barnett, S.A. and Tsai, T., "Solid-oxide fuel cells having nickel and yttria-stabilized anodes and method of manufacture," United States Patent 5,656,387.

162. Barnett, S.A. and Wang, L.S., "Solid-oxide fuel cells," United States Patent 5,395,704.

163. Wang, L.S. and Barnett, S.A., "Ag-perovskite cermets for thin film solid oxide fuel cell air-electrode applications," *Solid State Ionics*, **76**, 103-113 (1995).

164. Barnett, S.A. and Wang, L.S., "Ag-perovskite cermets for thin film solid oxide fuel cell air-electrode applications," United States Patent 6,004,696.

165. Hayashi, K., Yamamoto, O., Nishigaki, Y. and Minoura, H., "Sputtered Ni-yttria stabilized zirconia composite film electrodes for SOFC," *Denki Kagaku*, **64**, 1097-1101 (1996).

166. Hayashi, K., Yamamoto, O., Nishigaki, Y. and Minoura, H., “Sputtered $La_{0.5}Sr_{0.5}MnO_3$-yttria stabilized zirconia composite film electrodes for SOFC,” *Solid State Ionics*, **98**, 49-55 (1997).

167. Mitterdorfer, A. and Gauckler, L.J., “$La_2Zr_2O_7$ formation and oxygen reduction kinetics of the $La_{0.85}Sr_{0.15}Mn_yO_3$, $O_2(g)|YSZ$ system,” *Solid State Ionics*, **111**, 185-218 (1998).

168. Yamamoto, O., Chujyo, Y., Aoki, K. and Furuichi, T., “Platinum-stabilized zirconia composite solid oxide oxygen gas sensor,” *Sens. Actuators, B*, **13-14**, 31-33 (1993).

169. Torres-Huerta, A.M. and Vargas-Garcia, J.R., “Preparation and characterization of nano-composite electrodes by MOCVD,” *J. Metastable Nanocryst. Mater.*, **20-21**, 393-398 (2004).

170. Knoll, R.W. and Bradley, E.R., “Correlation between the stress and microstructure in bias-sputtered ZrO2 - Y2O3 films,” *Thin Solid Films*, **117**, 201-210 (1984).

171. Thornton, J.A., “Influence of apparatus geometry and deposition conditions on the structure and topography of thick sputtered coatings,” *J. Vac. Sci. Technol.*, **11**, 666-670 (1974).

172. Coating and Crystal Wafers, Inc. Personal Communication, February 2006.

173. Alconox, Inc., *Technical Bulletin*, (Alconox, Inc., White Plains, NY). Accessed 19 June 2006 at http://www.alconox.com/downloads/pdf/techbull_alconox.pdf

174. Moulder, J.F., Stickle, W.F., Sobol, P.E. and Bomben, K.D., *Handbook of X-ray Photoelectron Spectroscopy*, (Physical Electronics, Inc., Eden Prarie, MN) 1995.

175. Garvie, R.C. and Goss, M.F., “Intrinsic size dependence of the phase transformation temperature in zirconia microcrystals,” *J. Mater. Sci.*, **21**, 1253-1257 (1986).

176. Slavov, S.V., Sanger, A.R. and Chuang, K.T., “Mechanism of silation of alumina with hexamethyldisilazane,” *J. Phys. Chem. B.*, **102**, 5475-5482 (1998).

177. Matsumiya, M., Shin, W., Qiu, F., Izu, N., Matsubara, I. and Murayama, N., “Poisoning of platinum thin film catalyst by hexamethyldisiloxane (HMDS) for thermoelectric hydrogen gas sensor,” *Sens. Actuators, B*, **96**, 516-522 (2003).

178. Zhu, J., Albertsma, S., van Ommen, J.G. and Lefferts, L., “Role of surface defects in activation of O_2 and N_2O on Zr O_2 and yttrium-stabilized ZrO_2,” *J. Phys. Chem. B*, **109**, 9550-9555 (2005).

179. Ballabio, G., Bernasconi, M., Pietrucci, F. and Serra, S., “Ab initio study of yttria-stabilized cubic zirconia surfaces,” *Phys. Rev. B: Condens. Matter Mater. Phys.*, **70**, 075417 (2004).

180. Xia, C. and Liu, M., “Novel cathodes for low-temperature solid oxide fuel cells,” *Adv. Mater.*, **14**, 521-523 (2002).

181. Hyodo, T., Hertz, J.L. and Tuller, H.L., “Preparation of macroporous noble metal films by r.f. magnetron sputtering for electrochemical device applications,” in *Chemical Sensors VI: Chemical and Biological Sensors and Analytical Methods*, Bruckner-Lea, C., Vanysek, P., Hunter, G., Egashira, M., Miura, N. and Mizutani, F., eds., **2004-08**, 10-16 (Electrochemical Society Proceedings, Pennington, PA) 2004.

182. Yamamoto, N., M.S. thesis, Massachusetts Institute of Technology. In progress.

183. Mazanec, T.J., “Electropox gas reforming,” in *Ceramic Membranes*, Anderson, H.U., Khandkar, A. and Liu, M., eds., **95-24**, 16-28 (Electrochemical Society Proceedings, Pennington, PA) 1996.

184. Holm, R., *Electric Contacts Handbook*, 3^{rd} ed. (Springer-Verlag, Berlin) 1958.

185. Mamishev, A.V., Sundara-Rajan, K., Du, Y. and Zahn, M., "Interdigital sensors and transducers," *Proc. IEEE*, **92**, 808-845 (2004).

186. Sheppard, N.F., Tucker, R.C. and Wu, C., "Electrical conductivity measurements using microfabricated interdigitated electrodes," *Anal. Chem.*, **65**, 1199-1202 (1993).

187. Farnell, G., Cermak, I.A., Silvester, P. and Wong, S.K., "Capacitance and field distributions for interdigital surface-wave transducers," *IEEE Trans. Son. Ultrason.*, **SU-17**, 188-195 (1970).

188. Fleig, J. and Maier, J., "Finite element calculations of impedance effects at point contacts," *Electrochim. Acta*, **41**, 1003-1009 (1996).

189. Fleig, J. and Maier, J., "The influence of current constriction on the impedance of polarizable electrodes – application to fuel cell electrodes," *J. Electrochem. Soc.*, **144**, L302-L305 (1997).

190. Fleig, J. and Maier, J., "The influence of laterally inhomogeneous contacts on the impedance of solid materials: a three-dimensional finite-element study," *J. Electroceram.*, **1**, 73-89 (1997).